Understanding antifouling mechanisms of bio-inspired functional coatings and developing antifouling surfaces based on mussel-inspired wet adhesive chemistry

by

Sijia Li

A thesis submitted in partial fulfillment of the requirements for the degree of

Doctor of Philosophy

in

Chemical Engineering

Department of Chemical and Materials Engineering
University of Alberta

ABSTRACT

Bio-inspired antifouling materials have been widely studied in recent years in a variety of engineering fields, such as biomedical devices, marine industry, oil/water separation, and water treatment. However, studies on the corresponding intermolecular interactions between the bio-inspired antifouling materials and various contaminants including organic, inorganic foulants and biofoulants are still incomplete, significantly limiting the related fundamental research and practical applications. In this thesis, three original research works regarding the molecular design and engineering of bio-inspired antifouling materials are presented, and the surface interaction mechanisms between bio-inspired antifouling materials and mussel-inspired chemistry, proteins, silica, humic acid, and oil droplets are elucidated with the assistance of nanomechanical techniques based on atomic force microscope (AFM).

Lubricant-infused slippery surfaces have recently emerged as promising antifouling coatings, showing potential against proteins, cells, and marine mussels. However, a comprehensive understanding of the molecular binding behaviors and interaction strength of foulants to these surfaces is lacking. In the first work, mussel-inspired chemistry based on catechol-containing chemicals including 3,4-dihydroxyphenylalanine (DOPA) and polydopamine (PDA) was employed to investigate the antifouling performance and repellence mechanisms of fluorinated-based slippery surface, and the correlated interaction mechanisms were probed using AFM. Intermolecular force measurements and deposition experiments between PDA and the surface revealed the ability of lubricant film to inhibit the contact of PDA particles with the substrate. Further analysis using single-molecule force spectroscopy (SM-AFM) highlighted that the infused lubricant layer could remarkably influence the dissociation forces and weaken the binding strength

between DOPA and underneath per-fluorinated monolayer surface, offering deeper insights into the molecular binding behaviors that are essential for developing new antifouling materials.

Membrane fouling significantly impairs the efficiency and quality of contaminant removal in wastewater treatment. Understanding the molecular interactions between foulants and membranes, which drive foulant attachment and growth, is crucial for developing effective antifouling strategies. In the second work, typical contaminants that existed in water filtration systems including silica particles, bovine serum albumin (BSA), and humic acid (HA) were selected for the direct force measurements on polyvinylidene fluoride (PVDF) membranes with or without the modification of PDA or poly(sulfobetaine methacrylate) (PSBMA) employing an AFM. The interaction mechanisms driving adsorption and removal of various foulants on membranes with different wettability and surface chemistry were quantitatively analyzed using extended Derjaguin-Landau-Verwey-Overbeek (DLVO) theory. Adhesion energy from retraction curves indicated the release and regeneration ability of membranes. PDA-functionalized membranes exhibited good antifouling performance against silica but were less effective against organic foulants due to the influence of many intermolecular forces such as hydrophobic attraction, π-interactions, and hydrogen bonding. PSBMA-modified membranes showed excellent fouling resistance and self-cleaning capabilities, driven by dominant repulsive electric double layer (EDL) and hydration forces.

Developing novel membrane materials for oil-in-water (O/W) emulsion separation is of both fundamental and practical significance, but challenging, due to the serious membrane fouling issues. In the third work, a conductive antifouling coating formed by a conductive polymer blend of poly(3,4-ethylenedioxythiophene) and polystyrene sulfonate (PEDOT:PSS) and PSBMA was prepared on PVDF membrane. Electrochemical atomic force microscopy (EC-AFM) was employed to simultaneously probe the interfacial interaction mechanisms of different membranes with oil droplets at the nanoscale, which demonstrated that the conductive membranes possessed adjustable surface charge properties with the modulation of the electrochemical potentials, resulting in tunable EDL interaction to achieve adaptive antifouling performance in response to the emulsions. Filtration measurements demonstrated that adjusting the surface charge properties of the membranes could enhance antifouling performance, leading to high oil removal efficiency (99.9%) and improved membrane reusability (89%) when -0.4 voltages were applied.

This thesis work provides fundamental understandings of fouling resistance mechanisms of diverse bio-inspired materials at the molecular level and expands the application of marine mussels-derived interactions in the development of antifouling surfaces, which offers useful implications on developing novel antifouling strategies by manipulating interfacial interactions for various engineering applications such as oil production, water treatment and other industrial processes.

PREFACE

This thesis is an original work conducted by Sijia Li under the supervision of Dr. Hongbo Zeng, containing published and submitted contents from the peer-reviewed journals.

Part of **Chapter 1** has been published as Li, S.; Chen, J.; Wang, J.; Zeng, H., Anti-biofouling Materials and Surfaces based on Mussel-inspired Chemistry. *Mater. Adv.,* 2021, 2, 2216. Sijia Li was responsible for the manuscript composition, data collection, formal analysis, investigation, writing – original draft, writing – review & editing, visualization. Dr. Jingsi Chen and Dr. Jingyi Wang contributed to the manuscript revision. Dr. Hongbo Zeng was the supervisory author and got involved in the manuscript composition, writing – review & editing, visualization and funding acquisition.

Chapter 3 has been published as Li, S.; Zhao, Z.; Wang, J.; Xie, L.; Pan, M.; Wu, F.; Hu, Y.; Liu, J.; Zeng, H., Molecular Interaction Mechanisms Between Lubricant-infused Slippery Surfaces and Mussel-inspired Polydopamine Adhesive and DOPA Moiety, *Macromolecular Rapid Communications, 2024, 2400276*. Sijia Li was responsible for material synthesis, experimental design, data collection and analysis, as well as manuscript composition. Dr. Ziqian Zhao was responsible for validation and writing – review & editing. Dr. Jingyi Wang and Dr. Lei Xie helped with conceptualization, methodology and writing – review & editing. Dr. Mingfei Pan contributed to AFM measurement and Feiyu Wu helped with SEM and XRD measurement. Dr. Ying Hu and Dr. Jifang Liu helped with writing – review & editing. Dr. Hongbo Zeng was the supervisory author and got involved in the manuscript composition, writing – review & editing, visualization and funding acquisition.

Chapter 4 has been submitted as Li, S.; Wang, J.; Yang, D.; Zhao, Z.; Zhou, C.; Sun, Y.; Peng, X.; Zeng, H., Probing the Intermolecular Interaction Mechanisms Between Foulants and Membranes: Implications for Antifouling Properties of Water Treatment Membrane, *Water Research, 2024*. Sijia Li was responsible for membrane preparation, data collection and analysis, as well as the manuscript composition. Dr. Jingyi Wang contributed to conceptualization, methodology design, data analysis and manuscript revision. Dr. Diling Yang helped AFM force measurement. Dr. Ziqian Zhao helped conduct the polymer synthesis and SEM/XRD experiment. Dr. Chengliang Zhou helped with graphic visualization. Yongxiang Sun and Dr. Xuwen Peng contributed to the manuscript revision. Dr. Hongbo Zeng was the corresponding author and involved in the experimental design, manuscript composition, writing – review & editing and funding acquisition.

Chapter 5 has been submitted as Li, S., Wang, J.; Yang, D.; Zhao, Z.; Sun, Y.; Peng, X.; Zeng, H., Enhanced Separation Performance of Conductive PEDOT:PSS/PSBMA Coated PVDF Membrane for Emulsified Oily Wastewater Treatment under Electrochemical Assistance, *Advanced Functional Materials, 2024*. Sijia Li was responsible for membrane preparation, data collection and analysis, as well as the manuscript composition. Dr. Jingyi Wang contributed to conceptualization, methodology design, data analysis and manuscript revision. Dr. Diling Yang helped AFM force measurement. Dr. Ziqian Zhao helped conduct the polymer synthesis and SEM/XRD experiment. Yongxiang Sun and Dr. Xuwen Peng contributed to the manuscript revision. Dr. Hongbo Zeng was the corresponding author and involved in the experimental design, manuscript composition, writing – review & editing and funding acquisition.

Dedicate to

My Parents Mr. Feng Li and Ms. Qunying Li

My Little One

ACKNOWLEDGMENTS

I would like to express my deepest gratitude to my supervisor, Dr. Hongbo Zeng, for his unwavering support, guidance, and encouragement throughout my doctoral studies. I am also grateful to Dr. Hao Zhang, Dr. Qi Liu, Dr. Lingyun Chen, and Dr. Zhibin Yu for serving as my committee members as well as providing their valuable feedback and insightful discussions, which have greatly enriched the quality of this work.

I would also like to thank Dr. Jingyi Wang, who has been a constant source of inspiration and motivation, providing assistance and encouragement both in academic pursuits and in navigating life's challenges. My heartfelt appreciation goes to my colleagues Dr. Ziqian Zhao, Dr. Diling Yang, Dr. Xuwen Peng, Yongxiang Sun, and Dr. Zhuo Chen for their collaboration, support, and friendship.

I would like to acknowledge the financial support provided by Alberta Innovates, and the lab facilities supported by Natural Sciences and Engineering Research Council of Canada (NSERC), Canada Foundation for Innovation (CFI) and Department of Chemical and Materials Engineering at the University of Alberta, which enabled me to pursue my research goals and contribute to the advancement of knowledge in nanotechnology.

Lastly, I want to extend my sincere appreciation to my family members for their unconditional love, encouragement, and sacrifices.

TABLE OF CONTENTS

LIST OF FIGURES

LIST OF ABBREVIATIONS

PEG	poly(ethyleneglycol)
SLIPs	slippery liquid-infused porous surfaces
Mfps	mussel foot proteins
DOPA	3,4-dihydroxyphenylalanine
PDA	polydopamine
preCOLs	pre-polymerized collagens
PS	polystyrene
SI-ATRP	surface-initiated atom transfer radical polymerization
RAFT	reversible addition fragmentation transfer polymerization
NPs	nanoparticles
PTFE	polytetrafluoroethylene
PE	polyethylene
PVDF	polyvinylidene fluoride
RO	reverse osmosis
PSBMA	poly(sulfobetaine methacrylate)
BSA	Bovine Serum Albumin
NF	nanofiltration

GO	graphene oxide
LBL	layer-by-layer
PDMS	polydimethylsiloxane
HA	humic acid
QCM-D	quartz crystal microbalance with dissipation
AFM	atomic force microscopy
SM-AFM	single-molecule force spectroscopy based on AFM
VDW	van der Waals
EDL	electrical double layer
p	pressure
R	radius
HB	hydrophobic
SFA	surface force apparatus
DLVO	Derjaguin-Landau-Verwey-Overbeek
A_H	Hamaker constant
h	separation distance
κ	inverse Debye length
ε_0	the vacuum permittivity

ε	dielectric constant
φ	respective surface potentials
σ	respective surface charge density
C_0	constant relevant to the surface wettability
D_0	the decay length of hydrophobic interaction
SRYL	Stokes–Reynolds–Young–Laplace
γ	interfacial tension
PFO	perfluorooctane
F_{mpr}	most probable rupture forces
F_{ad}	adhesion force
MW	molecular weights
OTS	octadecyltrichlorosilane
r	the radical coordinate
μ	the dynamic viscosity
Π	overall disjoining pressure
θ	the static water contact angle
rms	root-mean-square
NaOH	sodium hydroxide

NaCl	Sodium chloride
HCl	hydrogen chloride
$CaCl_2$	Calcium chloride
SiO_2	silicon dioxide
k_B	the Boltzmann constant
e	the fundamental charge of an electron
XPS	X-ray photoelectron spectroscopy
FTIR	Fourier transformation infrared spectroscopy
SI	Supporting information
ΔG	Free energy

CHAPTER 1 INTRODUCTION

1.1. Background

1.1.1. Introduction of fouling issues

Fouling issues are generally initiated by the adsorption and accumulation of undesired substances such as mineral scales, oils, proteins, and microorganisms on the materials surface, and subsequently induce severe consequence such as destruction of the industrial devices or infection in biosystems, which attracts a great amount of attention in the past decade.[1] Generally, the fouling materials consist of either living organisms (refers to biofouling) or a non-living substance including inorganic and organic materials.[2,3] Biofouling, the colonization and growth of proteins, bacteria, microorganisms, or even animals on submerged surfaces, usually occurs in aquatic environments including marine and freshwater systems.[4,5] Especially in marine environment, fouling by living organisms is problematic and complex. It is reported that more than 4000 types of organisms including microorganisms, plants algae and animals are responsible for marine biofouling, which leads to biofilm formation, bacteria adhesion and attachment of large organisms.[6,7] These serious situations could result in additional functional and monetary costs to various vessels, such as reduced hull strength and fuel efficiency, high dry-dock maintenance costs and bio-corrosion problems.[8] Inorganic fouling typically comprises the deposition of mineral scales, such as calcium carbonate, silica, or iron oxide, which are commonly found in water systems. These deposits can obstruct flow passages, decrease heat transfer efficiency, and result in corrosion-related issues.[9] Organic fouling, on the other hand, involves the accumulation of organic compounds, such as oils, greases, or polymers on surfaces.[10] This type of fouling is encountered in various industrial processes, including food and beverage production, wastewater treatment, and oil refining. Organic fouling not only reduces operational efficiency but also poses hygiene and sanitation concerns, compromising product quality and safety.[11] Therefore, developing effective antifouling surfaces to prevent or eliminate the accumulation of fouling substances is highly desirable and economically significant to industries in diverse areas.

1.1.2. Development of antifouling strategies

To overcome the undesired fouling issues and associated side effects, fouling mechanisms and antifouling strategies have been widely investigated. The surface fouling issues can be mitigated through well-designed interfaces using a combination of passive (preventing adhesion) and active (detaching or degrading) strategies.[12] Since fouling behavior is initiated and mediated by the contact and attachment of foulants, one of the most effective ways to inhibit contaminant adsorption and accumulation is modifying the surfaces with fouling-repellent coatings. For example, antifouling properties have been achieved through functionalizing substrate surfaces with hydrophilic polymers such as poly(ethyleneglycol) (PEG) [13–15] and zwitterionic molecules [16–18] to resist oil and protein adsorption and reduce biofilm attachment. The key to their fouling-resistant properties is the steric exclusion effect and strongly hydrated charge groups on the hydrophilic polymer surfaces, which increases the energetic penalty removing the surface hydration layer during the attachment of contaminants.[19] For active strategies, biocides were commonly employed to prevent bio-foulants from attaching to the surfaces in early studies. Researchers designed a variety of coatings which steadily release biocidal compounds such as antibiotics, silver particles or nitric oxides into the surrounding environments to effectively degrade or even kill the fouling organisms.[20–22] However, due to the damage to the natural environment and human health, this type of material has been avoided, and other viable natural alternatives such as chitosan,[23] capsaicin[24] and enzymes[25] are attracting increasing attention to improve this strategy. Moreover, electrocatalysis and photocatalysis for water treatment is considered an advanced active antifouling method with high efficiency in recent years.[26,27] Anodic oxidation or light energy is able to form reactive oxygenated species (ROS) via oxidation of water at the interface, which can react directly with organic pollutants at the interface or form hydrogen peroxide, releasing it into solution for subsequent degradation reactions.[28,29]

1.1.3. Bio-inspired antifouling strategies

In recent years, natural creatures have inspired the development of numerous antifouling platforms with outstanding and universal antifouling performances. One novel strategy is based on the modulation of surface wettability mimicking the surface structures of biological materials. For example, inspired by the self-cleaning lotus leaf and fish scales, superhydrophobic and underwater superoleophobic surfaces have been developed by constructing special surface topographies with less anchoring points on the substrates, which significantly minimize the contact between potential contaminants and the surfaces and inhibit the adhesion of fouling substances. [30,31] Similarly, slippery liquid-infused porous surface (SLIPS) approach is developed based on the Nepenthes pitcher plants, which has shown powerful fouling resistance by infiltrating low-surface-energy porous or roughened solids with lubricating liquids to form a stably immobilized and low friction omniphobic surface. The SLIPS mainly use fluoropolymer/perfluorocarbons and elastomeric silicone binders as substrates due to their low surface energy and modulus.

Both properties facilitate the dynamic adsorption process of undesired species on the surface; specifically, low surface energy dominates the initial attachment of foulants to a surface due to the weak attractive van der Waals force between the foulants and substrates, while low modulus of the fluoropolymer /perfluorocarbons surface promotes the release of contaminants by allowing the hydrodynamic force to wash off the attachments.[32,33] Moreover, the antifouling performance is further enhanced by the addition of nonreactive liquid slip agents such as lubricant, showing powerful omniphobic capability to resist fouling liquids or organisms.[34,35]

In addition to the bio-inspired designs of nanostructures, the multi-functionality of natural components can also be mimicked and utilized to functionalize material surfaces.[36–38] Many bio-inspired hydrogels or surfaces were designed based on the natural polymer-based materials, such as proteins (e.g., collagen, gelatin, and fibrin), and polysaccharides (e.g., alginate chitosan, hyaluronic acid, dextran).[39,40] For example, Tang et al. prepared the antifouling hydrogel coating by adjusting the proportion of positive and negative charges of chitosan and dextran, which effectively resisted bacterial and cellular adsorption.[41] Buzzacchera et al. functionalized bioinspired chitosan hydrogels with efficient synthetic polymer brushes, and the polymer brush-coated chitosan layers displayed excellent antifouling performance against protein adsorption and eliminated platelet activation and leukocyte adhesion.[42] Lately, antifouling materials inspired by the adhesive secretions of marine mussels have attracted considerable interests.[43,44] In the following section, recent advances in mussel-inspired chemistry and its emerging applications in fabricating antifouling platforms will be introduced in details.

1.2. Mussel-inspired antifouling materials

The mussel foot proteins (Mfps) secreted by mussels could form a strongly adhesive interaction with various substrates in wet environment, allowing the mussels adhere on almost all types of substrates. It has been reported that 3,4-dihydroxyphenylalanine (DOPA), a critical functional component in Mfps, plays a critical role in the versatile adhesion properties of marine mussels. Various molecular interactions are detected in DOPA and its derivatives such as dopamine and polydopamine (PDA), which are commonly referred to as "DOPA chemistry" and have sprouted the development of many mussel-inspired materials such as functional coatings and hydrogels with diverse properties.[45,46] Mussel-inspired chemistry has been widely implemented in surface and interface engineering for multipurpose functionalization to construct superior interfaces, especially in aqueous environments.[47,48] In the antifouling area, much effort has been dedicated to the preparation of antifouling materials through DOPA chemistry-mediated cohesion and adhesion mechanisms.[49–51] Dopamine has the advantage of deposition and self-polymerization over various inorganic and organic substrates by forming PDA layers in the mild alkaline condition.[43] The hydrophilic PDA layers with intrinsic fouling resistance property[52,53] and intrinsic antimicrobial activity[53,54] behave as protective coatings to mitigate the fouling caused by proteins and microorganisms. Moreover, the catechol-containing molecules can react with various functional groups as adhesive agents due to the versatile adhesion derived from DOPA chemistry, constructing many inorganic/organic composite materials with excellent antifouling performance via surface modification or direct assembly.[55–58] During the preparation process of diverse antifouling materials, mussel-inspired chemistry could act as different roles such as surface modifiers, intermediate layers or adhesive moieties to bind other components for functionalizing materials with antifouling performance (Fig. 1-1).

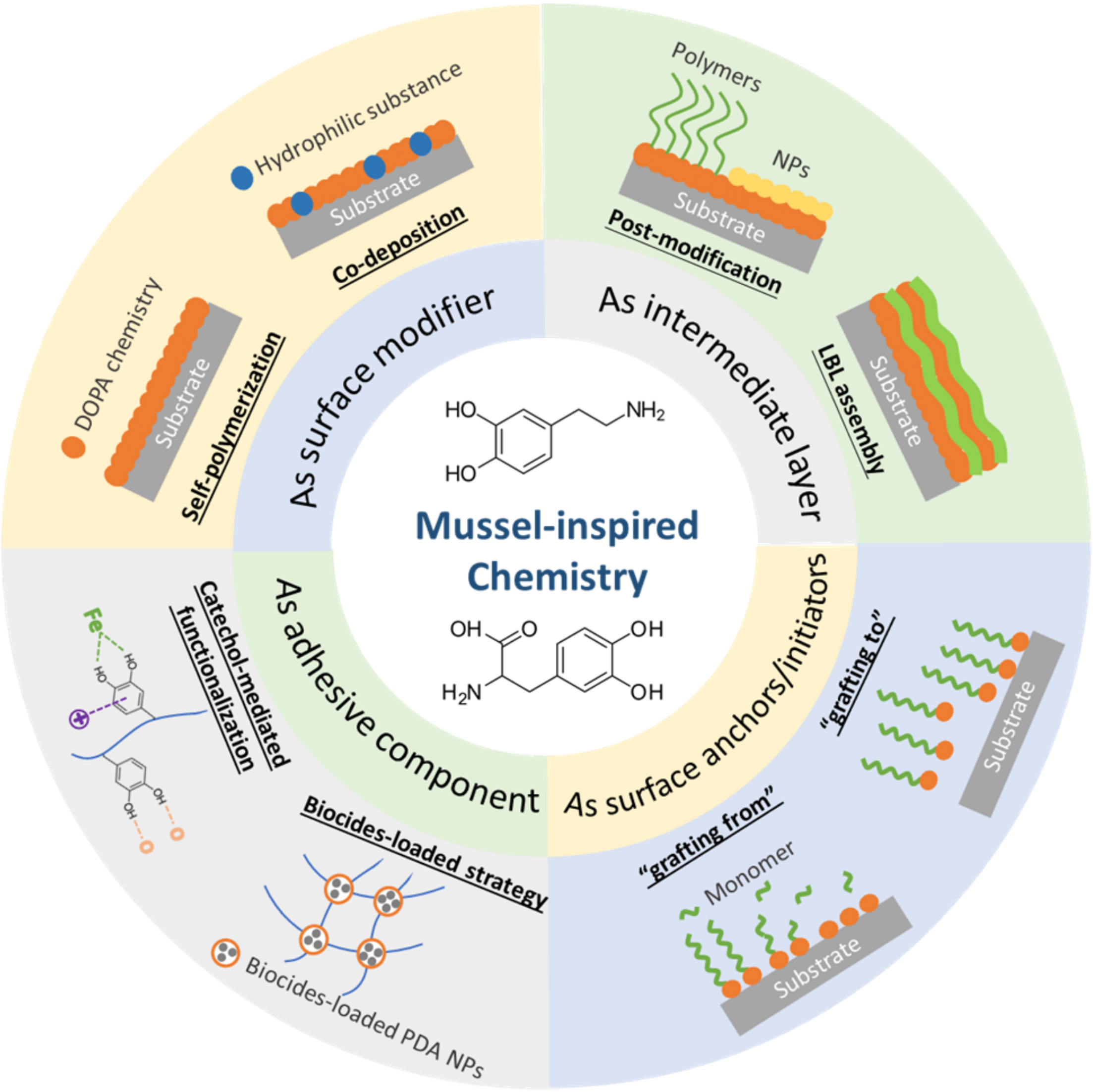

Fig. 1-1 The roles of mussel-inspired chemistry in the fabrication of antifouling materials and the associated preparation strategies.

1.2.1. Mussel adhesion mechanisms

Mussels tether themselves to diverse surfaces underwater such as rocks, metal, wood and even some well-known low-fouling materials like Teflon by the secreted adhesive foot proteins, via the formation of mussel byssus consisting of adhesive thread and plaque.[59–61] Upon the immobilization of the mussel foot to the desired attachment location, Mfps can form an adhesive plaque that securely anchors the mussel to substrate surface even under waves with high shear forces. It is reported that the byssus consists of over twenty different known protein components, in which the six types of important Mfps namely Mfp 1-6 have been well investigated and considered to have played critical roles in mussel adhesion. A schematic for the distribution of Mfp 1-6 confined to the byssal thread and plaque is shown in Fig. 1-2(a) and Fig. 1-2(b).[62] Mfp-1 is the first identified phenolic protein with a large molecular weight of ~108 KDa, which forms protective and stiff cuticles covering the byssal threads and plaques via oxidation or metal ion-mediated cross-linking.[63,64] Mfp-2 is the most abundant structural and cohesive component located in the inner part of the plaque, contributing to 25%-40% of the plaque proteins.[65,66] Mfp-3 and Mfp-5 are adhesive proteins with relatively small molecular mass and different variants located at the interface between the plaque and substrates, both of which are considered to act as important interfacial primers for mussel adhesion.[67–70] Mfp-4 is proposed to serve as a coupling agent at the thread-plaque junction to connect the pre-polymerized collagens (preCOLs) in the inner core of byssal thread and Mfp-2 in plaque.[71,72] Mfp-6 contains cysteine thiols, which creates an environment for redox reaction of the adhesive substances in the proteins.[73]

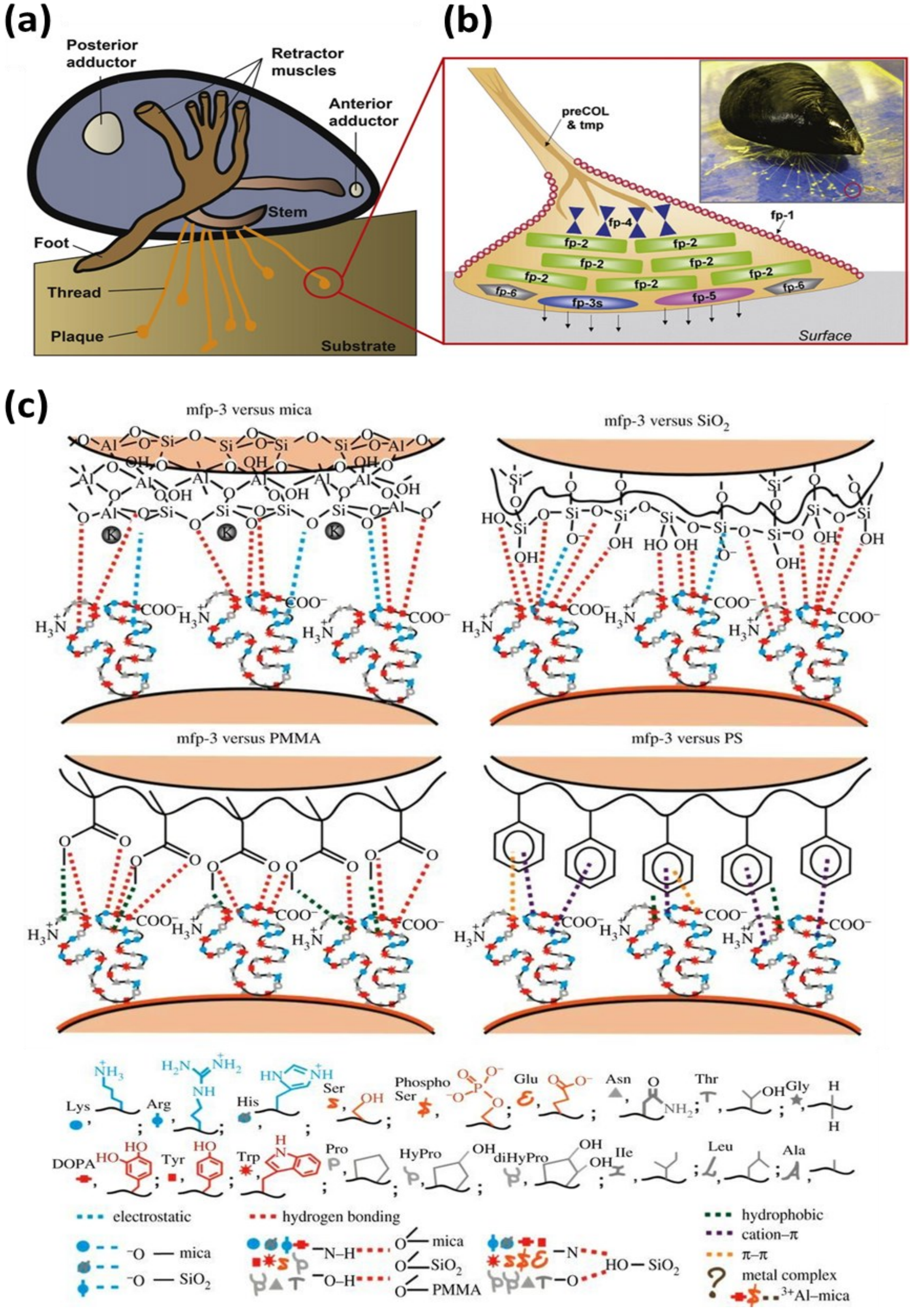

Fig. 1-2 (a) Schematic of a marine mussel that attaches to a substrate via byssal threads underwater. (b) Schematic of an enlarged byssal plaque (red circle in (a)) which

illustrates the approximate distribution of various mussel foot proteins (Mfps), with the inset showing a marine mussel attaching on a mica sheet. Reproduced with permission.[62] Copyright 2010, The American Society for Biochemistry and Molecular Biology. (c) Illustration of interaction mechanisms between Mfp-3 and four different surfaces (i.e., mica, SiO_2, polymethyl methacrylate (PMMA) and polystyrene (PS)). Reproduced with permission.[59] Copyright 2013, The Royal Society.

Previous studies have shown that the six mussel adhesive proteins in the byssus possess repetitive decapeptide sequences with a high DOPA content, demonstrated to mediate their high adhesion strength.[74,75] In particular, Mfp-3 and Mfp-5 found at the adhesive interface contain the highest content of DOPA residues (25 mol%-30 mol%) than other Mfps, indicating that DOPA plays a key role in achieving remarkable adhesion of mussel to diverse surfaces.[67,70] Various fundamental studies using nanomechanical techniques such as surface forces apparatus (SFA) and atomic force microscope (AFM) were conducted to investigate the interaction mechanisms of Mfps as well as single DOPA moiety to various substrates. For example, Lu et al. investigated and compared the molecular interaction forces between different Mfps (Mfp-1, Mfp-3, Mfp-5) and various surface chemistries by SFA, as shown in Fig. 1-2(c).[59] All Mfps showed adhesive versatility to both hydrophilic and hydrophobic substrates. It was reported that for hydrophilic surfaces like mica, the protein-surface adhesion mainly resulted from hydrogen bonding interaction between phenolic hydroxyl group and hydrogen-bonding acceptors, as well as the formation of covalent bonds. While hydrophobic or π-π interaction played a crucial role when catechol contacted non-polar polymers such as polystyrene (PS). The wet adhesion strength of Mfps to substrates depended on various factors such as the interplay of different amino acids, protein molecular weights and protein chain flexibility. Among them, the interactions of DOPA are one of the most essential contributors to Mfps adhesion to different surfaces. The interaction force of a single DOPA moiety with substrates such as Ti was characterized by single molecule force spectroscopy experiments using AFM, improving the fundamental understanding of adhesion between DOPA units and substrates in water.[76] Various interactions including hydrogen bonding, metal-catechol coordination, electrostatic, cation-π, anion-π and π-π aromatic interactions have been demonstrated to contribute to the versatile DOPA-mediated underwater adhesion to different substrates.[62,77–83]

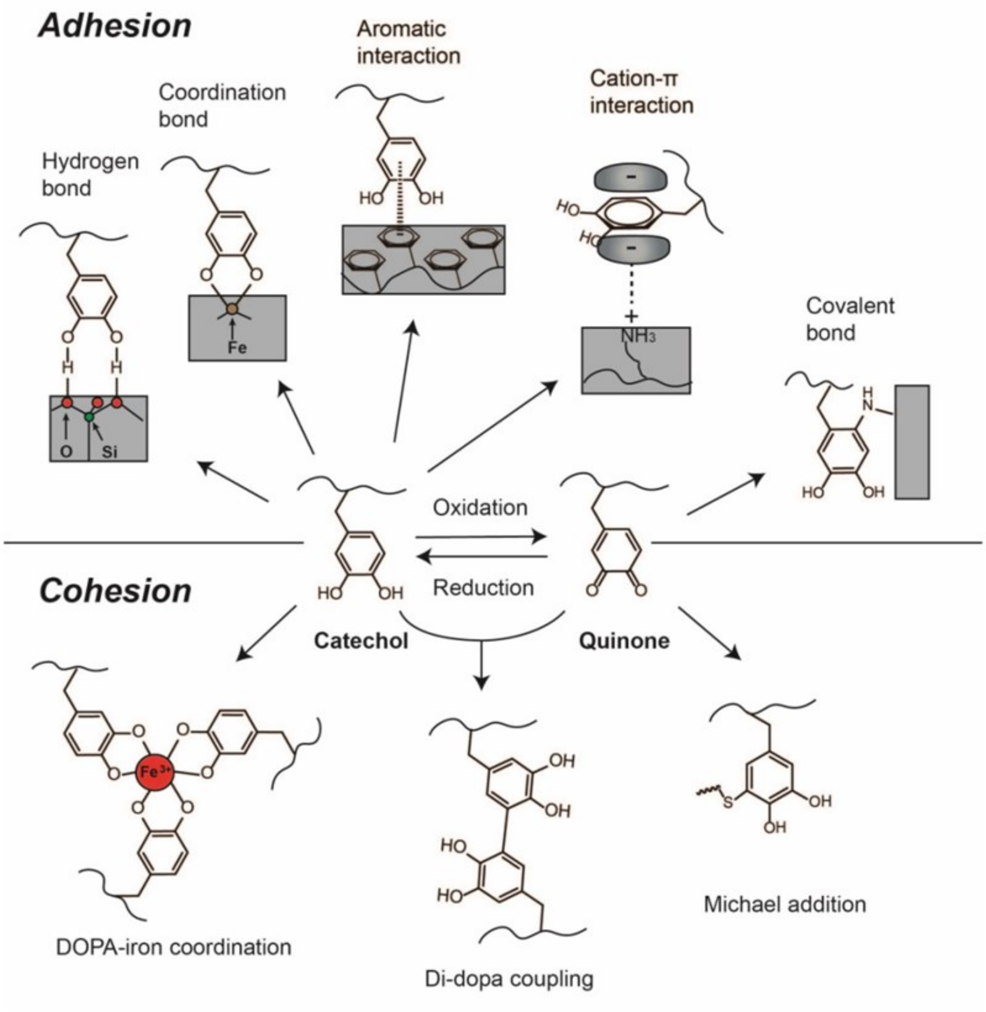

Fig. 1-3 DOPA-mediated reaction chemistry for adhesion and cohesion interactions. Reproduced with permission.[51] Copyright 2016, Elsevier.

To date, attributed to the strong and universal adhesion ability of catechol structure, DOPA chemistry, occurred in DOPA as well as its derivatives such as dopamine and PDA, has been employed for wide applications such as surface modification, and preparation of medical adhesives and biomaterials. In synthetic materials, the catechol structure of DOPA is often used for both adhesion (binding to substrates) and cohesion (crosslinking of the adhesive material) (Fig. 1-3).[84,85] Several strategies have been used for oxidizing or crosslinking DOPA to form covalently grafted functional layers, including reacting DOPA with various functional groups (e.g., thiols, amines) via Michael addition or Schiff base reaction.[58,86] Besides, the redox transition between catechol and quinone in mild condition enables a facile grafting and anchoring of polymer chains onto the catechol-modified surfaces through surface-initiated atom transfer radical polymerization (SI-ATRP) and reversible addition fragmentation transfer polymerization (RAFT).[87,88] Furthermore, the catechol and amino groups could also serve as nucleation sites to chelate metal ions, which usually act as the cross-linking points in the metal ion-bridged polymers and hydrogels.[89,90] For example, DOPA can form various complexes with Fe^{3+}, including bis- and tris-complexes of DOPA-Fe^{3+} coordination under alkaline environment, leading to strong cohesion of polymers, which indicates that catechols can interact with Fe^{3+} to form pH-dependent reversible cross-linking of materials.[91,92]

Moreover, catechol structure can form crosslinking networks via autoxidation and self-polymerization in alkali solutions, forming a PDA thin film attached on the substrates.[86,93] Till now, there is no final conclusions on the adhesion mechanisms and structures of the PDA yet. Several studies suggested that PDA is a supramolecular aggregate consisting of 5,6-dihydroxyindoline and its derivatives formed by charge transfer, π-π stacking and hydrogen bonding.[94,95] Similar to DOPA, PDA contains active groups including catechol and amine groups and can also trigger interfacial interactions with other functional groups. The DOPA-mediated adhesion and cohesion mechanisms have cultivated an effective and simple strategy for biomaterial synthesis and functionalization. The various physical and chemical interactions offered by DOPA chemistry have motivated the development of many functional materials.

1.2.2. Mussel-inspired antifouling membranes

The surface engineering of membranes has attracted much attention since the new generation of polymer membranes are required to meet the needs of both high permeation performance and multi-functional properties. The water permeation performance and fouling resistance property are usually determined by the membrane surface properties including wettability, charge, surface chemistry and roughness, etc.

In general, compared with hydrophobic surfaces, hydrophilic surfaces show better wettability and fouling resistance, which increases water permeation flux and limits foulants adsorption on the surface and pores of membrane by decreasing the hydrophobic attraction between organic substances and hydrophobic membrane surfaces. However, as many commercial polymer membranes are made of hydrophobic materials, surface fouling issue becomes one of the most crucial problems during the filtration process. To improve the performance of membranes, membrane hydrophilization strategies have been motivated and exploited to construct antifouling surfaces. Dopamine has been proven as an ideal candidate to minimize membrane fouling, which deposits and forms a self-polymerized PDA coating on the membrane surfaces under base condition. PDA strongly attaches to various substrates and displays hydrophilicity because of the presence of many hydrophilic functional groups such as carboxy, amino, imine and phenol groups. Dopamine deposition is generally a stable and controllable process, which can be adjusted by changing pH, dopamine concentration, deposition time and atmosphere. Zhu and coworkers reported dopamine as hydrophilic modifiers for hydrophobic polymer membranes.[96] Dopamine was oxidized and self-polymerized, which generated hydrophilic PDA coating on the membrane surface, leading to a 20%-30% decrease in the water contact angles of hydrophobic membranes including polytetrafluoroethylene (PTFE), polyethylene (PE), polyvinylidene fluoride (PVDF). According to the reports, the water contact angles of membranes after PDA deposition generally reduce to the range of 37-90°, depending on the inherent wettability of original membranes.[97] In addition, some DOPA-derivatives such as PDA and poly (3-(3,4-Dihydroxyphenyl)-L-alanine (L-DOPA)) molecules are proven to exhibit zwitterionic property due to the presence of diverse functional groups containing both positively-charged (amino group) and negatively-charged (phenolic hydroxyl and carboxylic acid) groups.[98,99] For example, the isoelectric point of PDA is determined to be around pH 4. At high pH, it exhibits net negative charge because of the deprotonation of the phenolic groups. Whereas at pH values below the isoelectric point, the amino groups will be protonated, leading to a positively-charged PDA layer on the membrane surface.[100] In this case, the membrane surfaces could be modified by the deposition of PDA or poly (L-DOPA) films with zwitterionic property to enhance the antifouling performance. Zou et al. applied self-polymerized L-DOPA film to form a zwitterionic coating on reverse osmosis (RO) membranes to alter their surface properties for fouling-resistant purposes, where the coated membranes showed an increase of water permeability and improved fouling resistance to the proteins and organic foulants. [99,101] However, for the pure PDA-coated membranes, the presence of aromatic rings would limit the hydrophilicity in PDA coating, and the pores of membranes could also be easily blocked by PDA aggregates, which limit the permeation and antifouling performance of modified membranes. To address these problems, a one-step co-deposition approach has been developed to introduce other hydrophilic species into PDA layers to further improve the hydrophilicity and antifouling property of membranes. Chen et al. constructed a composite layer by co-deposition of dopamine and non-ionic polymers such as polyvinyl alcohol (PVA) and PEG onto PVDF membranes (Fig. 1-4(a)).[102] The results suggested that the hydrophilicity and surface free energy of all modified membranes were significantly enhanced, which improved the hydration capability, oil/water separability and protein fouling resistance. In addition, dopamine was also reported to co-deposit with polyethyleneimine (PEI) to functionalize membranes.[103] Dopamine could react with PEI via Schiff base or Michael addition reaction, which effectively inhibits the non-covalent interactions among dopamine molecules thus reduces the PDA aggregation. As an amino-rich polymer, the interposition of PEI also provides hydrophilic groups for further hydrophilization. The addition of PEI significantly decreased the surface roughness of PDA coatings, thus improving water flux and reducing membrane fouling. Likewise, Zhang et al. modified polyacrylonitrile (PAN) membranes by the co-deposition of PDA, PDA/PEI, PDA/Co^{2+}, and PDA/PEI/Co^{2+}, which resulted in the water contact angles of 55°, 41°, 27°, and 18°, respectively.[104] As shown in Fig. 1-4(b), during the coating process, dopamine monomers can react with PEI and Co^{2+} in the ternary coating system through covalent bonds (PDA/PEI) or coordination bonds (PDA/Co^{2+}) to limit the formation of PDA aggregates, constructing a much thinner and smoother coating layer without blocking the membrane pores, as compared to the conventional PDA deposition methods. The covalent bond (CB)/coordination bond (COB) competitive reactions in the ternary coating system affected the hydrophilicity, thickness and roughness of the membrane surface, facilitating the fabrication of membranes with ultra-high permeance and excellent antifouling ability.

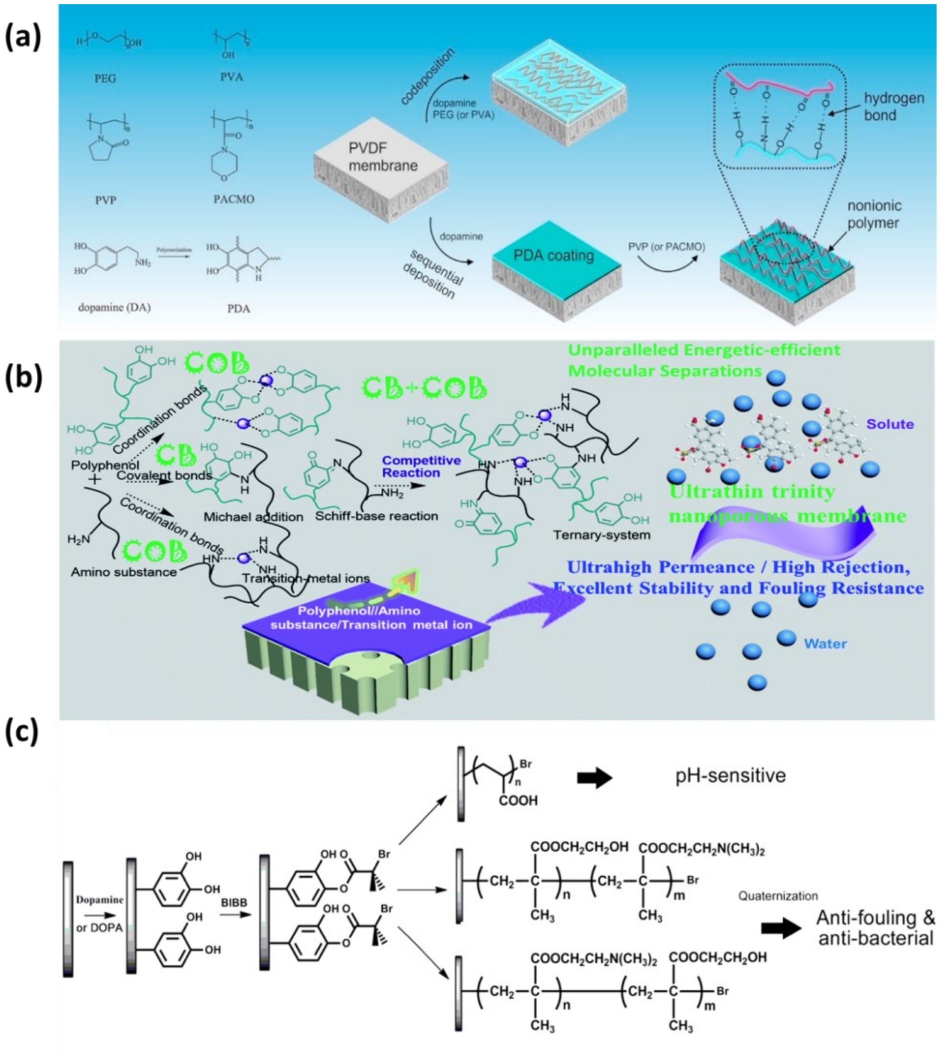

Fig. 1-4 (a) Illustration for the immobilization of non-ionic polymers on the PVDF membranes by applying mussel-inspired chemistry. Reproduced with permission.[102] Copyright 2017, Elsevier. (b) The scheme of the fabrication process of the ultrathin

trinity coating via covalent bond (CB)/coordination bond (COB) competitive reactions. Reproduced with permission.[104] Copyright 2020, The Royal Society of Chemistry. (c) Schematic diagram illustrating the process of SI-ATRP from the PVDF membrane for polyacrylic acid (PAA), poly(hydroxyethyl methylacrylate (HEMA)-g-dimethylamino ethyl methacrylate (DMAEMA)) and poly(DMAEMA-g-HEMA) grafting. Reproduced with permission.[105] Copyright 2012, Elsevier.

Beside direct deposition method, dopamine or PDA could also serve as a versatile intermediate layer for post-modification to introduce other functional materials to further modify the PDA-coated membranes. The membranes are pre-modified with PDA layers, which act as adherent platform to immobilize both organic and inorganic components such as polymers, oligomers and nanoparticles on the membrane surfaces. Functional polymers are usually grafted onto the surfaces of PDA-coated membranes through surface-initiated polymerization methods.[88,105,106] For example, the hydrophilic polymer brushes could be covalently anchored onto a PDA-coated membrane by SI-ATRP for constructing functional polymer membranes (Fig. 1-4(c)). Jiang et al. grafted poly(sulfobetaine methacrylate) (PSBMA), a commonly used zwitterionic polymer, onto PVDF membranes by PDA-mediated ATRP, which successfully improved the antifouling and antibacterial properties.[107] Similarly, Meng et al. covalently anchored zwitterionic random copolymers consisting methacryloyloxyethyl phosphorylcholine (MPC) and nitrophenoxycarbonyloxyethyl methacrylate (NPCEMA) monomers on PVDF micro-filtration membrane through a PDA mediation layer, which exhibited superhydrophilicity as well as excellent antifouling performance against oil, bacteria and Bovine Serum Albumin (BSA) protein.[108] PDA also provides a versatile intermediate layer for depositing inorganic materials for functionalizing membranes due to the excellent metal-ion coordination ability of catechol through bidentate chelation. For instance, silver nanoparticle-decorated membranes were prepared by immobilizing silver particles on a PDA-coated membrane via a facile redox reaction owing to the metal-binding ability of phenolic hydroxyl groups in PDA.[109–112] The Ag/PDA-coated membranes exhibited ultrahigh antibacterial activity, which eliminated the attachment of *Escherichia coli* (*E. coli*) with a high rejection rate. In addition, graphene oxide (GO) nanosheets were also applied to fabricate nanofiltration (NF) membranes with antifouling property via a PDA intermediate layer. Wang et al. prepared GO/PDA membrane by pre-modifying a PDA layer on the NF membrane surface, which acted as a strong adhesive agent to bind a layer of GO nanosheets on the surface.[113] The epoxy and carboxyl groups in GO were able to react with the amine group of PDA, making the prepared composite membrane to be chemically and mechanically stable. It was shown that the deposition of PDA and GO layer enhanced the hydrophilicity and smoothness of the membrane surface, which could significantly mitigate the adsorption of foulants and increase the fouling resistance to BSA. Furthermore, with the assistance of the mussel-inspired versatile platform, layer-by-layer (LBL) assembly strategy could also be utilized for preparing membranes with excellent antifouling performance and long-term stability.[114,115] For example, Guo et al. applied polyphenol tannic acid (with abundant catechol groups) and hydrophilic Jeffamine (containing amino groups) in a LBL process to fabricate composite NF membranes, which exhibited excellent resistance against BSA absorption due to the hydrophilic membrane surface.[116]

1.2.3. Mussel-inspired antifouling coatings

Catechol is able to deposit on both organic and inorganic substrates through diverse chemical interactions, which makes DOPA chemistry (especially PDA) a versatile surface modification strategy to functionalize different surfaces with antifouling property. On one hand, the hydrophilic PDA coatings can attract water molecules to form a hydration layer that resists foulants adhesion to the substrates.[117] It was demonstrated that the friction forces of diverse surfaces such as glass, polydimethylsiloxane (PDMS), and epoxy in water were significantly decreased after coated with PDA layer due to the presence of the hydration layer; thus, the PDA film was expected to serve as a water-based lubrication coating.[118] Moreover, the surface energy of both hydrophilic and hydrophobic substrates could also be drastically altered after coated with PDA. For example, the polar component of the surface energy of hydrophobic L-poly-(lactic-acid) (PLLA) increased from 9.6 mJ/m^2 to 47.2 mJ/m^2 after treatment with dopamine for 14 h in Tris buffer solution (pH 8.5), suggesting the surface became much more polar and hydrophilic after PDA deposition.[119] On the other hand, PDA has been found to possess intrinsic antimicrobial activity. Avis and co-workers reported that dopamine self-polymerized onto *E. coli* cells and encapsulated the bacteria in the PDA shells, creating a barrier between *E. coli* and the surroundings. The presence of PDA reduced the permeability of nutrition components for *E. coli* survival and hindered the release of toxic metabolic waste, which prevented further cell multiplication.[54] Many studies reported that PDA coating reduced the bacteria proliferation and enhanced antibacterial activity on different types of substrates such as metal,[120,121] zirconia,[122] cotton and glass.[123] However, compared to other antibacterial materials such as metals or polymers, the antibacterial performance of PDA was relatively weak. Therefore, researchers combined the PDA with other antibacterial materials to improve the antimicrobial efficacy of coatings. Nanoparticles (NPs) of various inorganic compounds such as metals, metal oxides and silica have been successfully coated with PDA films on substrates for antifouling purposes. For example, Ag NPs were preferentially selected for deposition with PDA to modify the surfaces of diverse materials including graphene,[124] Si wafer,[125] silk fibers,[126] titanium alloy,[127] etc. The reducing capability of PDA toward metal ions could ease the oxidization and aggregation of Ag NPs, which enhanced the stability and antibacterial functions against *E. coli* and *Staphylococcus aureus*. Magnetite NPs (e.g., Fe_3O_4[128–130]) were also incorporated into the PDA polymer matrix to yield a magnetic Fe_3O_4/PDA nanocomposite that was applied for the removal of multiple pollutants (Fig. 1-5(a)). The as-prepared nanocomposites loaded on different surfaces exhibited excellent biomedical properties, including antiviral, antibacterial and antitumor activities, and could be collected and recovered by using an external magnetic field.

Beside coupling with inorganic materials, the abundant catechol and amine/imine groups in dopamine/PDA molecules could serve as active sites to react with various functional groups of polymers.[53,133] The synthesis of mussel-inspired functional coatings is generally achieved either by “grafting from” method by the utilization of mussel-mimetic surface initiators, or “grafting to” method by employing adhesive anchors based on DOPA chemistry.[43,134]

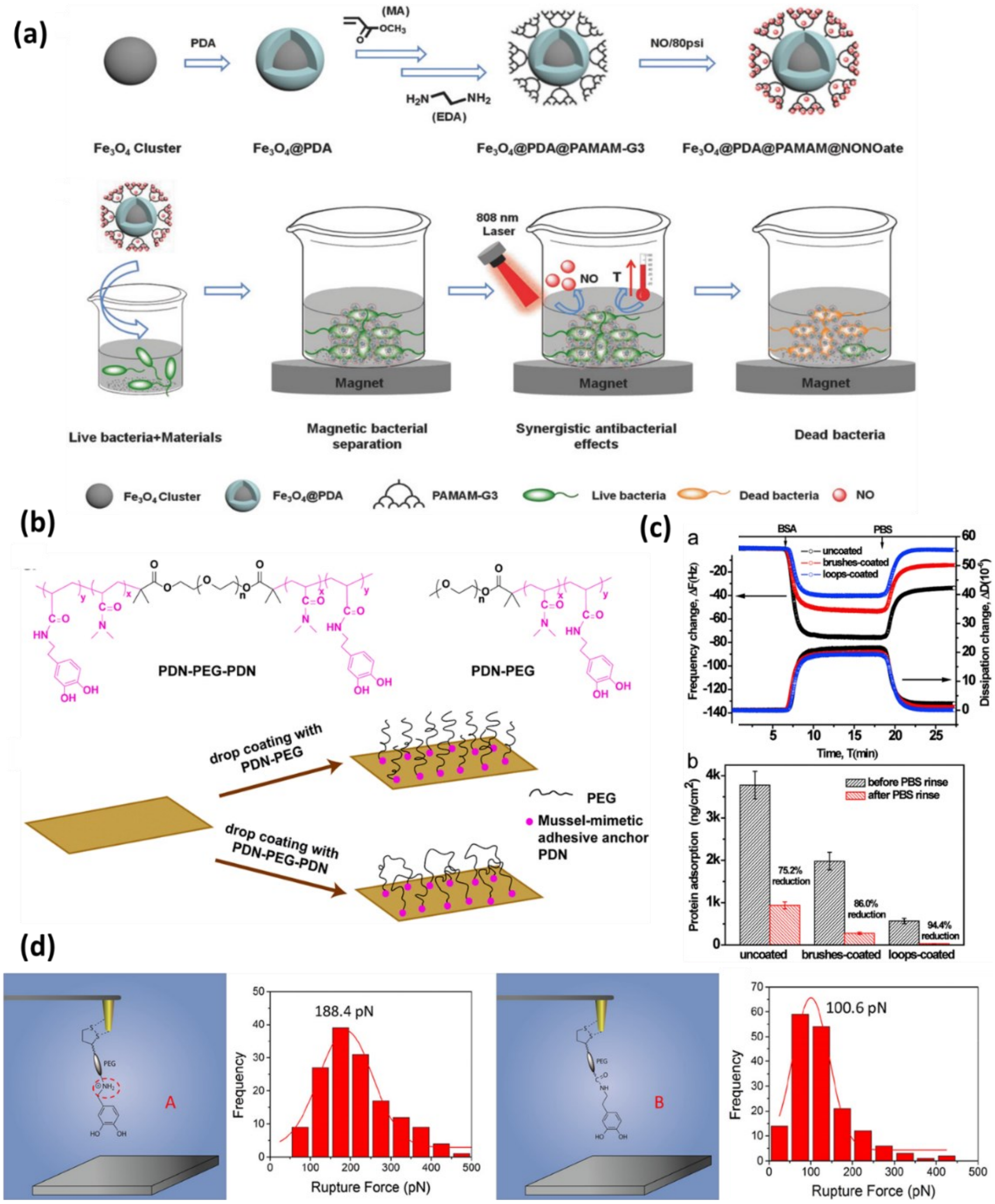

Fig. 1-5 (a) Synthetic process of Fe$_3$O$_4$@PDA@poly(amidoamine)@N-diazeniumdiolate nanocomposite, and its application for magnetic separation, synergistic photothermal and NO antibacterial effects against both *E. coli* and *S. aureus*. Reproduced with permission.[130] Copyright 2018, WILEY-VCH. (b) Chemical structure of the triblock copolymer PDN-PEG-PDN and the diblock copolymer PDN-PEG and schematics of the preparation of surfaces bearing polymer brushes and polymer loops using drop coating method. The anti-biofouling performance are shown in (c). The top image is the changes in frequency and dissipation associated with the adsorption of protein BSA on bare silica sensor, silica sensors coated with PDN-PEG brushes and PDN-PEG-PDN loops using a QCM-D. The bottom image shows protein adsorption on the three substrate surfaces (ng/cm^2) before and after rinsing with PBS buffer. Reproduced with permission.[131] Copyright 2015, The Royal Society of Chemistry. (d) Schematic illustration of the

experimental setup for measuring the interactions between amine-modified catechol ligand A and mica and unmodified catechol B and mica at a single-molecule level, and the correlated force distribution histograms of A-mica and B-mica interactions at the same loading rate (360 nN/s). Reproduced with permission.[132] Copyright 2018, American Chemical Society.

Mussel-inspired "grafting to" strategy was pioneered by Messersmith's group in 2003, where the monomethoxy-terminated PEG polymer conjugated with a mussel-inspired adhesive catechol ligand was first prepared, and then directly and covalently anchored on gold and titanium surfaces through adsorption process.[50] Following this idea, much effort has been dedicated to the preparation of antifouling polymers end-tethered mussel-inspired adhesive anchors such as single DOPA residues, which facilitated the polymers to stably bind to the target surfaces. Li et al, developed an antifouling coating bearing polymer loops using a mussel-inspired ABA triblock copolymer, which showed excellent protein-reduction performance as indicated by the adsorption tests using quartz crystal microbalance with dissipation (QCM-D) and direct force measurements using SFA.[131] As shown in Fig. 1-5(b), mussel-inspired catechol-functionalized poly(N,N-dimethylacrylamide) and PEG were selected as the adhesive A block and antifouling B block, respectively. This copolymer was synthesized by reversible RAFT polymerization and drop-coated on the mica substrate to form a layer consisting of polymer loops with the assistance of the mussel-mimetic adhesive anchors on both ends. The stable anchoring points provided by the catechol groups facilitated the grafting of PEG chains, which achieved a large volume to reduce the protein penetration and exhibited great potential in antifouling applications (Fig. 1-5(c)). The research group also reported a robust and substrate-independent anchoring strategy based on a modified catechol unit with a cationic amine at adjacent. The cationic amine-modified catechol ligand showed universal anchoring capability and superior binding stability for tethering anti-biofouling molecules on various substrates.[132] The interaction mechanisms between the hydrophilic mica surface and catechol with/without cationic amine modification were quantified at the molecular level using single-molecule force spectroscopy based on atomic force microscopy (SM-AFM). As shown in Fig. 1-5(d), the results indicated the enhanced stability of the hydrogen binding between cation amine-modified catechol and mica, suggesting the synergetic effect of the amine cation and catechol disrupted the hydration layer on mica and facilitated the anchoring of the mussel-inspired ligand on the hydrophilic substrate under water. Due to the ease of operation, the "grafting to" method carries great convenience and feasibility for modifying surfaces with antifouling polymers which were conjugated with stable and applicable surface anchors.

1.3.Objectives

Much effort has been devoted to the investigation of a wide range of bio-inspired functional coatings and surfaces, which have been successfully designed to resist the adhesion and fouling of a variety of contaminants. However, in practical applications, many materials cannot provide expected resistant performance against foulants or even lose antifouling functions after long-term use. Accordingly, probing the interaction mechanisms between various bio-inspired antifouling surfaces and diverse types of foulants is of both fundamental and practical importance, which helps to understand the effectiveness of antifouling strategies towards different types of contaminants and facilitate the design and development of materials with superior antifouling performance.

The main objective of this thesis is to quantify interfacial forces and reveal the fundamental interaction mechanisms among various types of foulants including inorganic particles, organic substances, or bio foulants and different bio-inspired antifouling coatings by employing nanomechanical techniques. Meanwhile, a mussel-inspired antifouling coating is developed, and the corresponding molecular interaction mechanisms are also investigated. More specifically, this thesis work has focused on the following three areas.

(1) Investigating the antifouling performance and repellence mechanisms of bio-inspired lubricant-infused slippery surfaces against mussel-derived adhesive chemicals. Probing the molecular binding behaviors and interaction strength of the versatile mussel-inspired chemistry including DOPA and PDA to lubricant-infused slippery surfaces.

(2) Understanding the complex molecular interaction mechanisms between typical foulants and mussel-inspired membranes in wastewater treatment systems. Analyzing the adsorption tendency of foulants on different membrane surfaces and evaluating the release and regeneration ability of membranes through AFM force measurements

(3) Developing a mussel-inspired conductive membrane bearing adjustable surface charge property, employing tunable long-range electric double layer interaction to achieve adaptive emulsion separation and antifouling performance in response to the varying external electrochemical potentials.

References

[1]I. Banerjee, R.C. Pangule, R.S. Kane, Antifouling coatings: recent developments in the design of surfaces that prevent fouling by proteins, bacteria, and marine organisms, Advanced Materials. 23 (2011) 690–718.

[2]E. Steinle-Darling, M. Zedda, M.H. Plumlee, H.F. Ridgway, M. Reinhard, Evaluating the impacts of membrane type, coating, fouling, chemical properties and water chemistry on reverse osmosis rejection of seven nitrosoalklyamines, including NDMA, Water Res. 41 (2007) 3959–3967.

[3]R. Sheikholeslami, Composite fouling ‐ inorganic and biological: A review, Environmental Progress. 18 (1999) 113 ‐ 122.

[4]A. Mutschler, L. Tallet, M. Rabineau, C. Dollinger, M.-H. Metz-Boutigue, F. Schneider, B. Senger, N.E. Vrana, P. Schaaf, P. Lavalle, Unexpected bactericidal activity of poly (arginine)/hyaluronan nanolayered coatings, Chemistry of Materials. 28 (2016) 8700–8709.

[5]H. Vaisocherová, E. Brynda, J. Homola, Functionalizable low-fouling coatings for label-free biosensing in complex biological media: advances and applications, Anal Bioanal Chem. 407 (2015) 3927–3953.

[6]W.E.G. Müller, X. Wang, P. Proksch, C.C. Perry, R. Osinga, J. Gardères, H.C. Schröder, Principles of biofouling protection in marine sponges: a model for the design of novel biomimetic and bio-inspired coatings in the marine environment?, Marine Biotechnology. 15 (2013) 375–398.

[7]E. Almeida, T.C. Diamantino, O. de Sousa, Marine paints: the particular case of antifouling paints, Prog Org Coat. 59 (2007) 2–20.

[8]M.P. Schultz, J.A. Bendick, E.R. Holm, W.M. Hertel, Economic impact of biofouling on a naval surface ship, Biofouling. 27 (2011) 87–98.

[9]S. Shirazi, C.-J. Lin, D. Chen, Inorganic fouling of pressure-driven membrane processes—A critical review, Desalination. 250 (2010) 236–248.

[10]Q. Li, M. Elimelech, Organic fouling and chemical cleaning of nanofiltration membranes: measurements and mechanisms, Environ Sci Technol. 38 (2004) 4683–4693.

[11]E. Diaz-Bejarano, E. Behranvand, F. Coletti, M.R. Mozdianfard, S. Macchietto, Organic and inorganic fouling in heat exchangers–Industrial case study: Analysis of fouling state, Appl Energy. 206 (2017) 1250–1266.

[12]S.B. Darling, Perspective: Interfacial materials at the interface of energy and water, J Appl Phys. 124 (2018) 30901.

[13]C. Yang, X. Ding, R.J. Ono, H. Lee, L.Y. Hsu, Y.W. Tong, J. Hedrick, Y.Y. Yang, Brush‐like polycarbonates containing dopamine, cations, and PEG providing a broad‐spectrum, antibacterial, and antifouling surface via one‐step coating, Advanced Materials. 26 (2014) 7346–7351.

[14]P. Kingshott, J. Wei, D. Bagge-Ravn, N. Gadegaard, L. Gram, Covalent attachment of poly (ethylene glycol) to surfaces, critical for reducing bacterial adhesion, Langmuir. 19 (2003) 6912–6921.

[15]J.H. Park, Y.H. Bae, Hydrogels based on poly (ethylene oxide) and poly (tetramethylene oxide) or poly (dimethyl siloxane): synthesis, characterization, in vitro protein adsorption and platelet adhesion, Biomaterials. 23 (2002) 1797–1808.

[16]S. Jiang, Z. Cao, Ultralow‐fouling, functionalizable, and hydrolyzable zwitterionic materials and their derivatives for biological applications, Advanced Materials. 22 (2010) 920‐932.

[17]S. Chen, S. Jiang, An new avenue to nonfouling materials, Advanced Materials. 20 (2008) 335–338.

[18]D. Chen, T. Liu, J. Kang, R. Xu, Y. Cao, M. Xiang, Enhancing the Permeability and Antifouling Properties of Polyamide Composite Reverse Osmosis Membrane by Surface Modification with Zwitterionic Amino Acid l‐Arginine, Adv Mater Interfaces. 6 (2019) 1900706.

[19]Q. Shao, S. Jiang, Molecular understanding and design of zwitterionic materials, Advanced Materials. 27 (2015) 15–26.

[20]D.M. Yebra, S. Kiil, K. Dam-Johansen, Antifouling technology—past, present and future steps towards efficient and environmentally friendly antifouling coatings, Prog Org Coat. 50 (2004) 75–104.

[21]E.M. Hetrick, M.H. Schoenfisch, Reducing implant-related infections: active release strategies, Chem Soc Rev. 35 (2006) 780–789.

[22]N. Barraud, D.J. Hassett, S.-H. Hwang, S.A. Rice, S. Kjelleberg, J.S. Webb, Involvement of nitric oxide in biofilm dispersal of Pseudomonas aeruginosa, J Bacteriol. 188 (2006) 7344–7353.

[23]R. Kumar, A.M. Isloor, A.F. Ismail, S.A. Rashid, T. Matsuura, Polysulfone–Chitosan blend ultrafiltration membranes: preparation, characterization, permeation and antifouling properties, RSC Adv. 3 (2013) 7855–7861.

[24]B. Peng, J. Wang, Z. Peng, S. Zhou, F. Wang, Y. Ji, Z. Ye, X. Zhou, T. Lin, X. Zhang, Studies on the synthesis, pungency and anti-biofouling performance of capsaicin analogues, Sci China Chem. 55 (2012) 435–442.

[25]M. Lejars, A. Margaillan, C. Bressy, Fouling release coatings: a nontoxic alternative to biocidal antifouling coatings, Chem Rev. 112 (2012) 4347–4390.

[26]F.C. Moreira, R.A.R. Boaventura, E. Brillas, V.J.P. Vilar, Electrochemical advanced oxidation processes: A review on their application to synthetic and real wastewaters, Appl Catal B. 202 (2017) 217–261. https://doi.org/https://doi.org/10.1016/j.apcatb.2016.08.037.

[27]M.N. Chong, B. Jin, C.W.K. Chow, C. Saint, Recent developments in photocatalytic water treatment technology: A review, Water Res. 44 (2010) 2997–3027. https://doi.org/https://doi.org/10.1016/j.watres.2010.02.039.

[28]E. Brillas, I. Sirés, M.A. Oturan, Electro-Fenton Process and Related Electrochemical Technologies Based on Fenton’s Reaction Chemistry, Chem Rev. 109 (2009) 6570–6631. https://doi.org/10.1021/cr900136g.

[29]E. Guinea, C. Arias, P.L. Cabot, J.A. Garrido, R.M. Rodríguez, F. Centellas, E. Brillas, Mineralization of salicylic acid in acidic aqueous medium by electrochemical advanced oxidation processes using platinum and boron-doped diamond as anode and cathodically generated hydrogen peroxide, Water Res. 42 (2008) 499–511. https://doi.org/https://doi.org/10.1016/j.watres.2007.07.046.

[30]P. Zhang, S. Wang, S. Wang, L. Jiang, Superwetting surfaces under different media: effects of surface topography on wettability, Small. 11 (2015) 1939–1946.

[31]M. Liu, S. Wang, Z. Wei, Y. Song, L. Jiang, Bioinspired design of a superoleophobic and low adhesive water/solid interface, Advanced Materials. 21 (2009) 665–669.

[32]R.F. Brady Jr, A fracture mechanical analysis of fouling release from nontoxic antifouling coatings, Prog Org Coat. 43 (2001) 188–192.

[33]M.P. Schultz, C.J. Kavanagh, G.W. Swain, Hydrodynamic forces on barnacles: Implications on detachment from fouling‐release surfaces, Biofouling. 13 (1999) 323–335.

[34]T.-S. Wong, S.H. Kang, S.K.Y. Tang, E.J. Smythe, B.D. Hatton, A. Grinthal, J. Aizenberg, Bioinspired self-repairing slippery surfaces with pressure-stable omniphobicity, Nature. 477 (2011) 443–447.

[35]C. Howell, T.L. Vu, C.P. Johnson, X. Hou, O. Ahanotu, J. Alvarenga, D.C. Leslie, O. Uzun, A. Waterhouse, P. Kim, Stability of surface-immobilized lubricant interfaces under flow, Chemistry of Materials. 27 (2015) 1792–1800.

[36]C.M. Magin, D.L. Alge, K.S. Anseth, Bio-inspired 3D microenvironments: a new dimension in tissue engineering, Biomedical Materials. 11 (2016) 22001.

[37]J.H. Ryu, S. Hong, H. Lee, Bio-inspired adhesive catechol-conjugated chitosan for biomedical applications: A mini review, Acta Biomater. 27 (2015) 101–115.

[38]S. Fleischer, T. Dvir, Tissue engineering on the nanoscale: lessons from the heart, Curr Opin Biotechnol. 24 (2013) 664–671.

[39]I. Buzzacchera, M. Vorobii, N.Yu. Kostina, A. de los Santos Pereira, T. Riedel, M. Bruns, W. Ogieglo, M. Möller, C.J. Wilson, C. Rodriguez-Emmenegger, Polymer Brush-Functionalized Chitosan Hydrogels as Antifouling Implant Coatings, Biomacromolecules. 18 (2017) 1983–1992.

[40]J. Zhu, Bioactive modification of poly(ethylene glycol) hydrogels for tissue engineering, Biomaterials. 31 (2010) 4639–4656.

[41]Y. Tang, X. Cai, Y. Xiang, Y. Zhao, X. Zhang, Z. Wu, Cross-linked antifouling polysaccharide hydrogel coating as extracellular matrix mimics for wound healing, J Mater Chem B. 5 (2017) 2989–2999.

[42]I. Buzzacchera, M. Vorobii, N.Yu. Kostina, A. de los Santos Pereira, T. Riedel, M. Bruns, W. Ogieglo, M. Möller, C.J. Wilson, C. Rodriguez-Emmenegger, Polymer Brush-Functionalized Chitosan Hydrogels as Antifouling Implant Coatings, Biomacromolecules. 18 (2017) 1983–1992.

[43]H. Lee, S.M. Dellatore, W.M. Miller, P.B. Messersmith, Mussel-inspired surface chemistry for multifunctional coatings, Science (1979). 318 (2007) 426–430.

[44]Y.H. Ding, M. Floren, W. Tan, Mussel-inspired polydopamine for bio-surface functionalization, Biosurf Biotribol. 2 (2016) 121–136.

[45]H.-C. Yang, J. Luo, Y. Lv, P. Shen, Z.-K. Xu, Surface engineering of polymer membranes via mussel-inspired chemistry, Journal of Membrane Science. 483 (2015) 42–59.

[46]H. Yang, R.Z. Waldman, M. Wu, J. Hou, L. Chen, S.B. Darling, Z. Xu, Dopamine: just the right medicine for membranes, Advanced Functional Materials. 28 (2018) 1705327.

[47]S.B. Darling, Perspective: Interfacial materials at the interface of energy and water, Journal of Applied Physics. 124 (2018) 30901.

[48]Z. Wang, H.-C. Yang, F. He, S. Peng, Y. Li, L. Shao, S.B. Darling, Mussel-inspired surface engineering for water-remediation materials, Matter. 1 (2019) 115–155.

[49]L. Li, Mussel-inspired Multifunctional Polymeric Materials with Bioengineering Applications, University of Alberta, 2017.

[50]J.L. Dalsin, B.-H. Hu, B.P. Lee, P.B. Messersmith, Mussel adhesive protein mimetic polymers for the preparation of nonfouling surfaces, Journal of the American Chemical Society. 125 (2003) 4253–4258.

[51]L. Li, H. Zeng, Marine mussel adhesion and bio-inspired wet adhesives, Biotribology. 5 (2016) 44–51.

[52]B.D. McCloskey, H.B. Park, H. Ju, B.W. Rowe, D.J. Miller, B.J. Chun, K. Kin, B.D. Freeman, Influence of polydopamine deposition conditions on pure water flux and foulant

adhesion resistance of reverse osmosis, ultrafiltration, and microfiltration membranes, Polymer. 51 (2010) 3472–3485.

[53]Y. Liu, K. Ai, L. Lu, Polydopamine and its derivative materials: synthesis and promising applications in energy, environmental, and biomedical fields, Chemical Reviews. 114 (2014) 5057–5115.

[54]Z. Iqbal, E.P.C. Lai, T.J. Avis, Antimicrobial effect of polydopamine coating on Escherichia coli, Journal of Materials Chemistry. 22 (2012) 21608–21612.

[55]H. Cho, S.K. Madhurakkat Perikamana, J. Lee, J. Lee, K.-M. Lee, C.S. Shin, H. Shin, Effective immobilization of BMP-2 mediated by polydopamine coating on biodegradable nanofibers for enhanced in vivo bone formation, ACS Applied Materials & Interfaces. 6 (2014) 11225–11235.

[56]X. Liu, J. Cao, H. Li, J. Li, Q. Jin, K. Ren, J. Ji, Mussel-inspired polydopamine: a biocompatible and ultrastable coating for nanoparticles in vivo, ACS Nano. 7 (2013) 9384–9395.

[57]W.-B. Tsai, W.-T. Chen, H.-W. Chien, W.-H. Kuo, M.-J. Wang, Poly (dopamine) coating of scaffolds for articular cartilage tissue engineering, Acta Biomaterialia. 7 (2011) 4187–4194.

[58]H. Lee, J. Rho, P.B. Messersmith, Facile conjugation of biomolecules onto surfaces via mussel adhesive protein inspired coatings, Advanced Materials. 21 (2009) 431–434.

[59]Q. Lu, E. Danner, J.H. Waite, J.N. Israelachvili, H. Zeng, D.S. Hwang, Adhesion of mussel foot proteins to different substrate surfaces, Journal of The Royal Society Interface. 10 (2013) 20120759.

[60]E.W. Danner, Y. Kan, M.U. Hammer, J.N. Israelachvili, J.H. Waite, Adhesion of mussel foot protein Mefp-5 to mica: an underwater superglue, Biochemistry. 51 (2012) 6511–6518.

[61]N. Bandara, H. Zeng, J. Wu, Marine mussel adhesion: biochemistry, mechanisms, and biomimetics, Journal of Adhesion Science and Technology. 27 (2013) 2139–2162.

[62]D.S. Hwang, H. Zeng, A. Masic, M.J. Harrington, J.N. Israelachvili, J.H. Waite, Protein-and metal-dependent interactions of a prominent protein in mussel adhesive plaques, Journal of Biological Chemistry. 285 (2010) 25850–25858.

[63]J.H. Waite, Evidence for a repeating 3, 4-dihydroxyphenylalanine-and hydroxyproline-containing decapeptide in the adhesive protein of the mussel, Mytilus edulis L., Journal of Biological Chemistry. 258 (1983) 2911–2915.

[64]D.R. Filpula, S. Lee, R.P. Link, S.L. Strausberg, R.L. Strausberg, Structural and functional repetition in a marine mussel adhesive protein, Biotechnology Progress. 6 (1990) 171–177.

[65]S.W. Taylor, J.H. Waite, M.M. Ross, J. Shabanowitz, D.F. Hunt, trans-2, 3-cis-3, 4-Dihydroxyproline, a new naturally occurring amino acid, is the sixth residue in the tandemly repeated consensus decapeptides of an adhesive protein from Mytilus edulis, Journal of the American Chemical Society. 116 (1994) 10803–10804.

[66]L.M. Rzepecki, K.M. Hansen, J.H. Waite, Characterization of a cystine-rich polyphenolic protein family from the blue mussel Mytilus edulis L, The Biological Bulletin. 183 (1992) 123–137.

[67]M.A. Even, J. Wang, Z. Chen, Structural information of mussel adhesive protein Mefp-3 acquired at various polymer/Mefp-3 solution interfaces, Langmuir. 24 (2008) 5795–5801.

[68]L.A. Burzio, J.H. Waite, Cross-linking in adhesive quinoproteins: studies with model decapeptides, Biochemistry. 39 (2000) 11147–11153.

[69]J.H. Waite, X. Qin, Polyphosphoprotein from the adhesive pads of Mytilus edulis, Biochemistry. 40 (2001) 2887–2893.

[70]H. Zhao, J.H. Waite, Linking adhesive and structural proteins in the attachment plaque of Mytilus californianus, Journal of Biological Chemistry. 281 (2006) 26150–26158.

[71]H. Zhao, J.H. Waite, Proteins in load-bearing junctions: the histidine-rich metal-binding protein of mussel byssus, Biochemistry. 45 (2006) 14223–14231.

[72]S.C. Warner, J.H. Waite, Expression of multiple forms of an adhesive plaque protein in an individual mussel, Mytilus edulis, Marine Biology. 134 (1999) 729–734.

[73]J. Yu, W. Wei, E. Danner, R.K. Ashley, J.N. Israelachvili, J.H. Waite, Mussel protein adhesion depends on interprotein thiol-mediated redox modulation, Nature Chemical Biology. 7 (2011) 588–590.

[74]J.H. Waite, M.L. Tanzer, Polyphenolic substance of Mytilus edulis: novel adhesive containing L-dopa and hydroxyproline, Science. 212 (1981) 1038–1040.

[75]Q. Lin, D. Gourdon, C. Sun, N. Holten-Andersen, T.H. Anderson, J.H. Waite, J.N. Israelachvili, Adhesion mechanisms of the mussel foot proteins mfp-1 and mfp-3, Proceedings of the National Academy of Sciences. 104 (2007) 3782–3786.

[76]H. Lee, N.F. Scherer, P.B. Messersmith, Single-molecule mechanics of mussel adhesion, Proceedings of the National Academy of Sciences. 103 (2006) 12999–13003.

[77]S. Kim, J. Huang, Y. Lee, S. Dutta, H.Y. Yoo, Y.M. Jung, Y. Jho, H. Zeng, D.S. Hwang, Complexation and coacervation of like-charged polyelectrolytes inspired by mussels, Proceedings of the National Academy of Sciences. 113 (2016) E847–E853.

[78]S. Kim, H.Y. Yoo, J. Huang, Y. Lee, S. Park, Y. Park, S. Jin, Y.M. Jung, H. Zeng, D.S. Hwang, Salt triggers the simple coacervation of an underwater adhesive when cations meet aromatic π electrons in seawater, ACS Nano. 11 (2017) 6764–6772.

[79]C. Lim, J. Huang, S. Kim, H. Lee, H. Zeng, D.S. Hwang, Nanomechanics of poly (catecholamine) coatings in aqueous solutions, Angewandte Chemie International Edition. 55 (2016) 3342–3346.

[80]Q. Lu, D.S. Hwang, Y. Liu, H. Zeng, Molecular interactions of mussel protective coating protein, mcfp-1, from Mytilus californianus, Biomaterials. 33 (2012) 1903–1911.

[81]Q. Lu, D.X. Oh, Y. Lee, Y. Jho, D.S. Hwang, H. Zeng, Nanomechanics of cation–π interactions in aqueous solution, Angewandte Chemie. 125 (2013) 4036–4040.

[82]M. Yu, J. Hwang, T.J. Deming, Role of L-3, 4-dihydroxyphenylalanine in mussel adhesive proteins, Journal of the American Chemical Society. 121 (1999) 5825–5826.

[83]J. Zhang, L. Xiang, B. Yan, H. Zeng, Nanomechanics of Anion− Π Interaction in Aqueous Solution, Journal of the American Chemical Society. 142 (2020) 1710–1714.

[84]C.A. Monnier, D.G. DeMartini, J.H. Waite, Intertidal exposure favors the soft-studded armor of adaptive mussel coatings, Nature Communications. 9 (2018) 1–9.

[85]N. Holten-Andersen, M.J. Harrington, H. Birkedal, B.P. Lee, P.B. Messersmith, K.Y.C. Lee, J.H. Waite, pH-induced metal-ligand cross-links inspired by mussel yield self-healing polymer networks with near-covalent elastic moduli, Proceedings of the National Academy of Sciences. 108 (2011) 2651–2655.

[86]M.J. LaVoie, B.L. Ostaszewski, A. Weihofen, M.G. Schlossmacher, D.J. Selkoe, Dopamine covalently modifies and functionally inactivates parkin, Nature Medicine. 11 (2005) 1214–1221.

[87]X. Fan, L. Lin, J.L. Dalsin, P.B. Messersmith, Biomimetic anchor for surface-initiated polymerization from metal substrates, Journal of the American Chemical Society. 127 (2005) 15843–15847.

[88]B. Zhu, S. Edmondson, Polydopamine-melanin initiators for surface-initiated ATRP, Polymer. 52 (2011) 2141–2149.

[89]H. Ceylan, M. Urel, T.S. Erkal, A.B. Tekinay, A. Dana, M.O. Guler, Mussel inspired dynamic cross‐linking of self‐healing peptide nanofiber network, Advanced Functional Materials. 23 (2013) 2081‐2090.

[90]M. Krogsgaard, M.A. Behrens, J.S. Pedersen, H. Birkedal, Self-healing mussel-inspired multi-pH-responsive hydrogels, Biomacromolecules. 14 (2013) 297–301.

[91]H. Zeng, D.S. Hwang, J.N. Israelachvili, J.H. Waite, Strong reversible Fe3+-mediated bridging between dopa-containing protein films in water, Proceedings of the National Academy of Sciences. 107 (2010) 12850–12853.

[92]B. Yang, C. Lim, D.S. Hwang, H.J. Cha, Switch of surface adhesion to cohesion by Dopa-Fe3+ complexation, in response to microenvironment at the mussel plaque/substrate interface, Chemistry of Materials. 28 (2016) 7982–7989.

[93]N. Huang, S. Zhang, L. Yang, M. Liu, H. Li, Y. Zhang, S. Yao, Multifunctional electrochemical platforms based on the Michael addition/Schiff base reaction of polydopamine modified reduced graphene oxide: construction and application, ACS Applied Materials & Interfaces. 7 (2015) 17935–17946.

[94]S. Hong, Y.S. Na, S. Choi, I.T. Song, W.Y. Kim, H. Lee, Non‐covalent self‐assembly and covalent polymerization co‐contribute to polydopamine formation, Advanced Functional Materials. 22 (2012) 4711‐4717.

[95]D.R. Dreyer, D.J. Miller, B.D. Freeman, D.R. Paul, C.W. Bielawski, Elucidating the structure of poly (dopamine), Langmuir. 28 (2012) 6428–6435.

[96]Z.-Y. Xi, Y.-Y. Xu, L.-P. Zhu, Y. Wang, B.-K. Zhu, A facile method of surface modification for hydrophobic polymer membranes based on the adhesive behavior of poly (DOPA) and poly (dopamine), Journal of Membrane Science. 327 (2009) 244–253.

[97]J. Jiang, L. Zhu, L. Zhu, H. Zhang, B. Zhu, Y. Xu, Antifouling and antimicrobial polymer membranes based on bioinspired polydopamine and strong hydrogen-bonded poly (N-vinyl pyrrolidone), ACS Applied Materials & Interfaces. 5 (2013) 12895–12904.

[98]B. Yu, J. Liu, S. Liu, F. Zhou, Pdop layer exhibiting zwitterionicity: a simple electrochemical interface for governing ion permeability, Chemical Communications. 46 (2010) 5900–5902.

[99]S. Azari, L. Zou, Using zwitterionic amino acid l-DOPA to modify the surface of thin film composite polyamide reverse osmosis membranes to increase their fouling resistance, Journal of Membrane Science. 401 (2012) 68–75.

[100]Q.L.B.Y.W.Y.F. Zhou, Highly Selective Uptake and Release of Charged Molecules by pH ‐ Responsive Polydopamine Microcapsules, Macromolecular Bioscience. 11 (2011) 1227 ‐ 1234.

[101]A. Nguyen, S. Azari, L. Zou, Coating zwitterionic amino acid l-DOPA to increase fouling resistance of forward osmosis membrane, Desalination. 312 (2013) 82–87.

[102]Y. He, L. Xu, X. Feng, Y. Zhao, L. Chen, Dopamine-induced nonionic polymer coatings for significantly enhancing separation and antifouling properties of polymer membranes: Codeposition versus sequential deposition, Journal of Membrane Science. 539 (2017) 421–431.

[103]L. Liu, B. Shao, F. Yang, Polydopamine coating–surface modification of polyester filter and fouling reduction, Separation and Purification Technology. 118 (2013) 226–233.

[104]Y. Zhang, J. Ma, L. Shao, Ultra-thin trinity coating enabled by competitive reactions for unparalleled molecular separation, Journal of Materials Chemistry A. 8 (2020) 5078–5085.

[105]Y. Sui, X. Gao, Z. Wang, C. Gao, Antifouling and antibacterial improvement of surface-functionalized poly (vinylidene fluoride) membrane prepared via dihydroxyphenylalanine-initiated atom transfer radical graft polymerizations, Journal of Membrane Science. 394 (2012) 107–119.

[106]C. Zhang, H.-N. Li, Y. Du, M.-Q. Ma, Z.-K. Xu, CuSO4/H2O2-triggered polydopamine/poly (sulfobetaine methacrylate) coatings for antifouling membrane surfaces, Langmuir. 33 (2017) 1210–1216.

[107]J. Jiang, P. Zhang, L. Zhu, B. Zhu, Y. Xu, Improving antifouling ability and hemocompatibility of poly (vinylidene fluoride) membranes by polydopamine-mediated ATRP, Journal of Materials Chemistry B. 3 (2015) 7698–7706.

[108]F.-N. Meng, M.-Q. Zhang, K. Ding, T. Zhang, Y.-K. Gong, Cell membrane mimetic PVDF microfiltration membrane with enhanced antifouling and separation performance for oil/water mixtures, Journal of Materials Chemistry A. 6 (2018) 3231–3241.

[109]H. Ma, P. Gao, Y. Zhang, D. Fan, G. Li, B. Du, Q. Wei, Engineering microstructured porous films for multiple applications via mussel-inspired surface coating, RSC Advances. 3 (2013) 25291–25295.

[110]K.P. Wai, C.H. Koo, Y.L. Pang, W.C. Chong, W.J. Lau, In situ immobilization of silver on polydopamine-coated composite membrane for enhanced antibacterial properties, Journal of Water Process Engineering. 33 (2020) 100989.

[111]H. Yang, Y. Lan, W. Zhu, W. Li, D. Xu, J. Cui, D. Shen, G. Li, Polydopamine-coated nanofibrous mats as a versatile platform for producing porous functional membranes, Journal of Materials Chemistry. 22 (2012) 16994–17001.

[112]L. Huang, S. Zhao, Z. Wang, J. Wu, J. Wang, S. Wang, In situ immobilization of silver nanoparticles for improving permeability, antifouling and anti-bacterial properties of ultrafiltration membrane, Journal of Membrane Science. 499 (2016) 269–281.

[113]C. Wang, M.J. Park, D.H. Seo, H.K. Shon, Inkjet printing of graphene oxide and dopamine on nanofiltration membranes for improved anti-fouling properties and chlorine resistance, Separation and Purification Technology. 254 (2021) 117604.

[114]C. Cheng, S. Li, W. Zhao, Q. Wei, S. Nie, S. Sun, C. Zhao, The hydrodynamic permeability and surface property of polyethersulfone ultrafiltration membranes with mussel-inspired polydopamine coatings, Journal of Membrane Science. 417 (2012) 228–236.

[115]H. Liu, G. Liu, M. Zhang, H. Zhao, Y. Jiang, J. Gao, Rapid preparation of Tannic acid (TA) based zwitterionic nanofiltration membrane via a multiple layer-by-layer (mLBL) assembly strategy for enhanced antifouling performance, Separation and Purification Technology. 253 (2020) 117519.

[116]D. Guo, Y. Xiao, T. Li, Q. Zhou, L. Shen, R. Li, Y. Xu, H. Lin, Fabrication of high-performance composite nanofiltration membranes for dye wastewater treatment: mussel-inspired layer-by-layer self-assembly, Journal of Colloid and Interface Science. 560 (2020) 273–283.

[117]E. Li, Z. Du, S. Yuan, Properties of a water layer on hydrophilic and hydrophobic self-assembled monolayer surfaces: A molecular dynamics study, Science China Chemistry. 56 (2013) 773–781.

[118]W. Zhang, F.K. Yang, Y. Han, R. Gaikwad, Z. Leonenko, B. Zhao, Surface and tribological behaviors of the bioinspired polydopamine thin films under dry and wet conditions, Biomacromolecules. 14 (2013) 394–405.

[119]A. Bourmaud, J. Riviere, A. Le Duigou, G. Raj, C. Baley, Investigations of the use of a mussel-inspired compatibilizer to improve the matrix-fiber adhesion of a biocomposite, Polymer Testing. 28 (2009) 668–672.

[120]T.S. Sileika, H.-D. Kim, P. Maniak, P.B. Messersmith, Antibacterial performance of polydopamine-modified polymer surfaces containing passive and active components, ACS Applied Materials & Interfaces. 3 (2011) 4602–4610.

[121]A. Liu, L. Zhao, H. Bai, H. Zhao, X. Xing, G. Shi, Polypyrrole actuator with a bioadhesive surface for accumulating bacteria from physiological media, ACS Applied Materials & Interfaces. 1 (2009) 951–955.

[122]M. Liu, J. Zhou, Y. Yang, M. Zheng, J. Yang, J. Tan, Surface modification of zirconia with polydopamine to enhance fibroblast response and decrease bacterial activity in vitro: A potential technique for soft tissue engineering applications, Colloids and Surfaces B: Biointerfaces. 136 (2015) 74–83.

[123]L. Su, Y. Yu, Y. Zhao, F. Liang, X. Zhang, Strong antibacterial polydopamine coatings prepared by a shaking-assisted method, Scientific Reports. 6 (2016) 1–8.

[124]Z. Zhang, J. Zhang, B. Zhang, J. Tang, Mussel-inspired functionalization of graphene for synthesizing Ag-polydopamine-graphene nanosheets as antibacterial materials, Nanoscale. 5 (2013) 118–123.

[125]J. Zhang, Y.S. Cheah, S. Santhanakrishnan, K.G. Neoh, C.L.L. Chai, Methoxy group substitution on catechol ring of dopamine facilitates its polymerization and formation of surface coatings, Polymer. 116 (2017) 5–15.

[126]Z. Lu, J. Xiao, Y. Wang, M. Meng, In situ synthesis of silver nanoparticles uniformly distributed on polydopamine-coated silk fibers for antibacterial application, Journal of Colloid and Interface Science. 452 (2015) 8–14.

[127]Z. Wang, J. Ou, Y. Wang, M. Xue, F. Wang, B. Pan, C. Li, W. Li, Anti-bacterial superhydrophobic silver on diverse substrates based on the mussel-inspired polydopamine, Surface and Coatings Technology. 280 (2015) 378–383.

[128]Y. Fang, C. Xing, S. Zhan, M. Zhao, M. Li, H. Liu, A polyoxometalate-modified magnetic nanocomposite: a promising antibacterial material for water treatment, Journal of Materials Chemistry B. 7 (2019) 1933–1944.

[129]S. Hemmati, M.M. Zangeneh, A. Zangeneh, CuCl2 anchored on polydopamine coated-magnetic nanoparticles (Fe3O4@ PDA/Cu (II)): Preparation, characterization and evaluation of its cytotoxicity, antioxidant, antibacterial, and antifungal properties, Polyhedron. 177 (2020) 114327.

[130]S. Yu, G. Li, R. Liu, D. Ma, W. Xue, Dendritic Fe3O4@ poly (dopamine)@ PAMAM nanocomposite as controllable NO‐releasing material: a synergistic photothermal and NO antibacterial study, Advanced Functional Materials. 28 (2018) 1707440.

[131]L. Li, B. Yan, L. Zhang, Y. Tian, H. Zeng, Mussel-inspired antifouling coatings bearing polymer loops, Chemical Communications. 51 (2015) 15780–15783.

[132]L. Han, L. Gong, J. Chen, J. Zhang, L. Xiang, L. Zhang, Q. Wang, B. Yan, H. Zeng, Universal mussel-inspired ultrastable surface-anchoring strategy via adaptive synergy of catechol and cations, ACS Applied Materials & Interfaces. 10 (2018) 2166–2173.

[133]F. Wu, N. Pu, G. Ye, T. Sun, Z. Wang, Y. Song, W. Wang, X. Huo, Y. Lu, J. Chen, Performance and mechanism of uranium adsorption from seawater to poly (dopamine)-inspired sorbents, Environmental Science & Technology. 51 (2017) 4606–4614.

[134]J.L. Dalsin, P.B. Messersmith, Bioinspired antifouling polymers, Materials Today. 8 (2005) 38–46.

[135]P. Li, X. Cai, D. Wang, S. Chen, J. Yuan, L. Li, J. Shen, Hemocompatibility and anti-biofouling property improvement of poly (ethylene terephthalate) via self-polymerization of dopamine and covalent graft of zwitterionic cysteine, Colloids and Surfaces B: Biointerfaces. 110 (2013) 327–332.

[136]N. Li, T. Li, X.-Y. Qiao, R. Li, Y. Yao, Y.-K. Gong, Universal strategy for efficient fabrication of blood compatible surfaces via polydopamine-assisted surface-initiated activators regenerated by electron transfer atom-transfer radical polymerization of zwitterions, ACS Applied Materials & Interfaces. 12 (2020) 12337–12344.

CHAPTER 2 MAJOR EXPERIMENTAL METHODS

2.1. Atomic force microscope (AFM)

The atomic force microscope (AFM) is a powerful technique for investigating a wide range of surfaces and materials at the nanoscale, including conductive and non-conductive materials, biological specimens, polymers, and liquids. The versality has made AFM an emerging tool in various scientific and technological disciplines such as nanotechnology, materials science, biology, and surface chemistry. The AFM operates based on the principle of probing surfaces using a sharp tip attached to a cantilever and detects forces between the tip and the sample surface to generate detailed topographic maps and gather information about various surface properties. The AFM technology offers several distinct measurements with exceptional sensitivity and accuracy, including, but not limited to, surface morphology and roughness measurement, nanomechanical properties characterization (such as elasticity and adhesion), surface and interfacial interaction investigation and even individual atoms and molecules manipulation.[1–5] In this thesis, we utilize the AFM as a fundamental tool to characterize the surface properties of prepared coatings and probe the molecular interactions and adhesion behaviors between substrate surfaces and foulants.

2.1.1. Characterization of surface morphology using AFM imaging

In this thesis, the morphology of the synthesised coatings and membranes will be characterized using a Bruker ICON AFM (Santa Barbara, CA, USA) with a silicon nitride probe (SCANASYST-FLUID, Bruker) in air. Tapping mode, one of the oscillating modes, is employed for the imaging of the coating morphology. The schematics of AFM imaging using tapping mode is illustrated in Fig. 2-1. At first, an oscillating signal is applied on the cantilever and drives the cantilever vibrating with constant amplitude. Then, the tip is driven to approach the sample and intermittently contact with surfaces. The interactions between tip and sample will affect the amplitude of tip and thus change the output signal. After the feedback control receives the transmitted error signals between the input signal and output signal, the position and height of tip will be adjusted to recover the amplitude, which is a measure for the calculation of the relative surface morphology. Tapping mode is mostly applied for imaging of soft samples because it is preferred to avoid the direct contact between the tip and sample surface.

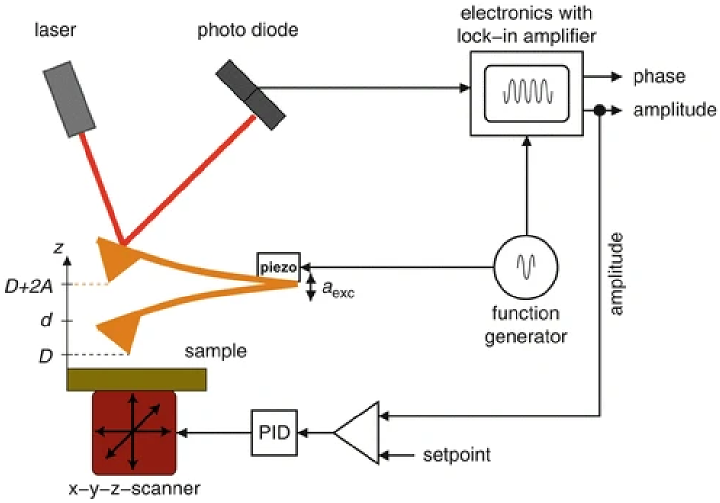

Fig. 2-1 Schematic of an AFM imaging setup in tapping mode. Reproduced with permission.[6] Copyright 2012, Springer.

2.1.2. Colloidal probe AFM techniques for force measurement

By utilizing a small colloidal particle as the probing tip, colloidal probe AFM techniques enable direct and accurate force measurements between the particle and a sample surface at the nanoscale. It involves immobilizing a single colloidal particle onto an AFM cantilever, creating a functionalized probing tip with a well-defined size and shape.[7] The choice of colloidal particle depends on the specific research objectives, but commonly used particles include microspheres, nanoparticles, or functionalized beads. These particles can be tailored to possess specific surface properties or functional groups, allowing for targeted investigations of interactions between different materials or biomolecules. In this thesis, a silica particle (radius~2.5 μm) was attached to a triangular tipless cantilever using epoxy glue to prepare a silica colloidal probe. After that, the surface of the silica colloidal probe was functionalized different polymer or biomolecule layers to reveal the interaction mechanisms between materials on the probe and different substrate surfaces. Then, the force measurements will be conducted by driving the colloidal AFM probe to the substrates at a constant driving velocity of 1 μm/s and the transmitted signal of interaction forces will be recorded as a function of time by MFP-3D AFM system (Asylum Research, Santa Barbara, CA, USA).

2.1.3. Drop probe AFM techniques for force measurement

The interaction mechanisms between a soft oil/water interface and the surface of coating materials will be measured through drop probe AFM techniques using the force modulation of MFP-3D AFM system (Asylum Research, Santa Barbara, CA, USA). During the force measurement experiments, the oil droplets will be generated by a custom-made ultrasharp glass pipet and attached to the apex of a hydrophobized rectangular AFM cantilever. Then, the drop AFM probe will be brought into contact with the substrate surfaces in a liquid environment to measure forces and adhesion between the droplet and the sample surface as a function of the separation distance, which enables the quantification of surface forces, such as van der Waals forces, EDL interactions, and hydrophobic interactions.[8]

2.1.4. AFM based single-molecule force spectroscopy (AFM-SMFS)

AFM-SMFS is a special AFM force measurement to study the mechanical properties and interactions of individual molecules at the nanoscale. For a typical single molecule force measurement, either the AFM probe or the substrate is modified by an extending single molecule.[9,10] Then, the AFM tip is driven into contact with the sample surface as shown in Fig. 2-2. Through controlled manipulation, such as pulling or pushing the tip, forces are applied to the individual molecule, leading to the unfolding, stretching, or bending of its structure. During probe-substrate approach, the molecule could bind specifically to the opposite substrate or AFM probe. While during probe-substrate separation, this molecule is stretched, and the specific bond will be ruptured. Rupture force could be largely affected by the loading rate. According to classic Bell-Evans theory, the kinetics and energetic parameters of the specific bond can be deciphered by counting out the most probably rupture force at different loading rate.[11,12]

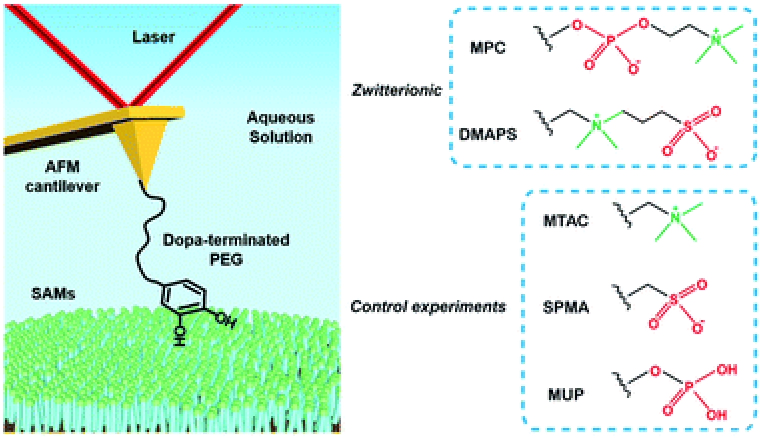

Fig. 2-2 Schematic illustration of the AFM-SMFS experimental setup for measuring the interaction between a single DOPA-terminated molecule and self-assembled monolayers (SAMs). Reproduced with permission.[13] Copyright 2019, Journal of Materials Chemistry A.

2.2. Scanning electrochemical microscopy (SECM)

SECM combines the principles of scanning probe microscopy and electrochemistry, which enables the imaging, mapping, and probing of electrochemical phenomena and electrochemical behaviours of various materials and systems with high spatial resolution. In the thesis, SECM is applied to characterize the local variations in electrochemical properties such as local electrochemical reactivity and electrochemical kinetics of conductive surfaces at the nanoscale. In SECM measurement, a microelectrode probe is used to scan the surface of a sample while maintaining a defined electrochemical potential or current at the probe. The tip of the microelectrode, typically a Pt wire, is positioned close to the sample surface, creating a small gap between the probe and the surface. This gap serves as a pathway for ion flux and allows for the detection of local electrochemical activity.[17,18] SECM offers several operating modes to probe different electrochemical properties and processes. In feedback mode, the probe is positioned at a constant distance from the sample surface, and the electrochemical current or potential is adjusted to maintain a predefined setpoint. This mode provides information about the local reactivity and electrochemical activity of the surface. In generation/collection mode, the microelectrode acts both as a generator and collector of electroactive species. By monitoring the feedback current or potential, information about the local concentration of electroactive species or the kinetics of electrochemical reactions can be obtained.

References

[1]H.H.P. Fang, K.-Y. Chan, L.-C. Xu, Quantification of bacterial adhesion forces using atomic force microscopy (AFM), J Microbiol Methods. 40 (2000) 89–97.

[2]S.-T. Lou, Z.-Q. Ouyang, Y. Zhang, X.-J. Li, J. Hu, M.-Q. Li, F.-J. Yang, Nanobubbles on solid surface imaged by atomic force microscopy, Journal of Vacuum Science & Technology B: Microelectronics and Nanometer Structures Processing, Measurement, and Phenomena. 18 (2000) 2573–2575.

[3]B. Cappella, G. Dietler, Force-distance curves by atomic force microscopy, Surf Sci Rep. 34 (1999) 1–104.

[4]S.L.S. Stipp, C.M. Eggleston, B.S. Nielsen, Calcite surface structure observed at microtopographic and molecular scales with atomic force microscopy (AFM), Geochim Cosmochim Acta. 58 (1994) 3023–3033.

[5]P. Eaton, P. West, Atomic force microscopy, Oxford university press, 2010.

[6]A. Aliano, G. Cicero, H. Nili, N.G. Green, P. Garcıa-Sánchez, A. Ramos, A. Lenshof, T. Laurell, A. Qi, P. Chan, AFM, tapping mode, Encyclopedia of Nanotechnology. (2012) 99.

[7]C. Zhang, L. Gong, L. Xiang, Y. Du, W. Hu, H. Zeng, Z.-K. Xu, Deposition and adhesion of polydopamine on the surfaces of varying wettability, ACS Appl Mater Interfaces. 9 (2017) 30943–30950.

[8]L. Gong, X. Qiu, L. Zhang, J. Huang, W. Hu, L. Xiang, D. Zhu, R. Sabbagh, M. Mahmoudi, V. Fattahpour, Probing the interaction mechanism between oil-in-water

emulsions and electroless nickel–phosphorus coating with implications for antifouling in oil production, Energy & Fuels. 33 (2018) 3764–3775.

[9]C. Wang, R. Hu, J.J. Morrissey, E.D. Kharasch, S. Singamaneni, Single molecule force spectroscopy to compare natural versus artificial antibody–antigen interaction, Small. 13 (2017) 1604255.

[10]T. Utzig, P. Stock, M. Valtiner, Resolving Non‐Specific and Specific Adhesive Interactions of Catechols at Solid/Liquid Interfaces at the Molecular Scale, Angewandte Chemie. 128 (2016) 9676–9680.

[11]E. Evans, K. Ritchie, Dynamic strength of molecular adhesion bonds, Biophys J. 72 (1997) 1541–1555.

[12]H. Lee, N.F. Scherer, P.B. Messersmith, Single-molecule mechanics of mussel adhesion, Proceedings of the National Academy of Sciences. 103 (2006) 12999–13003.

[13]L. Xie, L. Gong, J. Zhang, L. Han, L. Xiang, J. Chen, J. Liu, B. Yan, H. Zeng, A wet adhesion strategy via synergistic cation–π and hydrogen bonding interactions of antifouling zwitterions and mussel-inspired binding moieties, J Mater Chem A Mater. 7 (2019) 21944–21952.

[14]M.A. Hampton, C. Plackowski, A. V Nguyen, Physical and chemical analysis of elemental sulfur formation during galena surface oxidation, Langmuir. 27 (2011) 4190–4201.

[15]L. Xie, J. Wang, C. Shi, J. Huang, H. Zhang, Q. Liu, Q. Liu, H. Zeng, Probing surface interactions of electrochemically active galena mineral surface using atomic force microscopy, The Journal of Physical Chemistry C. 120 (2016) 22433–22442.

[16]G. Wittstock, I. Kartio, D. Hirsch, S. Kunze, R. Szargan, Oxidation of galena in acetate buffer investigated by atomic force microscopy and photoelectron spectroscopy, Langmuir. 12 (1996) 5709–5721.

[17]J. Wang, L. Xie, L. Han, X. Wang, J. Wang, H. Zeng, In-situ probing of electrochemical dissolution and surface properties of chalcopyrite with implications for the dissolution kinetics and passivation mechanism, J Colloid Interface Sci. 584 (2021) 103 – 113.

[18]J. Wang, L. Xie, S. Li, J. Wang, J. Zhang, H. Zeng, Probing the In Situ Redox Behavior of Selenium on a Pyrite Surface by Scanning Electrochemical Microscopy, The Journal of Physical Chemistry C. 125 (2021) 3018–3026.

CHAPTER 3 MOLECULAR INTERACTION MECHANISMS BETWEEN LUBRICANT-INFUSED SLIPPERY SURFACES AND MUSSEL-INSPIRED POLYDOPAMINE ADHESIVE AND DOPA MOIETY

3.1. Introduction

Bio-inspired materials have garnered significant scientific attention for both fundamental research and practical applications [1,2]. One of the most studied bio-inspirations is the mussel, known for its detrimental fouling to various types of surfaces such as rocks, metal, wood and even some well-known low-fouling materials [3–5]. Marine mussels produce and secret adhesive mussel foot proteins (Mfps), which form byssal threads and plaques via its foot organ, enabling strong and versatile underwater attachment. The excellent mechanical strength of mussel byssal threads is attributed to the introduction of cross-links between polymer chains of individual adhesive proteins. Previous studies have shown that 3,4-dihydroxyphenylalanine (DOPA) and its derivative polydopamine (PDA), are critical functional elements for moisture-resistant adhesion and cross-linking of Mfps due to the strong and universal adhesion ability of catechol group [6,7]. The interaction mechanisms between the catechol group and various substrates with different functional groups have been investigated at a molecular level using nanomechanical techniques such as the atomic force microscope (AFM) and surface forces apparatus (SFA) [3,8–10]. Substantial experiments revealed that DOPA and its derivatives such as dopamine and PDA can be facilely deposited on various substrates, including per-fluorinated and superhydrophobic surfaces, through covalent and non-covalent interactions such as hydrogen bonding, metal-catechol coordination, π-π interaction, and hydrophobic interaction [11–20]. The universality and versatility of mussel-derived adhesive chemicals make mussel-fouling control a key challenge. Therefore, considerable attention has been devoted to developing various chemical or physical strategies to prevent mussel adhesion in recent years [21–29].

A novel strategy inspired by the Nepenthes pitcher plants, the slippery liquid-infused porous surface (SLIPS) approach, has been developed to achieve outstanding anti-biofouling performance by infiltrating lubricating liquids into porous or roughened solids to form stably immobilized and low-friction omniphobic surfaces [30–34]. Compared with conventional antifouling strategies plagued with various problems that restrict their practical applications, the lubricant-infused surfaces outperform the counterparts in the capability to eliminate pinning and immobilization of liquids and solids, maintain low contact angle hysteresis and restore liquid-repellency after physical damage [32,35]. Previous studies have reported a series of model omni-repellent surfaces, presenting that the bio-inspired slippery surface could provide a smooth liquid-like interface to inhibit the attachment of bio-foulants. Particularly, Amini et. al fabricated a silicon oil-infused polydimethylsiloxane (PDMS) slippery surface, which showed remarkable non-fouling activity against the attachment of pervasive marine foulants–mussel, representing that lubricant-infused slippery coatings could be an effective strategy to mitigate marine biofouling [36]. Very recently, Hönes et. al investigated the interfacial behavior between a PDA layer and an antiadhesive self-lubricating gel (SLUG) surface, and found that the lubricant oil at the topmost surface acted as a protective barrier to effectively prevent the adsorption of PDA on the SLUG surface [37]. The studies explained the antiadhesion mechanisms of the slippery surfaces as a thermodynamically controllable phenomenon by thermodynamic calculations, where the ultralow interfacial energy of the lubricant/substrate interface indicated the infused lubricant layer on the topmost surface was more energetically favorable than surface wetting by the mussel adhesive proteins or PDA molecules, thereby allowing the infused lubricant to prevent foulants attachment as a protective barrier. Although these studies have provided valuable insights into the excellent antifouling properties of slippery surfaces against marine mussel adhesion as well as PDA deposition, conducting nanoscale contact mechanics experiments and thermodynamic stability characterization of the pairwise bonding between slippery surfaces and the foulants is essential to explore and verify the adhesion-resistant mechanisms of the lubricant-infused surface strategy. It is of great significance to unravel the interaction behaviors and quantitatively measure the molecular binding energy between lubricant-infused surfaces and key adhesive components in mussel adhesion, such as DOPA and PDA, at the nanoscale. Correlating the underlying molecular interaction mechanisms to their bulk mechanical behaviors will provide quantitative information and fundamental insights into understanding the antifouling mechanisms of lubricant-infused surfaces.

In this work, we focused on the fundamental contact mechanisms, binding energy and binding stability of the versatile catechol groups on per-fluorinated surfaces with or without a thin F-based lubricant layer, investigating how infusing lubricant on solid substrates can influence the binding mechanisms of catechol groups, thereby control mussel attachment. The deposition behaviors of PDA towards per-fluorinated monolayer surface and per-fluorinated slippery surface were quantitatively compared using quartz crystal microbalance with dissipation (QCM-D). And the adhesion mechanisms underlying the PDA deposition were unraveled by measuring the interaction forces between PDA-coated silica probes and different types of surfaces employing colloidal probe AFM technique. By correlating the underlying molecular interaction mechanisms to the bulk mechanical behaviors of the surfaces, the study provides an understanding of how these interactions influence overall antifouling performance. Then, to quantitively unveil the binding capability and interaction energy of a single DOPA moiety to fluorinated functional surfaces at a molecular level, the interaction forces between a single DOPA moiety and per-fluorinated monolayer surfaces with/without lubricant injection have been measured and analyzed using single-molecule force spectroscopy based on AFM (SM-AFM). The study goes beyond existing research by conducting nanoscale contact mechanics experiments to explore the pairwise bonding interactions between per-fluorinated surfaces and DOPA. Understanding the interaction mechanisms between slippery surfaces and mussel-inspired catechol-containing adhesives including PDA and single DOPA moiety is of both fundamental and practical importance, which helps provide bases to improve the performance of SLIPS against the versatile foulants and facilitate the design of antifouling materials.

3.2. Results and discussion

3.2.1. Characterization of perfluorocarbon silane (FS) coating and liquid perfluorocarbon (LF) coating

The preparation process of perfluorocarbon silane (FS) coating and lubricant-infused perfluorocarbon (LF) coating is illustrated in Figure 3-1 (A). FS surface was produced by applying self-assembled monolayers of hydrophobic organosilane (e.g. tridecafluoro-1,1,2,2-tetrahydrooctyl trichlorosilane) onto the plasma-activated silica surface. Then, LF surface was prepared through liquid phase deposition method by immersing the FS surface into FC-70 lubricant. Based on fluorous chemistry, the strong intermolecular interactions between the perfluoro silane chains and fluorinated lubricant immobilize the lubricant liquid onto the surface, creating a stable omniphobic lubricant-infused coating [38–40]. The fabrication details are described in Experimental section 3.3.2. The static water contact angles (WCA) of bare silica, FS-coated and LF-coated silica surfaces are shown in Figure 3-1 (B-D), which were measured to be 20 ± 2.3°, 107 ± 3.1° and 97 ± 3.5°, respectively. The wettability of substrates has been significantly altered from hydrophilic to hydrophobic before and after the application of FS or LF coating layers. For the LF surface, its WCA did not show a significant change compared to that of the FS surface. However, an outer "wrapping" layer could be observed around the water droplet, resulting from the spreading of a thin layer of infused low-surface-energy liquid (FC-70) over the droplet of high-surface-energy liquid (i.e., water). This observation also suggests the presence of the FC-70 lubricant layer. The topographic AFM images of the silica surfaces before and after coating with FS are shown in Figure 3-1 (E-F), with a root-mean-square (RMS) roughness of 0.21 nm and 0.31 nm, respectively. The low roughness and smoothness of the modified surface indicated the uniform coating of a monolayer of perfluorocarbon silane on the silica substrate, which was further confirmed by X-ray photoelectron spectroscopy (XPS) of the modified FS surface (see Figure 3-8 in supporting information). These smooth surfaces minimized the impact of surface roughness on surface force measurements. Fourier transform infrared spectroscopy (FTIR) was employed to characterize the chemistry of LF-coated substrate to confirm the presence of FC-70 lubricant on FS surface. In the FTIR spectrum of the LF surface, peaks at 1206, 1140, 1110, 984, 877, 773, 719 and 653 cm^{-1} were attributed to the $–CF_2$ and $–CF_3$ groups, with the peak at 1240 cm^{-1} corresponding to carbon sp^3 bound to nitrogen [41–43]. Therefore, the FTIR results confirmed the presence of FC-70 lubricant on FS surface.

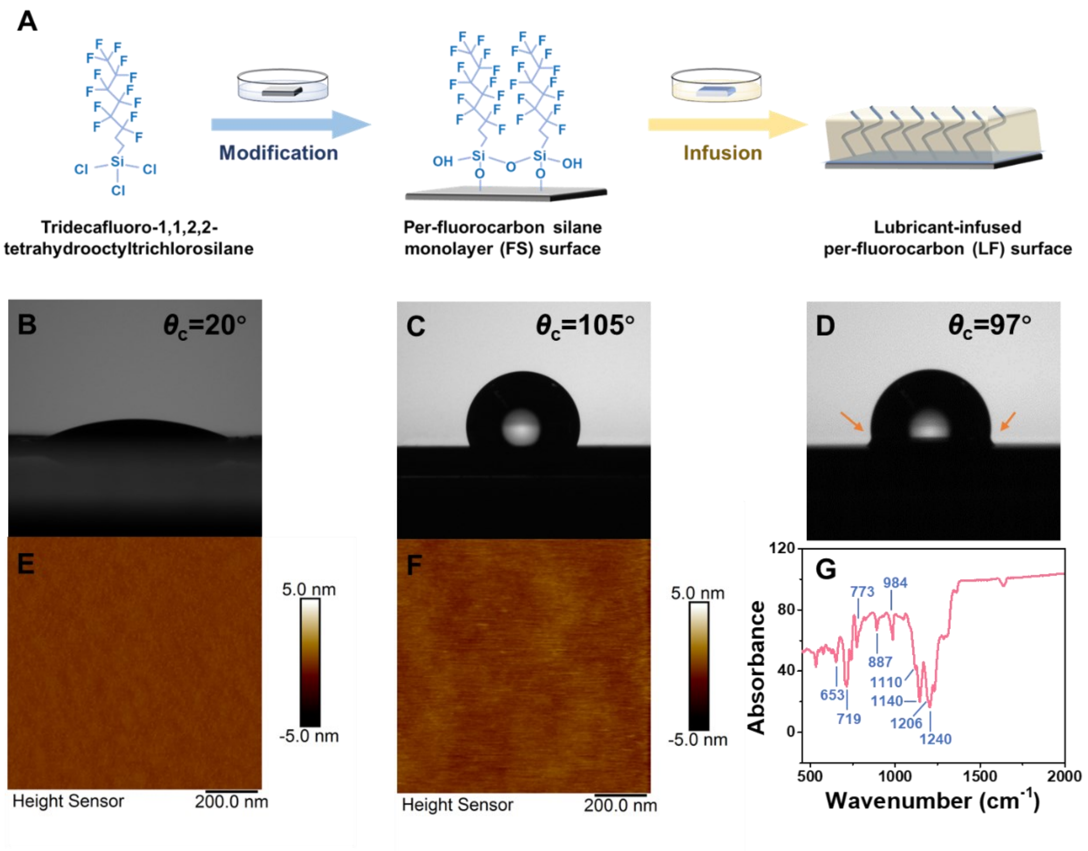

Fig. 3-1 (A) Schematic of the fabrication process of FS coating and LF coating on silica wafer substrate; Water contact angles of (B) bare silica surface, (C) FS-coated silica surface and (D) LF-coated silica surface; Topographic AFM images of (E) bare silica surface and (F) FS-coated silica surface; (G) FTIR spectrum of LF surface with wavenumber range from 500 to 2000 cm^{-1}.

The slippery behavior was examined by monitoring the motion of water droplets on both tilted FS-coated silica surface and LF-coated silica surface. A water droplet was released over the FS and LF surfaces sloped at an incline of 10 degrees. As shown in Figure 3-2 (A-D), the water droplet adhered and pinned on the FS surface over the time course of 3 s. In fact, the water droplet could maintain its shape for a long period until the droplet evaporated and vanished. In contrast, the water droplet was immediately repelled and slid down the LF surface within 0.3 s without leaving a visible residual water trail, showing a slippery and self-cleaning ability of the prepared lubricant-infused surface (Figure 3-2 (E-H)). These results further confirmed the successful coating of LF on silica surface.

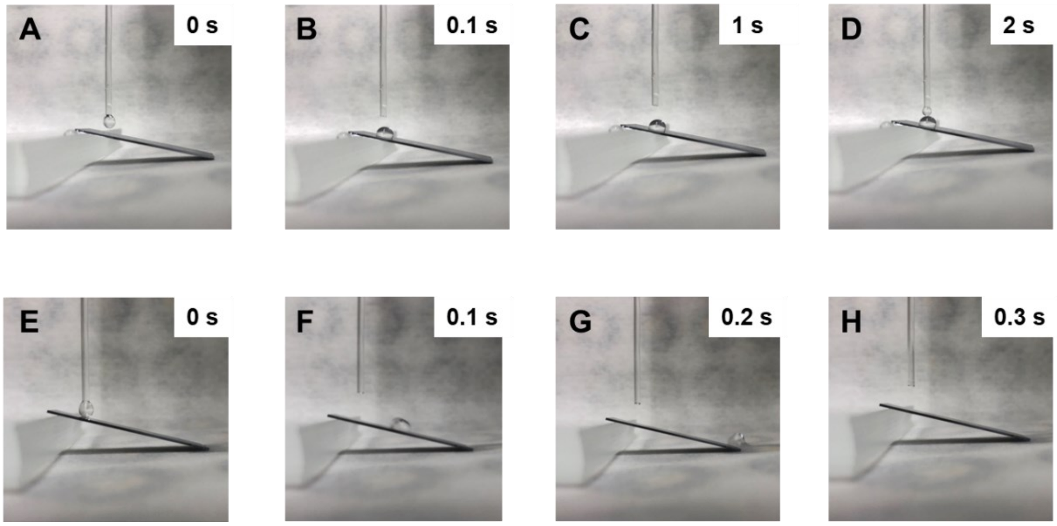

Fig. 3-2 Photographs of motion of the water droplet on A-D) FS-coated surface at an incline of 10 degrees; E-H) LF-coated surface at an incline of 10 degrees.

3.2.2. Interaction between PDA and different substrate surfaces

In this section, the deposition behaviors and interaction mechanisms of PDA with FS surface and LF surface were investigated. The aim was to elucidate how the presence of liquid lubricant can be leveraged to modulate the surface wettability of antifouling surfaces, thereby augmenting the resistance against adhesion and deposition of PDA.

The QCM-D technique was employed to quantitatively monitor the adsorption behavior of PDA on the pristine silica sensor and silica sensors with FS coating or LF coating. The changes in both resonance frequency (Δf) and dissipation of energy (ΔD) offered a real-time measurement of the mass variation of the sensor, which reflected the PDA adsorption and release on the sensor surface. As depicted in Figure 3-3, for three types of sensors, a negative frequency shift and a positive dissipation shift could be observed upon injecting the PDA-Tris solution (1 mg mL^{-1}, pH=8.5), indicating the adsorption of PDA molecules on all tested surfaces. After a certain time (1 h), Tris buffer was introduced into the chamber to remove the loosely-bound PDA, resulting in an increase in frequency and a decrease in dissipation. The introduction of PDA-Tris solution caused an obvious PDA adsorption on the bare silica sensor, evidenced by the significant frequency shift in Figure 3-3 (A). In contrast, a relatively smaller amount of PDA adsorbed on the FS coated sensor than on bare silica sensor (Figure 3-3 (B)). The Δf of the bare silica sensor after rinsing by Tris buffer was measured to be 30 Hz, which was approximately 3-fold higher than that of the FS surface.

As shown in Figure 3-3 (C), only a few amounts of PDA were pre-attached to the LF-coated sensor upon exposure to the PDA solution, and the frequency and dissipation gradually returned to zero over a period after injecting the Tris buffer solution, suggesting effective rinsing of foulants. The QCM-D results provided the comparison of fouling resistance performance between the bare silica sensor and the silica sensors modified with two synthetic coatings, wherein both FS surface and LF surface exhibited antifouling properties. Furthermore, the findings underscored that infusing lubricant into the FS surface could significantly inhibit the PDA deposition, and the attached foulants on the slippery surface could be effectively removed by rinsing water.

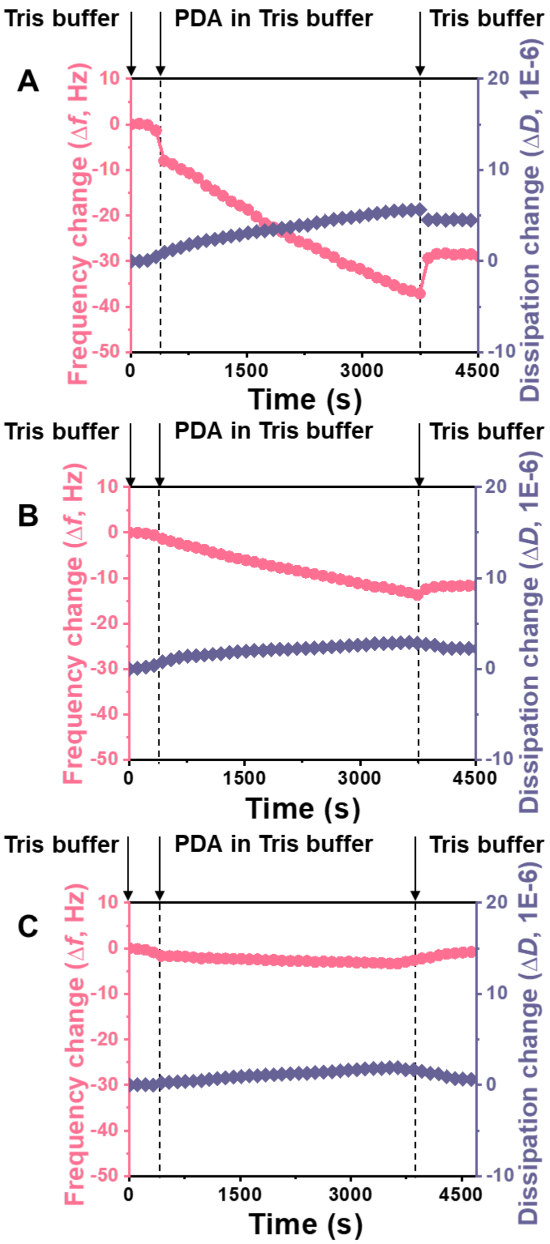

Fig. 3-3 Changes in frequency (pink lines) and dissipation (purple lines) associated with the adsorption of PDA on (A) bare silica sensor, (B) silica sensor coated with FS coating and (C) silica sensor coated with LF coating in 10 mM Tris buffer solution (pH=8.5) using a QCM-D.

AFM force measurements were conducted using colloidal probe techniques to further elucidate the varied microscopic adhesive behaviors and explain the deposition mechanisms of PDA onto FS surface and LF surface. The colloidal probe technique, using a microsphere attached to the AFM cantilever, is highly advantageous for studying the interactions of PDA with surfaces. The spherical shape of the colloidal probe increases the contact area between the probe and the surface, which is beneficial for accurately measuring interaction forces that involve multiple molecular interactions. Moreover, PDA usually forms robust adhesive layers. The colloidal probe technique is less sensitive to the surface roughness of the substrate compared to a sharp AFM tip, which is important as the uniform interaction surface of the colloidal probe minimizes the impact of surface irregularities on the force measurements. In this experiment, an AFM tip functionalized with a colloidal particle coated with a uniform PDA layer was utilized for AFM force measurements (as illustrated in Figure 3-4 (A)), aimed at revealing the interaction mechanisms between PDA and different substrate surfaces. As shown in Figure 3-4 (B), the SEM image of a PDA-coated silica probe depicted a silica microsphere firmly attached to the end of the probe cantilever. EDS images corroborated the successful and uniform fabrication of a PDA layer on the surface of the silica probe.

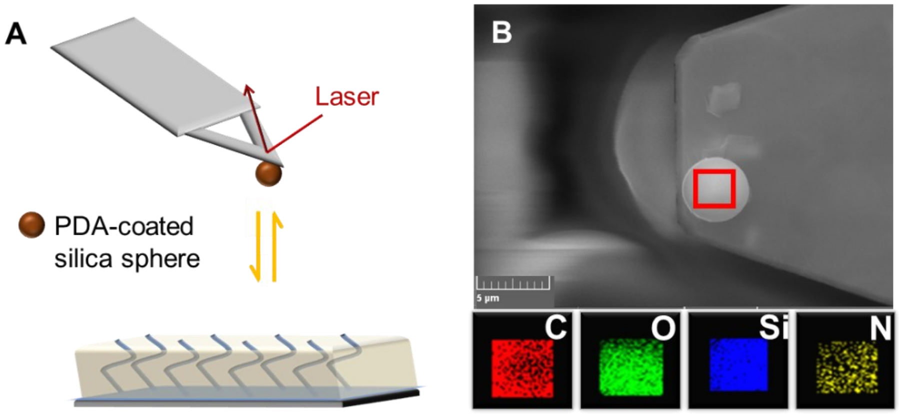

Fig. 3-4 (A) Schematic of AFM force measurements between a PDA-coated silica colloidal probe attached at the end of an AFM probe cantilever and LF surface. (B) SEM image of a PDA-coated AFM silica probe at the end of the probe cantilever and EDS elemental mappings of C, O, Si and N of the coated PDA layer.

Figure 3-5 shows typical force-distance curves for the approach and retraction of a PDA-modified silica colloid cantilever with silica surface, FS surface and LF surface, where positive force represents repulsive interaction and negative force denotes attractive interaction, respectively. The force experiments were conducted in a 10 mM Tris buffer (pH=8.5) to ensure the stability of the PDA-coated silica probe during measurement. To gain deeper insights into the interactions between the PDA probe and different surfaces, the experimental data were theoretically analyzed based on Derjaguin-Landau-Verwey-Overbeek (DLVO) theory, as shown in the solid red curves of Figure 3-5 (B), 3-5 (E) and 3-5 (H). The histograms depicting adhesion force measured during separation and the corresponding fitted Gaussian distributions between the PDA probe and silica substrate, as well as the FS substrate in 10 mM Tris buffer at pH 8.5, are presented in Figure 3-5 (C) and 3-5 (F), respectively. In the case of the bare silica surface (Figure 3-5 (A-C)), a noticeable repulsion was observed during approach at a distance of approximately 10 nm, followed by an attraction and evident "jump-in" behavior occurring at a distance of 5 nm. Given that the isoelectric point (Ip) of PDA particles and hydrophilic silica were reported to be pH 4.5 [44] and pH 4-5 [45,46], respectively, under the experiment condition at pH 8.5, both silica and PDA particles were negatively charged. According to DLVO theory, the repulsion at long range should be attributed to the electric double layer (EDL) interaction between the PDA-coated silica probe and silica surface, while the van der Waals (VDW) attraction became more dominant at short distance, which led to the “jump-in” behavior during the approach. The Hamaker constant between PDA surface and silica surfaces in 10 mM Tris buffer was calculated as 2.47×10^{-20} J using the Lifshitz theory based on the dielectric constants and refractive indexes of silica, PDA and water [47–49]. The zeta potential of silica is reported to be around −30.0 mV at pH 8.5 [50,51]. Fitting the measured force curves using the DLVO theory gives the surface potential of PDA in 10 mM Tris buffer (pH=8.5) as −20.0 mV, which falls within the value range in previous reports [52,53]. A strong "jump-out" behavior appeared when the probe was retracted from the uncoated surface, indicating a strong adhesion force between PDA and the silica surface. A force mapping experiment was further conducted on the bare silica surface, showing a normalized adhesion force (F_{ad}/R) between the PDA-coated silica probe and the bare silica surface of 1.25 ± 0.24 mN m^{-1}. The presence of numerous –OH residual groups on the bare silica surfaces suggested that the measured adhesion force during separation, in addition to VDW attraction, likely stemmed from hydrogen bonding between the –OH groups on the surface and the O-containing groups (e.g., –OH/=O groups) of PDA, as well as coordination interactions between O-hydroxy groups in the residues of PDA and the silica surface.

In the typical force-distance curve of FS surface (Figure 3-5 (D-F)), a repulsion started at 10 nm, followed by an attraction at 5 nm, as observed during the approach of the PDA-coated silica colloidal probe towards the FS surface. At pH 8.5, both FS surface and PDA particles were negatively charged, leading to EDL repulsion between the PDA-coated silica probe and the FS substrate surface. The subsequent attraction behavior during the approach of PDA-coated silica probe towards the FS surface could be attributed to VDW interaction. Furthermore, the measured WCA (105 ± 3.1°) indicated the hydrophobic nature of the FS surface, suggesting that hydrophobic interaction between the aromatic ring of PDA and the CF_3-terminated chains of the per-fluorinated surface should be considered. The measured force curves between PDA probe and FS substrate in 10 mM Tris buffer (pH=8.5) were theoretically analyzed using the extended DLVO theory incorporating hydrophobic interaction, as depicted by the solid curves in Figure 3-5 (E). The Hamaker constant between PDA and perfluorocarbon silane in aqueous solution was calculated as 1.34×10^{-21} J based on the reported Hamaker constant (A_H) of PDA, perfluorocarbon silane and water [47,48,54]. The surface potential of perfluorocarbon silane in 10 mM Tris buffer (pH=8.5) was further fitted and calculated as −22 mV, a value consistent with reported values [55,56]. Additionally, the hydrophobic force with a decay length of 0.9 nm was fitted and determined, indicating strong hydrophobic attraction between the hydrophobic moieties of PDA and the per-fluorinated monolayer. The measured normalized adhesion force (F_ad/R) of the PDA-coated silica probe with the FS surface through adhesion mapping experiment was calculated as 0.39 ± 0.04 mN m^{-1} (Figure 3-5 (F)), attributed to VDW interaction and hydrogen bonding originating from the hydroxyl groups on PDA bound to fluorine atoms of FS surface, which are highly electronegative atoms. The adhesion force of the PDA-coated silica probe with the FS surface was notably weaker than that observed with the silica surface, indicating that the modification of the FS coating on the silica surface significantly inhibited the adhesion behavior of PDA. The measured adhesion results were in good agreement with the adsorption results of QCM-D measurements.

Figure 3-5 (G) and 3-5 (H) illustrate the measured force-distance curve of the PDA-coated silica probe on the LF surface. During the approach, the cantilever moved towards the surface and encountered a repulsive force attributed to the EDL repulsion between the negatively charged PDA and negatively charged slippery oil. Subsequently, the PDA-coated probe was drawn towards the liquid film due to hydrophobic attraction, resulting in a “jump-in” behavior at a distance of 25 nm from the LF surface. As the probe approached further, a sharp linear increase in force was observed (hard wall), indicating that the PDA-coated colloidal probe was pressed to penetrate the oil film and contact the solid FS substrate under the external loading force. When the AFM probe was retracted from the LF surface, an obvious "jump-out" behavior occurred, which comprised the capillary force and the adhesion force between PDA and FC-70 lubricant. The lubricant film stretched and formed a meniscus with the PDA-coated silica particle as the probe retracted. The capillary force, resulting from the direct action of surface tension, is calculated using Equation (1) [57–60]:

$$F_{cap} = 2\pi\gamma R \sin\beta \sin\alpha = 2\pi\gamma R \sin\beta \sin(\beta + \theta) \tag{1}$$

As shown in Figure 3-5 (I), θ is the contact angle, β describes the position of the three-phase contact line on the particle surface, and α is the angle of the liquid surface with the horizontal. Therefore, from the geometry, the angles are related by $\alpha = 180° - \theta - \beta$. For a given contact angle θ, the maximum capillary force F_{cap} occurs at $\mathrm{d}F/\mathrm{d}\beta = 0$, which implies that $\sin(\beta + \theta) = 0$ and $2\beta + \theta = 180°$. Thus, the maximum capillary force required to pull the particle out of the liquid film is shown in Equation (2):

$$F_{cap-max} = 2\pi\gamma R \sin\left(90° - \frac{\theta}{2}\right) \sin\left(90° + \frac{\theta}{2}\right) = 2\pi\gamma R \cos^2\left(\frac{\theta}{2}\right) \tag{2}$$

The surface tension of FC-70 is 18 mN m^{-1}, and the radius of AFM probe is 2.5 μm. The contact angle of FC-70 on PDA-coated silica surface in 10 mM Tris buffer was measured to be 137°, and the maximum capillary force was calculated to be 38 nN. Thus, the strong capillary force with a capillary bridging distance of ~320 nm dominated the "jump-out" behavior. Consequently, the lubricant-infused slippery surface could mitigate PDA fouling in two ways under actual circumstance (without the application of external forces). First, the repulsive EDL interaction between the lubricant layer and PDA particles prevents initial contact when PDA approaches the lubricant-infused slippery surface. Additionally, the strong capillary bridging further obstructs PDA particles from penetrating the lubricant film and contacting the underlying fluorinated surface [61]. Based on the above analysis, it appears highly challenging for PDA to make contact with the FS surface in the presence of the lubricant layer. These AFM findings align with the QCM-D results, collectively suggesting that the presence of a lubricant film has great effects on the deposition behavior and molecular interactions of PDA with underneath substrates.

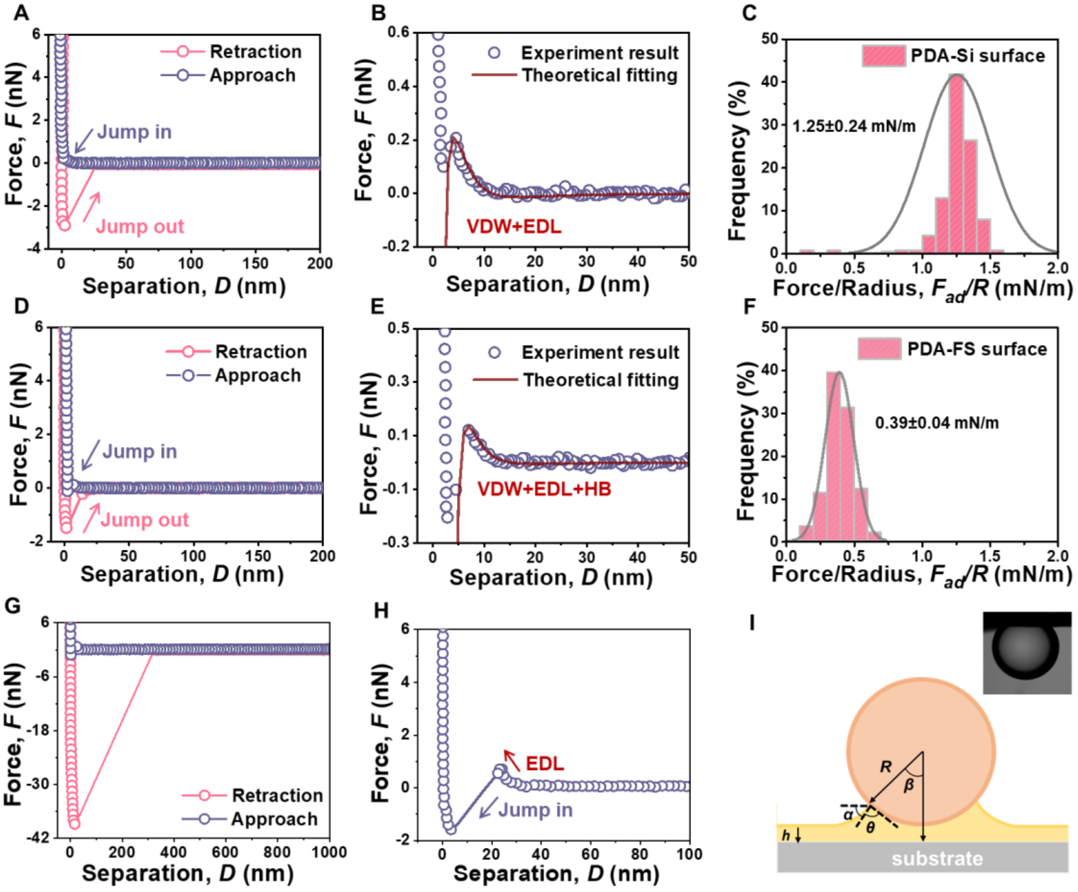

Fig. 3-5 Typical force-separation curves and the zoom-in force-separation approaching profiles between A-B) the PDA-coated silica probe and bare silica surface; D-E) the PDA-coated silica probe and FS surface; G-H) the PDA-coated silica probe and LF surface in 10 mM Tris buffer solution (Experiment results are shown in open symbols

and theoretical calculations are shown in red curves). The histograms of measured adhesion F_{ad}/R and the fitted Gaussian distributions between the C) PDA-coated silica probe and bare silica surface and F) the PDA-coated silica probe and FS surface in 10 mM Tris buffer solution. I) Schematic of the colloidal AFM probe and a meniscus formed with the FC 70 lubricant film on FS substrate. θ is the contact angle, β describes the position of the three-phase contact line on the particle surface, and α is the angle of the liquid surface with the horizontal, h is the thickness of lubricant layer, and R is the radius of AFM probe. And the insert is underwater contact angle of FC-70 droplet on a PDA substrate.

3.2.3. Interactions between DOPA moiety and liquid-infused slippery surfaces

Unlike PDA, which comprises various motifs such as catechol, dopamine quinone, 5,6-dihydroxyindole, amine and imine, the molecular structure of a single DOPA moiety is significantly different. Thus, the adhesion behaviors of PDA on different substrate surfaces are not able to accurately reveal the binding mechanisms and adhesion strength of a single catechol to FS surface and LF surface. SM-AFM technique enables the direct measurement of interactions between individual binding pairs, facilitating the inference of interaction mechanisms. Through analysis of rupture kinetics and bond dissociation energy, distinct binding modes between a single DOPA moiety and different surfaces can be identified, providing quantitative insights into how the addition of a lubricant layer affects the adhesion ability and binding strength of a single DOPA moiety on per-fluorinated surfaces. To elucidate the nanomechanical mechanisms of binding affinity of a DOPA moiety to FS surface and LF surface at the single-molecule scale, a single DOPA-terminated molecule (thioctic-PEG$_{4000}$-catechol) was synthesized and covalently immobilized on an AFM gold tip. Subsequently, their rupture forces with FS and LF surfaces were quantitatively measured in a 5 mM NaCl solution at pH 4 using SM-AFM. The pH of the NaCl solution was adjusted to 4 to prevent the oxidation of the DOPA moiety. The synthesis and dipcoating process details were provided in the Experimental section, and the experimental schematic was illustrated in Figure 3-6.

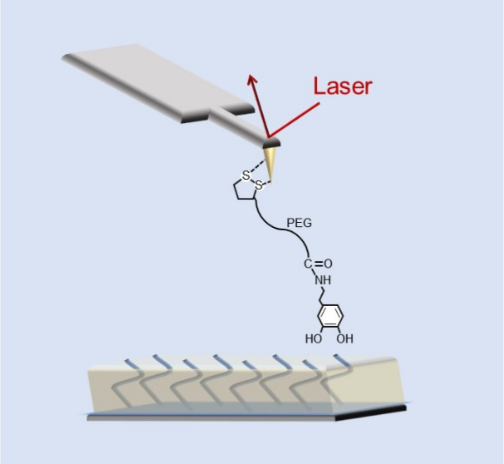

Fig. 3-6 Schematic illustration of the SM-AFM experimental setup for measuring the interaction between a single DOPA-terminated molecule and FC-70 lubricant-infused per-fluorinated surface at the single-molecule level.

In a typical single molecular force measurement, the modified AFM tip was moved to approach and contact with the substrates under a maximum loading force of 6 nN, which allows the formation of specific bonds between the DOPA molecule and the underneath surface. Upon retracting the AFM tip at a constant force loading rate, the PEG bridge of the single molecule was stretched, leading to the rupture and breaking of specific bonds. Figures 3-7 (A) and 3-7 (D) show the representative force-distance curves for the rupture events of a single DOPA moiety interacting with FS surface and LF surface under the same loading rate of 1.29×10^4 pN s^{-1}, respectively. The initial attractive force within 10 nm separation corresponds to nonspecific interactions between the modified AFM tip and the opposing surface. Then, the specific rupture events around 30 nm separation could be detected, corresponding to the specific molecular binding of the pair between the DOPA-terminated PEG chain on the AFM tip and per-fluorinated molecules on the substrate. The extension length of the rupture events in the force-distance curves, visible at a distance of ~30 nm, aligns with the reported length of PEG_{4000} chains [62]. The rupture distance could be utilized to differentiate the desired dissociation events, facilitating the rejection of initial adhesion and rupture events arising from impurities beyond the defined range. The measured rupture events were adequately fitted by the worm-like chain model (red line in Figures 3-7 (A) and 3-7 (D) with a characteristic PEG chain with the contour length around 33 nm. The fitted parameters were consistent with the reported mechanical parameters of PEG chains [62,63], confirming the successful stretching of the anchored PEG chain. To eliminate the influence of multiple binding sites on the substrate leading to various rupture events, more than 100 force profiles with a single specific rupture event within the range of 30 ± 10 nm were collected and subjected to Gaussian distribution fitting. The statistical histograms of rupture forces of DOPA with FS surface and LF surface at a constant force loading rate of 1.29×10^4 pN s^{-1} are displayed in Figures 3-7 (B) and 3-7 (E), respectively. Through the statistical approach, the most probable rupture forces of each pair were determined, providing a direct comparison of the interaction strength of a single DOPA moiety with different surfaces. Notably, the most probable rupture force of DOPA−FS surface (144.03 pN) was approximately twice that of DOPA−LF surface (73.15 pN). Despite its versatility as an adhesive, DOPA demonstrated adaptability for adsorption to both surface types. However, the presence of the FC-70 lubricant on the FS surface served as a barrier significantly weakening the binding strength between DOPA and per-fluorinated chains.

Generally, the rupture force increases with the force loading rate, and simply comparing the rupture force at a given pulling speed cannot provide complete insights into the nanomechanical mechanisms of each DOPA−surface interaction. To comprehensively understand the binding strength and binding mechanism of the molecular interactions, the dynamic force spectroscopy was conducted to quantitively evaluate the dissociation kinetics and establish the free energy landscapes underlying the unbinding processes of the single DOPA moiety with different surfaces. Herein, the most probable rupture forces on different surfaces were measured at five different loading rates (r) ranging from 1.29×10^4 to 1.93×10^5 pN s^{-1}, and the distribution histograms were summarized in Figures 3-9 and 3-10. It is evident from Figures 3-7 (C) and 3-7 (F) that the most probable rupture forces of both DOPA−FS surface and DOPA−LF surface responded linearly with the logarithm of the loading rates (F_{mpr} vs. $\ln r$). Based on the linear dependence between F_{mpr} and $\ln r$ fitted by the classical Bell-Evans theory, the structure information and dynamics of the molecular unbinding process could be detailly explored. The bond dissociation kinetics and energetic parameters of the specific bonds between the single DOPA moiety and two types of surfaces could be determined according to Equation (3) and Equation (4):

$$F_{\mathrm{mpr}} = \frac{k_{\mathrm{B}}T}{x_{\mathrm{B}}} \ln\left(\frac{x_{\mathrm{B}}}{k_{\mathrm{off}}k_{\mathrm{B}}T}\right) + \frac{k_{\mathrm{B}}T}{x_{\mathrm{B}}} \ln r \tag{3}$$

$$\Delta G = -k_{\mathrm{B}}T \ln \frac{k_{\mathrm{off}}}{A} \tag{4}$$

Where F_{mpr} is the most probable rupture force, r is the loading rate, k_{B} is the Boltzmann constant, T is the absolute temperature, x_{B} is the characteristic dissociation distance from the bound state to the transition state, and k_{off} is the spontaneous dissociation rate of the bond. Both x_{B} and k_{off} serve as important measures for the stability of interactions. ΔG stands for the free energy barrier for the bond dissociation pathways, which depends on the free energy difference between the bond state and the transition state. Therefore, the ΔG

for the rupture of a bond by force is the kinetic energy, relying on the reaction pathway. *A* is the Arrhenius prefactor, and we chose *A* to be 10^6 s^{-1} in the calculation.

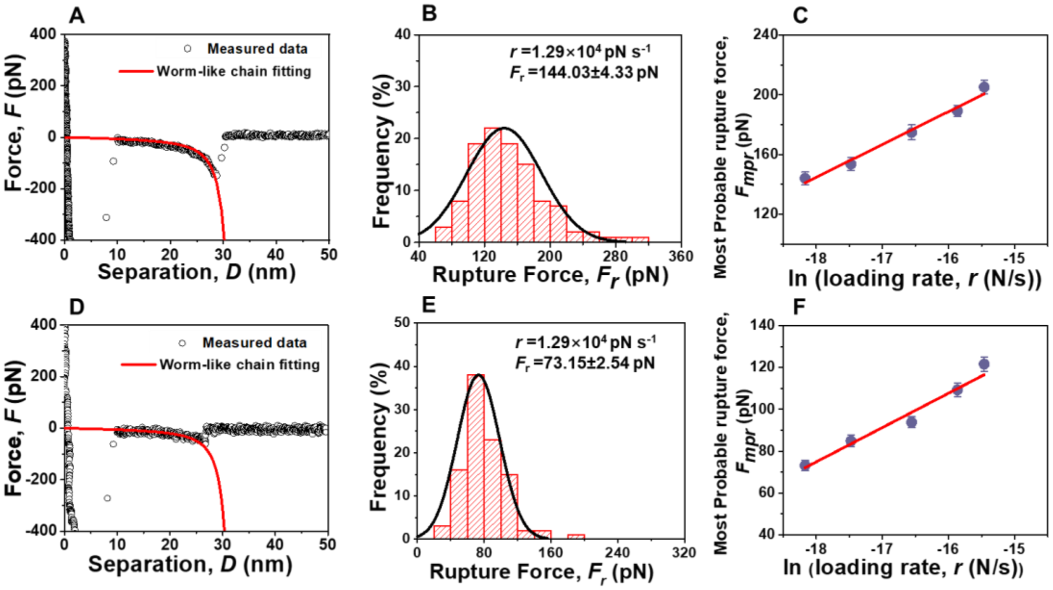

G

Kinetic Parameters	K_{off} (s^{-1})	x_B (Å)	△G (K_BT)
DOPA-FS surface	0.96	1.87	13.85
DOPA-LF surface	9.71	2.50	11.54

Fig. 3-7 SM-AFM results of a single DOPA moiety interacting with (A-C) FS surface and D-F) LF surface. Representative force-distance retraction curves (open symbols) at a loading rate of 1.29 × 10^4 pN s^{-1} and the worm-like chain fitting (red line) using a persistence length L_P of 0.38 nm for a single DOPA molecule interacting with (A) FS surface and (D) LF surface. The rupture force histograms and fitted Gaussian distribution of (B) FS surface and (E) LF surface at a loading rate of 1.29 × 10^4 pN s^{-1}. The logarithmic relation of the most probable rupture force F_{mpr} as a function of the loading rate *r* for (C) FS surface and (F) LF surface. (G) Summary of dissociation kinetics and energetic parameters based on the classical Bell-Evans theory.

The kinetic parameters for the rupture of interactions between DOPA and two types of surfaces are summarized in Figure 3-7 (G). The binding mechanism could be inferred and analyzed based on the free energy barrier, nanomechanical results of the molecular unbinding process, as well as the chemical composition of surfaces. Li et al. plotted the free energy barrier (ΔG) versus rupture distance (x_B) figure for various types of interactions between the DOPA moiety and different surfaces based on data from previously published papers [64]. According to the reported plot, for both DOPA−FS surface and DOPA−LF surface interactions, the measured values of dissociation kinetics and energetic parameters appeared in the crossover range of both hydrogen bonding and hydrophobic interaction, indicating that the binding interactions of the DOPA molecule with the two surfaces originated from the synergy effect of hydrogen bonding between the hydroxyl groups of the DOPA molecule and the F atoms, and hydrophobic interaction between the aromatic ring of DOPA and the per-fluorinated chains. It is noteworthy that the rupture force of the DOPA moiety with the LF surface at each specific loading rate was only half of that with the FS surface, revealing that the force required to break the bond between DOPA and the per-fluorinated chain was significantly decreased after infusing the lubricant into FS surface. The dissociation rate (k_{off}) of the specific bonding between DOPA−LF surface (9.71 s^{-1}) was significantly higher, ten times that of DOPA−FS surface (0.96 s^{-1}). Generally, the dissociation rate represents the lifetime of the molecular bond, indicating that the specific bond with a lower k_{off} requires a longer bond dissociation time, which suggests a more stable binding between the single catechol moiety and the FS surface [65]. Moreover, the dissociation distance (x_B) of DOPA−FS surface bonds was approximately 1.87 Å, while the unbinding process of the DOPA moiety with LF surface showed a longer dissociation distance of 2.50 Å. A smaller dissociation distance signifies a shorter length difference between the bound state and the dissociation transition state, suggesting the narrow width of energy barriers and the high binding affinity of DOPA molecules towards substrates. The free energy barrier ΔG of the DOPA−FS surface interaction was calculated to be 13.9

$k_\mathrm{B}T$ (~34.3 kJ/mol), while the free energy barrier ΔG obtained from DOPA−LF surface system was slightly lower, calculated to be 11.6 $k_\mathrm{B}T$ (~28.7 kJ/mol). Thus, in the absence of the lubricant layer, the interaction between the DOPA moiety and the per-fluorinated chains yielded a steeper and narrower energy landscape, revealing the molecules would bind to each other more tightly with higher stability.

The SM-AFM results demonstrated that compared to DOPA−FS surface interaction, the rupture force required to break the binding interaction of DOPA with perfluorocarbon silane chains was much lower in the presence of the lubricant film, and the stability of the bond between DOPA and perfluorocarbon silane chains could be greatly affected. For traditional antifouling surfaces, which are solid and static such as the FS surface, the interactions between the DOPA and surfaces depend on the surface chemistry and structural topography during the contact process, which are usually stable. However, for LF surface, when the DOPA moiety penetrated the lubricant film and contacted with the FS substrate, the surface mobility of the interfacial lubricant molecules weakened the binding strength and affinity of the DOPA molecule to the underneath per-fluorinated substrate. The addition of FC-70 lubricant film on FS surface could effectively prevent the anchoring of the versatile DOPA moiety by displacing the solid fluorinated monolayer at the interface and destabilizing the interactions, thereby enhancing the fouling resistance performance.

3.3. Experimental Section

3.3.1. Materials

Dopamine hydrochloride, ethanol, silica wafers, tridecafluoro-1,1,2,2-tetrahydrooctyl trichlorosilane, 3M^{TM} Fluorinert FC-70 were purchased from Sigma-Aldrich (Canada). Tris(hydroxymethyl)aminomethane, hydrogen peroxide and copper(II) sulfate pentahydrate were purchased from Fisher Scientific (Canada). The water used in experiments was deionized and ultra-filtered by ELGA LabWater system (France).

3.3.2. Preparation of FS surface and LF surface

Silica wafer substrates were exposed to low-pressure (150-250 mTorr) water plasma at Watts (PDC-21G plasma system, Harrick Plasma, US) followed by immediately immersed in 2% vol./vol. tridecafluoro-1,1,2,2-tetrahydrooctyl trichlorosilane in 99.9% anhydrous ethanol solution for 1 h at room temperature. Then the treated substrates were rinsed with ethanol three times and dried with nitrogen, and finally kept in an oven at 60 °C for 4 h. As a matter of convenience, the prepared perfluorocarbon silane coating was defined as FS surface.

Then, the prepared FS surface was immersed in perfluorotripentylamine (3M^{TM} Fluorinert FC-70) overnight to make the lubricant spread onto the whole substrates. Before use, the excess lubricant that was not bound to the surface was removed by tilting the surface for 5 minutes. The lubricant-infused perfluorocarbon coating was simplified as LF surface in the following experiment results.

3.3.3. Force measurement using the AFM colloidal probe techniques

The interaction between PDA and different surfaces was measured by the AFM colloidal technique. The colloidal AFM probe was prepared by gluing a silica sphere of diameter around 5 μm using a two-component epoxy resin at the end of a triangular tipless AFM cantilever (Bruker, Santa Barbara, USA). Before the experiment, the colloidal probe was firstly treated by ozone and then immersed in PDA-Tris solution (1 mg mL^{-1} dopamine hydrochloride in 10 mM Tris buffer solution with 2.5 mM $CuSO_4$ and 13 mM H_2O_2, pH=8.5) for 30 min to form a uniform PDA deposition layer. After that, the probe was washed with deionized water and blow-dried by nitrogen gas.

The force measurement was conducted by an MFP-3D AFM instrument (Asylum, Santa Barbara, USA). All experiments were carried out by immersing the silica substrates with/without coating modification of FS/LF coating in the fluid cell with 10 mM Tris buffer (pH=8.5), and then, the PDA-coated AFM silica probe was moved to approach towards and retract from the surfaces at a velocity of 1 µm s^{-1} at a loading force of 6 nN. For better data analysis, the adhesion force mapping was measured within a 2 µm × 2 µm area consisting of 20 × 20 points. The adhesion force distribution was analyzed and fitted by the Gaussian distribution. Prior to the measurement, the spring constant of probe was calibrated using the Hutter and Bechhoefer method. All experiments were repeated for two substrates of the same functionalization and on more than three locations on the same surface using two different PDA-coated silica colloidal probes.

For theoretically analyzing the force-separation profiles, the classical DLVO model coupled with non-DLVO forces which is named as the extended DLVO theory, has been applied. The DLVO forces, i.e., van der Waals force (F_{vdw}) and electric double layer force (F_{edl}) are given by Equation (5) and Equation (6), respectively [66,67].

$$F_{vdw} = -\frac{A_H R}{6D^2} \tag{5}$$

$$F_{edl} = \frac{\pi}{\varepsilon\varepsilon_0\kappa^2}\left[(\sigma_P^2+\sigma_S^2)(e^{-2\kappa D}+2\kappa D-1)e^{-2\kappa D}+4\sigma_P\sigma_S(e^{-\kappa D}+\kappa D-1)e^{-\kappa D}\right] \tag{6}$$

$$\sigma = \sqrt{8\varepsilon\varepsilon_0 \cdot k_B T \cdot CN_A}\sinh\left(\frac{e\Psi}{2k_B T}\right) \tag{7}$$

where A_H (J) is the Hamaker constant, R (m) is the radius of silica microsphere, D (m) is the separation distance between the colloidal probe and substrate, ε is the dielectric constant of the solution, ε_0 is the vacuum permittivity, $1/\kappa$ (m) is the Debye length, σ_P and σ_S (C m^{-2}) are the surface charge density of colloidal probe and substrate, respectively. k_B (J K^{-1}) is the Boltzmann constant, T (K) is the temperature, C (M) is the bulk concentration of ions, N_A (6.23×10^{23}) is the Avogadro's number, e (1.6×10^{-19}) is the elementary charge, and Ψ (V) is the surface potential.

Hydrophobic force (*HB*) also follows an exponential decay with distance as shown in Equation (8)[66,68],

$$HB = -CRe^{-D/D_0} \tag{8}$$

where C (N m^{-1}) is a constant and D_0 (m) is the decay length of hydrophobic interaction. The classical DLVO force F_{DLVO} and overall extended DLVO force $F_{\text{EX-DLVO}}$ of the system are given by Equation (9) and Equation (10), respectively,

$$F_{DLVO} = F_{vdw} + F_{edl} \tag{9}$$

$$F_{EX-DLVO} = F_{vdw} + F_{edl} + HB + \cdots \tag{10}$$

3.3.4. Deposition of PDA on different surfaces

QCM-D (Q-sense, Sweden) was applied to quantitatively monitor the adsorption behavior of PDA on silica sensors with/without the FS and LF coatings in Tris buffer (10 mM, pH=8.5). Before the experiment, the silica sensors were cleaned according to the protocol and functionalized as described in section 3.3.2. In the QCM-D measurement, the Tris buffer was passed through the measuring chamber to contact the silica crystal sensor at a slow flow rate of 50 μL min^{-1}. Once a stable baseline was obtained, the sensor surface was exposed to PDA solution (dopamine hydrochloride dissolved in the background solution for 30 min, 1 mg mL^{-1}, pH=8.5) at a flow rate of 50 μL min^{-1} for 1 h. After that, the Tris buffer was injected again to remove loosely bound PDA.

3.3.5. Force measurement using AFM-based single molecular force spectroscopy (SM-AFM)

The interaction between single DOPA moiety and different surfaces was measured by the SM-AFM. The functionalized AFM tips were prepared by the following procedures. HS-PEG$_{4000}$-DOPA (MW=4000) and HS-PEG$_{2000}$-CH$_3$ (MW=2000) were dissolved in deionized water with a molar concentration of 0.1 mM and 10 mM, respectively. The AFM gold tips (Bruker, Santa Barbara, US) were cleaned through UV/ozone treatment and immersed in the as-prepared solution overnight at room temperature. After reaction, a monolayer containing HS-PEG$_{4000}$-DOPA and HS-PEG$_{2000}$-CH$_3$ with a ratio of 1:100 was self-assembled on the gold tips. After being cleaned with deionized water three times and blow-dried with nitrogen gas, the tips were used for force measurement immediately.

Single molecular force experiments were conducted using AFM MFP-3D (Asylum Research, Santa Barbara, US). The FS/LF surfaces performed in the experiment were fresh-prepared. All experiments were carried out by immersing all the substrates in the fluid cell with 5 mM NaCl solution (pH=4). Before measurement, the probe was calibrated using the Hutter and Bechhoefer method to get the spring constant around 120 pN nm^{-1}. The probe was moved to approach and then retracted from the surface with a maximum loading force of 6 nN under a range of loading rates (from 100 nm s^{-1} to 1500 nm s^{-1}) to measure the force-distance curves. To collect more single-molecular rupture events, force mappings containing 20 × 20 points were also measured on the surfaces over a 2 μm × 2 μm area with different retracting rates.

Representative force-extension curves for the rupture events were fitted by the worm-like chain model (Equation (11)).

$$\frac{FLp}{k_B T} = \frac{1}{4}\left(1 - \frac{x}{Lc}\right)^{-2} - \frac{1}{4} + \frac{x}{Lc} \tag{11}$$

Herein, *F* is the applied force, *x* represents molecular extension, L_c is the contour length of the molecule and L_p refers to the persistence length of the chain. k_B is the Boltzmann constant, and *T* is the absolute temperature.

3.3.6. Characterization of monolayer surfaces and PDA-coated AFM silica probe

The surface morphologies of silica substrates before and after coating modification were characterized by atomic force microscopy (Icon, Bruker, Santa Barbara, USA) in tapping mode. An X-ray photoelectron spectroscopy (XPS) (PerkinElmer, USA) was applied to collect and analyze the element composition of the functionalized surface. The wettability of different surfaces was measured by static water contact angle by a contact angle goniometer (Rame-hart instrument Co., Succasunna, NJ, USA). The chemical composition of the LF surface was evaluated by Fourier transform infrared spectroscopy (FTIR) ((Nicolet iS50 FTIR spectrometer, Thermo Scientific, USA). The morphology and element analysis of the PDA-coated AFM silica probe was characterized by scanning electron microscopy (TESCAN, VEGA3, USA) with an energy-dispersive X-ray spectroscopy.

3.4. Conclusion

In this work, a fundamental understanding of the molecular binding behaviors and interaction strengths of mussel-inspired chemistry, specifically DOPA and PDA, to fluorinated-based slippery surfaces was investigated. The colloidal probe AFM technique was employed to unravel the interaction mechanisms between PDA and perfluorocarbon silane surfaces with/without a lubricant layer underlying the deposition behavior of PDA. Meanwhile, we further quantitatively determined the interaction energy and binding strength between versatile adhesive DOPA moiety and lubricant-infused slippery surface at the single molecular level using SM-AFM measurement.

(1) Combining the PDA deposition experiment and the surface force measurement, it was found that the infused lubricant layer exhibited a significant influence on deposition behavior of PDA on per-fluorinated surfaces, which prevented PDA from contacting and penetrating the lubricant film through EDL repulsion and capillary bridging.

(2) The bond dissociation energies of DOPA adhering on the two surfaces were similar, originating from the synergy effect of hydrogen bonding between the hydroxyl groups of DOPA molecule and the F atoms, and hydrophobic interaction between the aromatic ring of DOPA and the per-fluorinated chains.

(3) The kinetic parameters indicated that the lifetime and stability varied greatly for interactions between DOPA and the two fluorinated functional substrates. In particular, the strength and stability of the molecular interaction between DOPA and LF surface was obviously weaker as compared to that between DOPA and FS surface, suggesting the addition of the mobilized lubricant layer could disrupt the

contact and bonding between DOPA and per-fluorinated molecules, thus affecting the anchoring and deposition of DOPA moiety on per-fluorinated monolayer underneath the lubricant film.

Our study elucidated the antifouling performance and repellence mechanisms of lubricant-infused slippery surfaces against versatile mussel-chemistry in molecular level, which offer supplemental information for the understanding of mussel adhesion mechanisms as well as provide new insights into the development of novel antifouling coatings.

3.5. Supporting Information

3.5.1. XPS spectrum of FS surface

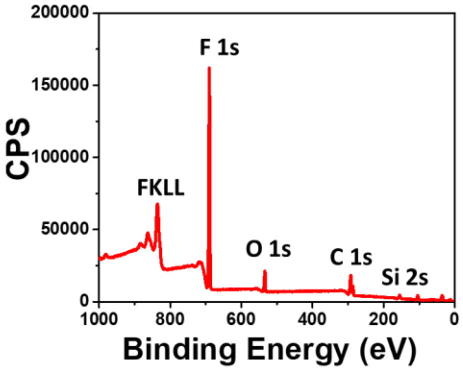

Name	Area	At%
O	15152.6	7.43
C	21954.1	31.54
F	170968.8	55.36
Si	3222.1	5.67

Fig. 3-8 XPS wide-scan spectra of a silicon substrate sample functionalized with tridecafluoro-1,1,2,2-tetrahydrooctyl trichlorosilane (FS surface). Fluorine was clearly present as evidenced by the F 1s and F KLL peaks, and the presence of the C 1s peak also suggested the successful grafting of the per-fluorinated silane [63,64].

3.5.2. The histogram of rupture forces between single DOPA moiety and FS surface and LF surface.

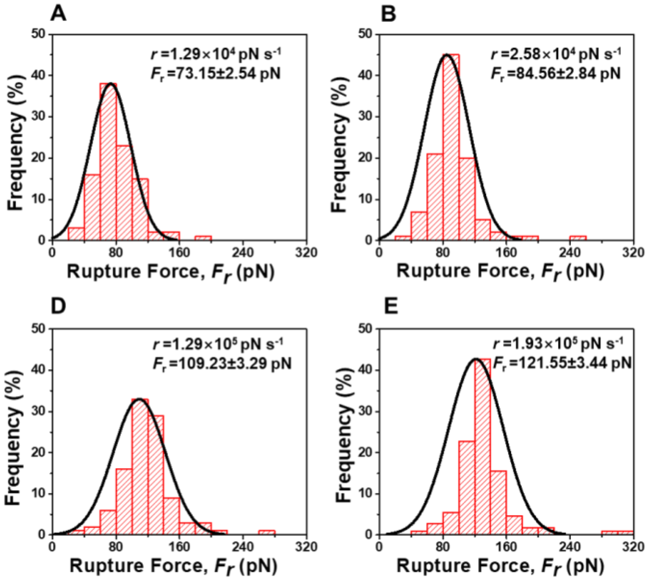

Fig. 3-9 (A-E) The histogram of rupture forces between single DOPA moiety and FS surface. The black curves are Gaussian fits to the corresponding histograms.

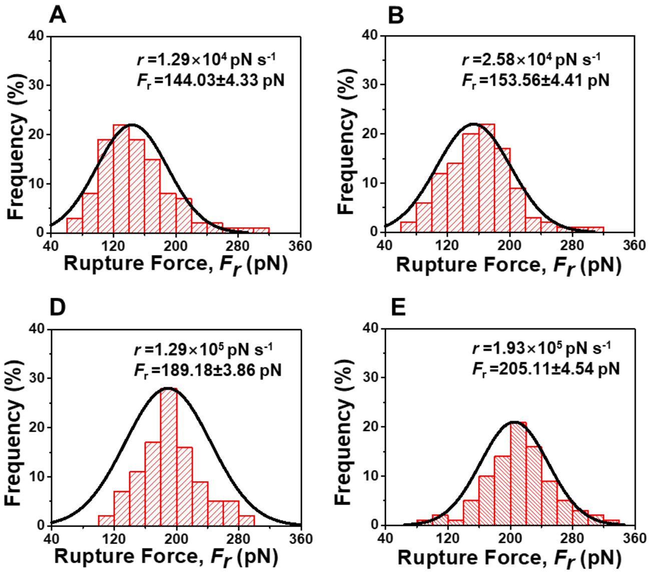

Fig. 3-10 (A-E) The histogram of rupture forces between single DOPA moiety and LF surface. The black curves are Gaussian fits to the corresponding histograms.

References

[1] J. Tian, X. Qi, C. Li, G. Xian, *ACS Appl Mater Interfaces* **2023**, *15*.

[2] J. Tian, C. Li, G. Xian, *J Mater Res Technol* **2022**, *21*.

[3] Q. Lu, E. Danner, J. H. Waite, J. N. Israelachvili, H. Zeng, D. S. Hwang, *J R Soc Interface* **2013**, *10*, 20120759.

[4] E. W. Danner, Y. Kan, M. U. Hammer, J. N. Israelachvili, J. H. Waite, *Biochemistry* **2012**, *51*, 6511.

[5] N. Bandara, H. Zeng, J. Wu, *J Adhes Sci Technol* **2013**, *27*, 2139.

[6] J. H. Waite, M. L. Tanzer, *Science (1979)* **1981**, *212*, 1038 LP.

[7] Q. Lin, D. Gourdon, C. Sun, N. Holten-Andersen, T. H. Anderson, J. H. Waite, J. N. Israelachvili, *Proc Natl Acad Sci* **2007**, *104*, 3782 LP.

[8] H. Lee, N. F. Scherer, P. B. Messersmith, *Proc Natl Acad Sci* **2006**, *103*, 12999 LP.

[9] S. Kim, J. Huang, Y. Lee, S. Dutta, H. Y. Yoo, Y. M. Jung, Y. Jho, H. Zeng, D. S. Hwang, *Proc Natl Acad Sci* **2016**, *113*, E847.

[10] N. Bandara, H. Zeng, J. Wu, *J Adhes Sci Technol* **2013**, *27*, 2139.

[11] D. S. Hwang, H. Zeng, A. Masic, M. J. Harrington, J. N. Israelachvili, J. H. Waite, *Journal of Biological Chemistry* **2010**, *285*.

[12] S. Kim, J. Huang, Y. Lee, S. Dutta, H. Y. Yoo, Y. M. Jung, Y. Jho, H. Zeng, D. S. Hwang, *Proc Natl Acad Sci* **2016**, *113*, E847 LP.

[13] S. Kim, H. Y. Yoo, J. Huang, Y. Lee, S. Park, Y. Park, S. Jin, Y. M. Jung, H. Zeng, D. S. Hwang, Y. Jho, *ACS Nano* **2017**, *11*, 6764.

[14] C. Lim, J. Huang, S. Kim, H. Lee, H. Zeng, D. S. Hwang, *Angew Chem Int Ed* **2016**, *55*, 3342.

[15] Q. Lu, D. S. Hwang, Y. Liu, H. Zeng, *Biomaterials* **2012**, *33*, 1903.

[16] Q. Lu, D. X. Oh, Y. Lee, Y. Jho, D. S. Hwang, H. Zeng, *Angew Chem Int Ed* **2013**, *52*, 3944.

[17] M. Yu, J. Hwang, T. J. Deming, *J Am Chem Soc* **1999**, *121*, 5825.

[18] J. Zhang, L. Xiang, B. Yan, H. Zeng, *J Am Chem Soc* **2020**, *142*, 1710.

[19] L. Lü, H. Lou, Y. Xiao, G. Zhang, C. Wang, Y. Deng, *RSC Adv* **2018**, *8*, 4604.

[20] D. Yao, J. Feng, J. Wang, Y. Deng, C. Wang, *J Power Sources* **2020**, *463*, 228188.

[21] D. M. Yebra, S. Kiil, K. Dam-Johansen, *Prog Org Coat* **2004**, *50*, 75.

[22] E. M. Hetrick, M. H. Schoenfisch, *Chem Soc Rev* **2006**, *35*, 780.

[23] B. Nicolas , H. D. J., H. Sung-Hei, R. S. A., K. Staffan, W. J. S., *J Bacteriol* **2006**, *188*, 7344.

[24] C. Yang, X. Ding, R. J. Ono, H. Lee, L. Y. Hsu, Y. W. Tong, J. Hedrick, Y. Y. Yang, *Adv Mater* **2014**, *26*, 7346.

[25] P. Kingshott, J. Wei, D. Bagge-Ravn, N. Gadegaard, L. Gram, *Langmuir* **2003**, *19*, 6912.

[26] J. H. Park, Y. H. Bae, *Biomaterials* **2002**, *23*, 1797.

[27] S. Jiang, Z. Cao, *Adv Mater* **2010**, *22*, 920.

[28] S. Chen, S. Jiang, *Adv Mater* **2008**, *20*, 335.

[29] D. Chen, T. Liu, J. Kang, R. Xu, Y. Cao, M. Xiang, *Adv Mater Interfaces* **2019**, *6*, 1900706.

[30] P. Zhang, S. Wang, S. Wang, L. Jiang, *Small* **2015**, *11*, 1939.

[31] M. Liu, S. Wang, Z. Wei, Y. Song, L. Jiang, *Adv Mater* **2009**, *21*, 665.

[32] T. S. Wong, S. H. Kang, S. K. Y. Tang, E. J. Smythe, B. D. Hatton, A. Grinthal, J. Aizenberg, *Nature* **2011**, *477*, 443.

[33] C. Howell, T. L. Vu, C. P. Johnson, X. Hou, O. Ahanotu, J. Alvarenga, D. C. Leslie, O. Uzun, A. Waterhouse, P. Kim, M. Super, M. Aizenberg, D. E. Ingber, J. Aizenberg, *Chem Mater* **2015**, *27*, 1792.

[34] S. M. Bennett, J. A. Finlay, N. Gunari, D. D. Wells, A. E. Meyer, G. C. Walker, M. E. Callow, J. A. Callow, F. V Bright, M. R. Detty, *Biofouling* **2009**, *26*, 235.

[35] C. Howell, A. Grinthal, S. Sunny, M. Aizenberg, J. Aizenberg, *Adv Mater* **2018**, *30*, 1802724.

[36] S. Amini, S. Kolle, L. Petrone, O. Ahanotu, S. Sunny, C. N. Sutanto, S. Hoon, L. Cohen, J. C. Weaver, J. Aizenberg, N. Vogel, A. Miserez, *Science (1979)* **2017**, *357*, 668 LP.

[37] R. Hönes, Y. Lee, C. Urata, H. Lee, A. Hozumi, *Langmuir* **2020**, *36*, 4496.

[38] D. C. Leslie, A. Waterhouse, J. B. Berthet, T. M. Valentin, A. L. Watters, A. Jain, P. Kim, B. D. Hatton, A. Nedder, K. Donovan, E. H. Super, C. Howell, C. P. Johnson, T. L. Vu, D. E. Bolgen, S. Rifai, A. R. Hansen, M. Aizenberg, M. Super, J. Aizenberg, D. E. Ingber, *Nat Biotechnol* **2014**, *32*.

[39] J. A. Gladysz, D. P. Curran, *Tetrahedron* **2002**, *58*.

[40] T. S. Wong, S. H. Kang, S. K. Y. Tang, E. J. Smythe, B. D. Hatton, A. Grinthal, J. Aizenberg, *Nature* **2011**, *477*, 443.

[41] J. Yin, M. L. Mei, Q. Li, R. Xia, Z. Zhang, C. H. Chu, *Sci Rep* **2016**, *6*, 25924.

[42] N. Lyu, Z. Du, H. Qiu, P. Gao, Q. Yao, K. Xiong, Q. Tu, X. Li, B. Chen, M. Wang, *Adv Sci* **2020**, *7*, 2002330.

[43] Y. Lu, G. He, C. J. Carmalt, I. P. Parkin, *RSC Adv* **2016**, *6*, 106491.

[44] J. Xu, A. Ma, T. Liu, C. Lu, D. Wang, H. Xu, *ChemComm* **2013**, *49*, 10871.

[45] P. Tengvall, "Protein Interactions with Biomaterials," Elsevier, Oxford **2011**.

[46] B. J. Kirby, E. F. Hasselbrink Jr, *Electrophoresis* **2004**, *25*, 187.

[47] M. Vega, E. M. Martín del Valle, M. Pérez, C. Pecharromán, G. Marcelo, *ChemPhysChem* **2018**, *19*, 3418.

[48] V. K. Thakur, M.-F. Lin, E. J. Tan, P. S. Lee, *J Mater Chem* **2012**, *22*, 5951.

[49] L. Bergström, *Adv Colloid Interface Sci* **1997**, *70*, 125.

[50] P. Xu, H. Wang, R. Tong, Q. Du, W. Zhong, *Colloid Polym Sci* **2006**, *284*, 755.

[51] J. A. A. Júnior, J. B. Baldo, *New Journal of Glass and Ceramics* **2014**, *4*, 29.

[52] M. Duan, Q. Tang, M. Wang, M. Luo, S. Fang, X. Wang, P. Shi, Y. Xiong, *Water Science and Technology* **2020**, *82*, 2353.

[53] J. Xu, A. Ma, T. Liu, C. Lu, D. Wang, H. Xu, *ChemComm* **2013**, *49*, 10871.

[54] M. Takenaga, S. Jo, M. Graupe, T. R. Lee, *J Colloid Interface Sci* **2008**, *320*, 264.

[55] D. Ambrożewicz, F. Ciesielczyk, M. Nowacka, J. Karasiewicz, A. Piasecki, H. Maciejewski, T. Jesionowski, *J Nanomater* **2013**, *2013*.

[56] X. Dai, J. Boll, M. E. Hayes, D. E. Aston, *Colloids Surf B Biointerfaces* **2004**, *34*, 259.

[57] H.-J. Butt, M. Kappl, *Adv Colloid Interface Sci* **2009**, *146*, 48.

[58] B. Cappella, *Micron* **2017**, *93*, 20.

[59] W. Pietsch, H. Rumpf, *Chemie Ingenieur Technik* **1967**, *39*, 885.

[60] J. Ally, E. Vittorias, A. Amirfazli, M. Kappl, E. Bonaccurso, C. E. McNamee, H.-J. Butt, *Langmuir* **2010**, *26*, 11797.

[61] L. Xie, X. Cui, J. Liu, Q. Lu, J. Huang, X. Mao, D. Yang, J. Tan, H. Zhang, H. Zeng, *ACS Appl Mater Interfaces* **2021**, *13*.

[62] L. Xie, L. Gong, J. Zhang, L. Han, L. Xiang, J. Chen, J. Liu, B. Yan, H. Zeng, *J Mater Chem A Mater* **2019**, *7*, 21944.

[63] S. Raman, T. Utzig, T. Baimpos, B. R. Shrestha, M. Valtiner, *Nat Commun* **2014**, *5*, 1.

[64] Y. Li, M. Qin, Y. Li, Y. Cao, W. Wang, *Langmuir* **2014**, *30*, 4358.

[65] L. Han, L. Gong, J. Chen, J. Zhang, L. Xiang, L. Zhang, Q. Wang, B. Yan, H. Zeng, *ACS Appl Mater Interfaces* **2018**, *10*, 2166.

[66] J. N. Israelachvili, *Intermolecular and surface forces*, Academic press, **2015**.

[67] B. Cappella, G. Dietler, *Surf Sci Rep* **1999**, *34*, 1.

[68] L. Xie, C. Shi, J. Wang, J. Huang, Q. Lu, Q. Liu, H. Zeng, *Langmuir* **2015**, *31*, 2438.

CHAPTER 4 PROBING THE INTERMOLECULAR INTERACTION MECHANISMS BETWEEN FOULANTS AND MEMBRANES: IMPLICATIONS FOR ANTIFOULING PROPERTIES OF WATER TREATMENT MEMBRANE

4.1. Introduction

Water resource contamination has been one of the greatest challenges due to the abundance of the population and the rapid pace of industrialization around the world. The demands for water are increased tremendously especially in domestic, agriculture, industry and energy sectors, resulting in the generation of large amounts of wastewater. The wastewater or produced water contains various organic and inorganic components, which could pollute surface and underground water and soil, and eventually affect the eco-environmental security. In order to mitigate the water crisis issues, developing novel water treatment technologies is an urgent need that prevents the negative effects of water pollution on human health and the environment.

Among various wastewater treatment techniques, membrane technology is one of the most popular techniques that performs efficient, selective, and reliable separation and reclamation for both potable and industrial water. Membranes are widely applied for the removal of soluble and insoluble organic, inorganic, and biological pollutants. However, membrane fouling issues have been the bottleneck that restricts filtration process efficiency, deteriorates product water quality and limits the commercialization of membranes across a variety of water purification applications (Le-Clech et al., 2006; Shannon et al., 2008). It is well recognized that modifying membrane surfaces with hydrophilic components is an effective strategy to increase surface energy and improve the resistance to foulants (Jiang and Cao, 2010; Zhao et al., 2011). Polydopamine (PDA) has been proven as an ideal candidate for membrane surface modification to increase water permeability and improve fouling resistance against proteins and organic foulants by altering its surface hydrophilicity (Azari and Zou, 2012; Nguyen et al., 2013). Moreover, the presence of the catechol group makes PDA layer a versatile intermediate platform to immobilize other hydrophilic materials, among which zwitterionic polymers have achieved superior antifouling performance to oil, bacteria and proteins. (Li et al., 2021; Yang et al., 2015). The anionic and cationic groups on the zwitterionic polymer brushes can bind with water molecules through both electrostatic interactions and hydrogen bonding, resulting in a dense adsorbed water layer, which imposes a strong steric hindrance and increases the energetic penalty during the attachment of foulants (Leng et al., 2015; Li et al., 2020).

Membrane fouling is usually initiated by the deposition or adsorption of miscellaneous kinds of foulants in the feed solution such as particles, macromolecules, proteins and oils on the membrane surface, leading to a drastic decline in permeability, selectivity, and membrane lifespan (Matin et al., 2011; Rana and Matsuura, 2010). Accordingly, the antifouling property of the membranes could be achieved by altering the attachment and detachment behaviors of the foulants, which are governed by the interactions between foulants and membrane surfaces (Al-Amoudi, 2010; Lu et al., 2018). Therefore, it is of both fundamental and practical importance to understand the dynamic adsorption behaviors and interaction mechanisms of the diverse foulants with different membranes especially at molecular level, which will provide useful implications for developing intelligent antifouling membrane materials. Some investigations on the interfacial force measurement between foulants and membranes have been carried out over the past few decades to study the membrane fouling mechanisms (Ang and Elimelech, 2008, 2007; Boo et al., 2018; Herzberg et al., 2009; Johnson and Hilal, 2015; Miao et al., 2017). For example, Miao et al. (Miao et al., 2017) and Boo et al. (Boo et al., 2018) investigated the fouling behaviors in the membrane distillation process by evaluating the adhesion forces and interaction energy between a range of organic foulants and model membrane surfaces with different surface wettability using atomic force microscopy (AFM). However, simply measuring the overall adhesion forces could not quantitatively reveal the interaction mechanisms since various molecular interactions (e.g., hydrogen bonding, hydrophobic interaction, and EDL interaction) contribute together to the foulants adsorption process. The isolated effect of each type of interaction could be individually calculated by fitting the interaction force curves through extended Derjaguin-Landau-Verwey-Overbeek (DLVO) theory, based on which the key factors that govern the initial adsorption behavior of the foulants and antifouling mechanisms of the membrane coatings would be unraveled. In this paper, for the first time, we focused on the theoretical fitting and quantitative analysis of the interaction forces of the attachment and adhesion energies of different foulants on diverse membrane surfaces. It is necessary to report a systematic understanding of the intermolecular interaction mechanisms of the intact dynamic adsorption processes of the fouling development, including the initial foulant attachment and further deposition behaviors, and the essence of the adsorption and removal of foulants on membranes could be revealed. More importantly, systemically studying the fundamental intermolecular interactions between fouling substances and membranes with different surface chemistry and different wettability would promise an effective strategy for the development and evaluation of antifouling materials to eliminate membrane-fouling issues during the water treatment.

In this work, three types of membranes including polyvinylidene fluoride (PVDF) membrane, PDA-coated PVDF membrane and poly(sulfobetaine methacrylate) (PSBMA)-modified PVDF membrane were fabricated to explore the antifouling performance and interaction mechanisms with various foulants at nanoscale. The wettability and surface chemistries of the diverse membranes were tested to understand the surface properties of membranes, which were able to endow the membrane surface with different fouling resistance performances against various foulants. Herein, according to the categories of membrane fouling such as colloidal fouling, bio-fouling and organic fouling, three common types of foulants in the feed solution including silica particles, bovine serum albumin (BSA), and humic acid (HA) were used as model foulants, due to their following characteristics: (1) silica particle, the major component of fine solids in various water systems and soils, is considered as one of the causes for the fouling issues in wastewater treatment and recycle; (2) BSA is ubiquitous in wastewater effluents and other source waters, and adsorption of the protein could lead to microbial colonization and severe bio-fouling troubles; (3) HA contains a variety of functional groups, which makes HA a major organic foulant of natural waters in soil and aquatic ecosystems. The interaction forces between different membranes and foulants were directly measured using the AFM colloidal probe technique in aqueous solutions. By analyzing the measured force-separation profiles using theoretical models, the driving forces of different foulants attaching to membranes and the adhesion forces of different foulants detaching from membranes could be quantitively revealed. Then, filtration tests with individual foulants were conducted to identify the antifouling mechanism of diverse membranes, which then built up a correlation with force measurement results. Our results provide useful insights into the fundamental interaction mechanisms associated with fouling issues and antifouling strategies of membrane surfaces with typical foulants in feed water at the nanoscale, which discloses implications for the development of antifouling membrane surfaces to eliminate the adsorption and facilitate the removal of foulants for efficient and universal water treatment.

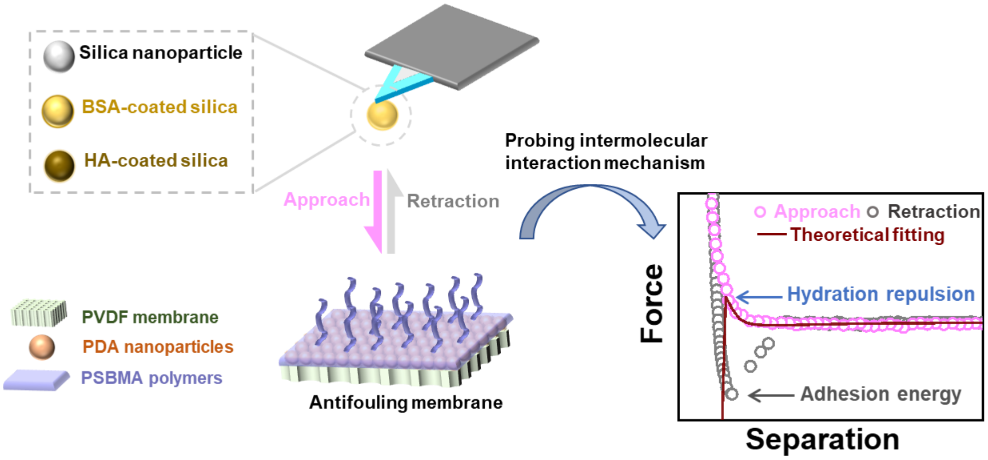

Fig. 4-1 Schematic of direct force measurement between foulant and membrane surface using AFM. The colloidal probes are prepared as model foulants: silica, BSA, and HA. The typical approaching and retracting force-separation curves could be obtained for further theoretical analysis.

4.2. Experimental

4.2.1. Chemicals and materials

Polyvinylidene fluoride (PVDF) powder (M_w ~534000) and N,N-Dimethylformamide (DMF) (assay GC area > 99%) purchased from Sigma-Aldrich, Germany were used as the membrane polymer and the solvent, respectively. Other chemicals such as dopamine hydrochloride, BSA, HA, [2-(methacryloyloxy)ethyl]dimethyl-(3-sulfopropyl) ammonium hydroxide (SBMA), sodium bisulfite ($NaHSO_3$), 30% hydrogen peroxide (H_2O_2) were also supplied by Sigma-Aldrich, Germany, whereas lithium chloride (LiCl), sodium chloride (NaCl), ammonium persulfate (APS) and tris(hydroxymethyl)aminomethane were provided by Fisher Chemical, USA.

4.2.2. Preparation of PVDF membrane

The PVDF membranes used in this study were prepared via the immersed phase inversion method as follows. 4 g PVDF powders and 2 g LiCl were dispersed in 31.5 g DMF solvent and vigorously stirred at 60 °C for 30 min. Then, the homogenous polymer solution was placed in a vacuum oven for 16 h at room temperature to remove the air bubbles in the solution. After being degassed, the polymer solution was uniformly spread on a glass plate using a 200 μm casting knife, and the glass plate was immediately immersed in a DI water bath to allow the PVDF membrane to peel off from the substrate. The nascent membranes were then rinsed with DI water to remove the residual solvent and immersed in DI water before use.

4.2.3. Synthesis of PSBMA polymer

PSBMA polymer was synthesized through the conventional free radical polymerization method in aqueous solution, using $(NH_4)_2S_2O_8$ (APS)-$NaHSO_3$ redox initiation system. SBMA monomer (5.59 g, 800 mM) was first dissolved in 25 mL DI water and added into a 50 mL round-bottomed flask. APS (228 mg, 40 mM) was added slowly as an initiator to the flask, which was then placed into a 45 °C water bath under a nitrogen atmosphere for 10 min with continuous mechanical stirring until the mixed ingredients were completely dissolved. After adding $NaHSO_3$ (104 mg, 40 mM) to the solution dropwise, the polymerization was carried out at 45 °C with vigorous stirring under a nitrogen atmosphere for 24 h.

4.2.4. Modification of PVDF membranes

The PDA-coated PVDF membrane (PDA membrane) was prepared following the below procedures. Dopamine hydrochloride (2 mg/mL) was dissolved in 50 mM Tris buffer (pH

8.5) with oxidants including $CuSO_4$ (1.25 mg/mL)/H_2O_2 (0.67 mg/mL), and then the pristine PVDF membranes were submerged in the solution for 30 min with constantly stirring at room temperature. The prepared PVDF/PDA membranes were rinsed with DI water to remove the unbonded PDA molecules and blow-dried by nitrogen gas for further experiments.

To prepare the PSBMA modified PDA-coated PVDF membrane (PSBMA membrane), the as-prepared PSBMA polymer solution was diluted four times with DI water, and 200 mM NaCl was added to the solution. The prepared PVDF/PDA membranes were immersed in the polymer solution overnight for deposition of PSBMA on the PDA-coated PVDF membrane surfaces. After that, the modified PVDF membranes were rinsed with DI water and dried with nitrogen gas.

4.2.5. Membrane characterization

The morphologies of the pristine and modified PVDF membranes were obtained using a Bruker Icon AFM (Bruker, Santa Barbara, CA) using the PeakForce Quantitative Nano-Mechanics (PF-QNM) model and a field-emission scanning electron microscope (SEM) (Zeiss Sigma 300 VP-FESEM, Germany) with energy-dispersive X-ray spectroscopy (EDS) at the electron acceleration voltage of 10.2 keV. The functional groups on the membrane surface were measured by All Fourier transform infrared (FTIR) spectra over a range of 500-4000 cm^{-1} with a resolution of 4 cm^{-1} (Nicolet iS50 FTIR spectrometer, Thermo Scientific, USA). The wettability of the three membranes was evaluated via the water contact angle (WCA) and underwater oil contact angle (OCA) measurements on a contact angle goniometer (Ramé-Hart instrument, NJ). The OCA was acquired using dodecane droplets.

Membrane porosity (ε) was determined by measuring the wet weight and dry weight of prepared membranes (Xu et al., 2014). The prepared membrane was firstly weighed after mopping water on the membrane surface, which was then placed in an oven at 40 °C overnight before measuring the dry weight. Porosity was calculated using Eq.1:

$$\varepsilon = \frac{w_1 - w_2}{A \times l \times d_{\mathrm{w}}} \times 100\% \tag{1}$$

where w_1 (g) is the wet weight and w_2 (g) is the dry weight of the calculated membrane. A (m^2) is the membrane effective area, l (m) is the thickness of the membrane, and d_{w} (9.98×10^5 g/m^3) is the water density. Moreover, the membrane mean pore radius (r_{m}) could be determined using the Guerout-Elford-Ferry equation (Eq.2):

$$r_{\mathrm{m}} = \sqrt{\frac{(2.9 - 1.75\varepsilon) \times 8\mu l Q}{\varepsilon \times A \times TMP}} \tag{2}$$

where μ is water viscosity (8.9×10^{-4} Pa·s), Q (m^3/s) is the volume of the permeate pure water per unit time, and TMP is the operation pressure (7×10^5 Pa).

4.2.6. Preparation of silica, BSA, and HA probes

The silica probe was prepared by gluing a silica microsphere (radius ~2.5 μm) on the end of a tipless AFM cantilever (NP-O10, Bruker, Santa Barbara, CA) using two-component epoxy glue (EP2LV, MasterBond, USA). Then, the silica probe was placed at room temperature for at least 24 hours for epoxy curing. Before force measurement or next step functionalization, the AFM silica probes were treated in a UV-Ozone cleaner for 15 min to remove the organic contaminants, then rinsed with DI water and dried with nitrogen gas.

BSA probe was prepared by immersing the cleaned silica probe in 10 μg/mL BSA in 0.1 M NaCl (pH 5.8) for 30 min, followed by rinsing with DI water and drying with nitrogen gas. Fig. 4-8 shows the AFM images of the silica wafer before and after BSA adsorption, proving a full and smooth coverage of BSA molecules on the silica substrate, which could demonstrate the successful coating of BSA on the silica probe.

To deposit HA, the silica probe was treated with UV-ozone for 10 min and then exposed to 0.1% (v/v) APTES solution for 10 min. Followed by water rinsing and vacuum drying, the APTES modified silica probe was immersed in 10 μg/mL HA in 0.1 M NaCl (pH 5.8) and kept for 10 min. The AFM images of the silica wafer before and after HA adsorption were shown in Fig. 4-8, which revealed a relatively smooth HA layer on support substrates. Prior to force measurements, the HA probe was washed using DI water and dried with nitrogen.

4.2.7. Force measurement using the AFM colloidal probe technique

The interaction forces between silica, BSA, or HA probe and three types of membrane substrates in 10 mM NaCl were directly and quantitatively measured on an Asylum MFP-3D AFM (Asylum Research, Santa Barbara, CA). Before force measurement, the spring constant of the probes was calibrated to be ~120 pN/nm for the silica probe using the Hutter and Bechhoefer thermal tune method. Then, the probe was driven to approach the membrane surfaces at a velocity of 1 μm/s until attachment and then retracted from the surfaces at the same velocity. The corresponding interaction force curves between the probe and the substrates were recorded and calculated based on the deflection of the cantilever and the spring constant by Hooke's Law. The approaching force-separation profiles were theoretically analyzed using the theoretical models.

4.2.8. Theoretical model for interaction force analysis

For theoretically analyzing the force-separation profiles between the membranes and silica, BSA or HA probe, the classical Derjaguin-Landau-Verwey-Overbeek (DLVO) model coupled with non-DLVO forces which is named as the extended DLVO theory, has been applied.

For sphere−smooth plate interactions, the van der Waals (VDW) interaction is determined using the following formula (Cappella and Dietler, 1999; Israelachvili, 2015):

$$W_{\mathrm{VDW}}^{Smooth} = \frac{-A_{\mathrm{H}}R}{6D} \tag{3}$$

where A_{H} is the Hamaker constant, R is the radius of the silica microsphere, D is the separation distance between the colloidal probe and substrate.

The electric double layer (EDL) interaction between a sphere and a smooth plate is given by Eq.4 and Eq.6, respectively (Cappella and Dietler, 1999; Israelachvili, 2015).

$$W_{\mathrm{EDL}}^{Smooth} = \pi\varepsilon\varepsilon_0 R\left[2\varphi_{\mathrm{S}}\varphi_{\mathrm{M}} \ln\left(\frac{1+e^{-\kappa D}}{1-e^{-\kappa D}}\right) + (\varphi_{\mathrm{P}}^2 + \varphi_{\mathrm{M}}^2)\ln(1-e^{-2\kappa D})\right] \tag{4}$$

where D is the separation distance between the colloidal probe and substrate, ε is the dielectric constant of the solution, ε_0 is the vacuum permittivity (8.854×10^{-12} C/(V·m)), φ_{M} and φ_{S} are the surface potentials of membrane and colloidal probe, respectively. k_{B} is the Boltzmann constant, T is the temperature, C is the bulk concentration of ions, N_{A} (6.23×10^{23}) is the Avogadro's number, e (1.6×10^{-19}) is the elementary charge, and κ is the inverse of the Debye length, which could be calculated through Eq.5:

$$\kappa = \sqrt{\frac{\sum \rho_0 e^2}{\varepsilon\varepsilon_0 k_{\mathrm{B}}T}} \tag{5}$$

Here ρ_0 is the number density of ions in NaCl solution.

The hydration force (W_{H}) of smooth surface is expressed in Eq.6 (Kralchevsky and Nagayama, 2001; Petsev, 2004),

$$W_{\mathrm{H}}^{Smooth} = -W_0 e^{-D/D_a} \tag{6}$$

where D is the film thickness (m), D_{a} is the decay length (m) and W_0 (J) is the surface free energy at contact (mJ/m^2).

Hydrophobic force (W_{HB}) also follows an exponential decay with distance as shown in Eq.7 (Israelachvili, 2015; Xie et al., 2015),

$$W_{\mathrm{HB}}^{Smooth} = -CRe^{-D/D_0} \tag{7}$$

where C (N) is a constant and D_0 (m) is the decay length of hydrophobic interaction.

To be noted, the surface roughness of membrane surfaces has a considerable influence on DLVO energy. Here, we applied a methodology called DLVO-R which accounts for the effects of surface roughness in the standard extended DLVO theory of surfaces (Parsons et al., 2019, 2014).

According to the calculation of Parsons, the roughened van der Waals interaction free energy could be obtained by adding a simple analytical correction for roughness to the standard van der Waals expression for smooth flat surfaces:

$$W_{\mathrm{VDW}}^{Rough} = [1 + 3\left(\frac{\sigma_m}{D}\right)^2] \times W_{\mathrm{VDW}}^{Smooth} \tag{8}$$

Here a Gaussian distribution with RMS roughness σ_1 and σ_2 is used to describe the roughness of the surface and AFM probe, respectively, and a mean RMS roughness σ_m is calculated by combining σ_1 and σ_2,

$$\sigma_m = \sqrt{\sigma_1^2 + \sigma_2^2} \tag{9}$$

In this work, a mean RMS roughness σ_m at the contact was calculated to be 2 nm, and the detailed information could be found in Supporting Information.

While for exponentially decaying long-range forces such as EDL interaction, hydration force and hydrophobic interaction, the approximate roughened interaction energy W_e^{Rough} is yielded by adding the effect of roughness with a simple multiplicative factor to the interaction energy of smooth surfaces W_e^{Smooth},

$$W_{\mathrm{e}}^{Rough} = \exp\left(\frac{\sigma_m^2}{2\lambda^2}\right) \times W_{\mathrm{e}}^{Smooth} \tag{10}$$

Here, in order to simplify the calculation, we used an exponential decay $\lambda=\kappa^{-1}$, where κ^{-1} is the Debye length of the solution (2.99 nm) (Parsons et al., 2019).

The roughened DLVO-R force $F_{\mathrm{DLVO\text{-}R}}$ and overall extended DLVO-R force $F_{\mathrm{EX\text{-}DLVO\text{-}R}}$ of the system are given by Eq.11 and Eq.12, respectively,

$$F_{DLVO-R} = F_{\mathrm{VDW}}^{Rough} + F_{\mathrm{EDL}}^{Rough} \tag{11}$$

$$F_{EX-DLVO-R} = F_{\mathrm{VDW}}^{Rough} + F_{\mathrm{EDL}}^{Rough} + F_{\mathrm{H}}^{Rough} + F_{\mathrm{HB}}^{Rough} \tag{12}$$

$$F = -\frac{dW}{dD} \tag{13}$$

4.2.9. Filtration and antifouling performance assessment

The antifouling behavior of the pristine and two modified PVDF membranes against the foulants was characterized by conducting a filtration test. The foulants (silica nanoparticles, BSA, and HA) were suspended in DI water with a concentration of 20 mg/L. The water flux was measured by placing the membranes in a dead-end membrane filtration cell connected to a pressure pump at 0.7 bar. After filtering the foulants solution, the membranes were washed with DI water for 5 minutes to remove loosely bounded foulants from the membrane surface, and the pure water flux was measured once again to analyze the antifouling properties. The flux *J* was calculated according to Eq.14,

$$J = Q/(A \cdot t \cdot \Delta P) \tag{14}$$

where *J* is the water flux (L/(m^2·h·bar)), *Q* is the volume of the permeation water (L), *A* is the effective separation area of the membrane (m^2), and *t* is the filtration time (h), ΔP is the pressure difference between ambient and evacuation pressure.

The membrane antifouling performance was evaluated using the normalized flux (NF) (Eq. 15) and flux recovery ratio (FRR) (Eq. 16),

$$NF = J_{\mathrm{wf}}/J_{\mathrm{w0}} \tag{15}$$

$$FRR = J_{\mathrm{w1}}/J_{\mathrm{w0}} \tag{16}$$

where J_{w0} is the pure water flux, J_{wf} is the water flux of foulants solutions, and J_{w1} is the re-measured pure water flux after washing the membranes.

4.3. Results and discussions

4.3.1. Characterization of the membrane surfaces

PDA and PSBMA coating materials have been deposited on PVDF membrane surfaces, and the fabrication process was illustrated in Fig. 4-2(a). Dopamine molecules could generate crosslinking networks via autoxidation and self-polymerization under mild alkaline aqueous conditions, forming a PDA layer on the pristine PVDF membrane surface, which could further act as an intermediate adherent platform to introduce the synthetic PSBMA polymers. As a matter of convenience, the pristine PVDF, PDA-coated PVDF and PSBMA-modified PDA-coated PVDF membranes were named as PVDF, PDA and PSBMA membranes, respectively. AFM imaging analysis of the three types of membranes with an area of 5 μm × 5 μm was performed to study the surface morphology of the membranes, as shown in Fig. 4-2(b-d). The PVDF membrane (Fig. 4-2(b)) showed a porous structure with an RMS roughness value of 52 nm. After PDA modification, the membrane surface (Fig. 4-2(c)) exhibited a steady layer of PDA nanoparticles attaching to the substrate with an RMS value of around 83 nm. While compared to the PDA membrane, the PSBMA membrane (Fig. 4-2(d)) showed a relatively smooth and homogenous morphology with a smaller RMS value of 41 nm, indicating the immobilization of PSBMA polymers could uniformly cover the pre-modified PDA agglomerations and minimize the surface roughness. The SEM images and FTIR spectra of the prepared membrane surfaces are shown in Fig. 4-10 and Fig. 4-11, respectively. Membrane porosity and pore size were determined according to the methods provided in Sec. 4.2.5. The thickness of PVDF membranes prepared via the immersed phase inversion method was 200 μm, and the membrane porosity and mean pore radius (r_m) were calculated to be 68.5% and 0.16 μm, respectively.

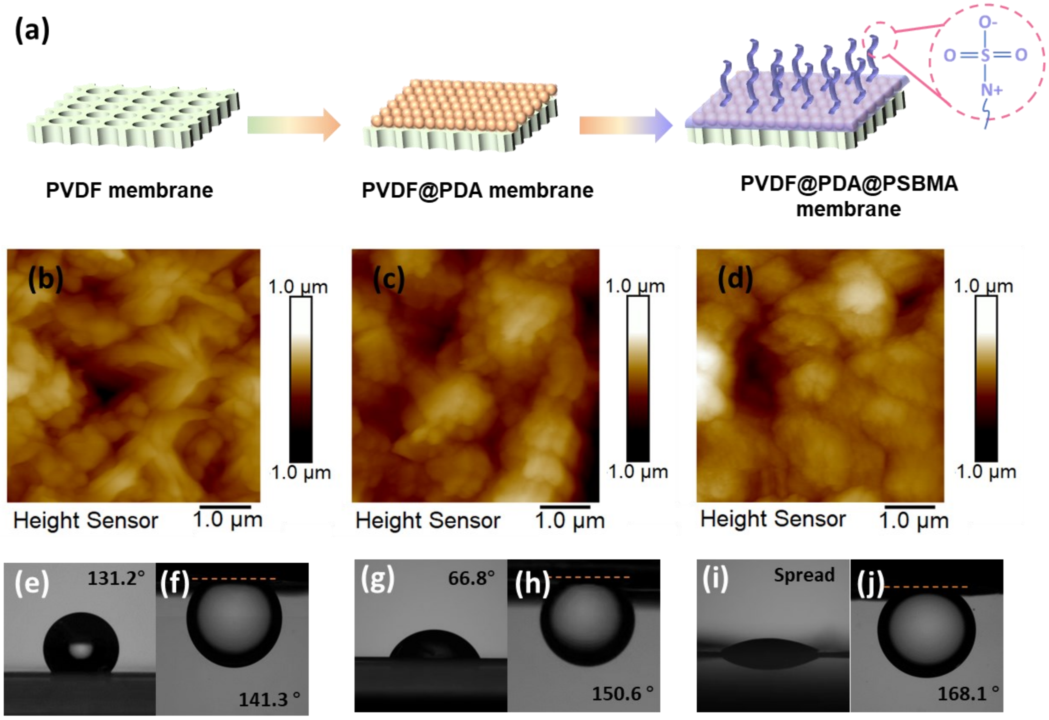

Fig. 4-2 (a) Schematic of for the fabrication of PDA and PDA@PSBMA coatings on PVDF membrane substrate; Topographic AFM images of (b) PVDF membrane ($R_q \sim 52$ nm), (c) PDA membrane ($R_q \sim 83$ nm) and (d) PSBMA membrane ($R_q \sim 41$ nm); WCA of (e) PVDF membrane, (g) PDA membrane and (i) PSBMA membrane in air; underwater OCA of oil droplets of (f) PVDF membrane, (h) PDA membrane and (j) PSBMA membrane in 10 mM NaCl solution at pH 5.8.

The wettability of the pristine PVDF membrane, PDA membrane and PSBMA membrane surfaces was evaluated by WCA measurement in air and underwater OCA measurement of oil droplets on different membrane surfaces in 10 mM NaCl solution, as shown in Fig. 4-2(e-j). Due to the presence of fluorinated polymers, PVDF membrane showed amphiphobic (both hydrophobic and oleophobic) property, displaying WCA larger than 130° in air and OCA larger than 140° underwater. After PDA modification, the membrane surface became relatively hydrophilic with a WCA of 66.8° and an OCA of 150.6°. For PSBMA membrane, it is noted that the water droplet rapidly spread over and wetted the membrane surface due to the excellent hydrophilicity and wettability of zwitterionic polymer. In addition, the contact angle of dodecane droplet on PSBMA membrane increased to 168.1°, indicating a superior repellence property of zwitterionic polymer against the attachment of oil.

4.3.2. Interaction between silica particles and different membranes

Silica is a common solid on the earth and is very abundant in natural water systems. The presence of silica in feed solution has made the membrane separation processes and the production of purified water extremely difficult. Especially in oil production processes, silica particles originating from the reservoir ground or oil sands are recognized as one of the major components that cause detrimental fouling and plugging problems. In this section, the force measurements between the silica probe and different membrane substrates including PVDF, PDA and PSBMA membranes in 10 mM NaCl solution were conducted using the colloidal probe technique to investigate the interaction mechanisms of silica with the membranes. Before the experiment, a silica microsphere with a radius of ~2.5 μm was glued to the end of the tipless cantilever, and the SEM image of the silica probe is shown in Fig. 4-12(a).

The measured approaching force-separation profiles of PVDF, PDA and PSBMA membranes are shown in Fig. 4-3(a-c). For PVDF membrane (Fig. 4-3(a)), a long-range repulsion arising at around 10 nm followed by a noticeable “jump-in” at ~5 nm was observed. By theoretically analyzing the experimental force-separation profile, both the VDW and EDL interactions contribute to the surface interaction between the silica probe and PVDF membrane surface in 10 mM NaCl solution. The Hamaker constant A_H between silica and PVDF in NaCl solution is calculated as 1.40×10^{-20} J, using the Lifshitz theory and the reported dielectric constant and reflective index of the surfaces and medium (Gao et al., 2006; Gaur and Rana, 2019). Since the isoelectric points (IEP) of PVDF membrane and silica particles are determined to be pH 3.5 (Schulze et al., 2016) and pH 2 (Franks, 2002; Kosmulski, 1998), respectively, the long-range repulsion is attributed to the EDL interaction between the negatively charged silica and negatively charged PVDF membrane in NaCl solution at pH 5.8. The VDW attraction led to the "jump-in" behavior during the approach. The surface potential of silica in 10 mM NaCl solution measured by Zetasizer Nano is -20 mV (shown in Fig. 4-13), which is consistent with the surface potential value in references (Dishon et al., 2009; Seo et al., 2016). The theoretical analysis indicates the surface potential of PVDF membrane is fitted to be -12 mV, which falls into the range of the reported values (Chen et al., 2017; Li et al., 2014; Sakarkar et al., 2021). Similarly, the approaching force-separation profile of PDA–silica (Fig. 4-3(b)) also shows the synergic contributions of EDL and VDW forces. The Hamaker constant A_{H} between silica and PDA in 10 mM NaCl solution is calculated as 1.92×10^{-20} J (Chen et al., 2019; Jung et al., 2015; Thakur et al., 2012; Zheng et al., 2016). By theoretical fitting of the approaching force-distance curve, the surface potential of PDA membrane is determined to be -15 mV (Xu et al., 2013). Comparing Fig. 4-3(a) and (b), it is noted that A_{H} for these two cases lies in the same range, indicating the VDW attraction between silica–PVDF and silica–PDA is similar. While the surface potential of PDA is more negative than that of PVDF, which reveals the EDL repulsion between silica and PDA is stronger than that between silica and PVDF. Thus, the observed "jump-in" behavior of silica with PDA surface was much weaker than that with PVDF. The approaching force-separation profile of PSBMA–silica is significantly different from those of PVDF–silica and PDA–silica. As shown in Fig. 4-3(c), the "jump-in" behavior disappeared, and a long-range repulsion starting from ~10 nm was observed and then a short-range repulsion within 2 nm was detected. PSBMA membrane was slightly negatively charged at pH 5.8 (De Vera et al., 2018; Guo et al., 2015), thus EDL interaction contributed to the long-range EDL repulsion during the approach. It is noted that the discrepancy at separation D < 2 nm is mainly attributed to the effects of surface roughness and hydration. The synergistic effect of EDL repulsion appeared at long range and hydration repulsion appeared at short distances completely overcame the VDW attraction. The Hamaker constant A_H between silica and PSBMA in 10 mM NaCl solution is calculated as 1.92×10^{-20} J (Chen et al., 2019; Zhao et al., 2014). By fitting the measured force results using the extended DLVO theory with incorporated hydration interaction, the surface potential of PSBMA membrane was fitted to be -11 mV and the decay length of hydration force was determined to be $D_a = 0.80$ nm. Due to the superhydrophilicity of PSBMA membrane (Fig. 4-2(f)), the dense water layer on the zwitterionic PSBMA surface is attributed to the short-range hydration repulsion at small separation. Based on the theoretical calculation, it was evident that compared with PVDF membrane, the silica particle was less likely to attract and deposit on PDA membrane surfaces due to the strong EDL repulsion between silica and PDA molecules. While for PSBMA surface, the hydrated surface exerted a hydration repulsion force originating from the energy barrier required for perturbation of the ordered structure of the bound water molecules, which effectively prevented the approach and attachment of silica particles to PSBMA membrane.

A jump-out behavior appeared when the silica probe was retracted from the membrane surfaces, indicating an adhesion between silica and membranes. To accurately obtain their adhesion forces, an adhesion mapping experiment was executed on the surface. Figs. 4-

3(d-f) show the histograms of normalized adhesion F_{ad}/R during probe retraction and the fitted Gaussian distributions (red solid curve) between the silica probe and PVDF, PDA and PSBMA membrane in 10 mM NaCl solution, respectively. The average adhesion force followed the trend: PVDF membrane (0.55 ± 0.12 mN/m) > PDA membrane (0.37 ± 0.06 mN/m) > PSBMA membrane (0.22 ± 0.03 mN/m), which was the reverse trend of repulsive force during approach. The average adhesion energy W_{ad} was determined through the Johnson−Kendall−Roberts (JKR) contact model (Helm et al., 1991; Johnson et al., 1971):

$$W_{\text{ad}} = F_{\text{ad}}/1.5\pi R \tag{17}$$

where R refers to the radius (2.5 μm) of the silica particle on the AFM probe. The adhesion energy was calculated to be ~0.12 mJ/m^2 for PVDF membrane, ~0.08 mJ/m^2 for PDA membrane, and ~0.05 mJ/m^2 for PSBMA membrane. The strong adhesion energy between the silica particle and PVDF surface during the separation arose from the VDW interaction after the intimate contact between the two surfaces, which indicated the robust adherence and hard release of silica on the PVDF membrane surface. The adhesion of silica with PDA surface reduced compared to that with PVDF surface, and it was speculated that the adhesion was suppressed by the enhanced electrostatic repulsion due to the more negatively charged PDA membrane surface. However, the weak adhesion energy of PSBMA membrane indicated the weak attraction between silica and the zwitterionic surface, which greatly facilitates the release and removal of the adsorbed silica particles on the PSBMA surface. Both approaching and retracting force-separation curves demonstrated the interaction mechanisms of silica with the three membrane surfaces, among which the PSBMA membrane showed outstanding fouling resistance against silica particles.

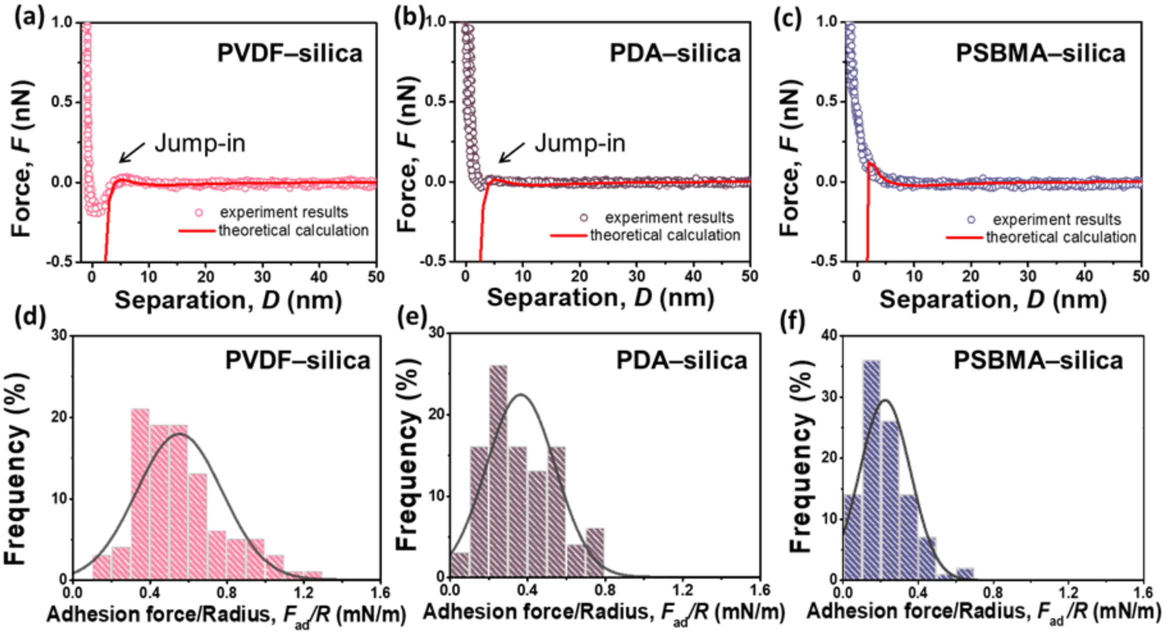

Fig. 4-3 (a-c) Experimental approaching force-separation profiles (open symbols) and theoretical calculations (red curves) and (d-f) histograms of measured adhesion F_{ad}/R and fitted Gaussian distributions between silica probe and (a)(d) PVDF membrane, (b)(e) PDA membrane and (c)(f) PSBMA membrane in 10 mM NaCl at pH 5.8.

4.3.3. Interaction between BSA and different membranes

During microfiltration processes, protein fouling is another critical factor governing the effectiveness of separation and purification of solutions. Here, BSA was selected as the typical fouling protein to investigate the underlying chemical and physical mechanisms that influence the initiation and growth of the fouling layer on different membranes due to its abundance in water systems and adsorption to many surfaces. Before conducting force experiment, a BSA-coated colloidal probe was prepared following the procedure in Sec. 4.2.6, and the SEM and EDS images of the BSA-coated AFM probe are shown in Fig. 4-12(b). Typical approaching force-distance curves of BSA-coated AFM probes with PVDF, PDA and PSBMA membrane in 10 mM NaCl solution are shown in Fig. 4-4(a-c), respectively. The approaching curves of PVDF and PDA membrane showed similar trends

(Fig. 4-4(a) and (b)), where no “jump-in” behavior occurred when the BSA molecules were brought close to different membrane surfaces, and the repulsive forces were detected starting from a distance of ~20 nm. The approach curve of PSBMA membrane was distinguishing from the formers, where the repulsion force started from ~20 nm but rapidly increased within a distance of ~2 nm. It is noted that the interaction forces for three membranes showed a repulsive trend and no “jump-in” behavior could be observed, indicating the repulsive interactions completely overcame VDW attraction and dominated the interaction during the approach. Since the IEP of BSA was specified to be 4.7 (Miao et al., 2017), BSA had a net negative charge under the experiment condition with pH 5.8. Hence, EDL interaction between BSA probe and PVDF, PDA and PSBMA membrane surface greatly contributed to the repulsive force. However, the Debye length of the electrical double layer in the studied salt concentrations of NaCl solutions (10 mM) was calculated to be ~3 nm. The repulsion that happened over 10 nm was supposed to be originated from other repulsive interactions. BSA is a macromolecule with a long polymer chain (66 kDa). When the AFM tip approached the membrane surface, BSA was compressed in solutions under the increased osmotic pressure, leading to the steric repulsion between BSA-coated AFM tip and membranes. Here, the long-range repulsion (~20 nm) originated from the steric force, and EDL interaction contributed to the median-range repulsion (~10 nm), while the drastic short-range repulsion (~2 nm) was dominated by the hydration force of the hydration layer absorbed on PSBMA membrane surface. Moreover, the polymer chains of BSA contain various amino acid groups with aromatic side chains and hydrophobic domains; therefore, the hydrophobic moieties of BSA can interact with fluorinated polymers of PVDF membrane as well as hydrophobic aromatic ring of PDA membrane via the hydrophobic attraction at small separations. The measured force curves between the BSA probe and PVDF and PDA membrane in 10 mM NaCl solutions were also theoretically analyzed based on extended DLVO theory with incorporated hydrophobic interaction, while the measured force results for PSBMA membrane could be well fitted by extended DLVO theory with hydration interaction, which were shown by the red solid curves in Fig. 4-4(a-c). The Hamaker constant between BSA and PVDF, PDA and PSBMA membrane in NaCl solution was determined to be 7.01×10^{-21} J, 1.06×10^{-20} J and 1.05×10^{-20} J, respectively, based on the reported Hamaker constant of BSA (Valle-Delgado et al., 2004). According to the previously fitted surface potentials of different membrane surfaces in 10 mM NaCl solution (Fig. 4-4(a-c)), the surface potential of BSA was fitted to be -10 mV, which fell within the reported value ranges (Salgin et al., 2012) and was coincident with the measured zeta potential of BSA (Fig. 4-13). The decay length of hydrophobic interaction (D_0) between BSA molecules and PVDF and PDA membrane was determined to be 0.72 nm and 0.75 nm, respectively. Therefore, for PVDF and PDA membranes, both EDL repulsion between the negatively charged BSA molecules and negatively charged membrane surfaces and steric repulsion caused by the long polymer chains of BSA could prevent the approach and contact of BSA towards the opposite membrane surfaces at long distance, while the hydrophobic attraction facilitates the tendency of BSA adsorption on membrane surfaces at short distance. For PSBMA membrane surface, fitting the measured force curves gave the D_a of hydration force as 0.81 nm. Hence, in addition to EDL interaction and steric repulsion, the hydration layer enhanced the repellence performance against organic foulants especially at short distances and lowered the possibility of the BSA approaching and attaching to the PSBMA membrane surface.

The adhesion profiles between BSA-coated AFM tip and PVDF, PDA, and PSBMA membrane in NaCl solution have also been recorded in the force measurements during AFM probe retraction, as shown in Fig. 4-4(d-f). It is noted that the normalized adhesion of BSA with PDA membrane was slightly stronger than that with PVDF membrane, and the adhesion energy was determined to be ~0.023 mJ/m^2 for PDA membrane and ~0.021 mJ/m^2 for PVDF membrane, respectively, based on JKR contact model. At short distances, BSA polymer segments may occur some conformation changes, interpenetration and interdigitation, which favor the formation of a variety of short-range interactions such as hydrogen bonding, cation-π interactions, anion-π interactions and hydrophobic interaction (Gong et al., 2021, 2019; Lu et al., 2013; Ma and Dougherty, 1997; Salonen et al., 2011). Thus, the measured adhesion energy between BSA and PVDF membrane surface was attributed to the combination of EDL interaction, VDW attraction and hydrophobic attraction between the local hydrophobic areas of BSA and the hydrophobic fluorinated polymers of PVDF membrane. While for PDA membrane, in addition to EDL repulsion and VDW attraction, diverse short-range interactions, including hydrophobic attraction between BSA and the hydrophobic aromatic ring of PDA, cation-π and/or anion-π interactions between cations and/or anions in BSA and the π ring of PDA, and hydrogen bonding between amino acids of BSA and hydroxyl groups of PDA molecules significantly contributed to the adhesion energy between BSA and PDA membrane. The adhesion results demonstrated that BSA might be more difficult to remove or clean from PDA membrane surface, leading to serious fouling issues. However, the measured force curves of PSBMA membrane exhibited low adhesion, and the adhesion energy was calculated to be ~0.013 mJ/m^2. The superhydrophilic surface discouraged hydrophobic attraction. Moreover, as pointed out earlier, the strongly bound water layer on PSBMA membrane acted as a buffer and minimized direct BSA−surface interaction. The weak adhesion between BSA and PSBMA membrane suggested that BSA molecules were less likely to strongly absorb on the zwitterionic surface, and the deposited BSA molecules could be easily washed away with water, indicating the excellent antifouling performance of PSBMA membrane against the proteins in feed water.

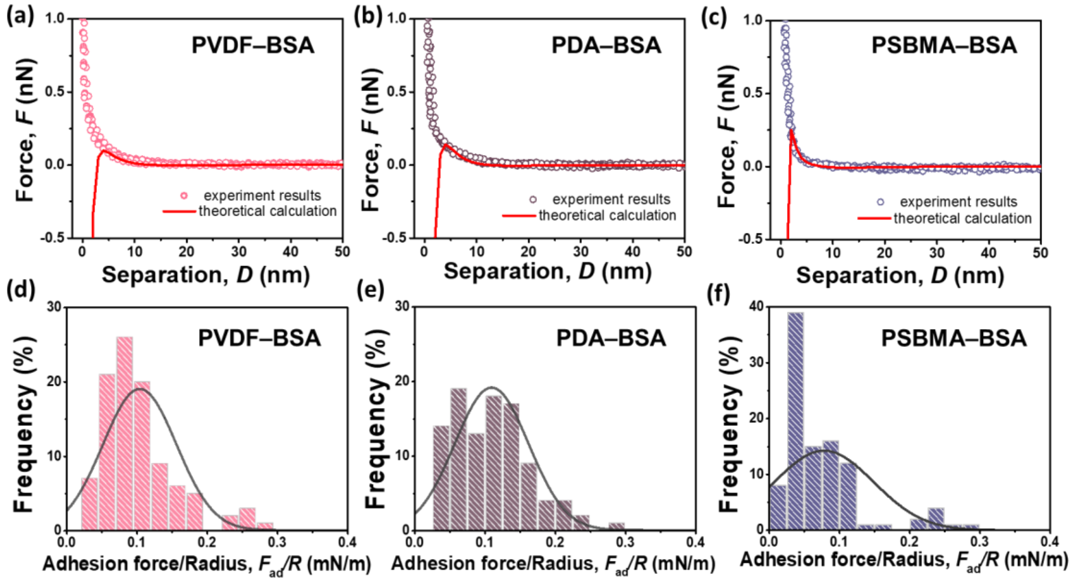

Fig. 4-4 (a-c) Experimental approaching force-separation profiles (open symbols) and theoretical calculations (red curves) and (d-f) histograms of measured adhesion F_{ad}/R and fitted Gaussian distributions between the BSA-coated colloidal AFM tip and (a)(d) PVDF membrane, (b)(e) PDA membrane and (c)(f) PSBMA membrane in 10 mM NaCl at pH 5.8.

4.3.4. Interaction between humic acid (HA) and different membranes

Humic acid is a major organic foulant that widely exists in water-based engineering systems. HA is comprised of multiple functional groups, which trigger the adsorption of HA onto diverse nanoparticles and surfaces through different interaction mechanisms. For instance, HA could quickly deposit and adhere to membrane surfaces during membrane separation processes, leading to membrane fouling and pore blocking. In this section, the intermolecular interactions underlying the adsorption of humic acid on the three types of membranes were quantitively probed. The AFM colloidal probe functionalized with HA was fabricated following the procedure in Sec. 4.2.6, and the SEM and EDS images of the HA-coated AFM probe were presented in Fig. 4-12(c). The approaching interaction forces between the HA-coated AFM probe and PVDF, PDA and PSBMA membrane in 10 mM NaCl at pH 5.8 are shown in Fig. 4-5(a-c), respectively. The measured force profiles displayed a repulsion from ~10 nm for PVDF membrane, which was attributed to EDL repulsion between the negatively charged membrane surfaces and negatively charged HA, as the IEP of HA was determined to be 3-4 (Ishiguro et al., 2007; Reyes-Bozo et al., 2015). Then, a “jump-in” behavior starting from a separation distance of ~5 nm occurred during the approaching of HA-coated probe toward PVDF membrane. For PDA membrane, EDL repulsion from ~10 nm followed by a strong attractive force from ~8 nm could be observed between HA and PDA membrane. HA contains a variety of moieties such as quinone, phenol and catechol, and the hydrophobic aromatic groups endow HA with moderately hydrophobic properties in nature. Therefore, the hydrophobic moieties of HA can interact with hydrophobic groups of PVDF and PDA membrane via hydrophobic attraction. For PVDF and PDA membrane, the measured force results were fitted using the extended

DLVO theory with incorporated hydrophobic interaction, which were shown as red curves in Fig. 4-5(a-b), respectively. For PSBMA membrane, the force-separation profile showed the same trend as the previously measured results (Fig. 4-3(c) and Fig. 4-4(c)), where no "jump-in" behavior was exhibited and the repulsion rapidly increased in the short range (~2 nm), thus the force curve between HA and PSBMA membrane surface was fitted through the extended DLVO theory with hydration interaction (Fig. 4-5(c)). The Hamaker constant between HA and PVDF, PDA and PSBMA membrane in NaCl solution was calculated as 1.04×10^{-20} J, 1.43×10^{-20} J, and 1.43×10^{-20} J, respectively, from the estimated Hamaker constant of HA (Tong et al., 2011; Wang et al., n.d.). Based on the surface potentials of the three membranes in 10 mM NaCl (-12 mV for PVDF membrane, -15 mV for PDA membrane, and -11 mV PSBMA membrane), the surface potential of HA was fitted to be -24 mV. The fitted value agreed very well with the reported zeta potential values of HA at pH 5.8, which was also verified by the measured zeta potential of HA through Zetasizer Nano (Fig. 4-13). It confirmed that the repulsion around 10 nm was contributed by EDL interaction, while PDA membrane showed a stronger EDL repulsion between HA-coated probe and PDA membrane due to the more negative surface potential of PDA. By fitting the approaching force-separation curves, the decay length (D_0) of hydrophobic force was determined to be 0.92 nm for PVDF membrane and 0.87 nm for PDA membrane. Thus, the "jump-in" behaviors originated from the combination of VDW force and hydrophobic force. The measured attraction of HA with PDA membrane was stronger than that with PVDF membrane, owing to the stronger VDW attraction and hydrophobic interaction between aromatic rings of PDA molecules and the hydrophobic moieties of HA. As for PSBMA membrane, the pure repulsion shown in the force profile suggested that there was negligible attraction during the approaching process of HA towards PSBMA membrane. Fitting the measured force curve (Fig. 4-5(c)) gave the decay length (*D*a) of hydration force of PSBMA surface in 10 mM NaCl as 0.78 nm, which was very close to the previously fitted *D*a results (Fig. 4-3(c) and Fig. 4-4(c)). This repulsion was mainly due to the EDL repulsion and surface hydration of the well-hydrated zwitterionic polymer chains overwhelmingly depressed the VDW attraction, thus preventing the attachment of HA onto PSBMA membrane surface.

The histograms of normalized adhesion F_{ad}/R measured during separation and the fitted Gaussian distributions between the HA-coated AFM probe and PVDF, PDA and PSBMA membrane in 10 mM NaCl were shown in Fig. 4-5(d-f), respectively. The force measurements also showed higher adhesion energy between HA and PDA membrane (~0.049 mJ/m^2) than between HA and PVDF membrane (~0.031 mJ/m^2), indicating the strong strength of the interaction between the catechol groups of PDA and HA. Unlike the HA−PVDF membrane system, in which the adhesion energy originated dominantly from VDW force and hydrophobic attraction, the enhanced HA−PDA membrane adhesion strength was mainly ascribed to the addition of other potential adhesive interactions such as hydrogen bonding, π-π stacking and anion-π interaction. The various attractive interactions of HA onto PDA molecules were favorable for the robust adherence of HA particles on PDA membrane. Moreover, the PSBMA membrane still exhibited a relatively weak adhesion with the HA molecules (adhesion energy ~0.018 mJ/m^2), demonstrating the tightly bound hydration layer on the PSBMA surface could suppress the interaction strength of HA, which effectively facilitated HA removal and inhibited the fouling phenomena.

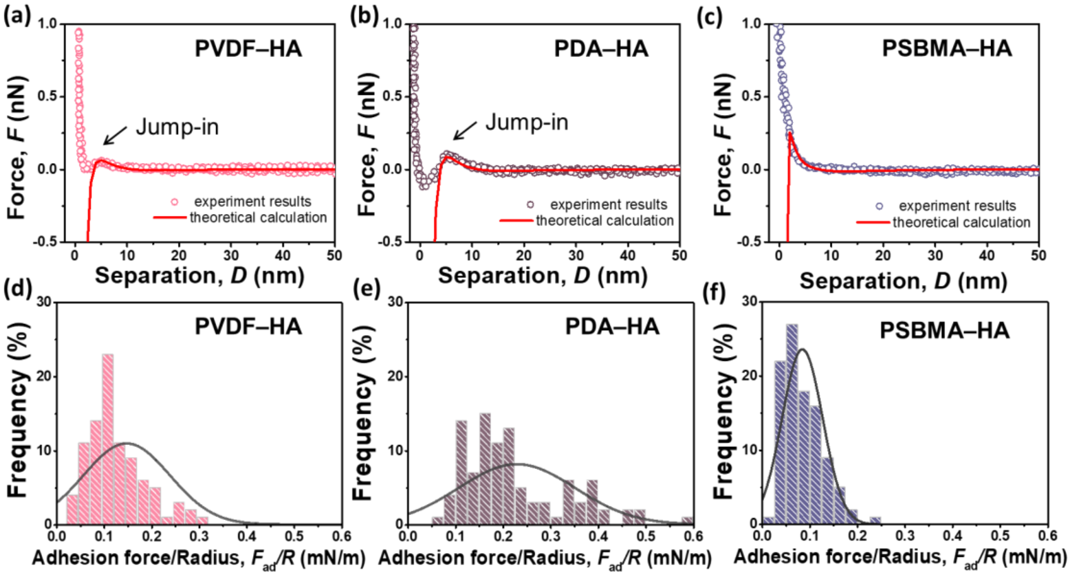

Fig. 4-5 (a-c) Experimental approaching force-separation profiles (open symbols) and theoretical calculations (red curves) and (d-f) histograms of measured adhesion F_{ad}/R and fitted Gaussian distributions between the HA-coated colloidal AFM tip and (a)(d) PVDF membrane, (b)(e) PDA membrane and (c)(f) PSBMA membrane in 10 mM NaCl at pH 5.8.

4.3.5. Filtration tests and water flux

The antifouling performance of the three membranes against the various foulants was investigated by the permeation test. The three types of foulants (silica nanoparticles, BSA, and HA) were suspended in DI water with a certain concentration as the model feed solution. To evaluate the fouling behaviors of membranes, the normalized flux and flux recovery ratio were introduced based on the relationship between the water flux of the original membrane, the water flux of the feed solution, and the water flux of the cleaned membrane after the filtration process, which characterized the foulants resistance and antifouling property of the membranes. The schematic is shown in Fig. 4-6(a). The detailed calculation equations were demonstrated in the experimental section. Moreover, a summary of fitted parameters of the approaching force curves and the measured adhesion energy between the PVDF, PDA and PSBMA membrane surface and the three types of foulants could be found in Fig. 4-7(a) and (b), respectively. Typically, the antifouling properties rely on both the ability to repel foulant during initial attachment and the low adhesion between foulant and membrane, where the former affects the feed solution permeation, and the latter has an influence on the reusability and regeneration of the membranes. In this case, the performance of different membranes could be further explained by comparing the filtration test results with the parameters of the force measurement.

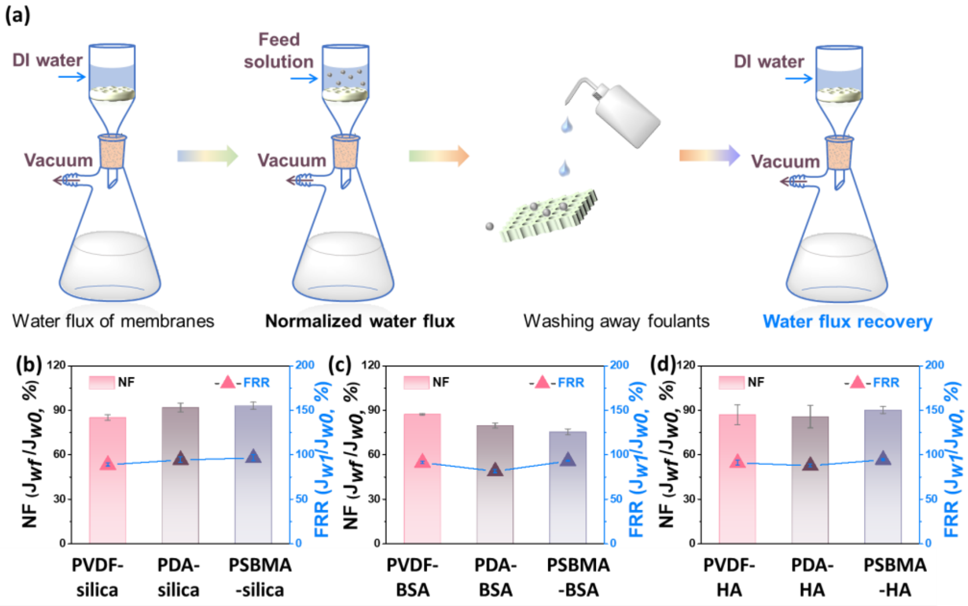

	PVDF-silica	PDA-silica	PSBMA-silica	PVDF-BSA	PDA-BSA	PSBMA-BSA	PVDF-HA	PDA-HA	PSBMA-HA
NF (%)	84.95	91.72	92.95	80.86	79.56	78.13	86.87	85.61	90.05
FRR(%)	88.81	94.22	96.48	87.17	84.60	92.94	90.95	87.72	94.42

Fig. 4-6 (a) Schematic of the vacuum filtration setup and the experiment processes of the permeation tests; Comparison of the normalized flux and FRR in the PVDF membrane, PDA membrane and PSBMA membrane with (b) silica nanoparticles, (c) BSA, and (d) HA.

Fig. 4-6(b) shows the filtration experiments results of different membranes with 20 mg/L silica particle feed solution. The NF of the PVDF, PDA and PSBMA membranes in the presence of silica nanoparticles were 84.95%, 91.72%, and 92.95%, respectively. The dramatic decline of the water flux indicated that serious fouling occurred on the membrane surface. PVDF membrane had the most significant fouling potential and membrane flux decline behavior among the three membranes in the whole filtration process. As for the measured approaching forces between silica and different membranes in Sec.4.3.2, it could be found that the PVDF−silica interaction force during the approach showed a strong attraction (Fig. 4-3(a)). The summarized parameters in Fig. 4-7(a) indicated the strong attraction between silica and PVDF membrane was a synergy of a strong attractive VDW force and a weak repulsive EDL interaction, resulting in severe silica deposition on the surface during the filtration process, thus leading to a severe membrane flux decline. The initial adsorption of silica on both PDA membrane and PSBMA membrane was prevented due to the strong repulsive forces (either EDL interaction or hydration interaction). Then, FRR value was calculated to assess the extent of flux recovery after silica fouling, where a higher value revealed the superior regeneration property of the membrane. FRR of pristine PVDF membrane was 88.81%, while FRR of PDA membrane (94.22%) was obviously higher than that of pristine PVDF membrane. In the best case, FRR of the PSBMA membrane was 96.48%, which indicated the superior antifouling properties of PSBMA membrane. Additionally, the strong adhesion energy (Fig. 4-7(b)) between silica and PVDF membrane during the separation implied that the tightly entrapped silica nanoparticles within the pores could not be easily removed from the membrane surface, indicating a relatively serious irreversible fouling phenomenon. By contrast, the

PSBMA−silica interaction forces during both the approach and retraction were the weakest. Hence, the adsorbed amount of silica significantly decreased on the PSBMA membrane compared with that on the PVDF membrane. After membrane cleaning, the silica adsorption on PSBMA membrane could be reduced apparently, and the irreversible resistance was thereby improved.

The BSA fouling of different membranes at a concentration of 20 mg/L was also systematically investigated, and the results are shown in Fig. 4-6(c). The NF of the three membranes followed this trend: PVDF membrane (80.86%) > PDA membrane (79.56%) > PSBMA membrane (78.13%). According to the parameters calculated in the approaching force curves (Fig. 4-7(a)), both attractive VDW interaction and hydrophobic interaction contributed to the adsorption of BSA molecules on the PDA layer. Moreover, the slight flux decline of PDA and PSBMA membranes could be attributed to the reduced porosity and pore size after being modified with PDA and PSBMA polymers (Liu et al., 2020). The convective deposition of large BSA aggregates on the membrane surface served as nucleation or attachment sites for the continued deposition of proteins, which caused severe pore blockage and accelerated flux decline rate, especially for smaller pore-size membranes (Kelly and Zydney, 1995). However, PSBMA membrane exhibited the highest flux recovery after cleaning (FRR ~92.94%), which demonstrated that the loosely adsorbed BSA layer on the PSBMA membrane could be easily removed by hydraulic washing so that the irreversible adherence of BSA was remarkably alleviated. Obviously, the introduction of PSBMA polymer significantly improved the hydrophilicity of the membrane surface and consequently endowed the membrane with outstanding antifouling resistance. Besides, PVDF membrane presented a higher FRR of 87.17% than that of PDA membrane (84.60%). The low value of NF and FRR of PDA membrane suggested that a relatively severe and irreversible BSA fouling occurred when BSA deposited and adhered to PDA membrane surface. The FRR results were also in line with the measured adhesion energy between BSA and various membranes (Fig. 4-7(b)), where PDA membrane showed the strongest adhesion energy while PSBMA membrane Therefore, the severe fouling phenomenon of PDA membrane could be explained by the strong adhesion energy originating from a variety of short-range interactions including hydrophobic attraction, cation-π interactions, anion-π interactions and hydrogen bonding between amino acids of BSA and functional groups of PDA molecules.

Fig. 4-6(d) illustrated the influences of HA on water permeation flux and the extent of flux recovery of different membranes through the filtration system, in which the concentration of the feed solution was 20 mg/L. The observed NF was approximately 86.87%, 85.61%, and 90.05% in the case of PVDF, PDA, and PSBMA membranes, respectively. According to the approaching force curves of HA towards PVDF membrane and PDA membrane (Fig. 4-5(a-b)) and the calculated parameters listed in Fig. 4-7(a), it was proved that at short distances the attractive VDW interaction and hydrophobic interaction overcame the repulsive EDL interaction, resulting a tough adherence of HA to PVDF and PDA membrane. However, the situation was the opposite for PSBMA membrane, in which the combination of repulsive EDL interaction and hydration interaction rose above attractive interaction, leading to a decreased contaminant adsorption and a minimum water flux decline. After 5 min of washing with DI water, the relative water flux was restored to 90.95%, 87.72%, and 94.42%, respectively. The filtration test results were in good agreement with the adhesion energy trends (Fig. 4-7(b)), where the interaction forces of

HA with PDA membrane during retraction were the strongest compared to that with PVDF and PSBMA membrane, accompanied by the most serious membrane fouling. While the weak adhesion energy between HA and PSBMA membrane resulted in the highest FRR and the minimum ratio of irreversible to the total resistance. Comparing the filtration tests and the interaction force measurements, it could be found that the calculated or fitted parameters from approaching force curves such as surface potentials, Hamaker constants, and decay lengths could be utilized to explain the different water flux declines of various membranes, and the measured adhesion energy from the retracting force curves are in good line with the trend of water flux recovery of membranes after cleaning. Hence, the fundamental research could further construct a model of water treatment membranes for antifouling evaluation and membrane surface engineering.

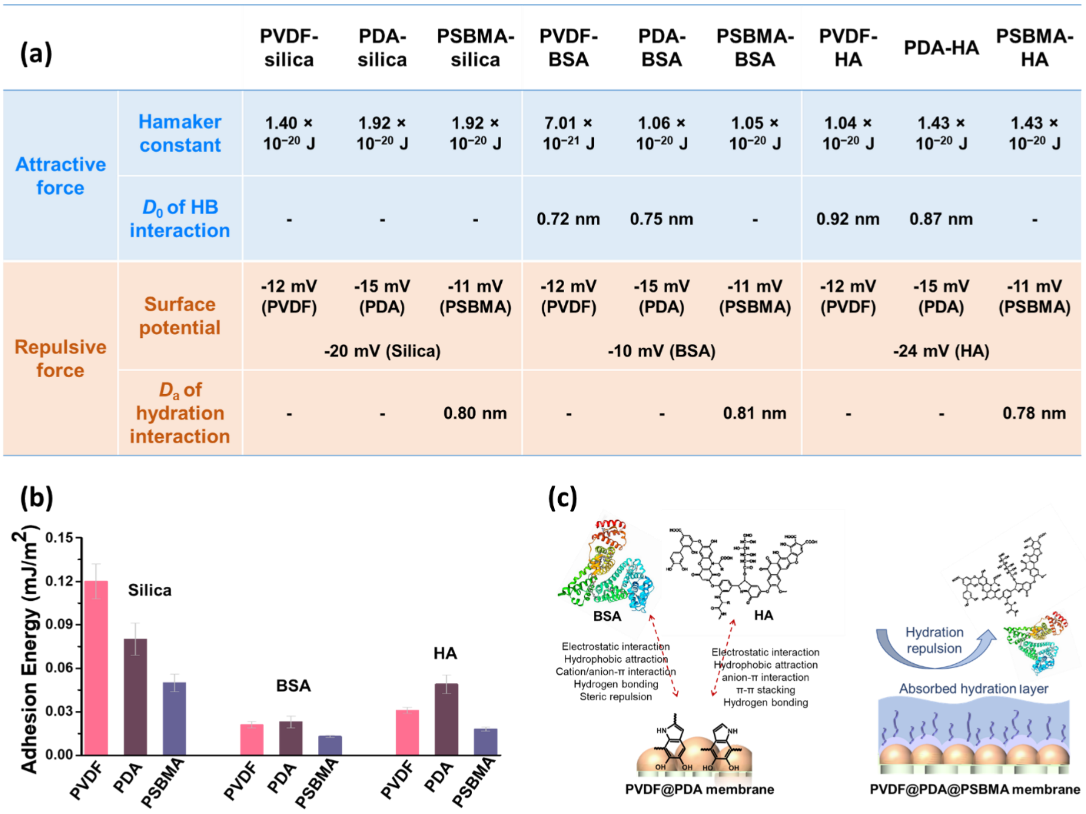

(a)

		PVDF-silica	PDA-silica	PSBMA-silica	PVDF-BSA	PDA-BSA	PSBMA-BSA	PVDF-HA	PDA-HA	PSBMA-HA
Attractive force	Hamaker constant	1.40 × 10^{-20} J	1.92 × 10^{-20} J	1.92 × 10^{-20} J	7.01 × 10^{-21} J	1.06 × 10^{-20} J	1.05 × 10^{-20} J	1.04 × 10^{-20} J	1.43 × 10^{-20} J	1.43 × 10^{-20} J
	D_0 of HB interaction	-	-	-	0.72 nm	0.75 nm	-	0.92 nm	0.87 nm	-
Repulsive force	Surface potential	-12 mV (PVDF)	-15 mV (PDA) -20 mV (Silica)	-11 mV (PSBMA)	-12 mV (PVDF)	-15 mV (PDA) -10 mV (BSA)	-11 mV (PSBMA)	-12 mV (PVDF)	-15 mV (PDA) -24 mV (HA)	-11 mV (PSBMA)
	D_a of hydration interaction	-	-	0.80 nm	-	-	0.81 nm	-	-	0.78 nm

Fig. 4-7 (a) A summary of calculated and fitted parameters of approaching force curves and (b) measured adhesion energy between the PVDF, PDA and PSBMA membrane surface and the three types of foulants; (c) Schematic of potential interaction schemes between the organic foulants (BSA and HA) and PDA membrane as well as PSBMA membrane surface.

4.4. Conclusion

This work systematically investigated the interaction mechanisms of PVDF, PDA, and PSBMA membranes with three kinds of typical contaminants in water systems. The contribution of each type of interaction force between different types of foulants and surfaces was quantitatively calculated and independently analyzed, from which the factors that affected the foulants adsorption and removal behaviors was unraveled. Silica particles showed the strongest driving force adsorbing on the PVDF membrane and the most stable adhesion force detaching from the PVDF membrane among the three types of membrane surfaces. In contrast, two organic foulants including BSA and HA were more prone to adsorb and accumulate on PDA membrane than PVDF membrane. The presence of a variety of interactions such as hydrophobic attraction, cation/anion-π interactions and hydrogen bonding between the functional groups of BSA and HA and PDA molecules made a considerable contribution to the attractive force of BSA/HA toward PDA membrane, causing a higher adsorption rate and a higher irreversible fouling on PDA membrane. Nevertheless, the weak interactions between PSBMA membrane and various foulants in both approaching and retracting force-distance curves revealed the nanomechanical mechanisms of the antifouling property of the zwitterionic membrane. It was achieved through the short-range hydration repulsion originating from the hydration layer of the PSBMA membrane surface, which significantly overcame other attractive interactions between foulants and membrane as a physical barrier, prevented the attachment of foulants on the surface and accelerated the removal of foulants to enhance permeability and reusability of membranes. The antifouling performance of the three membranes against different foulants was further verified through filtration tests, where PDA membrane exhibited better antifouling capability against silica, but poor performance to HA and BSA compared with PVDF membrane. While the resistance ability of the PSBMA membrane was found to be excellent towards all kinds of foulants, which was consistent with the force measurements. Although the filtration tests could be influenced by many factors, it seems that the force measurement results could be further applied as an evaluation model to explain or even predict the trends of water flux decline and water flux recovery of different membranes. Our study explored the interaction mechanisms underlying the adsorption and removal behaviors of diverse foulants on membranes based on the theoretical analysis of interaction forces measured during approach and retraction, which will open new avenues for future research into the fouling mechanisms of various kinds of organic/inorganic foulants with different membranes and the development of antifouling membranes for effective applications in many engineering processes such as membrane filtration.

4.5. Supporting Information

4.5.1. AFM images of silica wafers

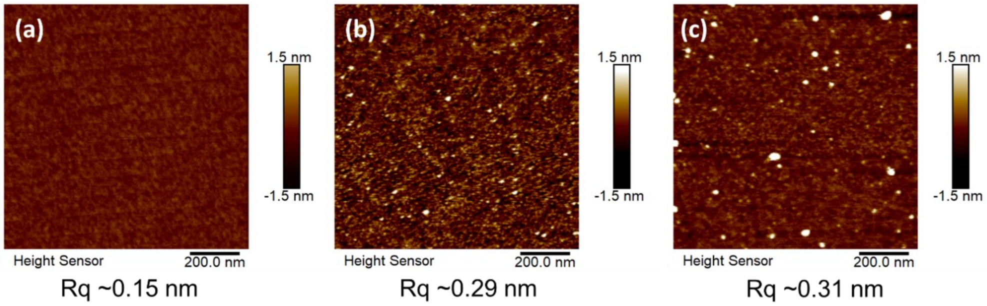

Fig. 4-8 AFM images of (a) bare silica wafer (root mean square roughness *R*q 0.15 ± 0.03 nm); (b) BSA on silica substrate (*R*q 0.29 ± 0.04 nm); and (c) HA on APTES-silica substrate (*R*q 0.31 ± 0.03 nm).

4.5.2. Calculation of a mean RMS roughness σ_m of the contact between membrane surface and AFM probe:

According to the classical contact mechanics, when an elastic sphere with radius R indents an elastic half-space where total deformation is d, causing a contact area of radius: (Johnson and Johnson, 1987; Knothe, 2011)

$$a = \sqrt{Rd} \tag{18}$$

Herein, the contact radius a was calculated to be 50 nm when the AFM probe with a radius of 2500 nm was indented on the membrane surface to a depth of 1 nm. Through AFM images of membrane with an area of 100 ×100 nm, the average roughness σ_1 was analyzed around 2 nm (shown in Fig. 4-9). While for smooth AFM silica probe, the roughness σ_2 was only measured to be 0.15 nm (Fig. 4-8(a)). Thus, the mean RMS roughness σ_m at contact was calculated to be 2 nm according to Eq.9.

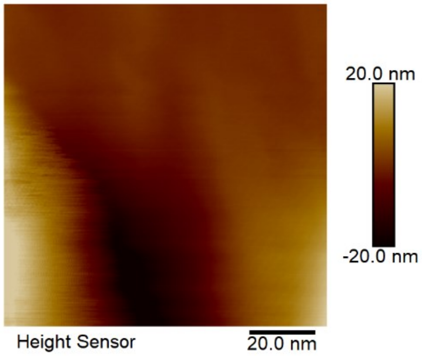

Fig. 4-9 AFM images of PVDF membrane with an area of 100 ×100 nm (RMS~2 nm)

4.5.3. SEM images of different membranes

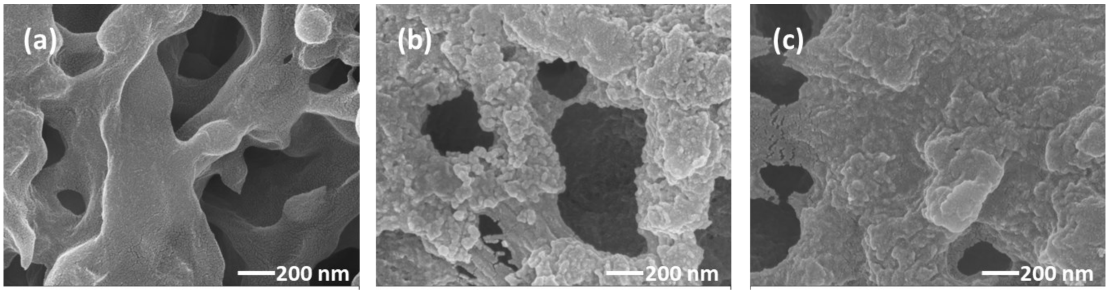

Fig. 4-10 SEM images of (a) pristine (b) PDA-coated, and (c) PSBMA-coated PVDF membrane at 25 k X magnification. The morphology of the three membranes measured by SEM was in good agreement with AFM images, where PDA membrane exhibited a layer of PDA nanoparticles on the originally smooth PVDF membrane surface. While after the deposition of PSBMA polymers, the membrane surface showed a more uniform layer, and the surface roughness was minimized.

4.5.4. Chemical composition of PVDF membranes with/without modification

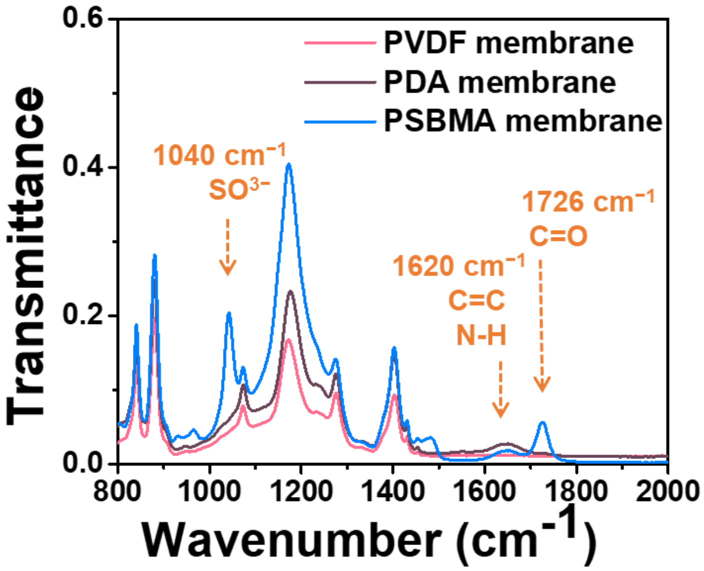

Fig. 4-11 The chemical composition of the PVDF membranes before and after modification was investigated by FTIR analysis. All membranes displayed $-CF_2$ stretching vibration absorption bands of the PVDF membrane, which ranges from 1180 to 1400 cm^{-1} (Jeong et al., 2017; Zhao et al., 2017). After PDA was coated on the PVDF membrane, an absorption peak at 1620 cm^{-1} appeared in the FTIR spectra, corresponding to the overlap of C=C resonance vibrations in aromatic ring and N–H bending vibrations

(Jiang et al., 2014). For the PSBMA/PDA/PVDF membrane, new absorption signals at 1726 cm^{-1} and 1040 cm^{-1} were presented in the FTIR spectra, which can be attributed to the C=O stretch vibration and symmetric stretch vibrations of sulfonate (SO^{3-}) groups of PSBMA in the membrane surface, respectively (Chiao et al., 2020; Wang et al., 2018).

4.5.5. Characterization of AFM probes

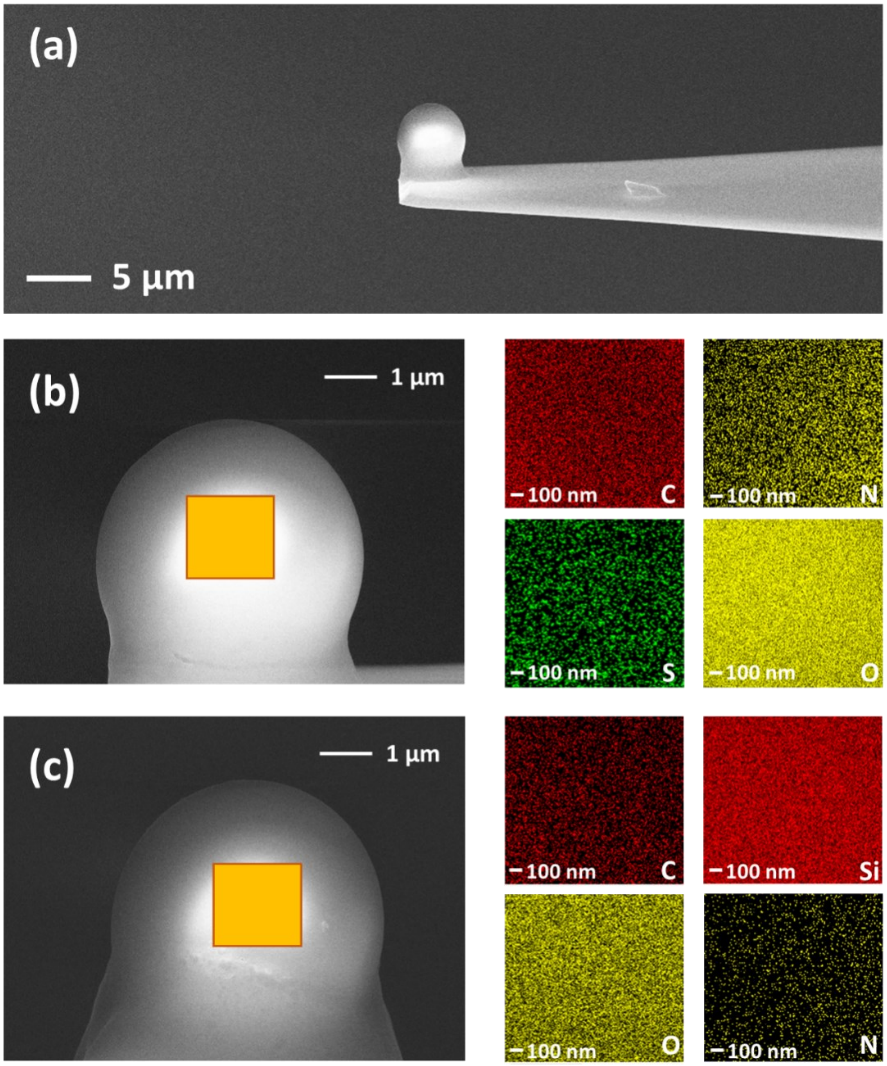

Fig. 4-12 (a) The SEM image of the silica AFM probe; (b) The SEM image of the BSA-coated silica AFM probe and EDS results of the selected area (orange square) of the BSA-coated silica AFM probe; (c) The SEM image of the HA-coated silica AFM probe and EDS results of the selected area (orange square) of the HA-coated silica AFM probe.

4.5.6. Surface potentials of silica, BSA and HA

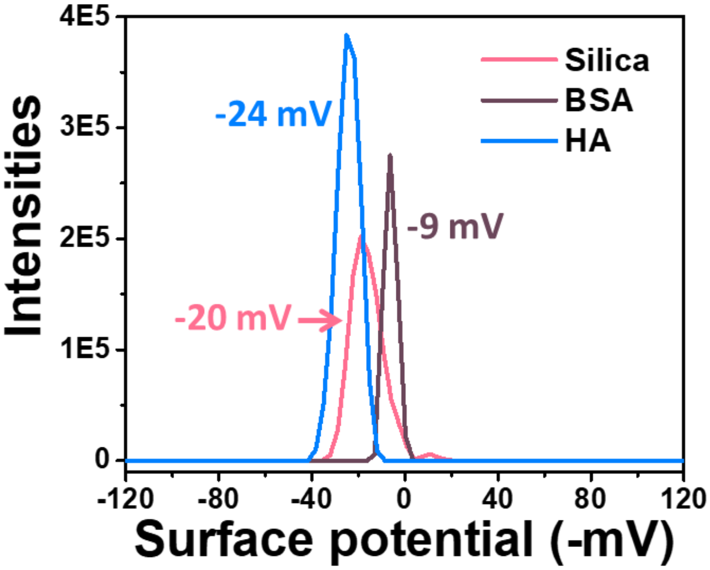

Fig. 4-13 Surface potential of silica nanoparticles, BSA molecules and HA molecules in 10 mM NaCl solution at pH 5.8 measured by Zetasizer Nano.

References

Al-Amoudi, A.S., 2010. Factors affecting natural organic matter (NOM) and scaling fouling in NF membranes: a review. Desalination 259, 1–10.

Ang, W.S., Elimelech, M., 2008. Fatty acid fouling of reverse osmosis membranes: Implications for wastewater reclamation. Water research 42, 4393–4403.

Ang, W.S., Elimelech, M., 2007. Protein (BSA) fouling of reverse osmosis membranes: implications for wastewater reclamation. Journal of Membrane Science 296, 83–92.

Azari, S., Zou, L., 2012. Using zwitterionic amino acid l-DOPA to modify the surface of thin film composite polyamide reverse osmosis membranes to increase their fouling resistance. Journal of Membrane Science 401, 68–75.

Boo, C., Hong, S., Elimelech, M., 2018. Relating organic fouling in membrane distillation to intermolecular adhesion forces and interfacial surface energies. Environmental science & technology 52, 14198–14207.

Cappella, B., Dietler, G., 1999. Force-distance curves by atomic force microscopy. Surface science reports 34, 1–104.

Chen, M., Xiao, C., Wang, C., Liu, H., 2017. Study on the structural design and performance of novel braid-reinforced and thermostable poly (m-phenylene isophthalamide) hollow fiber membranes. RSC advances 7, 20327–20335.

Chen, Q., Yuan, L., Duan, R., Huang, P., Fu, J., Ma, H., Wang, X., Zhou, Y., Song, B., 2019. Zwitterionic Polymer: A Facile Interfacial Material Works at Both Anode and Cathode in p‐i‐n Perovskite Solar Cells. Solar RRL 3, 1900118.

Chiao, Y.-H., Chen, S.-T., Sivakumar, M., Ang, M.B.M.Y., Patra, T., Almodovar, J., Wickramasinghe, S.R., Hung, W.-S., Lai, J.-Y., 2020. Zwitterionic polymer brush grafted on polyvinylidene difluoride membrane promoting enhanced ultrafiltration performance with augmented antifouling property. Polymers 12, 1303.

De Vera, J.S., Venault, A., Chou, Y.-N., Tayo, L., Chiang, H.-C., Aimar, P., Chang, Y., 2018. Self-cleaning interfaces of polydimethylsiloxane grafted with pH-responsive zwitterionic copolymers. Langmuir 35, 1357–1368.

Dishon, M., Zohar, O., Sivan, U., 2009. From repulsion to attraction and back to repulsion: the effect of NaCl, KCl, and CsCl on the force between silica surfaces in aqueous solution. Langmuir 25, 2831–2836.

Franks, G. V, 2002. Zeta potentials and yield stresses of silica suspensions in concentrated monovalent electrolytes: isoelectric point shift and additional attraction. Journal of colloid and interface science 249, 44–51.

Gao, Y., Guo, N., Gauvreau, B., Rajabian, M., Skorobogata, O., Pone, E., Zabeida, O., Martinu, L., Dubois, C., Skorobogatiy, M., 2006. Consecutive solvent evaporation and co-rolling techniques for polymer multilayer hollow fiber preform fabrication. Journal of materials research 21, 2246–2254.

Gaur, A.M., Rana, D.S., 2019. In situ measurement of dielectric permittivity and electrical conductivity of CoCl 2/BaCl 2 doped PVDF composite at elevated temperature. Journal of Inorganic and Organometallic Polymers and Materials 29, 1637–1644.

Gong, L., Wang, J., Xiang, L., Huang, J., Fattahpour, V., Roostaei, M., Mamoudi, M., Fermaniuk, B., Luo, J.-L., Zeng, H., 2021. Characterizing foulants on slotted liner and probing the surface interaction mechanisms in organic media with implication for an antifouling strategy in oil production. Fuel 290, 120008.

Gong, L., Wang, J., Zhang, L., Fattahpour, V., Mamoudi, M., Roostaei, M., Fermaniuk, B., Luo, J.-L., Zeng, H., 2019. Fouling mechanisms of asphaltenes and fine solids on bare and electroless nickel-phosphorus coated carbon steel. Fuel 252, 188–199.

Guo, S., Jańczewski, D., Zhu, X., Quintana, R., He, T., Neoh, K.G., 2015. Surface charge control for zwitterionic polymer brushes: Tailoring surface properties to antifouling applications. Journal of colloid and interface science 452, 43–53.

Helm, C.A., Knoll, W., Israelachvili, J.N., 1991. Measurement of ligand-receptor interactions. Proceedings of the National Academy of Sciences 88, 8169–8173.

Herzberg, M., Kang, S., Elimelech, M., 2009. Role of extracellular polymeric substances (EPS) in biofouling of reverse osmosis membranes. Environmental science & technology 43, 4393–4398.

Ishiguro, M., Tan, W., Koopal, L.K., 2007. Binding of cationic surfactants to humic substances. Colloids and Surfaces A: Physicochemical and Engineering Aspects 306, 29–39.

Israelachvili, J.N., 2015. Intermolecular and surface forces. Academic press.

Jeong, J., Cho, E., Yun, D., Kim, T., Lee, I.-S., Jung, S., 2017. Label-free colorimetric detection of influenza antigen based on an antibody-polydiacetylene conjugate and its coated polyvinylidene difluoride membrane. Polymers 9, 127.

Jiang, S., Cao, Z., 2010. Ultralow-Fouling, Functionalizable, and Hydrolyzable Zwitterionic Materials and Their Derivatives for Biological Applications. Advanced Materials 22, 920–932.

Jiang, J.-H., Zhu, L.-P., Zhang, H.-T., Zhu, B.-K., Xu, Y.-Y., 2014. Improved hydrodynamic permeability and antifouling properties of poly (vinylidene fluoride) membranes using polydopamine nanoparticles as additives. Journal of membrane science 457, 73–81.

Johnson, K.L., 1987. Contact mechanics. Cambridge university press.

Johnson, D., Hilal, N., 2015. Characterisation and quantification of membrane surface properties using atomic force microscopy: A comprehensive review. Desalination 356, 149–164.

Johnson, K.L., Kendall, K., Roberts, aAD, 1971. Surface energy and the contact of elastic solids. Proceedings of the royal society of London. A. mathematical and physical sciences 324, 301–313.

Jung, S.Y., Won, Y.-J., Jang, J.H., Yoo, J.H., Ahn, K.H., Lee, C.-H., 2015. Particle deposition on the patterned membrane surface: Simulation and experiments. Desalination 370, 17–24.

Kelly, S.T., Zydney, A.L., 1995. Mechanisms for BSA fouling during microfiltration. Journal of Membrane Science 107, 115–127.

Knothe, K., 2011. Contact mechanics and friction: physical principles and applications.

Kosmulski, M., 1998. Positive electrokinetic charge of silica in the presence of chlorides. Journal of colloid and interface science 208, 543–545.

Kralchevsky, P., Nagayama, K., 2001. Particles at fluid interfaces and membranes: attachment of colloid particles and proteins to interfaces and formation of two-dimensional arrays. Elsevier.

Le-Clech, P., Chen, V., Fane, T.A.G., 2006. Fouling in membrane bioreactors used in wastewater treatment. Journal of membrane science 284, 17–53.

Leng, C., Hung, H.-C., Sun, S., Wang, D., Li, Y., Jiang, S., Chen, Z., 2015. Probing the surface hydration of nonfouling zwitterionic and PEG materials in contact with proteins. ACS applied materials & interfaces 7, 16881–16888.

Li, D., Wei, Q., Wu, C., Zhang, X., Xue, Q., Zheng, T., Cao, M., 2020. Superhydrophilicity and strong salt-affinity: Zwitterionic polymer grafted surfaces with significant potentials particularly in biological systems. Advances in colloid and interface science 278, 102141.

Li, S., Chen, J., Wang, J., Zeng, H., 2021. Anti-biofouling Materials and Surfaces based on Mussel-inspired Chemistry. Materials Advances.

Li, X., Chen, Y., Hu, X., Zhang, Y., Hu, L., 2014. Desalination of dye solution utilizing PVA/PVDF hollow fiber composite membrane modified with TiO2 nanoparticles. Journal of membrane science 471, 118–129.

Liu, C., Song, D., Zhang, W., He, Q., Huangfu, X., Sun, S., Sun, Z., Cheng, W., Ma, J., 2020. Constructing zwitterionic polymer brush layer to enhance gravity-driven membrane performance by governing biofilm formation. Water Research 168, 115181.

Lu, Q., Huang, J., Maan, O., Liu, Y., Zeng, H., 2018. Probing molecular interaction mechanisms of organic fouling on polyamide membrane using a surface forces apparatus: Implication for wastewater treatment. Science of The Total Environment 622, 644–654.

Lu, Q., Oh, D.X., Lee, Y., Jho, Y., Hwang, D.S., Zeng, H., 2013. Nanomechanics of Cation–π Interactions in Aqueous Solution. Angewandte Chemie International Edition 52, 3944–3948. https://doi.org/https://doi.org/10.1002/anie.201210365

Ma, J.C., Dougherty, D.A., 1997. The cation− π interaction. Chemical reviews 97, 1303–1324.

Matin, A., Khan, Z., Zaidi, S.M.J., Boyce, M.C., 2011. Biofouling in reverse osmosis membranes for seawater desalination: phenomena and prevention. Desalination 281, 1–16.

Miao, R., Wang, L., Zhu, M., Deng, D., Li, S., Wang, J., Liu, T., Lv, Y., 2017. Effect of hydration forces on protein fouling of ultrafiltration membranes: the role of protein charge, hydrated ion species, and membrane hydrophilicity. Environmental science & technology 51, 167–174.

Nguyen, A., Azari, S., Zou, L., 2013. Coating zwitterionic amino acid l-DOPA to increase fouling resistance of forward osmosis membrane. Desalination 312, 82–87.

Parsons, D.F., Eom, N., Walsh, R.B., Craig, V.S.J., 2019. A new DLVO-R theory: surface roughness and nanoparticle stability, in: Harnessing Nanoscale Surface Interactions. Elsevier, pp. 129–147.

Parsons, D.F., Walsh, R.B., Craig, V.S.J., 2014. Surface forces: Surface roughness in theory and experiment. The Journal of chemical physics 140, 164701.

Petsev, D.N., 2004. Emulsions: structure, stability and interactions. Elsevier.

Rana, D., Matsuura, T., 2010. Surface modifications for antifouling membranes. Chemical reviews 110, 2448–2471.

Reyes-Bozo, L., Escudey, M., Vyhmeister, E., Higueras, P., Godoy-Faúndez, A., Salazar, J.L., Valdés-González, H., Wolf-Sepúlveda, G., Herrera-Urbina, R., 2015. Adsorption of biosolids and their main components on chalcopyrite, molybdenite and pyrite: Zeta potential and FTIR spectroscopy studies. Minerals Engineering 78, 128–135.

Sakarkar, S., Muthukumaran, S., Jegatheesan, V., 2021. Tailoring the effects of titanium dioxide (Tio2) and polyvinyl alcohol (pva) in the separation and antifouling performance of thin-film composite polyvinylidene fluoride (pvdf) membrane. Membranes 11, 241.

Salgin, S., Salgin, U., Bahadir, S., 2012. Zeta potentials and isoelectric points of biomolecules: the effects of ion types and ionic strengths. Int. J. Electrochem. Sci 7, 12404–12414.

Salonen, L.M., Ellermann, M., Diederich, F., 2011. Aromatic rings in chemical and biological recognition: energetics and structures. Angewandte Chemie International Edition 50, 4808–4842.

Schulze, A., Went, M., Prager, A., 2016. Membrane functionalization with hyperbranched polymers. Materials 9, 706.

Seo, J., Kim, J.H., Lee, M., Moon, J., Yi, D.K., Paik, U., 2016. Size-dependent interactions of silica nanoparticles with a flat silica surface. Journal of colloid and interface science 483, 177–184.

Shannon, M.A., Bohn, P.W., Elimelech, M., Georgiadis, J.G., Marinas, B.J., Mayes, A.M., 2008. Science and technology for water purification in the coming decades. Nature 452, 301–310.

Thakur, V.K., Lin, M.-F., Tan, E.J., Lee, P.S., 2012. Green aqueous modification of fluoropolymers for energy storage applications. Journal of Materials Chemistry 22, 5951–5959.

Tong, M., Zhu, P., Jiang, X., Kim, H., 2011. Influence of natural organic matter on the deposition kinetics of extracellular polymeric substances (EPS) on silica. Colloids and Surfaces B: Biointerfaces 87, 151–158.

Valle-Delgado, J.J., Molina-Bolívar, J.A., Galisteo-González, F., Gálvez-Ruiz, M.J., Feiler, A., Rutland, M., 2004. Interactions between bovine serum albumin layers adsorbed on different substrates measured with an atomic force microscope. Physical Chemistry Chemical Physics 6, 1482–1486.

Wang, D., Zhang, W., Zhou, D., n.d. Supporting Information Antagonistic Effects of Humic Acid and Iron Oxyhydroxide Grain-Coating on Biochar Nanoparticle Transport in Saturated Sand.

Wang, S.-Y., Fang, L.-F., Cheng, L., Jeon, S., Kato, N., Matsuyama, H., 2018. Novel ultrafiltration membranes with excellent antifouling properties and chlorine resistance using a poly (vinyl chloride)-based copolymer. Journal of Membrane Science 549, 101–110

Xie, L., Shi, C., Wang, J., Huang, J., Lu, Q., Liu, Q., Zeng, H., 2015. Probing the interaction between air bubble and sphalerite mineral surface using atomic force microscope. Langmuir 31, 2438–2446.

Xu, J., Ma, A., Liu, T., Lu, C., Wang, D., Xu, H., 2013. Janus-like Pickering emulsions and their controllable coalescence. Chemical Communications 49, 10871–10873. https://doi.org/10.1039/C3CC46738D

Xu, Z., Zhang, J., Shan, M., Li, Y., Li, B., Niu, J., Zhou, B., Qian, X., 2014. Organosilane-functionalized graphene oxide for enhanced antifouling and mechanical properties of polyvinylidene fluoride ultrafiltration membranes. Journal of Membrane Science 458, 1–13.

Yang, H.-C., Luo, J., Lv, Y., Shen, P., Xu, Z.-K., 2015. Surface engineering of polymer membranes via mussel-inspired chemistry. Journal of membrane science 483, 42–59.

Zhao, C., Zhang, G., Xu, X., Yang, F., Yang, Y., 2017. Rapidly self-assembled polydopamine coating membranes with polyhexamethylene guanidine: Formation, characterization and antifouling evaluation. Colloids and Surfaces A: Physicochemical and Engineering Aspects 512, 41–50.

Zhao, J., Shi, Q., Luan, S., Song, L., Yang, H., Shi, H., Jin, J., Li, X., Yin, J., Stagnaro, P., 2011. Improved biocompatibility and antifouling property of polypropylene non-woven fabric membrane by surface grafting zwitterionic polymer. Journal of Membrane Science 369, 5–12.

Zhao, W., Ye, Q., Hu, H., Wang, X., Zhou, F., 2014. Grafting zwitterionic polymer brushes via electrochemical surface-initiated atomic-transfer radical polymerization for anti-fouling applications. Journal of Materials Chemistry B 2, 5352–5357.

Zheng, N., Huang, Y., Sun, W., Du, X., Liu, H.-Y., Moody, S., Gao, J., Mai, Y.-W., 2016. In-situ pull-off of ZnO nanowire from carbon fiber and improvement of interlaminar toughness of hierarchical ZnO nanowire/carbon fiber hydrid composite laminates. Carbon 110, 69–78.

CHAPTER 5 ENHANCED SEPARATION PERFORMANCE OF CONDUCTIVE PEDOT: PSS/PSBMA COATED PVDF MEMBRANE FOR EMULSIFIED OILY WASTEWATER TREATMENT UNDER ELECTROCHEMICAL ASSISTANCE

5.1. Introduction

Oil-in-water (O/W) emulsions widely exist in oily wastewater generated by various industries such as oil/gas industries, cosmetics manufacturing, food processing, and mining exploration[1,2]. Removing the oil phase from water ensures the safe discharge of oil, promotes environmentally friendly disposal, facilitates the reuse of both domestic and industrial water, and achieves economic benefits[3]. Many efforts have been devoted to O/W emulsion separation and oil recovery including mechanical separation, chemical treatment, and biological methods [4–6], among which membrane filtration technology stands out due to the high separation efficiency and selectivity, wide applicability in industry, low energy cost, and economically friendliness[7–9].

Membrane filtration technology has experienced unprecedented growth in recent years, and how to improve efficiency while ensuring the safety of dialysis membranes is also an inescapable problem to be discussed. Moreover, membrane fouling is another inevitable problem as the sludge particles and oil colloids usually deposit onto or even into the membrane pores, leading to the severe permeate flux decline and filtration failure, which greatly limits the application of membrane technology into full-scale practical operation [10].

Combining electrochemical processes or electrical assistance into membrane filtration has been proven to be an excellent method to improve emulsion separation and oil recovery performance and, at the same time, control the deposition of foulants onto the membrane surface [11,12]. Relevant reports indicated that some materials with fascinating electrical/electrochemical properties such as carbon nanotubes (CNTs) and graphene oxide (GO) make it possible to improve emulsion separation and eliminate organic fouling by electrochemical oxidation and electrostatic repulsion between the oil and membranes[13–18]. Fan et, al. developed a self-sustained carbon nanotube hollow fiber scaffold supported polyamide thin film composite (CNT TFC-FO) membrane, which improved flux by about 50% during the oil−water emulsion separation from electrochemical forward osmosis process due to the synergic effect of electric-conductivity and hydrophilicity [19]. Yi et, al. designed carbon nanotube polyvinyl alcohol (CNT-PVA) composite membranes serving as cathode during the treatment of oily wastewater, which significantly enhanced the oil removal efficiency and alleviated membrane fouling benefited from the function of electrostatic repulsion [20].

Applying the strategy, a new conductive membrane was developed in this work by grafting the conductive polymer blend of poly(3,4-ethylenedioxythiophene) and polystyrene sulfonate (known as PEDOT:PSS) and zwitterionic polymer poly(sulfobetaine methacrylate) (PSBMA) on poly(vinylidene fluoride) (PVDF) membrane surface with the help of versatile mussel-inspired polydopamine (PDA). PEDOT:PSS possesses a high and controllable conductivity, excellent chemical and electrochemical stability, good optical transparency, and good biocompatibility, making it useful as electrodes in electrochemical devices, solar cells, organic thin film transistors, and so on [21–25]. Moreover, PSBMA polymer, known as a zwitterionic polymer, has been applied as a promising class of antifouling agents to improve organic fouling resistance. The outstanding antifouling performance is attributed to the tightly bound hydration layer on the zwitterionic surfaces, which serves as a steric and energetic barrier against the adsorption of organic and biological entities [26–29]. Here, a PEDOT:PSS and PSBMA polymers modified PVDF membrane was first proposed with high porosity, good hydrophilicity, and excellent electro-conductivity, where the bio-inspired super glue PDA was applied as the versatile intermediate layer to connect the PVDF membrane and the two polymers. An electrochemistry-assistant system was designed in this work to investigate the O/W emulsion separation and antifouling performance under different external electrochemical potentials. In order to clarify the interaction mechanism between oil droplets and the conductive membranes during electrochemical processes, an electrochemical atomic force microscope (EC-AFM) was employed [30–32]. The conductive AFM technology is able to control the interfacial electrochemical reactions and probe the change of surface forces simultaneously, facilitating the direct characterization of interactions evolutions between oil and membranes under varying potentials at the nanoscale, which has not been reported to our knowledge. Then, the extended Derjaguin−Landau−Verwey−Overbeek (DLVO) theory including the effect of hydrophobic interaction was applied to analyze the measured forces between oil droplets and different membrane surfaces potentiostatically treated at various electrochemical potentials in aqueous solution. The antifouling performance of different membranes was evaluated by the filtration and rejection test. Our work provides useful insights into the development of functional conductive membrane surfaces to improve O/W separation efficiency and eliminate the fouling problems as well as the fundamental interaction mechanisms associated with antifouling properties of O/W emulsions on conductive membranes under various potentials.

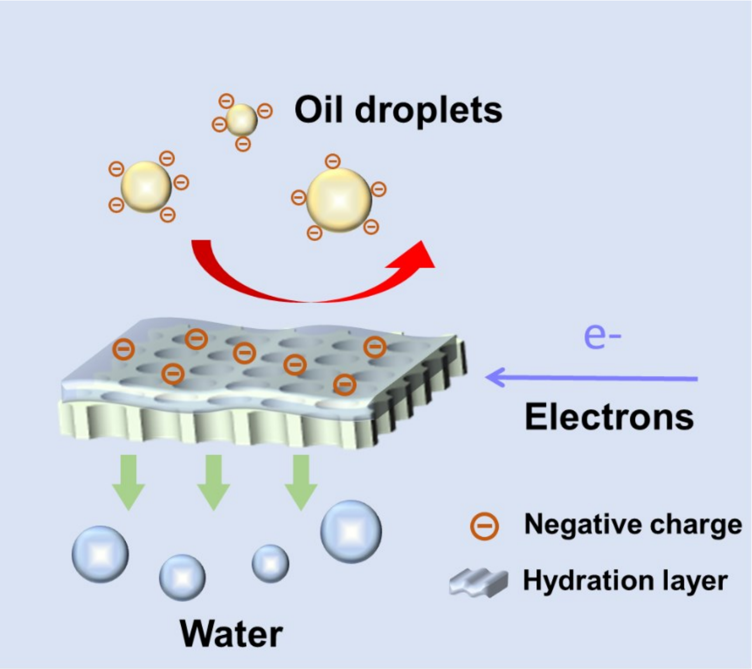

Fig. 5-1 Schematic illustration of O/W emulsion separation mechanism of conductive PEDOT:PSS/PSBMA coated PVDF membrane under electrochemical assistance.

5.2. Results and discussion

5.2.1. Characterization of PVDF membrane, PEDOT:PSS-coated PVDF membranes and PEDOT:PSS/PSBMA-coated membranes

The PVDF membranes were prepared via an immersed phase inversion method. The thickness of the prepared PVDF membranes was around 200 μm, and the membrane porosity (ε) and mean pore radius (r_m) were calculated to be 68.5% and 0.16 μm, respectively, based on the dry weight and wet weight of the prepared PVDF membrane. The PEDOT:PSS-coated PVDF membranes (PP membrane) and PEDOT:PSS/PSBMA-coated membranes (PP/PSBMA membrane) were prepared based on the as-prepared PVDF membranes, and the polymerization process of polymers and preparation procedure of coatings are illustrated in Experimental Section. For PP membrane, a PDA layer was first self-polymerized on the pristine PVDF membrane surface under mild alkaline aqueous conditions of pH 8.5, serving as an intermediate versatile platform to introduce the PEDOT:PSS polymer. The fabrication process of the PP/PSBMA membrane, as illustrated in Fig. 5-2, began with the co-deposition of a PDA/PEDOT:PSS layer onto a PVDF membrane. Following this, a PSBMA layer was introduced to the membrane surface via surface modification to further enhance the hydrophilicity and antifouling properties of the membrane.

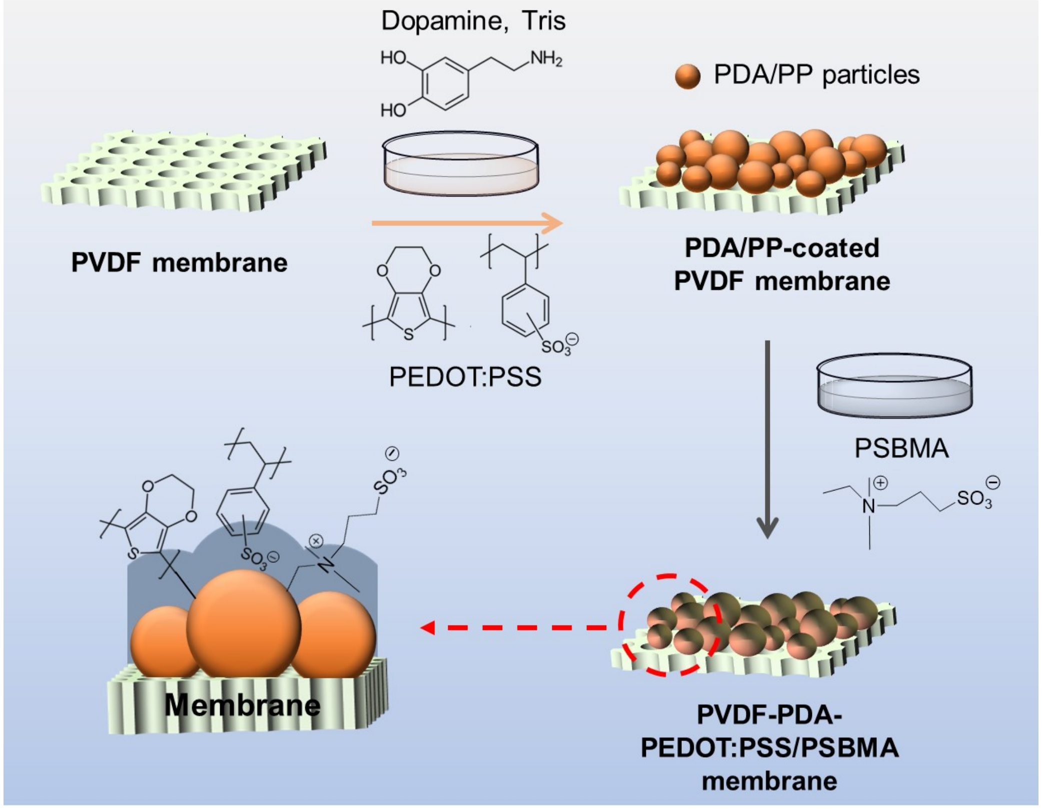

Fig. 5-2 Schematic of the fabrication process of PDA-PEDOT: PSS/PSBMA coating on PVDF membrane.

Figs. 5-3 a–c show the scanning electron microscope (SEM) images of the pristine PVDF membrane, PP membrane, and PP/PSBMA membrane, respectively. Compared to the pristine PVDF membrane, PP membrane maintained similar porous structures, while large quantities of agglomerations of PEDOT:PSS polymers were attached to the membrane substrate surface, exhibiting a stacked structure (Fig. 5-3 b). Meanwhile, the co-deposition of PEDOT:PSS and PSBMA polymers on the PVDF membrane surface formed a compact and homogeneous coating with high uniformity and less agglomeration (Fig. 5-3 c). The morphology of the three types of membranes was analogous to that observed on the topographic AFM images. Figs. 5-3 d–f show AFM imaging analysis of pristine PVDF membrane, PP membrane and PP/PSBMA membrane with an area of 2 μm × 2 μm, respectively. Pristine PVDF membrane (Fig. 5-3 d) exhibited a flat morphology structure with a root mean square roughness (RMS) value of 50.9 nm. After the deposition of PEDOT:PSS polymers (Fig. 5-3 e), it could be observed that large agglomerations were attached to the membrane surface, and the RMS value of the membrane surface was increased to 52.7 nm. However, the PP/PSBMA membrane (Fig. 5-3 f) showed a relatively smooth morphology with a smaller RMS value of 30.2 nm, which indicated that the PEDOT:PSS and PSBMA polymers could uniformly co-deposited on the pre-modified PDA layer and minimize the surface roughness. The wettability of the pristine PVDF membrane, PP membrane and PP/PSBMA membrane are also shown in Figs. 5-3 d–f. For the PVDF membrane (Fig. 5-3 d), the water drop could stably stand on the membrane surface due to the hydrophobicity and roughness of fluorinated polymers, showing a water contact angle (WCA) of 131.2˚. After being modified by PEDOT:PSS polymer, the measured WCA of the membrane surface was reduced to 75.1˚. For PP/PSBMA membrane, the water droplet partially spread on and readily attached to the membrane surface with a WCA of 20.1˚, which indicates the successful deposition of hydrophilic zwitterionic polymer. The surface chemical functionality of the PDA-PEDOT:PSS coating and PDA-PEDOT:PSS-PSBMA coating on PVDF membrane surfaces was characterized using the Fourier transform infrared (FTIR) spectrometer shown in Fig. 5-3 g. The transmittance peaks associated with the PDA-PEDOT:PSS coating (spectrum in purple line) were observed at 1520 cm^{-1} for the C=C skeletal vibrational spectral range for the benzene ring, which is present in both PDA and PEDOT:PSS molecules. While for the PDA-PEDOT:PSS/PSBMA coating (spectrum in green line), except the peaks for the $-CF_2$ stretching vibration absorption bands of the PVDF membrane (1180 cm^{-1}) and aromatic C=C skeleton stretching vibration (1520 cm^{-1}) [33], the new absorption signal at 1725 cm^{-1} corresponded to the carboxylic C=O stretching vibration of PSBMA in the membrane surface [34]. Moreover, a novel characterization method Optical PhotoThermal InfraRed (O-PTIR) microspectroscopy was applied to visualize the chemical composition distribution across a small area (2 × 2 μm^2) on the PP membrane and PP/PSBMA membrane surfaces. In the O-PTIR spectra maps of the PP membrane (Fig. 5-3 h), the characteristic band of PEDOT:PSS molecules–aromatic C=C skeleton stretching vibration (1520 cm^{-1}) could be observed throughout the whole characterized membrane surface. Additionally, a C=O band at 1725 cm^{-1} was also detected on the bulk PP/PSBMA membrane (Fig. 5-3 i). The O-PTIR images further verified the uniformity of the coated PDA-PEDOT:PSS coating and PDA-PEDOT:PSS/PSBMA coating on PVDF membrane surfaces.

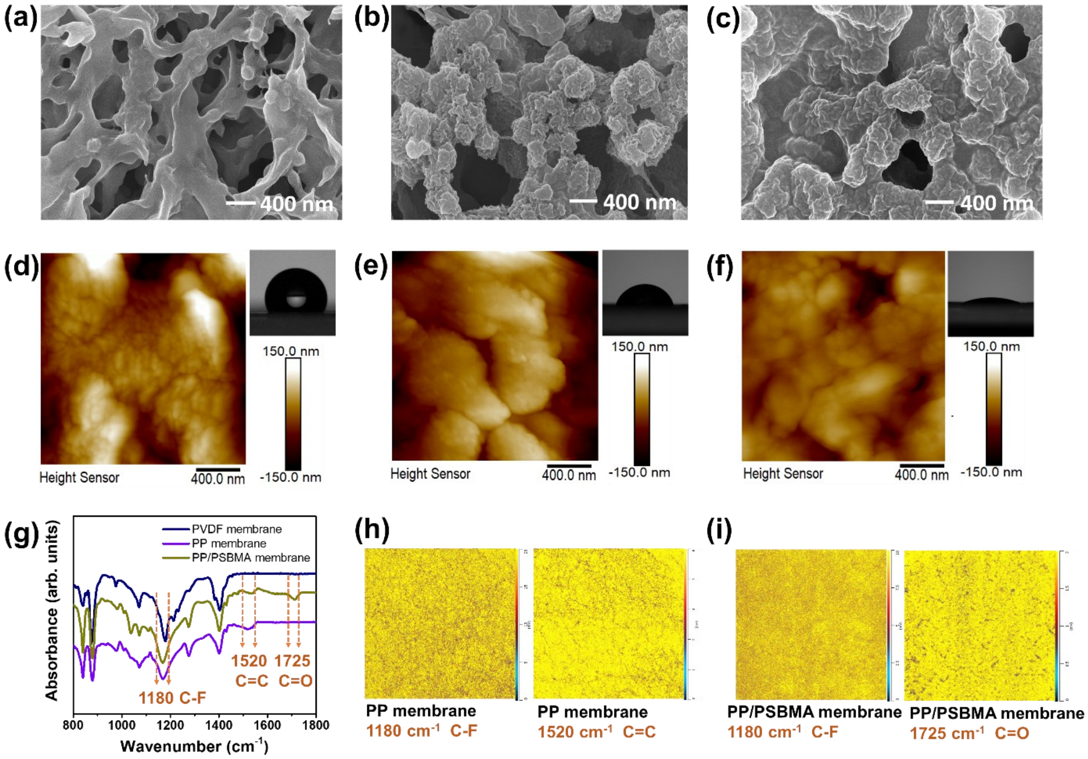

Fig. 5-3 SEM images of (a) pristine PVDF membrane (b) PDA-PEDOT:PSS-coated PVDF membrane, and (c) PDA-PEDOT:PSS/PSBMA coated PVDF membrane at 25k X magnification; Typical AFM images of surface morphologies and WCAs of (d) pristine PVDF membrane (RMS~50.9 nm, WCA~131.2˚) (e) PDA-PEDOT:PSS-coated PVDF membrane (RMS~52.7 nm, WCA~75.1˚), and (f) PDA-PEDOT:PSS/PSBMA coated PVDF membrane (RMS~30.2 nm, WCA~20.1˚); (g) The chemical composition of the PVDF membrane (blue), PDA-PEDOT:PSS-coated PVDF membrane (purple) and PDA-PEDOT:PSS/PSBMA coated PVDF membrane (green) investigated by FTIR analysis; (h) O-PTIR images of C-F (1180 cm^{-1}) and C=C (1520 cm^{-1}) groups in characterized areas of the PP membrane surface; (i) O-PTIR images of C-F (1180 cm^{-1}) and C=O (1725 cm^{-1}) groups in characterized areas of the PP/PSBMA membrane surface.

5.2.2. Electrochemical measurements

In In this work, the surface reactivity and electrochemical behaviors of PVDF membrane before and after modification of conductive PEDOT:PSS and PSBMA polymers were analyzed using the scanning electrochemical microscopy (SECM) technique. In order to study surface electrical charges and electrochemical reactions that occur on the membrane surfaces, the open circuit potential (OCP) and point of zero charge (PZC) of different membranes were determined prior to the SECM experiment using differential capacitance/potential curves, as shown in Supporting information. To assess the conductivity of membranes, the Pt tip was gradually brought closer to the membrane surface at a speed of 2 μm s^{-1}. The process involved measuring a tip approach curve, which allowed the contact point to be identified. For conductive or semi-conductive substrates, this was characterized by a sudden and sharp increase in tip current, while for insulating substrates, it was marked by a sudden drop to zero current. By recording changes in tip current as the distance between the tip and membrane varied, the electron transfer ability of different membranes was determined. The normalized current I_T vs normalized distance L curves of three types of membranes at different electrochemical potentials were presented in Fig. 5-4 a. Then, the SECM tip approach curves were theoretically fitted to determine the apparent rate constant k of the electrochemical reaction of PEDOT:PSS on membranes, and the theoretical calculation can be found in the Supporting Information. The pristine PVDF membrane displayed an insulator approach curve. It could be noted that the modification of PSBMA polymer affected the conductivity of the membrane as the k values of PP/PSBMA membrane were lower than that of PP membrane, while PP/PSBMA membrane still showed the conductive property compared with the curve of insulators. The obtained k values at various electrochemical potentials are plotted in Fig. 5-4 b. For both PP membrane and PP/PSBMA membrane, k values follow this trend: -0.4 V < OCP < 0.4 V. The conductivity of PEDOT:PSS is mainly determined by the oxidation state of the PEDOT component, which can be controlled by adjusting the electrochemical potential. The conductive PEDOT:PSS polymer intrinsically in a doped or oxidized state turns electrically insulating when being reduced by applying negative potentials, as shown in this electrochemical reaction (Equation (1)) [35]:

$$EDOT_n^+ \cdot SS^- + e^- + C^+ \rightarrow EDOT_n^0 \cdot SS^- \cdot C^+ \tag{1}$$

(doped or oxidized state) (dedoped or reduced state)

At 0.4 V, PEDOT:PSS was more oxidized, which generally resulted in a higher k value, meaning electron transfer behaviors were easier at the surface. At -0.4 V, the k slightly decreased as PEDOT:PSS was tuning into the reduced state, which typically led to lower conductivity compared to its oxidized state. However, the conductivity of PP membrane and PP/PSBMA membrane surface at -0.4 V was still much higher than an insulator, indicating active electron transfer behaviors at the conductive membrane/solution interfaces.

Then the Pt tip was retracted 10 μm and a 60 × 60 μm^2 image was taken at a tip scan rate of 50 $\mu m\ s^{-1}$. The SECM images of PP membrane and PP/PSBMA membrane at the same location at various potentials are shown in Figs. 5-4 c-f, with the Pt tip biased at 0.5 V. The mapping obtained at E_{sub} was set to 0.4 V showed a larger value than that obtained at E_{sub} was set to -0.4 V, indicating it was easier for electrons to flow from the PEDOT:PSS to the surroundings when the membrane surface was potentiostatically treated at a positive electrochemical potential. However, the electron-transfer reactions on the PP membrane and PP/PSBMA membrane surfaces were still active when an electrochemical potential of -0.4 V is applied as the feedback currents were in a high range.

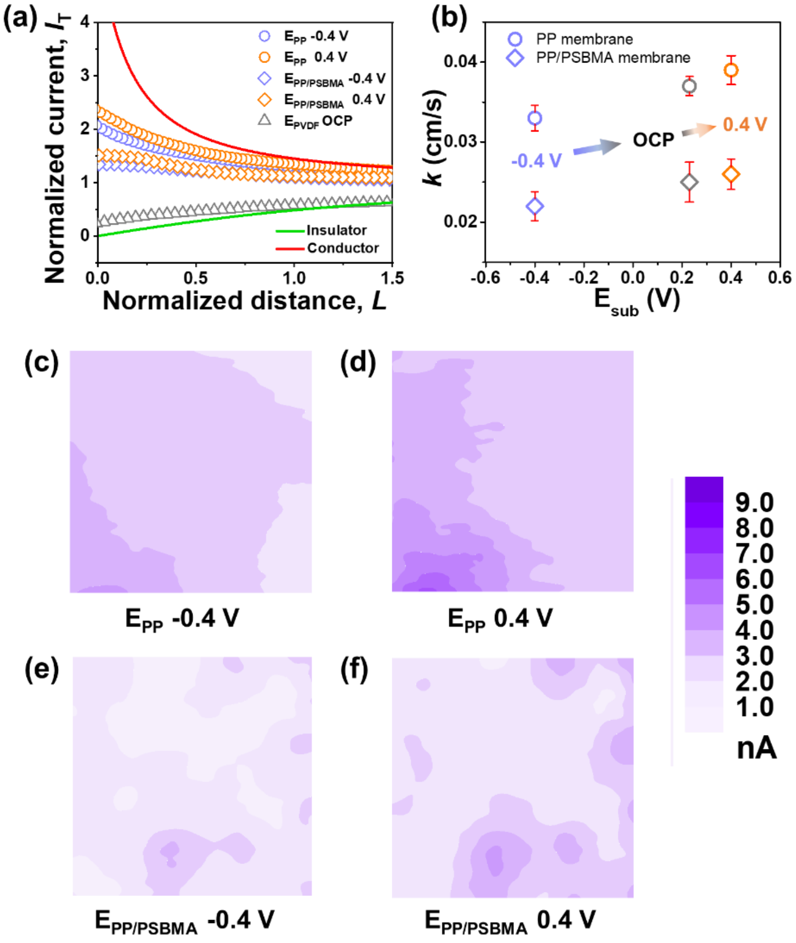

Fig. 5-4 (a) SECM tip approach curves measured in 1 mM FcMeOH and 0.1 M KCl on PVDF membrane, PP membrane and PP/PSBMA membrane. The SECM tip was biased at 0.5 V. The Red solid line and green solid line are the theoretical tip approach curves for the conductor and insulator, respectively. (b) Average k values for the corresponding tip approach curves in (a). SECM images of PP membrane and PP/PSBMA membrane at electrochemical potential of (c) (e) -0.4 V and (d) (f) 0.4 V in 1 mM FcMeOH and 0.1 M KCl solution with Pt tip biased at 0.5 V. Tip-substrate separation distance: 10 μm. Image size: 60 × 60 μm^2.

5.2.3. Underwater oil contact angle and surface potential measurements using EC-AFM

The wettability of the PFO droplets on the conductive PP coating at different electrochemical potentials was evaluated by measuring the underwater oil contact angle

(OCA) measurement in 10 mM NaCl solution. Fig. 5-5 a shows the underwater OCA on potentiostatically treated PP membrane surfaces. At open circuit potential (0.23 V), the PP membrane was naturally oleophobic with an underwater OCA of ~145°. As the applied potential increased to 0.4 V, the underwater OCA decreased to ∼133°. However, as the applied potential shifted to -0.4 V, the PP membrane surface turned slightly more oleophobic with underwater OCA increased to 157°, indicating the oil droplet was less likely to adhere to the membrane surface at a negative potential.

Then the surface potentials of the different membranes applied by various electrochemical potentials were measured through EC-AFM. After each electrochemical potential was applied on the membrane surface for 30 s, the AFM probe was immediately used to measure the surface forces. Then the surface forces between the AFM tip and membrane surfaces were further theoretically fitted based on the DLVO model, through which the surface charge of the membrane surfaces could be calculated. The interaction force profiles between silicon nitride AFM tip and PVDF membrane, PP membrane, and PP/PSBMA membrane potentiostatically treated at different electrochemical potentials in 10 mM NaCl are shown in Figs. 5-5 b-d, respectively. In our previous study, the silicon nitride cantilevers were verified to be hydrophilic with a water contact angle of less than 5° [36]. In this case, hydrophobic interaction between the AFM tip and membrane surfaces will not be counted. For the PVDF surface, the measured force curves (Fig. 5-5 b) at electrochemical potential ranging from -0.4 to 0.4 V almost overlap during approach (open symbols) due to the insulative property of the PVDF membrane, which indicates that the effect of the external electrochemical potential on interactions between silicon nitride tip and PVDF surface can be neglected. The Hamaker constant for Si_3N_4−water−PVDF was calculated as 1.0×10^{-20} J based on the reported Hamaker constant of Si_3N_4 [37] and refractive index and dielectric constant of PVDF membrane [38,39], and the surface potential of silicon nitride tip was reported to be -32 mV in 10 mM NaCl at pH 5.8 [40,41]. Analyzing the measured forces between the silicon nitride tip and PVDF surface based on the classical DLVO theory (red curve), the surface potential of PVDF membrane was fitted to be -12 mV at different electrochemical potentials, which agrees well with the previously reported surface potential value at pH 5.8 [42–44]. However, after modifying with PEDOT:PSS, the PP membrane exhibited conductive properties and the interaction force curves showed distinguishing trends at different electrochemical potentials. Fig. 5-5 c shows the interaction force curves between the silicon nitride tip and PP membrane surface potentiostatically treated at various electrochemical potentials ranging from -0.4 V to 0.4 V in 10 mM NaCl at pH 5.8. With the potential increasing from -0.4 V to OCP and finally reaching 0.4 V, the contribution of repulsive EDL interaction was decreased. The experimental data was theoretically analyzed based on the DLVO theory to calculate the surface potentials of PP membranes at different electrochemical potentials, as shown in the solid curves of Fig. 5-5 c. According to the previous studies, the Hamaker constant of PEDOT:PSS is variable at reduced and oxidized states since the dielectric constant of PEDOT:PSS is different upon redox switching. The Hamaker constant between PP membrane and silica nitride AFM tip at electrochemical potentials of -0.4 V, OCP and 0.4 V in NaCl solution was roughly calculated as 5.23×10^{-20} J, 5.23×10^{-20} J, and 5.22×10^{-20} J, respectively, using the Lifshitz theory and the reported dielectric constant and reflective index of PEDOT-PSS, silica nitride and water [45,46]. Fitting the measured force curves using the DLVO theory gives the surface potentials of PP membrane at electrochemical potentials of -0.4 V, OCP and 0.4 V in 10 mM NaCl as -57 mV, -38 mV, and -15 mV, respectively. For PP/PSBMA membrane, the Hamaker constant for Si_3N_4−water−PSBMA estimated from the reported dielectric constant and reflective index of PSBMA was 3.95 × 10^{-20} J [47,48]. However, the PP/PSBMA membrane still showed a conductive property due to the presence of PEDOT:PSS, which was verified by electrochemical measurements. In this case, the force curves of PP/PSBMA membrane showed different trends when applying various electrochemical potentials (Fig. 5-5 d). After theoretical calculation (solid curves in Fig. 5-5 d), the surface potentials of PP/PSBMA membrane at electrochemical potentials of -0.4 V, OCP and 0.4 V in 10 mM NaCl solution were fitted to be -40 mV, -28 mV and -8 mV, respectively.

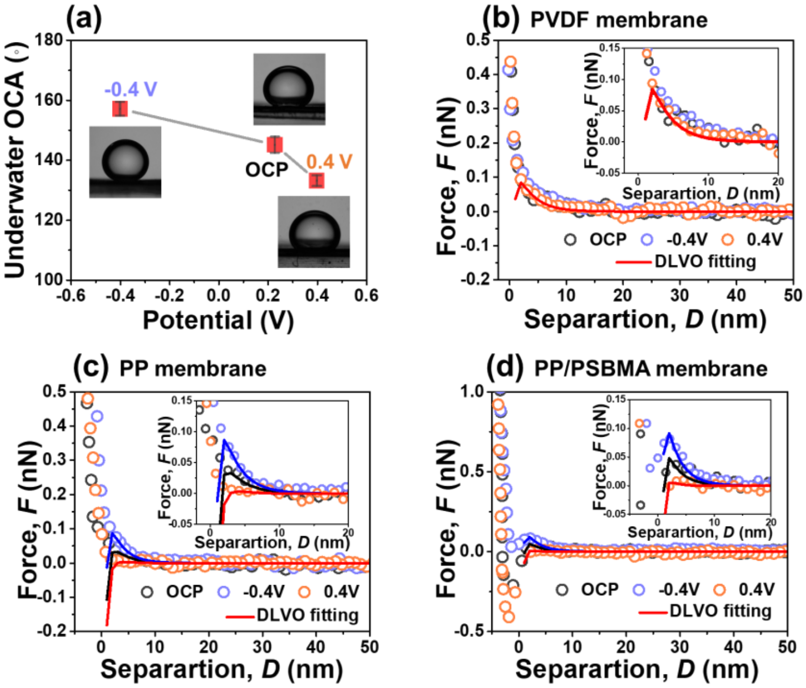

(e)

Surface potential	-0.4 V	OCP	0.4 V
PP membrane	-57 mV	-38 mV	-15 mV
PP/PSBMA membrane	-40 mV	-28 mV	-8 mV

Fig. 5-5 (a) Underwater oil contact angle (OCA) of PFO droplets on PP membrane surface as a function of electrochemical potential in 10 mM NaCl solution. Interaction force *F* between silicon nitride AFM tip and (b) PVDF membrane surface, (c) PP membrane surface and (d) PP/PSBMA membrane surface potentiostatically treated at electrochemical potentials of -0.4 V, OCP and 0.4 V in 10 mM NaCl as a function of separation distance *D*. The inset shows zoomed-in view at short separation. Experimental results are shown as open symbols, and DLVO calculations are shown as solid curves. (e) Summary of fitted PP membrane and PP/PSBMA membrane at different electrochemical potentials.

5.2.4. Force measurements between oil drop and different membrane surfaces via EC-AFM

Oil-in-water emulsions are a common type of mixture that needs to be separated and purified both in industrial and domestic water, and understanding the molecular interaction mechanisms of emulsion droplets with diverse membranes can help to evaluate and improve the separation efficiency and selectivity of the different membranes. Herein, PFO is used as a model oil to unveil the fouling behaviors and interaction mechanisms of different membranes in O/W emulsion systems. An oil probe EC-AFM technique, based on a system combining an Asylum Research MFP-3D AFM and an electrochemical workstation, was employed to measure the interaction forces between PFO droplets and different membranes in 10 mM NaCl solution at pH 5.8. Fig. 5-6 shows the schematic of EC-AFM controlling the interfacial electrochemical reaction and simultaneously probing the change of surface interaction forces between membrane surfaces and the oil droplet.

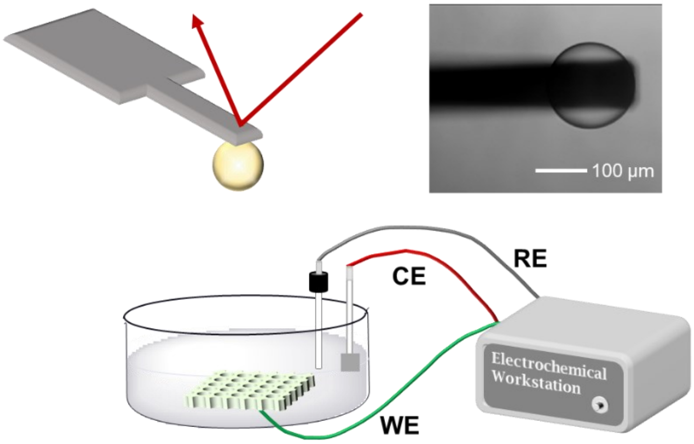

Fig. 5-6 Schematic of EC-AFM for the force measurements between oil droplets and membrane surfaces during a typical electrochemical AFM experiment using the drop probe AFM technique and inset shows the microscopic image of a typical drop probe.

For the PVDF membrane, only the interaction force at OCP (no electrochemical potential applied) was collected due to the insulating property. For the conductive PP membrane and PP/PSBMA membrane, the interaction forces at -0.4 V, OCP and 0.4 V were measured to probe the evolution of surface characteristics by controlling the interfacial chemical reactions. In these cases, after each electrochemical potential was applied on the membrane surface for 30 s, the oil AFM probe was immediately driven onto the membrane surfaces till a pre-set maximum loading force of 20 nN was applied. Fig. 5-7 a shows the interaction force profile between PFO droplet and PVDF membrane in a 10 mM NaCl solution. A jump-in behavior was observed during the approaching process of the oil probe, which could be fitted with the theoretical model based on the Reynolds lubrication equation and augmented Young−Laplace equation (SRYL model, the detailed information was clarified in Experimental). For this PFO-water-PVDF membrane system, the Hamaker constant was calculated to be 1.01×10^{-21} J using the combining relations of the Hamaker constants of the different materials involved. The surface potential of PFO in 1 mM NaCl at pH 5.8 was

-33 mV. The zeta potential of PVDF surface at pH 5.8 were fitted to be -12 ± 3 mV, which was in line with the surface potential of PVDF membrane calculated in Sec. 2.3. The decay length of hydrophobic interaction was determined to be $D_0 \sim 1.2$ nm during the PFO−PVDF interaction. Upon the oil probe retraction from the membrane, the oil droplet immediately detached from the AFM cantilever and attached to the membrane surface. The rigid adherence originated from the intermolecular interactions between the oil drop with the PVDF surface such as attractive VDW force and hydrophobic force, indicating the oil foulants on PVDF membrane were hardly removed and cleaned resulting in fouling issues.

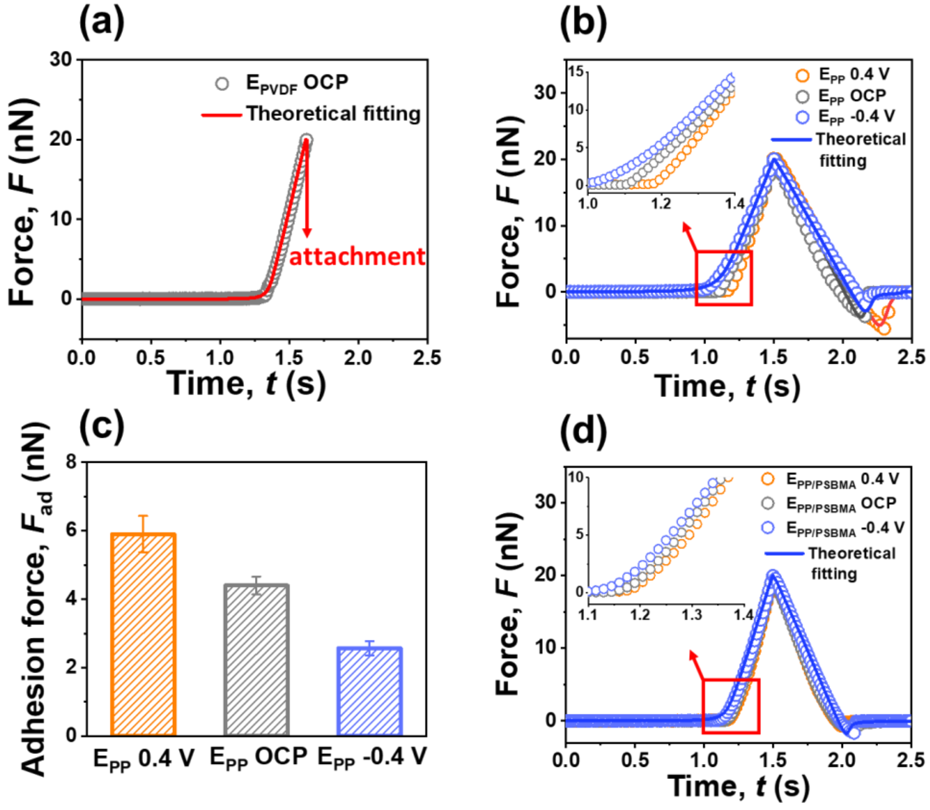

Fig. 5-7 (a) Experimentally measured interaction force profile (open symbols) and the theoretical fitting result (red solid curve) of a PFO droplet (radius R = 70 μm) and PVDF membrane at OCP in 10 mM NaCl at pH 5.8. (b) Experimentally measured interaction force profiles (open symbols) and the theoretical fitting results (solid curves) of a PFO droplet (radius R = 80 μm) and PP membrane at -0.4 V, OCP and 0.4 V in 10 mM NaCl at pH 5.8. The inset shows a zoomed-in view at a short separation. (c) Measured adhesion

F_{ad} between the PFO droplet and PP membrane potentiostatically treated at different electrochemical potentials. (d) Experimentally measured interaction force profiles (open symbols) and the theoretical fitting results (solid curves) of a PFO droplet (radius R = 65 μm) and PP/PSBMA membrane at -0.4 V, OCP and 0.4 V in 10 mM NaCl at pH 5.8. The inset shows a zoomed-in view at a short separation.

In contrast, only repulsive forces were detected in the approaching force curves of PP membrane at different electrochemical potentials, as shown in Fig. 5-7 b. The Hamaker constant for PFO−water−PP membrane system varies at diverse electrochemical potentials due to the variable dielectric constant of PEDOT:PSS upon redox switching. According to the reported dielectric constant and refractive index of PEDOT:PSS, the Hamaker constants at the electrochemical potential of 0.4 V, OCP, and -0.4 V were calculated to be -6.26×10^{-22} J, -6.06×10^{-22} J, and -5.58×10^{-22} J, respectively. It is noted that after modifying PVDF membrane with PEDOT:PSS polymers, the VDW interactions of PFO−water−PP membrane were repulsive. By fitting the measured force data (open symbols) using the SRYL model (solid curves), the surface potentials of PP membrane were determined as -55 ± 5 mV, -35 ± 3 mV, and -15 ± 3 mV, respectively, at electrochemical potentials of -0.4 V, OCP and 0.4 V in 10 mM NaCl at pH 5.8, which were in good agreement with that fitted in the previous section. For PP membrane, the decay length of hydrophobic force was determined to be 0.7 nm. Therefore, the short-range VDW repulsion, long-range EDL repulsion and hydrodynamic interaction competed with the weak hydrophobic attraction and dominated the behavior of PFO droplets during the approaching force measurement process. During the retraction process, jump-out behaviors were observed, which determined the adhesion force between PFO droplets and PP membranes at different electrochemical potentials. The average adhesion force was measured to be 2.57 ± 0.21 nN, 4.40 ± 0.26 nN and 5.90 ± 0.52 nN at electrochemical potentials of -0.4 V, OCP and 0.4 V, respectively, which showed an increase with the rise of applied electrochemical potentials. Therefore, the PFO droplets were less likely to adhere to the PP membrane under the assistance of negative electrochemical potential.

Fig. 5-7 d displays the interaction force results between PP/PSBMA membrane and oil droplets at electrochemical potentials of -0.4 V, OCP and 0.4 V in 10 mM NaCl at pH 5.8, respectively. PP/PSBMA membranes showed similar force-time profiles while interacting with oil droplets at various electrochemical potentials, where pure repulsion was discovered during the approach and no obvious adhesion was detected during the retraction of the oil droplet from the membrane surfaces. However, a more repulsive trend in the approaching force curves could be observed while a more negative electrochemical potential was applied. For the PSBMA−oil interactions, there is no hydrophobic force because of the hydrophilic nature of PSBMA. The theoretical Hamaker constant between PFO and PP/PSBMA membrane was calculated to be -1.00×10^{-21} J, indicating VDW force was repulsive. The theoretical fittings (solid curves in Fig. 5-7 d) show that the surface potentials of the PP/PSBMA membrane were -38 ± 5 mV, -25 ± 3 mV, and -10 ± 3 mV in 10 mM NaCl at electrochemical potentials of -0.4 V, OCP and 0.4 V, respectively, which are also consistent with the measured surface potential results in Fig. 5-5 d. Figs. 5-8 a−c show the disjoining pressure profiles due to the VDW, EDL and hydrodynamic interactions between PFO droplets and PP/PSBMA membrane surface at electrochemical potentials of 0.4 V, OCP and -0.4 V, respectively, during their approaching process. The theoretical results indicated that applying negative electrochemical potential on the conductive membrane surface led to more negative surface potential of the membrane surface, which was then attributed to the enhanced EDL repulsion between the PFO droplet and the PP/PSBMA membrane surface. Thus, the approaching behavior of PFO droplets was contributed by the synergistic effect of repulsive VDW, EDL and hydrodynamic interaction. Moreover, under the maximum load force applied (i.e., ~20 nN), a layer of water was confined between the oil drop and membrane surface, where thicker water film helped prevent the oil-surface attachment. As illustrated in Fig. 5-8 d−f, the minimum thickness h_{min} of the thin water film was determined to be 14.1 nm, 14.9 nm and 17.2 nm for the PP/PSBMA membrane at the electrochemical potential of 0.4 V, OCP and -0.4 V, respectively. Meanwhile, when the PFO droplets were retracted from the membrane surface, no attachment behavior of oil droplets interacting with PP/PSBMA membrane was observed (only a slight hydrodynamic suction), which demonstrated that the oil droplets on PP/PSBMA membrane surface could be easily removed. Therefore, the modification of zwitterionic polymers endowed the conductive membrane with excellent antifouling properties to the oil-in-water emulsions for the following reasons. First, the conductive membrane surface turned from neutrally charged to negatively charged by applying negative electrochemical potential, resulting in oil droplet−membrane surface interactions becoming more repulsive due to the enhanced EDL repulsion during the approaching process. Second, the presence of zwitterionic polymers tuned the wettability of the membrane surface and eliminated the attractive hydrophobic interaction. Moreover, the superhydrophilic PSBMA polymers attracted a dense water layer, which effectively prevented contact between the oil droplet and the membrane surface.

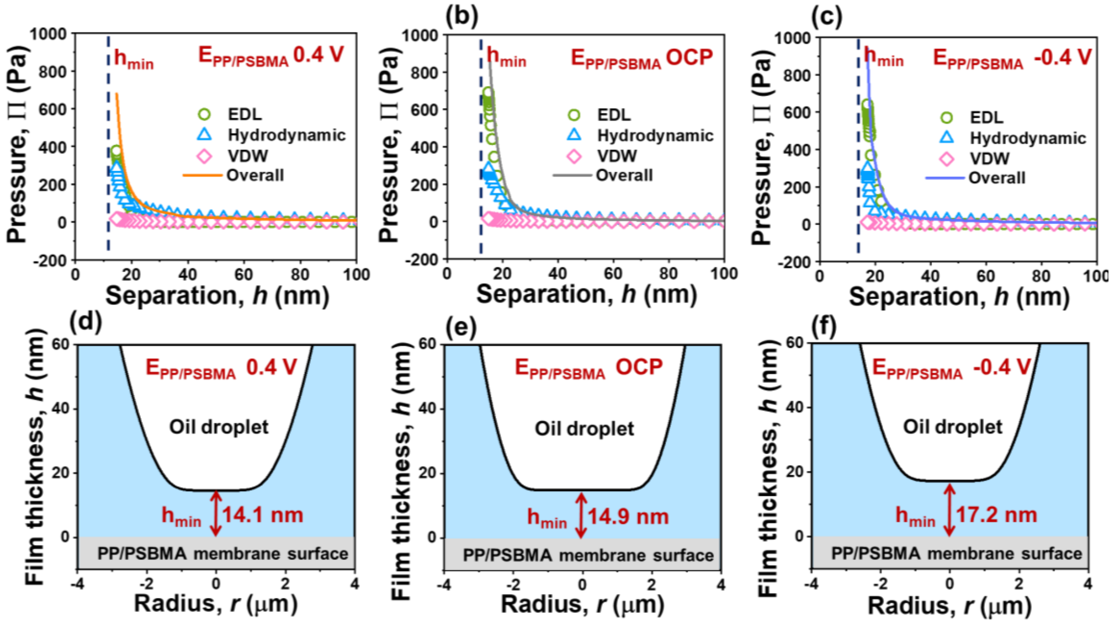

Fig. 5-8 Calculated profiles of VDW disjoining pressure, EDL disjoining pressure, hydrophobic pressure, and hydrodynamic pressures between a PFO droplet interacting with (a) PP/PSBMA membrane surface at 0.4 V, (b) PP/PSBMA membrane surface at OCP, and (c) PP/PSBMA membrane surface at -0.4 V at the central position of the droplet in 10 mM NaCl solution, respectively. The calculated drop profile at maximum force load during the approach process where a layer of water with minimum thickness h_{min} (at central point) confined between the oil droplet and (d) PP/PSBMA membrane surface at 0.4 V, (e) PP/PSBMA membrane surface at OCP, and (f) PP/PSBMA membrane surface at -0.4 V at the central position of the droplet in 10 mM NaCl solution, respectively.

5.2.5. Oil/water separation and antifouling performance of PP membrane and PP/PSBMA membrane under electrochemical assistance

Based on the force measurement results, the conductive PP membrane and PP/PSBMA membrane showed strong repulsive electrical double-layer force against the oil droplet at an electrochemical potential of -0.4 V. Herein, the oil/water separation performance and the fouling resistance of the conductive PP membrane and PP/PSBMA membrane under electrochemical assistance were investigated by PFO−in−10 mM NaCl solution emulsion. Fig. 5-9 a illustrates the schematic of the vacuum filtration setup for oil/water separation with a piece of PP or PP/PSBMA membrane placed at the filter holder and connected with an electrochemical workstation as the working electrode, and the reference electrode and counter electrode were immersed in the feed water. The effective separation area of the membrane is 6.15 cm^2 and the pressure difference between ambient and evacuation pressure is 0.07 MPa.

The O/W separation performance and antifouling property of membranes can be evaluated by the normalized flux, flux recovery ratio, and oil removal efficiency. These parameters are calculated based on the water flux of the original membrane, the water flux of the feed solution, the water flux of the cleaned membrane after the filtration process and the TOC value of the filtrate, which were demonstrated in the experimental section. Fig. 5-9 b shows the water flux decline results of the PVDF membrane without electrochemical assistant, PP membrane and PP/PSBMA membrane at both OCP and electrochemical potential of -0.4 V for the oil/water separation, respectively. PVDF membrane showed the most significant water flux decline behavior among the three membranes, and the permeation flux of PVDF membrane significantly decreased to 54% of the original water flux of the membrane. The dramatic decline of the water flux suggested that the oil droplet adhered to the PVDF surface and blocked the membrane pores, thus seriously affecting the O/W emulsion separation efficiency. PVDF membrane had the most significant fouling potential and membrane in the whole filtration process. After modifying PEDOT:PSS, the NF of PP membrane at OCP was calculated to be 55%, which maintained a similar value as that of PVDF membrane. However, the NF of PP membrane potentiostatically treated at electrochemical potentials of -0.4 V increased to 61%, implying the amount of oil droplets attached to the PP membrane significantly decreased under the electrochemical assistant.

The NF of the O/W emulsion in the PP/PSBMA membrane at OCP was found to be 62%, which is in line with the low fouling tendency of PP/PSBMA membrane due to the superhydrophilicity of the zwitterionic PSBMA polymer. This result underscored the effectiveness of PSBMA modification in reducing fouling and enhancing the performance of original membranes. Moreover, by applying an electrochemical potential of -0.4 V, the permeation flux of PP/PSBMA membrane only decreased to 79% of that at the initial, displaying excellent emulsion separation and antifouling performance. Then, the concentration of oil in both O/W emulsion and filtrate was analyzed by TOC measurement, through which the oil removal efficiencies of different membranes could be determined. As shown in Fig. 5-9 c, the oil removal efficiency of diverse membranes followed this trend: E_{PVDF} OCP (98.5%) < E_{PP} OCP (98.9%) < $E_{\mathrm{PP/PSBMA}}$ OCP (99.1%) < E_{PP} -0.4 V (99.9%) ≈ $E_{\mathrm{PP/PSBMA}}$ -0.4 V (99.9%). The calculated oil removal efficiencies in both electrochemically assisted PP membrane and PP/PSBMA membrane were exceptionally high, implying that the PFO-in-water emulsions are successfully separated with the assistance of electrochemical processes.

After 5 min of washing with deionized water to remove the absorbed oil droplets on the membrane surface and pores, the water flux recovery ratio of membranes was calculated to monitor the fouling resistance and self-cleaning property. As shown in Fig. 5-9 c, the water flux of the PVDF membrane and PP membrane at OCP was only restored to 58% and 60%, and this severe reduction in the water flux related to the high irreversible fouling caused by oil droplets. FRR of PP membrane potentiostatically treated at electrochemical potential of -0.4 V was elevated up to 72%. Especially, PP/PSBMA membrane possessed a high FRR of 80% compared with the other two types of membranes even without the support of electrochemical potential. After applying an external electrochemical potential, PP/PSBMA membrane not only displayed a substantial superiority in separation efficiency but also showed a significant enhancement of the antifouling performance with the FRR of 89%. There were two dominant factors responsible for the excellent O/W emulsion separation performance and fouling resistance for PP/PSBMA membrane under electrochemical assistance. One was the hydration layer attributed to the strong water affinity charged groups on zwitterionic polymers, creating a repulsive force that inhibits the adhesion of oil droplets to the membrane surface. Another factor was the accumulated negative charges on membrane surfaces originating from the external electrochemical potential, which prevented the adherence and adsorption of negatively charged oil droplets through EDL repulsion interaction.

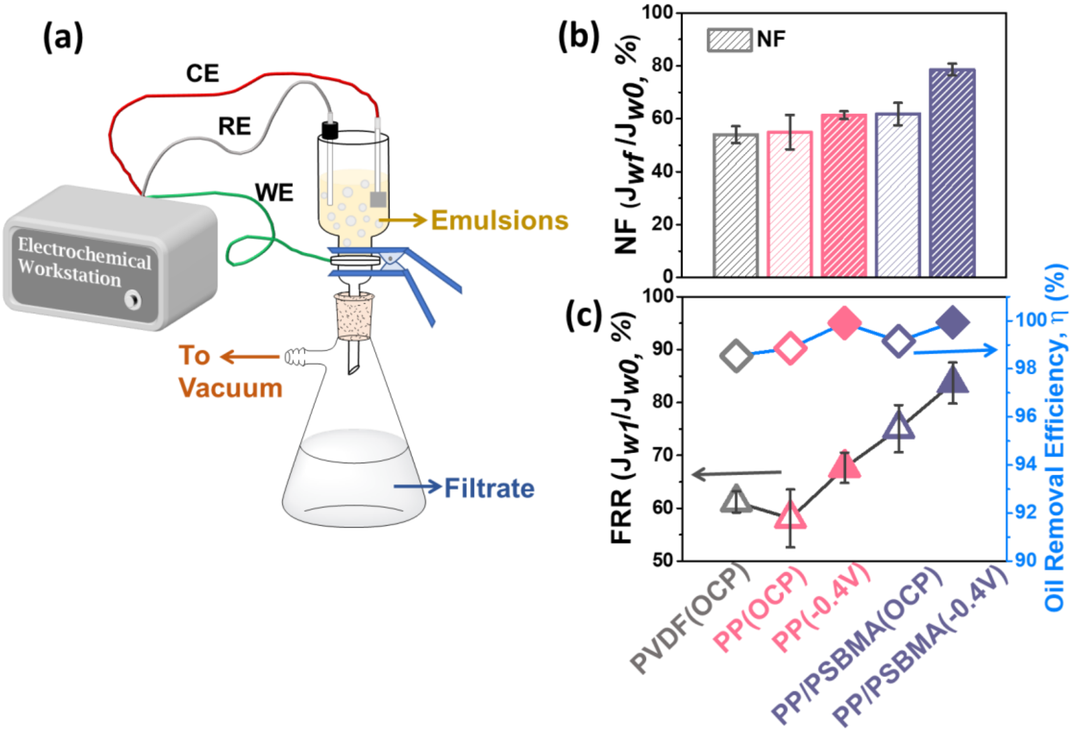

Fig. 5-9 (a) Schematic of the vacuum filtration setup combined with the electrochemical system, where PP and PP/PSBMA membranes were working electrodes, and the reference electrode (Ag/AgCl) and counter electrode (Pt) were immersed in the feed water. (b) Normalized flux and (c) flux recovery ratio and oil removal efficiency of PVDF membrane, PP membrane and PP/PSBMA membrane at different electrochemical potentials.

5.3. Experimental Section

5.3.1. Chemicals

Polyvinylidene fluoride (PVDF) powder (M_w ~534000) and N,N-Dimethylformamide (DMF) (assay GC area > 99%) were purchased from Sigma-Aldrich, Canada. Dopamine hydrochloride, 30% hydrogen peroxide (H_2O_2), poly(2,3-dihydrothieno-1,4-dioxin)-poly(styrenesulfonate), (PEDOT:PSS), [2-(methacryloyloxy)ethyl]dimethyl-(3-sulfopropyl) ammonium hydroxide (SBMA), sodium bisulfite ($NaHSO_3$), perfluorooctane (PFO) and ferrocenemethanol (FcMeOH) were obtained by Sigma-Aldrich, Canada. Lithium chloride (LiCl), sodium chloride (NaCl), potassium chloride (KCl), ammonium persulfate (APS) and tris(hydroxymethyl)aminomethane (Tris) were supplied by Fisher Chemical, Canada.

5.3.2. Polymerization of PSBMA polymer

PSBMA polymer was synthesized through $(NH_4)_2S_2O_8$ (APS)-$NaHSO_3$ redox initiation system using the conventional free radical polymerization method. 5.59 g SBMA monomer was dissolved in 25 mL deionized (DI) water (800 mM) in a 50 mL round-bottomed flask. 228 mg APS as initiator was slowly added into the flask (40 mM). The solution was then placed into a 45 °C water bath with continuous mechanical stirring until the solid ingredients were dissolved entirely under a nitrogen atmosphere. After 104 mg $NaHSO_3$

was added to the solution dropwise (40 mM), the polymerization process was carried out under a nitrogen atmosphere for 24 h at 45 °C with vigorous stirring.

5.3.3. Preparation of different membrane

Hydrophobic PVDF membranes were prepared via an immersed phase inversion method. 8 g PVDF powder (M_w ~534000) and 4 g LiCl were dissolved in 63 g DMF by vigorous stirring at 60 °C for 30 min until a homogenous polymer solution was obtained. After degassing for 16 h in a vacuum oven, the polymer solution was cast on a glass plate using a 200 μm casting knife. After that, the glass plate was immediately immersed in a coagulation bath of DI water to allow the PVDF membrane to peel off. The nascent membranes were then rinsed with DI water to remove the residual solvent.

To prepare of PVDF-PDA-PEDOT:PSS membrane (PP membrane), the as-prepared PVDF membranes were washed with ethanol and DI water to remove the adsorbed impurities. 2 mg mL^{-1} dopamine hydrochloride was dissolved in 10 mM Tris buffer (pH 8.5) to prepare PDA coating solution. The cleaned PVDF membranes were immersed into the coating solution with constant stirring at room temperature. After 30 min, a PDA layer was uniformly coated on the PVDF membrane surface. Subsequently, the PDA-coated PVDF membranes were submerged in PEDOT:PSS solution (1.1% in H_2O) for 24 h, which were thoroughly washed by ethanol/DI water alternatively three times. As a convenience, the PVDF-PDA-PEDOT:PSS membrane was named as PP membrane.

As for the preparation of PVDF-PDA-PEDOT:PSS/PSBMA membrane (PP/PSBMA membrane), the nascent PVDF membranes were firstly modified with a PDA layer as described above. The prepared PSBMA polymer solution was diluted four times with DI water, and PEDOT:PSS (1.1%) was added to the solution to obtain a co-deposition coating solution. Then the PDA-coated PVDF membranes were immersed in the mixed solution for 24 h and washed with ethanol and DI water before use. The modified PVDF-PDA-PEDOT:PSS/PSBMA membrane was named as PP/PSBMA membrane.

5.3.4. Membrane surface characterization

The surface morphology and the element distribution of as-fabricated PVDF membrane, PP membrane, and PP/PSBMA membrane were characterized by a field-emission scanning electron microscope (SEM) (Zeiss Sigma 300 VP-FESEM, Germany) with energy-dispersive X-ray spectroscopy (EDS) at the electron acceleration voltage of 10.2 keV. The surface roughness of the three types of membrane surfaces was characterized by imaging using a Bruker Icon AFM (Bruker, Santa Barbara, USA) using the PeakForce Quantitative Nano-Mechanics (PF-QNM) model. The chemical functional groups of the coating materials on the PVDF membrane were identified by applying a proprietary technique based on optical photothermal IR (O-PTIR) spectroscopy (Mirage, Santa Barbara, USA). The wetting property of the PDA-PAA-PMTAC coating was evaluated via the water contact angle (WCA) as well as underwater oil contact angle (OCA) measurements of PFO droplets in 10 mM NaCl aqueous solution using contact angle goniometer (Ram´e-Hart instrument, NJ).

The membrane porosity (ε) of the prepared PVDF membrane was calculated by the wet weight and dry weight of PVDF membranes. The prepared membrane was firstly weighed after mopping water on the membrane surface, which was then placed in an oven at 40 °C overnight before measuring the dry weight. Porosity was calculated using Equation (2):

$$\varepsilon = \frac{w_1 - w_2}{A \times l \times d_w} \times 100\% \tag{2}$$

Where w_1 (g) is the wet weight and w_2 (g) is the dry weight of the calculated membrane. A (m^2) is the effective membrane area, l (m) is the thickness of the membrane, and d_w (9.98×10^5 g m^{-3}) is the water density. Moreover, the membrane mean pore radius (r_m) could be determined using the Guerout-Elford-Ferry equation (Equation (3)):

$$r_m = \sqrt{\frac{(2.9-1.75\varepsilon)\times 8\mu l Q}{\varepsilon\times A\times TMP}} \tag{3}$$

Where μ is water viscosity (8.9×10^{-4} Pa·s), Q (m^3 s^{-1}) is the volume of the permeate pure water per unit time, and TMP is the operation pressure (7×10^5 Pa).

5.3.5. SECM measurements

The SECM experiments were conducted on a CHI920C electrochemical workstation equipped with a scanning electrochemical microscope (CH Instruments, TX, US). The membrane electrode was mounted at the bottom of the SECM cell with an exposed surface area of ~0.28 cm^2. The reference electrode was an Ag/AgCl (1 M KCl) electrode, and the counter electrode was a Pt wire. In SECM experiments, a Pt ultramicroelectrode with a radius (a) of 5 μm and an RG (RG = r_g/a; r_g is the radius of glass sheath) of 10 was used as an SECM tip. The Pt tip was polished on a micro polishing cloth with 0.05 μm alumina powder suspension, sonicated in Milli-Q water, and thoroughly rinsed with Milli-Q water before use. First, the Pt tip was brought close to the membrane substrate in 1 mM FcMeOH and 0.1 M KCl solution. A tip approach curve was recorded, through which the tip-substrate distance d was then determined. During the approach, the Pt tip was biased at 0.5 V to ensure a diffusion-controlled electro-oxidation of FcMeOH, and the tip current was influenced by the apparent rate constant k of the regeneration reaction of FcMeOH on the substrate. The theoretical details of the tip approach curves have been clarified in our previous works [49–51]. Then, the Pt tip was kept to a desired distance from the substrate (In this work, the Pt tip was positioned 10 μm above the substrate surface to maintain high ion collection efficiency), and the polarization of the membrane electrode was carried out under various potentials, and the dissolved ions were collected by the Pt tip. Subsequently, the Pt tip was driven to scan across the substrate to acquire SECM images in a 200 × 200 μm^2 region; as such, the SECM experiments were conducted, and the SECM images were collected in the substrate generation-tip collection (SG-TC) mode. In the electrochemical experiments, all potentials quoted were referred to the reference electrode unless otherwise specified.

5.3.6. Force measurement using electrochemical atomic force microscope (EC-AFM) with drop probe technique

The interaction forces between PFO droplets and PVDF membrane, PP membrane, and PP/PSBMA membrane surfaces at different electrochemical potentials in 10 mM NaCl solution were directly measured by the AFM drop probe technique using an EC-AFM (Asylum Research, Santa Barbara, CA, USA). The basic working principle of EC-AFM is similar to that of AFM, while EC-AFM requires an electrochemical cell accommodating the working electrode (conductive membrane surface), counter electrode (Pt wire), and reference electrode (Ag/AgCl electrode). At the beginning of the experiment, the drop probe was prepared as follows. Oil droplets were generated by introducing PFO droplets on the glass substrate of the AFM fluid cell that was previously filled with 10 mM NaCl solution through a custom-made ultrasharp glass pipet. Then, one of the oil droplets with a suitable size (radius ~50–100 μm) was carefully picked up by the AFM tipless rectangular cantilever with a circular gold patch on end (Bruker, Santa Barbara, CA), which was hydrophobized by immersion in 10 mM dodecane thiol in ethanol solution overnight. After that, the drop probe was moved and located over the membrane surfaces in the fluid cell for force measurements. Before force measurement, the spring constant of the probe was calibrated to be ~400 pN nm^{-1} using the Hutter and Bechhoefer thermal tune method. During the experiment, after each electrochemical potential was applied on the membrane surface for 60 s, the drop probe was immediately driven to approach the membrane substrate at a velocity of 1 μm s^{-1} until a pre-set deflection was detected and then retracted from the surface. The interaction force was further converted based on the spring constant and the deflection of the cantilever by Hooke's Law.

5.3.7. Theoretical analysis of force profiles

A theoretical model based on the combination of Reynolds lubrication theory and augmented Young−Laplace equation (SRYL) was applied to analyze the measured force profiles between the membrane surfaces and PFO droplets in aqueous solutions [52–54]. During the AFM force measurement, the approach of the oil AFM probe towards the substrate could generate hydrodynamic interaction, which is attributed to the flow of the confined fluid (i.e., 10 mM NaCl solution) between the oil drop and the membrane surface. The hydrodynamic drainage behavior of confined water film between the oil drop and the flat surface (oil-water-surface system) could be described by the Reynolds lubrication theory (Equation (4)) [55–58]:

$$\frac{\partial h}{\partial t} = \frac{\partial}{12\mu r \partial r}\left(r h^3 \frac{\partial p}{\partial r}\right) \tag{4}$$

where h is the thickness of the water film confined between the oil drop and the flat surface, t is the time, μ is the viscosity of the NaCl solutions, r is the radical coordinate of the oil drop, and p is the excess hydrodynamic pressure. Moreover, the augmented Young-Laplace equation is used to describe the deformation of the oil drop surface caused by the external pressure, including hydrodynamic pressure and disjoining pressure, as shown in Equation (5) [57]:

$$\frac{\gamma}{r}\frac{\partial}{\partial r}\left(r\frac{\partial h}{\partial r}\right) = \frac{2\gamma}{R} - p - \prod \tag{5}$$

where γ is the oil/water interfacial tension at the equilibrium state, R is the radius of the oil droplet, p and $\prod$ are the hydrodynamic and disjoining pressure, respectively. The disjoining pressure $\prod$ generally arises from various intermolecular forces involving the van der Waals (VDW) interaction, electrical double layer (EDL) interaction and hydrophobic (HB) interaction between oil droplet and solid surface, given by Equation (6)–(10), respectively [59]:

$$\prod = \prod_{VDW} + \prod_{EDL} + \prod_{HB} + \cdots \tag{6}$$

$$\prod_{VDW} = -\frac{A_H}{6\pi h^3} \tag{7}$$

$$\prod_{EDL} = \frac{2\varepsilon\varepsilon_0\kappa^2\left[\left(e^{\kappa D}+e^{-\kappa D}\right)\Psi_{oil}\Psi_{surface}-\left(\Psi_{oil}^2+\Psi_{surface}^2\right)\right]}{\left(e^{\kappa D}+e^{-\kappa D}\right)^2} \tag{8}$$

$$\prod_{HB} = -\frac{C_0}{2\pi D_0}exp\left(-\frac{h(r,t)}{D_0}\right) \tag{9}$$

$$C = 2\pi\gamma(1 - cos\,\theta) \tag{10}$$

where $\prod_{VDW}$, $\prod_{EDL}$ and $\prod_{HB}$ are the disjoining pressure components due to the VDW, EDL and hydrophobic interactions, respectively. A_H is the Hamaker constant between the oil drop and substrate surface in NaCl solution; κ is the inverse of the Debye length, ε_0 is the vacuum permittivity, ε is the dielectric constant of the aqueous solution, Ψ_{oil} and $\Psi_{surface}$ are the surface potential of the oil drop and membrane surface, respectively. The inverse of the Debye length could be calculated by Equation (11):

$$\kappa = \sqrt{\frac{\sum \rho_0 e^2}{\varepsilon\varepsilon_0 k_B T}} \tag{11}$$

Here ρ_0 is the number density of ions in NaCl solution, e is the elementary electric charge, T is temperature, and k_B is the Boltzmann constant. D_0 is the decay length of the hydrophobic interaction, and C is a constant (N/m) related to the static water contact angle θ on the substrate.

The overall interaction force F(t) can be determined by the integration of the hydrodynamic pressure p and the disjoining pressure $\prod$ according to the Derjaguin approximation:

$$F(t) = 2\pi \int_0^\infty [p(r,t) + \prod(r,t)] r dr \tag{12}$$

5.3.8. Filtration and antifouling performance assessment

The PVDF membrane, PP membrane, and PP/PSBMA membrane were applied in the separation performance and antifouling behavior characterization of oil-in-water (O/W) emulsions. During the filtration test, the membrane surfaces were connected to the CHI920C electrochemical workstation (CH Instruments, TX, US) as working electrodes, and a Pt wire and an Ag/AgCl electrode were also inserted in the electrochemical cell as the counter electrode and reference electrode. The O/W emulsion containing 1% (V/V) PFO-in-10 mM NaCl solution was obtained by a homogenizer (IKA T-18 Ultra Turrax, Germany) at 12, 000 rpm for 10 min and used as the model emulsion solution for O/W filtration experiment. In the separation experiment, the membrane was placed in a dead-end membrane filtration setup connected to a pressure pump at 0.7 bar, and a certain electrochemical potential was applied on the membrane surface during the process. The water flux was measured by prewetting the membrane surface with 10 mM NaCl solution. After filtering the O/W emulsion, the membranes were washed with DI water for 5 minutes to remove absorbed oil droplets from the membrane surface, and the water flux was measured by 10 mM NaCl solution once again to analyze the antifouling properties. The flux J was calculated according to Equation (13),

$$J_{w0} = \frac{V}{A \cdot t \cdot \Delta P} \tag{13}$$

where J_{w0} is water flux (L m^{-2} h^{-1} bar^{-1}), V is the volume of the permeation water (L), A is the effective separation area of the membrane (m^2), and t is the filtration time (h), ΔP is the pressure difference between ambient and evacuation pressure (bar).

The membrane antifouling performance was evaluated using the normalized flux (NF) (Equation (14)) and flux recovery ratio (FRR) (Equation (15)),

$$NF = \frac{J_{O/W}}{J_{w0}} \tag{14}$$

$$FRR = \frac{J_{w1}}{J_{w0}} \tag{15}$$

where J_{w0} is water flux, $J_{O/W}$ is the water flux of O/W emulsion, and J_{w1} is the re-measured pure water flux after washing the membranes.

The filtrates were collected and then the total organic carbon (TOC) analysis (SHIMADZU ASIL, Japan) was conducted to calculate the oil separation efficiency (η) based on the initial (C_i) and final (C_f) oil content according to Equation (16):

$$\eta(\%) = \left(1 - \frac{C_f}{C_i}\right) \times 100 \tag{16}$$

5.4. Conclusions

In this work, a facile PDA-PEDOT:PSS-PSBMA coating was successfully applied to the PVDF membrane for O/W emulsion separation. The prepared PP/PSBMA membrane demonstrated conductivity and superhydrophilicity, significantly enhancing both O/W emulsion separation efficiency and antifouling performance via a tunable surface force-based strategy. EC-AFM technique monitored the surface charges of PP membrane and

PP/PSBMA membrane at different electrochemical potentials, which were found to be varied with the external electrochemical potentials due to the conductivity of PEDOT:PSS polymer. Nanomechanical mechanisms behind the antifouling behavior of membranes were further explored under different electrochemical potentials using the drop probe EC-AFM technique. A negative potential applied to the membranes induced strong negative surface charges, increasing EDL repulsion and preventing oil droplet attachment. Additionally, the modification of PSBMA polymer coating endowed the membrane with superhydrophilicity and eliminated the hydrophobic attraction between oil and membrane surfaces, contributing to excellent antifouling performance. Oil/water separation tests demonstrated that water permeability was influenced by surface chemistry and electrochemical potentials. With EDL repulsion at a negative potential (-0.4 V), both the PP and PP/PSBMA membranes exhibited strong fouling resistance, minimal flux decline, and separation efficiency exceeding 99.9%. The zwitterionic PSBMA coating also enabled easy regeneration of the membrane through immersion in 10 mM NaCl, reducing irreversible fouling and improving reusability. This study highlights EC-AFM as a valuable tool for probing interfacial properties and surface interaction mechanisms in conductive membranes under electrochemically assistance, providing insights for designing conductive and regenerable membranes with tunable surface interactions for water treatment.

5.5. Supporting Information

5.5.1. Differential capacitance/potential curves

The linear sweep voltammetry (LSV) method was used to obtain these curves by measuring the response of the material-electrolyte interface to a linearly varying potential. A 10 mL glass flat-bottomed electrochemical cell with appropriate access ports was used for the experiment. The prepared membrane surfaces with an exposed geometric surface area of ~1 cm^2 were attached to the bottom of the electrochemical cell, and a section of copper wire electrically contacting the membrane surface was inserted through the access port of the cell, making the membrane surfaces the working electrodes. An Ag/AgCl (1 M KCl) electrode (0.222 V vs. standard hydrogen electrode) was used as the reference electrode, and a platinum wire was utilized as the counter electrode. A sufficient 10 mM NaCl electrolyte was then added to the cell to immerse the electrodes. The SPECS experiments were conducted on a CHI920C electrochemical workstation (CH Instruments, TX, US). The potential window used for this system was -0.2 V to 1.0 V versus Ag/AgCl electrode. Starting at -0.2 V, a potential step of +0.1 V was applied to the working electrode and held for 60 s (T) while the electrode equilibrated. During each rest period, the current of the electrodes (I) as a function of time was recorded. This step process was repeated until the working electrode potential had reached the maximum potential of 1.0 V. The differential capacitance and differential potential curves can be obtained by calculating the differential capacitance ($I \times T$) and differential potential from the measured current and potential values, respectively.

5.5.2. Theoretical calculation of SECM tip approach curves

The tip current at an infinite tip-substrate separation is expressed as Equation (17) [60, 61]

$$I_{tip,\infty} = 4nFDaC^0 \tag{17}$$

where n is the number of transferred electrons, F is the Faraday constant, D is the diffusion coefficient, a is the tip radius, and C^0 is the bulk concentration of reactant. When the tip approaches the substrate, the normalized tip current $I_{\mathrm{T}}=I_{\mathrm{tip}}/I_{\mathrm{tip},\infty}$ is described as [60]

$$I_T = I_{\mathrm{S}}\left(1 - \frac{I_{\mathrm{T}}^{\mathrm{ins}}}{I_{\mathrm{T}}^{c}}\right) + I_{\mathrm{T}}^{\mathrm{ins}} \tag{18}$$

$$I_{\mathrm{T}}^{\mathrm{ins}} = \frac{1}{0.15+\frac{1.5358}{L}+0.58\exp\left(\frac{-1.14}{L}\right)+0.0908\exp\left(\frac{L-6.3}{1.017L}\right)} \tag{19}$$

$$I_{\mathrm{T}}^{c} = \frac{0.78377}{L} + 0.3315\exp\left(\frac{-1.0672}{L}\right) + 0.68 \tag{20}$$

$$I_{\mathrm{S}} = \frac{0.78377}{L+\frac{1}{\kappa}} + \frac{0.68+0.3315\exp\left(\frac{-1.0672}{L}\right)}{1+F(L,\kappa)} \tag{21}$$

$$F(L,\kappa) = \frac{\left(\frac{11}{\kappa L}\right)+7.3}{110-40L} \tag{22}$$

$$\kappa = ka/D \tag{23}$$

where I_{S} is the normalized substrate current, $I_{\mathrm{T}}^{\mathrm{ins}}$ is the normalized tip current for the insulator, and $I_{\mathrm{T}}^{\mathrm{c}}$ is the normalized tip current diffusion-controlled regeneration of a redox mediator. The Equation 18-23 are valid in the range of $0.1 \leq L \leq 1.5$ and $0.01 \leq \kappa \leq 1000$. The diffusion coefficient of FcMeOH is 7.46×10^{-6} cm^{2} s^{-1}[62]. As $k=\kappa D/a$, the above theoretical model is valid in the range of 1.492×10^{-4} cm s^{-1}$\leq k \leq$14.92 cm s^{-1}.

5.5.3. Electrochemical reaction of PEDOT:PSS at different potentials

The conductivity of PEDOT:PSS is mainly determined by the oxidation state of the PEDOT component, which can be controlled by adjusting the electrochemical potential. The conductive PEDOT:PSS polymer intrinsically in a doped or oxidized state turn electrically insulating when being reduced by applying negative potentials, as shown in this electrochemical reaction:

$$EDOT_n^{+} \cdot SS^{-} + e^{-} + C^{+} \rightarrow EDOT_n^{0} \cdot SS^{-} \cdot C^{+}$$

(doped or oxidized state)   (dedoped or reduced state)

At 0.4 V, PEDOT:PSS was more oxidized, which generally resulted in higher *k* value, meaning electron transfer behaviors were easier at the surface. At -0.4 V, the *k* slightly decreased as PEDOT:PSS was tuning into the reduced state, which typically led to lower conductivity compared to its oxidized state[63, 64].

.

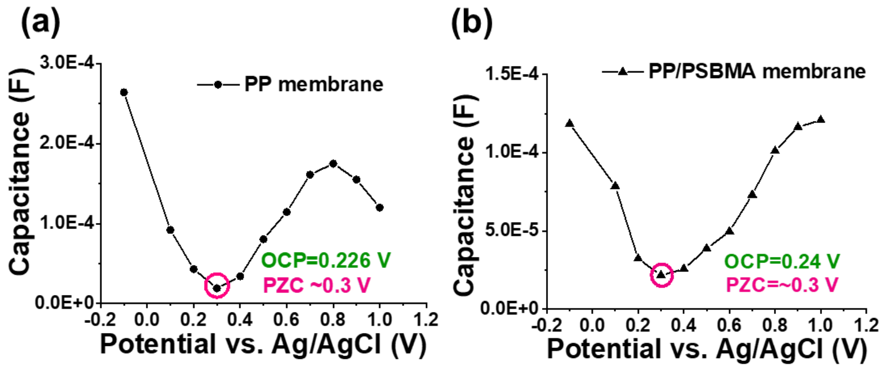

Fig. 5-10 Differential capacitance/potential curves of (a) PP membrane and (b) PP/PSBMA membrane. The OCP and PZC of different membranes are indicated.

References

[1] Y. Hu, M. Yue, F. Yuan, L. Yang, C. Chen, D. Sun, J Memb Sci 2021, 621, 118982.

[2] G. Kong, L. Fan, L. Zhao, Y. Feng, X. Cui, J. Pang, H. Guo, H. Sun, Z. Kang, D. Sun, J Memb Sci 2021, 622, 119045.

[3] E. Velayi, R. Norouzbeigi, Surf Coat Technol 2020, 385, 125394.

[4] K. K. Laali, W. J. Greves, S. J. Correa-Smits, A. T. Zwarycz, S. D. Bunge, G. L. Borosky, A. Manna, A. Paulus, A. Chanan-Khan, J Fluor Chem 2018, 206, 82.

[5] R. K. Gupta, G. J. Dunderdale, M. W. England, A. Hozumi, J Mater Chem A Mater 2017, 5, 16025.

[6] L. Yu, M. Han, F. He, Ara J Chem 2017, 10, S1913.

[7] M. B. Tanis-Kanbur, S. Velioğlu, H. J. Tanudjaja, X. Hu, J. W. Chew, J Memb Sci 2018, 566, 140.

[8] G. Kwon, A. K. Kota, Y. Li, A. Sohani, J. M. Mabry, A. Tuteja, Adv Mat 2012, 24, 3666.

[9] W. Chen, Z. Gu, G. Ran, Q. Li, Waste Manag 2021, 121, 127.

[10] K. Kimura, N. Yamato, H. Yamamura, Y. Watanabe, Environ Sci Technol 2005, 39, 6293.

[11] L. Liu, J. Liu, B. Gao, F. Yang, Sep Purif Technol 2012, 86, 106.

[12] S. Putatunda, S. Bhattacharya, D. Sen, C. Bhattacharjee, International journal of environmental science and technology 2019, 16, 2525.

[13] X. Fan, H. Zhao, Y. Liu, X. Quan, H. Yu, S. Chen, Environ Sci Technol 2015, 49, 2293.

[14] I. A. Prikhno, E. Y. Safronova, A. B. Yaroslavtsev, Int J Hydrogen Energy 2016, 41, 15585.

[15] W. Wang, L. Zhu, B. Shan, C. Xie, C. Liu, F. Cui, G. Li, J Memb Sci 2018, 548, 459.

[16] K. C. Ho, Y. H. Teow, A. W. Mohammad, W. L. Ang, P. H. Lee, J Memb Sci 2018, 552, 189.

[17] I. A. Prikhno, E. Y. Safronova, A. B. Yaroslavtsev, Int J Hydrogen Energy 2016, 41, 15585.

[18] X. Fan, H. Zhao, X. Quan, Y. Liu, S. Chen, Water Res 2016, 88, 285.

[19] X. Fan, Y. Liu, X. Quan, S. Chen, Environ Sci Technol 2018, 52, 1444.

[20] G. Yi, S. Chen, X. Quan, G. Wei, X. Fan, H. Yu, Sep Purif Technol 2018, 197, 107.

[21] J. R. Reynolds, B. C. Thompson, T. A. Skotheim, Conjugated Polymers: Properties, Processing, and Applications, CRC press, 2019.

[22] D. Nilsson, M. Chen, T. Kugler, T. Remonen, M. Armgarth, M. Berggren, Adv Mat 2002, 14, 51.

[23] D. Nilsson, N. Robinson, M. Berggren, R. Forchheimer, Adv Mat 2005, 17, 353.

[24] H. Sirringhaus, T. Kawase, R. H. Friend, T. Shimoda, M. Inbasekaran, W. Wu, E. P. Woo, Science (1979) 2000, 290, 2123.

[25] P. Tehrani, A. Kanciurzewska, X. Crispin, N. D. Robinson, M. Fahlman, M. Berggren, Solid State Ion 2007, 177, 3521.

[26] J. B. Schlenoff, Langmuir 2014, 30, 9625.

[27] M. Cloutier, D. Mantovani, F. Rosei, Trends Biotechnol 2015, 33, 637.

[28] S. Jiang, Z. Cao, Adv Mat 2010, 22, 920.

[29] C. Leng, H.-C. Hung, S. Sun, D. Wang, Y. Li, S. Jiang, Z. Chen, ACS Appl Mater Interfaces 2015, 7, 16881.

[30] L. Xie, J. Wang, C. Shi, J. Huang, H. Zhang, Q. Liu, Q. Liu, H. Zeng, J Phys Chem C 2016, 120, 22433.

[31] G. Wittstock, I. Kartio, D. Hirsch, S. Kunze, R. Szargan, Langmuir 1996, 12, 5709.

[32] M. A. Hampton, C. Plackowski, A. V Nguyen, Langmuir 2011, 27, 4190.

[33] F. Xu, B. Wang, D. Yang, X. Ming, Y. Jiang, J. Hao, Y. Qiao, Y. Tian, Energy Convers Manag 2018, 175, 288.

[34] J. Zhang, D. T. Sekyere, N. Niwamanya, Y. Huang, A. Barigye, Y. Tian, ACS Omega 2022.

[35] H.-S. Park, S.-J. Ko, J.-S. Park, J. Y. Kim, H.-K. Song, Sci Rep 2013, 3, 2454.

[36] L. Xie, J. Wang, C. Shi, J. Huang, H. Zhang, Q. Liu, Q. Liu, H. Zeng, J Phys Chem C 2016, 120, 22433.

[37] H. D. Ackler, R. H. French, Y.-M. Chiang, J Colloid Interface Sci 1996, 179, 460.

[38] Y. Gao, N. Guo, B. Gauvreau, M. Rajabian, O. Skorobogata, E. Pone, O. Zabeida, L. Martinu, C. Dubois, M. Skorobogatiy, J Mater Res 2006, 21, 2246.

[39] A. M. Gaur, D. S. Rana, J Inorg Organomet Polym Mater 2019, 29, 1637.

[40] B. Cappi, J. Ebert, R. Telle, J Am Ceram Soc 2011, 94, 111.

[41] G. Pezzotti, F. Boschetto, E. Ohgitani, Y. Fujita, W. Zhu, E. Marin, B. J. McEntire, B. S. Bal, O. Mazda, Sci Rep 2021, 11, 1.

[42] S. Sakarkar, S. Muthukumaran, V. Jegatheesan, Membranes (Basel) 2021, 11, 241.

[43] M. Chen, C. Xiao, C. Wang, H. Liu, RSC Adv 2017, 7, 20327.

[44] X. Li, Y. Chen, X. Hu, Y. Zhang, L. Hu, J Memb Sci 2014, 471, 118.

[45] J. Garnier, Polymer electrochromism and surface plasmons combined on metallic diffraction gratings, Institutionen för fysik, kemi och biologi, 2008.

[46] V. Singh, T. Kumar, Journal of Science: Advanced Materials and Devices 2019, 4, 538.

[47] W. Zhao, Q. Ye, H. Hu, X. Wang, F. Zhou, J Mater Chem B 2014, 2, 5352.

[48] Q. Chen, L. Yuan, R. Duan, P. Huang, J. Fu, H. Ma, X. Wang, Y. Zhou, B. Song, Solar RRL 2019, 3, 1900118.

[49] J. Wang, L. Xie, L. Han, X. Wang, J. Wang, H. Zeng, J Colloid Interface Sci 2021, 584, 103.

[50] J. Wang, L. Xie, Q. Lu, X. Wang, J. Wang, H. Zeng, J Colloid Interface Sci 2020, 570, 350.

[51] J. Wang, Q. Liu, H. Zeng, J Phys Chem C 2013, 117, 20089.

[52] C. Shi, L. Xie, L. Zhang, X. Lu, H. Zeng, J Colloid Interface Sci 2020, 558, 173.

[53] X. Cui, C. Shi, S. Zhang, L. Xie, J. Liu, D. Jiang, H. Zeng, Chemistry–An Asian Journal 2017, 12, 1568.

[54] L. Xie, C. Shi, X. Cui, H. Zeng, Langmuir 2017, 33, 3911.

[55] L. G. Leal, Advanced transport phenomena: fluid mechanics and convective transport processes, Vol. 7, Cambridge University Press, 2007.

[56] C. K. Batchelor, G. K. Batchelor, An introduction to fluid dynamics, Cambridge university press, 2000.

[57] D. Y. C. Chan, E. Klaseboer, R. Manica, Adv Colloid Interface Sci 2011, 165, 70.

[58] D. Y. C. Chan, E. Klaseboer, R. Manica, Soft Matter 2011, 7, 2235.

[59] J. N. Israelachvili, Intermolecular and surface forces, Academic press, 2015.

[60] C. Wei, A. J. Bard, M. V Mirkin, J Phys Chem 1995, 99, 16033.

[61] A. J. Bard, F. R. F. Fan, Juhyoun. Kwak, Ovadia. Lev, Anal Chem 1989, 61, 132.

[62] J. Wang, Q. Liu, H. Zeng, The Journal of Physical Chemistry C 2013, 117, 20089.

[63] G. Rebetez, O. Bardagot, J. Affolter, J. Réhault, N. Banerji, Adv Funct Mater 2022, 32, 2105821.

[64] H.-S. Park, S.-J. Ko, J.-S. Park, J. Y. Kim, H.-K. Song, Sci Rep 2013, 3, 2454.

CHAPTER 6 CONCLUSIONS, CONTRIBUTIONS, AND RECOMMENDATIONS

6.1 Major Conclusions and Contributions

Bio-inspired materials have been developed as effective antifouling platforms via dramatically reducing the contact and adhesion between contaminants by tuning the surface properties or interfacial phenomena of material surfaces. In this thesis work, the interaction mechanisms including interfacial forces, adhesion behaviors and binding energies between different types of foulants and diverse bio-inspired antifouling surfaces have been systematically quantified by using nanomechanical technologies. Moreover, the intermolecular interactions inspired by the marine mussel biological system have been orchestrated to functionalize antifouling surfaces for oil/water separation and water treatment. The thesis work is entirely original, and significantly enhanced the fundamental understanding of the nanoscale surface interaction mechanisms between bio-inspired antifouling materials and typical contaminants including inorganic foulant (silica), organic foulants (oil droplets and humic acid), and bio foulants (PDA, DOPA and BSA) in aqueous solutions, which provide valuable insights into the development and design of novel antifouling materials for various engineering applications such as marine engineering, waste water treatment, and oil/water emulsion separation.

The major conclusions and original contributions are listed below:

(1) The antifouling performance and repellence mechanisms of bio-inspired lubricant-infused slippery surface towards the versatile mussel-inspired chemistry including polydopamine (PDA) and 3,4-dihydroxyphenylalanine (DOPA) were investigated

using AFM technique, and the correlated interaction energy and binding strength were probed. The deposition behaviors of PDA molecules towards the fluorinated monolayer surface and lubricant-infused slippery surface were investigated and compared using QCM-D, which found that infusing lubricant could significantly inhibit the PDA deposition and the loosely bound PDA molecules could be easily washed. The intermolecular force measurements employing colloidal probe AFM technique indicated that the strong capillary bridging prevented the PDA molecules from penetrating the infused lubricant layer and contacting the underlying substrates, thus decreasing foulant adhesion. Moreover, the SM-AFM results demonstrated that the presence of the lubricant layer acted as a barrier and significantly weaken the interaction stability and binding strength of a single DOPA moiety to fluorinated functional surfaces, thereby enhancing the biofouling resistance performance. This work elucidated the nanoscale interaction strength and thermodynamic stability of the pairwise bonding between the lubricant-infused surfaces and versatile mussel-inspired catechol groups from the standpoint of energy and kinetics mechanism, which enhanced the fundamental understanding of antifouling strategies of bio-inspired slippery surfaces and illuminated the development of bio-inspired antifouling materials.

(2) In the second part of the thesis work, interaction mechanisms of three kinds of typical contaminants in water systems including silica, BSA and HA with PVDF membrane with/without PDA, and PSBMA polymer coatings in aqueous media have been quantitatively characterized employing an AFM. The individual contribution of different types of interactions between diverse foulants and

membrane surfaces was quantitatively fitted and analyzed applying extended DLVO theory, unveiling the primary factors influencing foulant adhesion and removal. Among the membranes, silica particles exhibited the most potent adsorption to PVDF membrane, whereas BSA and HA were more inclined to accumulate on PDA membranes. The accumulation behaviors of organic foulants were attributed to the combination of various interaction forces, including hydrophobic attraction, cation/anion-π interactions and hydrogen bonding between BSA/HA and PDA molecules, leading to increased adsorption and irreversible fouling on the PDA surface. Conversely, the zwitterionic nature of PSBMA membrane displayed excellent antifouling performance with various foulants. This efficiency was a result of hydration repulsion from the PSBMA membrane surface, acting as a formidable physical barrier against foulant adhesion, ensuring enhanced permeability and reusability. This work contributes significant nanomechanical insights into the fundamental antifouling mechanisms of bio-inspired antifouling membranes for water treatment, which also holds implications for the design of novel antifouling platforms in various bioengineering and engineering applications.

(3) In the third part of the thesis work, a facile and conductive PDA-PEDOT:PSS-PSBMA coating was successfully fabricated and applied for membrane filtration of O/W emulsions via a electrochemical-tunable surface force-based strategy. The surface potentials of the conductive membrane varied with the adjustment of applied electrochemical potentials, leading to tunable EDL interaction between the membrane and emulsions. The interaction mechanisms revealed that applying a negative electrochemical potential to PP membrane and PP/PSBMA membrane

could enhance EDL repulsion between the PFO droplets and the conductive membrane surfaces. The zwitterionic PSBMA polymer coating on the membrane further eliminated hydrophobic attraction between oil and membrane surfaces, thereby hindering oil attachment and improving antifouling performance. Remarkably, PP/PSBMA membranes subjected to a negative potential (-0.4 V) exhibited favorable resistance to oil fouling, evidenced by superior oil removal efficiency surpassing 99.9% and excellent membrane regeneration ability. The study has practical implications for the design and development of conductive and regenerable membrane surfaces with tunable surface interactions, offering promising prospects for improving the efficiency and sustainability of oil/water emulsion separation.

6.2 Prospects

(1) In this study, we have improved the fundamental understanding of the nanoscale surface interaction mechanisms of antifouling surfaces against various contaminants including organic foulants, inorganic foulants and biofoulants, which provide potential solutions to challenges in many industrial areas such as marine industry, oil production and wastewater treatment. In practical applications, some industrial processes are usually conducted under complex environment, such as high temperature, high pressure and high salinity. Future studies will focus on advancing the characterization and modulation of surface interactions under more complex fluid conditions (e.g., water chemistry, solvent concentration, and interface-active species) and environment conditions (e.g., temperature, pressure, and strong hydrodynamics) close to practical industrial processes.

(2) In this work, the superhydrophilic surfaces with tunable electrical properties achieved remarkable antifouling performances through the synergistic effects of short-range hydration force and long-range EDL interactions. However, practical applications still face challenges due to the insufficient mechanical strength of the soft polymer coating, which may greatly limit the duration and reliability. To address this issue, potential avenues for future work could be explored. One promising approach is to prepare composite membranes by incorporating the conductive materials into the membrane matrix. The mechanical strength of the composite membrane can be significantly improved by dispersing conductive materials throughout the membrane matrix, which helps to prevent the detachment of the conductive layer during operation, thereby enhancing the duration in real-world applications. Another possible direction for future research is to develop self-healing functionalities within the antifouling coating. For example, the controllable release healing agents in the coating layer are able to repair damage autonomously, thereby extending lifespan of coatings and reducing maintenance or replacement frequency.

BIBLIOGRAPHY

Ackler, H.D., French, R.H., Chiang, Y.-M., 1996. Comparisons of Hamaker constants for ceramic systems with intervening vacuum or water: From force laws and physical properties. J Colloid Interface Sci 179, 460–469.

Al-Amoudi, A.S., 2010. Factors affecting natural organic matter (NOM) and scaling fouling in NF membranes: a review. Desalination 259, 1–10.

Aliano, A., Cicero, G., Nili, H., Green, N.G., Garcıa-Sánchez, P., Ramos, A., Lenshof, A., Laurell, T., Qi, A., Chan, P., 2012. AFM, tapping mode. Encyclopedia of Nanotechnology 99.

Ally, J., Vittorias, E., Amirfazli, A., Kappl, M., Bonaccurso, E., McNamee, C.E., Butt, H.-J., 2010. Interaction of a Microsphere with a Solid-Supported Liquid Film. Langmuir 26, 11797–11803. https://doi.org/10.1021/la1010924

Almeida, E., Diamantino, T.C., de Sousa, O., 2007. Marine paints: the particular case of antifouling paints. Prog Org Coat 59, 2–20.

Ambrożewicz, D., Ciesielczyk, F., Nowacka, M., Karasiewicz, J., Piasecki, A., Maciejewski, H., Jesionowski, T., 2013. Fluoroalkylsilane versus alkylsilane as hydrophobic agents for silica and silicates. J Nanomater 2013.

Amini, S., Kolle, S., Petrone, L., Ahanotu, O., Sunny, S., Sutanto, C.N., Hoon, S., Cohen, L., Weaver, J.C., Aizenberg, J., Vogel, N., Miserez, A., 2017. Preventing mussel adhesion using lubricant-infused materials. Science (1979) 357, 668 LP – 673. https://doi.org/10.1126/science.aai8977

Ang, W.S., Elimelech, M., 2008. Fatty acid fouling of reverse osmosis membranes: Implications for wastewater reclamation. Water Res 42, 4393–4403.

Ang, W.S., Elimelech, M., 2007. Protein (BSA) fouling of reverse osmosis membranes: implications for wastewater reclamation. J Memb Sci 296, 83–92.

Azari, S., Zou, L., 2012a. Using zwitterionic amino acid l-DOPA to modify the surface of thin film composite polyamide reverse osmosis membranes to increase their fouling resistance. J Memb Sci 401, 68–75.

Azari, S., Zou, L., 2012b. Using zwitterionic amino acid l-DOPA to modify the surface of thin film composite polyamide reverse osmosis membranes to increase their fouling resistance. J Memb Sci 401, 68–75.

Bandara, N., Zeng, H., Wu, J., 2013a. Marine mussel adhesion: biochemistry, mechanisms, and biomimetics. J Adhes Sci Technol 27, 2139–2162.

Bandara, N., Zeng, H., Wu, J., 2013b. Marine mussel adhesion: biochemistry, mechanisms, and biomimetics. J Adhes Sci Technol 27, 2139–2162.

Banerjee, I., Pangule, R.C., Kane, R.S., 2011. Antifouling coatings: recent developments in the design of surfaces that prevent fouling by proteins, bacteria, and marine organisms. Advanced materials 23, 690–718.

Bard, A.J., Fan, F.R.F., Kwak, Juhyoun., Lev, Ovadia., 1989. Scanning electrochemical microscopy. Introduction and principles. Anal Chem 61, 132–138. https://doi.org/10.1021/ac00177a011

Barraud, N., Hassett, D.J., Hwang, S.-H., Rice, S.A., Kjelleberg, S., Webb, J.S., 2006. Involvement of nitric oxide in biofilm dispersal of Pseudomonas aeruginosa. J Bacteriol 188, 7344–7353.

Batchelor, C.K., Batchelor, G.K., 2000. An introduction to fluid dynamics. Cambridge university press.

Bennett, S.M., Finlay, J.A., Gunari, N., Wells, D.D., Meyer, A.E., Walker, G.C., Callow, M.E., Callow, J.A., Bright, F. V, Detty, M.R., 2009. The role of surface energy and water wettability in aminoalkyl/fluorocarbon/hydrocarbon-modified xerogel surfaces in the control of marine biofouling. Biofouling 26, 235–246. https://doi.org/10.1080/08927010903469676

Bergström, L., 1997. Hamaker constants of inorganic materials. Adv Colloid Interface Sci 70, 125–169.

Boo, C., Hong, S., Elimelech, M., 2018. Relating organic fouling in membrane distillation to intermolecular adhesion forces and interfacial surface energies. Environ Sci Technol 52, 14198–14207.

Bourmaud, A., Riviere, J., Le Duigou, A., Raj, G., Baley, C., 2009. Investigations of the use of a mussel-inspired compatibilizer to improve the matrix-fiber adhesion of a biocomposite. Polym Test 28, 668–672.

Brady Jr, R.F., 2001. A fracture mechanical analysis of fouling release from nontoxic antifouling coatings. Prog Org Coat 43, 188–192.

Brillas, E., Sirés, I., Oturan, M.A., 2009. Electro-Fenton Process and Related Electrochemical Technologies Based on Fenton's Reaction Chemistry. Chem Rev 109, 6570–6631. https://doi.org/10.1021/cr900136g

Burzio, L.A., Waite, J.H., 2000. Cross-linking in adhesive quinoproteins: studies with model decapeptides. Biochemistry 39, 11147–11153.

Butt, H.-J., Kappl, M., 2009. Normal capillary forces. Adv Colloid Interface Sci 146, 48–60.

Buzzacchera, I., Vorobii, M., Kostina, N.Yu., de los Santos Pereira, A., Riedel, T., Bruns, M., Ogieglo, W., Möller, M., Wilson, C.J., Rodriguez-Emmenegger, C., 2017a. Polymer Brush-Functionalized Chitosan Hydrogels as Antifouling Implant Coatings. Biomacromolecules 18, 1983–1992. https://doi.org/10.1021/acs.biomac.7b00516

Buzzacchera, I., Vorobii, M., Kostina, N.Yu., de los Santos Pereira, A., Riedel, T., Bruns, M., Ogieglo, W., Möller, M., Wilson, C.J., Rodriguez-Emmenegger, C., 2017b. Polymer Brush-Functionalized Chitosan Hydrogels as Antifouling Implant Coatings. Biomacromolecules 18, 1983–1992. https://doi.org/10.1021/acs.biomac.7b00516

Cappella, B., 2017. Force-distance curves on lubricant films: An approach to the characterization of the shape of the AFM tip. Micron 93, 20–28.

Cappella, B., Dietler, G., 1999a. Force-distance curves by atomic force microscopy. Surf Sci Rep 34, 1–104.

Cappella, B., Dietler, G., 1999b. Force-distance curves by atomic force microscopy. Surf Sci Rep 34, 1–104.

Cappi, B., Ebert, J., Telle, R., 2011. Rheological Properties of Aqueous Si3N4 and MoSi2 Suspensions Tailor-Made for Direct Inkjet Printing. Journal of the American Ceramic Society 94, 111–116. https://doi.org/https://doi.org/10.1111/j.1551-2916.2010.04052.x

Ceylan, H., Urel, M., Erkal, T.S., Tekinay, A.B., Dana, A., Guler, M.O., 2013. Mussel inspired dynamic cross - linking of self - healing peptide nanofiber network. Adv Funct Mater 23, 2081 – 2090.

Chan, D.Y.C., Klaseboer, E., Manica, R., 2011a. Theory of non-equilibrium force measurements involving deformable drops and bubbles. Adv Colloid Interface Sci 165, 70–90.

Chan, D.Y.C., Klaseboer, E., Manica, R., 2011b. Film drainage and coalescence between deformable drops and bubbles. Soft Matter 7, 2235–2264.

Chen, D., Liu, T., Kang, J., Xu, R., Cao, Y., Xiang, M., 2019a. Enhancing the Permeability and Antifouling Properties of Polyamide Composite Reverse Osmosis Membrane by Surface Modification with Zwitterionic Amino Acid l - Arginine. Adv Mater Interfaces 6, 1900706.

Chen, D., Liu, T., Kang, J., Xu, R., Cao, Y., Xiang, M., 2019b. Enhancing the Permeability and Antifouling Properties of Polyamide Composite Reverse Osmosis Membrane by Surface Modification with Zwitterionic Amino Acid l-Arginine. Adv Mater Interfaces 6, 1900706. https://doi.org/https://doi.org/10.1002/admi.201900706

Chen, M., Xiao, C., Wang, C., Liu, H., 2017. Study on the structural design and performance of novel braid-reinforced and thermostable poly (m-phenylene isophthalamide) hollow fiber membranes. RSC Adv 7, 20327–20335.

Chen, Q., Yuan, L., Duan, R., Huang, P., Fu, J., Ma, H., Wang, X., Zhou, Y., Song, B., 2019. Zwitterionic Polymer: A Facile Interfacial Material Works at Both Anode and Cathode in p‐i‐n Perovskite Solar Cells. Solar RRL 3, 1900118.

Chen, Shengfu, Jiang, S., 2008. An new avenue to nonfouling materials. Advanced Materials 20, 335–338.

Chen, S, Jiang, S., 2008. An New Avenue to Nonfouling Materials. Advanced Materials 20, 335–338. https://doi.org/https://doi.org/10.1002/adma.200701164

Chen, W., Gu, Z., Ran, G., Li, Q., 2021. Application of membrane separation technology in the treatment of leachate in China: A review. Waste Management 121, 127–140.

Cheng, C., Li, S., Zhao, W., Wei, Q., Nie, S., Sun, S., Zhao, C., 2012. The hydrodynamic permeability and surface property of polyethersulfone ultrafiltration membranes with mussel-inspired polydopamine coatings. J Memb Sci 417, 228–236.

Chiao, Y.-H., Chen, S.-T., Sivakumar, M., Ang, M.B.M.Y., Patra, T., Almodovar, J., Wickramasinghe, S.R., Hung, W.-S., Lai, J.-Y., 2020. Zwitterionic polymer brush grafted on polyvinylidene difluoride membrane promoting enhanced ultrafiltration performance with augmented antifouling property. Polymers (Basel) 12, 1303.

Cho, H., Madhurakkat Perikamana, S.K., Lee, Ji-hye, Lee, Jinkyu, Lee, K.-M., Shin, C.S., Shin, H., 2014. Effective immobilization of BMP-2 mediated by polydopamine coating on biodegradable nanofibers for enhanced in vivo bone formation. ACS Appl Mater Interfaces 6, 11225–11235.

Chong, M.N., Jin, B., Chow, C.W.K., Saint, C., 2010. Recent developments in photocatalytic water treatment technology: A review. Water Res 44, 2997–3027. https://doi.org/https://doi.org/10.1016/j.watres.2010.02.039

Cloutier, M., Mantovani, D., Rosei, F., 2015. Antibacterial coatings: challenges, perspectives, and opportunities. Trends Biotechnol 33, 637–652.

Cui, X., Shi, C., Zhang, S., Xie, L., Liu, J., Jiang, D., Zeng, H., 2017. Probing the effect of salinity and pH on surface interactions between air bubbles and hydrophobic solids: implications for colloidal assembly at air/water interfaces. Chemistry–An Asian Journal 12, 1568–1577.

Dai, X., Boll, J., Hayes, M.E., Aston, D.E., 2004. Adhesion of Cryptosporidium parvum and Giardia lamblia to solid surfaces: the role of surface charge and hydrophobicity. Colloids Surf B Biointerfaces 34, 259–263.

Dalsin, J.L., Hu, B.-H., Lee, B.P., Messersmith, P.B., 2003. Mussel adhesive protein mimetic polymers for the preparation of nonfouling surfaces. J Am Chem Soc 125, 4253–4258.

Dalsin, J.L., Messersmith, P.B., 2005. Bioinspired antifouling polymers. Materials today 8, 38–46.

Danner, E.W., Kan, Y., Hammer, M.U., Israelachvili, J.N., Waite, J.H., 2012a. Adhesion of mussel foot protein Mefp-5 to mica: an underwater superglue. Biochemistry 51, 6511–6518.

Danner, E.W., Kan, Y., Hammer, M.U., Israelachvili, J.N., Waite, J.H., 2012b. Adhesion of mussel foot protein Mefp-5 to mica: an underwater superglue. Biochemistry 51, 6511–6518.

Darling, S.B., 2018a. Perspective: Interfacial materials at the interface of energy and water. J Appl Phys 124, 30901.

Darling, S.B., 2018b. Perspective: Interfacial materials at the interface of energy and water. J Appl Phys 124, 30901.

De Vera, J.S., Venault, A., Chou, Y.-N., Tayo, L., Chiang, H.-C., Aimar, P., Chang, Y., 2018. Self-cleaning interfaces of polydimethylsiloxane grafted with pH-responsive zwitterionic copolymers. Langmuir 35, 1357–1368.

Diaz-Bejarano, E., Behranvand, E., Coletti, F., Mozdianfard, M.R., Macchietto, S., 2017. Organic and inorganic fouling in heat exchangers–Industrial case study: Analysis of fouling state. Appl Energy 206, 1250–1266.

Ding, Y.H., Floren, M., Tan, W., 2016. Mussel-inspired polydopamine for bio-surface functionalization. Biosurf Biotribol 2, 121–136.

Dishon, M., Zohar, O., Sivan, U., 2009. From repulsion to attraction and back to repulsion: the effect of NaCl, KCl, and CsCl on the force between silica surfaces in aqueous solution. Langmuir 25, 2831–2836.

Dreyer, D.R., Miller, D.J., Freeman, B.D., Paul, D.R., Bielawski, C.W., 2012. Elucidating the structure of poly (dopamine). Langmuir 28, 6428–6435.

Eaton, P., West, P., 2010. Atomic force microscopy. Oxford university press.

Evans, E., Ritchie, K., 1997. Dynamic strength of molecular adhesion bonds. Biophys J 72, 1541–1555.

Even, M.A., Wang, J., Chen, Z., 2008. Structural information of mussel adhesive protein Mefp-3 acquired at various polymer/Mefp-3 solution interfaces. Langmuir 24, 5795–5801.

Fan, X., Lin, L., Dalsin, J.L., Messersmith, P.B., 2005. Biomimetic anchor for surface-initiated polymerization from metal substrates. J Am Chem Soc 127, 15843–15847.

Fan, X., Liu, Y., Quan, X., Chen, S., 2018. Highly permeable thin-film composite forward osmosis membrane based on carbon nanotube hollow fiber scaffold with electrically enhanced fouling resistance. Environ Sci Technol 52, 1444–1452.

Fan, X., Zhao, H., Liu, Y., Quan, X., Yu, H., Chen, S., 2015. Enhanced Permeability, Selectivity, and Antifouling Ability of CNTs/Al2O3 Membrane under Electrochemical Assistance. Environ Sci Technol 49, 2293–2300. https://doi.org/10.1021/es5039479

Fan, X., Zhao, H., Quan, X., Liu, Y., Chen, S., 2016. Nanocarbon-based membrane filtration integrated with electric field driving for effective membrane fouling mitigation. Water Res 88, 285–292. https://doi.org/https://doi.org/10.1016/j.watres.2015.10.043

Fang, H.H.P., Chan, K.-Y., Xu, L.-C., 2000. Quantification of bacterial adhesion forces using atomic force microscopy (AFM). J Microbiol Methods 40, 89–97.

Fang, Y., Xing, C., Zhan, S., Zhao, M., Li, M., Liu, H., 2019. A polyoxometalate-modified magnetic nanocomposite: a promising antibacterial material for water treatment. J Mater Chem B 7, 1933–1944.

Filpula, D.R., Lee, S., Link, R.P., Strausberg, S.L., Strausberg, R.L., 1990. Structural and functional repetition in a marine mussel adhesive protein. Biotechnol Prog 6, 171–177.

Fleischer, S., Dvir, T., 2013. Tissue engineering on the nanoscale: lessons from the heart. Curr Opin Biotechnol 24, 664–671.

Franks, G. V, 2002. Zeta potentials and yield stresses of silica suspensions in concentrated monovalent electrolytes: isoelectric point shift and additional attraction. J Colloid Interface Sci 249, 44–51.

Gao, Y., Guo, N., Gauvreau, B., Rajabian, M., Skorobogata, O., Pone, E., Zabeida, O., Martinu, L., Dubois, C., Skorobogatiy, M., 2006a. Consecutive solvent evaporation and co-rolling techniques for polymer multilayer hollow fiber preform fabrication. J Mater Res 21, 2246–2254.

Gao, Y., Guo, N., Gauvreau, B., Rajabian, M., Skorobogata, O., Pone, E., Zabeida, O., Martinu, L., Dubois, C., Skorobogatiy, M., 2006b. Consecutive solvent evaporation and co-rolling techniques for polymer multilayer hollow fiber preform fabrication. J Mater Res 21, 2246–2254.

Garnier, J., 2008. Polymer electrochromism and surface plasmons combined on metallic diffraction gratings.

Gaur, A.M., Rana, D.S., 2019a. In situ measurement of dielectric permittivity and electrical conductivity of CoCl 2/BaCl 2 doped PVDF composite at elevated temperature. J Inorg Organomet Polym Mater 29, 1637–1644.

Gaur, A.M., Rana, D.S., 2019b. In situ measurement of dielectric permittivity and electrical conductivity of CoCl 2/BaCl 2 doped PVDF composite at elevated temperature. J Inorg Organomet Polym Mater 29, 1637–1644.

Gong, L., Qiu, X., Zhang, L., Huang, J., Hu, W., Xiang, L., Zhu, D., Sabbagh, R., Mahmoudi, M., Fattahpour, V., 2018. Probing the interaction mechanism between oil-in-water emulsions and electroless nickel–phosphorus coating with implications for antifouling in oil production. Energy & Fuels 33, 3764–3775.

Gong, L., Wang, J., Xiang, L., Huang, J., Fattahpour, V., Roostaei, M., Mamoudi, M., Fermaniuk, B., Luo, J.-L., Zeng, H., 2021. Characterizing foulants on slotted liner and probing the surface interaction mechanisms in organic media with implication for an antifouling strategy in oil production. Fuel 290, 120008.

Gong, L., Wang, J., Zhang, L., Fattahpour, V., Mamoudi, M., Roostaei, M., Fermaniuk, B., Luo, J.-L., Zeng, H., 2019. Fouling mechanisms of asphaltenes and fine solids on bare and electroless nickel-phosphorus coated carbon steel. Fuel 252, 188–199.

Guinea, E., Arias, C., Cabot, P.L., Garrido, J.A., Rodríguez, R.M., Centellas, F., Brillas, E., 2008. Mineralization of salicylic acid in acidic aqueous medium by electrochemical advanced oxidation processes using platinum and boron-doped diamond as anode and cathodically generated hydrogen peroxide. Water Res 42, 499–511. https://doi.org/https://doi.org/10.1016/j.watres.2007.07.046

Guo, D., Xiao, Y., Li, T., Zhou, Q., Shen, L., Li, R., Xu, Y., Lin, H., 2020. Fabrication of high-performance composite nanofiltration membranes for dye wastewater treatment: mussel-inspired layer-by-layer self-assembly. J Colloid Interface Sci 560, 273–283.

Guo, S., Jańczewski, D., Zhu, X., Quintana, R., He, T., Neoh, K.G., 2015. Surface charge control for zwitterionic polymer brushes: Tailoring surface properties to antifouling applications. J Colloid Interface Sci 452, 43–53.

Gupta, R.K., Dunderdale, G.J., England, M.W., Hozumi, A., 2017. Oil/water separation techniques: a review of recent progresses and future directions. J Mater Chem A Mater 5, 16025–16058.

Hampton, M.A., Plackowski, C., Nguyen, A. V, 2011a. Physical and chemical analysis of elemental sulfur formation during galena surface oxidation. Langmuir 27, 4190–4201.

Hampton, M.A., Plackowski, C., Nguyen, A. V, 2011b. Physical and chemical analysis of elemental sulfur formation during galena surface oxidation. Langmuir 27, 4190–4201.

Han, L., Gong, L., Chen, J., Zhang, J., Xiang, L., Zhang, L., Wang, Q., Yan, B., Zeng, H., 2018. Universal mussel-inspired ultrastable surface-anchoring strategy via adaptive synergy of catechol and cations. ACS Appl Mater Interfaces 10, 2166–2173.

He, Y., Xu, L., Feng, X., Zhao, Y., Chen, L., 2017. Dopamine-induced nonionic polymer coatings for significantly enhancing separation and antifouling properties of polymer membranes: Codeposition versus sequential deposition. J Memb Sci 539, 421–431.

Helm, C.A., Knoll, W., Israelachvili, J.N., 1991. Measurement of ligand-receptor interactions. Proceedings of the National Academy of Sciences 88, 8169–8173.

Hemmati, S., Zangeneh, M.M., Zangeneh, A., 2020. CuCl2 anchored on polydopamine coated-magnetic nanoparticles (Fe3O4@ PDA/Cu (II)): Preparation, characterization and evaluation of its cytotoxicity, antioxidant, antibacterial, and antifungal properties. Polyhedron 177, 114327.

Herzberg, M., Kang, S., Elimelech, M., 2009. Role of extracellular polymeric substances (EPS) in biofouling of reverse osmosis membranes. Environ Sci Technol 43, 4393–4398.

Hetrick, E.M., Schoenfisch, M.H., 2006a. Reducing implant-related infections: active release strategies. Chem Soc Rev 35, 780–789.

Hetrick, E.M., Schoenfisch, M.H., 2006b. Reducing implant-related infections: active release strategies. Chem Soc Rev 35, 780–789. https://doi.org/10.1039/B515219B

Ho, K.C., Teow, Y.H., Mohammad, A.W., Ang, W.L., Lee, P.H., 2018. Development of graphene oxide (GO)/multi-walled carbon nanotubes (MWCNTs) nanocomposite conductive membranes for electrically enhanced fouling mitigation. J Memb Sci 552, 189–201. https://doi.org/https://doi.org/10.1016/j.memsci.2018.02.001

Holten-Andersen, N., Harrington, M.J., Birkedal, H., Lee, B.P., Messersmith, P.B., Lee, K.Y.C., Waite, J.H., 2011. pH-induced metal-ligand cross-links inspired by mussel yield self-healing polymer networks with near-covalent elastic moduli. Proceedings of the National Academy of Sciences 108, 2651–2655.

Hönes, R., Lee, Y., Urata, C., Lee, H., Hozumi, A., 2020. Antiadhesive Properties of Oil-Infused Gels against the Universal Adhesiveness of Polydopamine. Langmuir 36, 4496–4502. https://doi.org/10.1021/acs.langmuir.0c00062

Hong, S., Na, Y.S., Choi, S., Song, I.T., Kim, W.Y., Lee, H., 2012. Non‐covalent self‐assembly and covalent polymerization co‐contribute to polydopamine formation. Adv Funct Mater 22, 4711–4717.

Howell, C., Grinthal, A., Sunny, S., Aizenberg, M., Aizenberg, J., 2018. Designing liquid‐infused surfaces for medical applications: a review. Advanced materials 30, 1802724.

Howell, C., Vu, T.L., Johnson, C.P., Hou, X., Ahanotu, O., Alvarenga, J., Leslie, D.C., Uzun, O., Waterhouse, A., Kim, P., 2015a. Stability of surface-immobilized lubricant interfaces under flow. Chemistry of Materials 27, 1792–1800.

Howell, C., Vu, T.L., Johnson, C.P., Hou, X., Ahanotu, O., Alvarenga, J., Leslie, D.C., Uzun, O., Waterhouse, A., Kim, P., Super, M., Aizenberg, M., Ingber, D.E., Aizenberg, J., 2015b. Stability of Surface-Immobilized Lubricant Interfaces under Flow. Chemistry of Materials 27, 1792–1800. https://doi.org/10.1021/cm504652g

Hu, Y., Yue, M., Yuan, F., Yang, L., Chen, C., Sun, D., 2021. Bio-inspired fabrication of highly permeable and anti-fouling ultrafiltration membranes based on bacterial cellulose for efficient removal of soluble dyes and insoluble oils. J Memb Sci 621, 118982.

Huang, L., Zhao, S., Wang, Z., Wu, J., Wang, J., Wang, S., 2016. In situ immobilization of silver nanoparticles for improving permeability, antifouling and anti-bacterial properties of ultrafiltration membrane. J Memb Sci 499, 269–281.

Huang, N., Zhang, S., Yang, L., Liu, M., Li, H., Zhang, Y., Yao, S., 2015. Multifunctional electrochemical platforms based on the Michael addition/Schiff base reaction of polydopamine modified reduced graphene oxide: construction and application. ACS Appl Mater Interfaces 7, 17935–17946.

Hwang, D.S., Zeng, H., Masic, A., Harrington, M.J., Israelachvili, J.N., Waite, J.H., 2010a. Protein-and metal-dependent interactions of a prominent protein in mussel adhesive plaques. Journal of biological chemistry 285, 25850–25858.

Hwang, D.S., Zeng, H., Masic, A., Harrington, M.J., Israelachvili, J.N., Waite, J.H., 2010b. Protein- and metal-dependent interactions of a prominent protein in mussel adhesive plaques. Journal of Biological Chemistry 285. https://doi.org/10.1074/jbc.M110.133157

Iqbal, Z., Lai, E.P.C., Avis, T.J., 2012. Antimicrobial effect of polydopamine coating on Escherichia coli. J Mater Chem 22, 21608–21612.

Ishiguro, M., Tan, W., Koopal, L.K., 2007. Binding of cationic surfactants to humic substances. Colloids Surf A Physicochem Eng Asp 306, 29–39.

Israelachvili, J.N., 2015. Intermolecular and surface forces. Academic press.

Jeong, J., Cho, E., Yun, D., Kim, T., Lee, I.-S., Jung, S., 2017. Label-free colorimetric detection of influenza antigen based on an antibody-polydiacetylene conjugate and its coated polyvinylidene difluoride membrane. Polymers (Basel) 9, 127.

Jiang, J., Zhang, P., Zhu, L., Zhu, B., Xu, Y., 2015. Improving antifouling ability and hemocompatibility of poly (vinylidene fluoride) membranes by polydopamine-mediated ATRP. J Mater Chem B 3, 7698–7706.

Jiang, J., Zhu, Liping, Zhu, Lijing, Zhang, H., Zhu, B., Xu, Y., 2013. Antifouling and antimicrobial polymer membranes based on bioinspired polydopamine and strong hydrogen-bonded poly (N-vinyl pyrrolidone). ACS Appl Mater Interfaces 5, 12895–12904.

Jiang, J.-H., Zhu, L.-P., Zhang, H.-T., Zhu, B.-K., Xu, Y.-Y., 2014. Improved hydrodynamic permeability and antifouling properties of poly (vinylidene fluoride) membranes using polydopamine nanoparticles as additives. J Memb Sci 457, 73–81.

Jiang, S., Cao, Z., 2010a. Ultralow ‐ fouling, functionalizable, and hydrolyzable zwitterionic materials and their derivatives for biological applications. Advanced materials 22, 920 ‐ 932.

Jiang, S., Cao, Z., 2010b. Ultralow-Fouling, Functionalizable, and Hydrolyzable Zwitterionic Materials and Their Derivatives for Biological Applications. Advanced Materials 22, 920–932. https://doi.org/https://doi.org/10.1002/adma.200901407

Jiang, S., Cao, Z., 2010c. Ultralow-Fouling, Functionalizable, and Hydrolyzable Zwitterionic Materials and Their Derivatives for Biological Applications. Advanced Materials 22, 920–932. https://doi.org/https://doi.org/10.1002/adma.200901407

Johnson, D., Hilal, N., 2015. Characterisation and quantification of membrane surface properties using atomic force microscopy: A comprehensive review. Desalination 356, 149–164.

Johnson, K.L., Johnson, K.L., 1987. Contact mechanics. Cambridge university press.

Johnson, K.L., Kendall, K., Roberts, aAD, 1971. Surface energy and the contact of elastic solids. Proceedings of the royal society of London. A. mathematical and physical sciences 324, 301–313.

Jung, S.Y., Won, Y.-J., Jang, J.H., Yoo, J.H., Ahn, K.H., Lee, C.-H., 2015. Particle deposition on the patterned membrane surface: Simulation and experiments. Desalination 370, 17–24.

Júnior, J.A.A., Baldo, J.B., 2014. The behavior of zeta potential of silica suspensions. New Journal of Glass and Ceramics 4, 29.

Kelly, S.T., Zydney, A.L., 1995. Mechanisms for BSA fouling during microfiltration. J Memb Sci 107, 115–127.

Kim, S., Huang, J., Lee, Y., Dutta, S., Yoo, H.Y., Jung, Y.M., Jho, Y., Zeng, H., Hwang, D.S., 2016a. Complexation and coacervation of like-charged polyelectrolytes inspired by mussels. Proceedings of the National Academy of Sciences 113, E847–E853.

Kim, S., Huang, J., Lee, Y., Dutta, S., Yoo, H.Y., Jung, Y.M., Jho, Y., Zeng, H., Hwang, D.S., 2016b. Complexation and coacervation of like-charged polyelectrolytes inspired by mussels. Proceedings of the National Academy of Sciences 113, E847 LP-E853. https://doi.org/10.1073/pnas.1521521113

Kim, S., Yoo, H.Y., Huang, J., Lee, Y., Park, S., Park, Y., Jin, S., Jung, Y.M., Zeng, H., Hwang, D.S., 2017a. Salt triggers the simple coacervation of an underwater adhesive when cations meet aromatic π electrons in seawater. ACS Nano 11, 6764–6772.

Kim, S., Yoo, H.Y., Huang, J., Lee, Y., Park, S., Park, Y., Jin, S., Jung, Y.M., Zeng, H., Hwang, D.S., Jho, Y., 2017b. Salt Triggers the Simple Coacervation of an Underwater Adhesive When Cations Meet Aromatic π Electrons in Seawater. ACS Nano 11, 6764–6772. https://doi.org/10.1021/acsnano.7b01370

Kimura, K., Yamato, N., Yamamura, H., Watanabe, Y., 2005. Membrane fouling in pilot-scale membrane bioreactors (MBRs) treating municipal wastewater. Environ Sci Technol 39, 6293–6299.

Kingshott, P., Wei, J., Bagge-Ravn, D., Gadegaard, N., Gram, L., 2003a. Covalent attachment of poly (ethylene glycol) to surfaces, critical for reducing bacterial adhesion. Langmuir 19, 6912–6921.

Kingshott, P., Wei, J., Bagge-Ravn, D., Gadegaard, N., Gram, L., 2003b. Covalent Attachment of Poly(ethylene glycol) to Surfaces, Critical for Reducing Bacterial Adhesion. Langmuir 19, 6912–6921. https://doi.org/10.1021/la034032m

Kirby, B.J., Hasselbrink Jr, E.F., 2004. Zeta potential of microfluidic substrates: 1. Theory, experimental techniques, and effects on separations. Electrophoresis 25, 187–202.

Knothe, K., 2011. Contact mechanics and friction: physical principles and applications.

Kong, G., Fan, L., Zhao, L., Feng, Y., Cui, X., Pang, J., Guo, H., Sun, H., Kang, Z., Sun, D., 2021. Spray-dispersion of ultra-small EMT zeolite crystals in thin-film composite membrane for high-permeability nanofiltration process. J Memb Sci 622, 119045.

Kosmulski, M., 1998. Positive electrokinetic charge of silica in the presence of chlorides. J Colloid Interface Sci 208, 543–545.

Kralchevsky, P., Nagayama, K., 2001. Particles at fluid interfaces and membranes: attachment of colloid particles and proteins to interfaces and formation of two-dimensional arrays. Elsevier.

Krogsgaard, M., Behrens, M.A., Pedersen, J.S., Birkedal, H., 2013. Self-healing mussel-inspired multi-pH-responsive hydrogels. Biomacromolecules 14, 297–301.

Kumar, R., Isloor, A.M., Ismail, A.F., Rashid, S.A., Matsuura, T., 2013. Polysulfone–Chitosan blend ultrafiltration membranes: preparation, characterization, permeation and antifouling properties. RSC Adv 3, 7855–7861.

Kwon, G., Kota, A.K., Li, Y., Sohani, A., Mabry, J.M., Tuteja, A., 2012. On‐demand separation of oil‐water mixtures. Advanced materials 24, 3666–3671.

Laali, K.K., Greves, W.J., Correa-Smits, S.J., Zwarycz, A.T., Bunge, S.D., Borosky, G.L., Manna, A., Paulus, A., Chanan-Khan, A., 2018. Novel fluorinated curcuminoids and their pyrazole and isoxazole derivatives: Synthesis, structural studies, Computational/Docking and in-vitro bioassay. J Fluor Chem 206, 82–98.

LaVoie, M.J., Ostaszewski, B.L., Weihofen, A., Schlossmacher, M.G., Selkoe, D.J., 2005. Dopamine covalently modifies and functionally inactivates parkin. Nat Med 11, 1214–1221.

Leal, L.G., 2007. Advanced transport phenomena: fluid mechanics and convective transport processes. Cambridge University Press.

Le-Clech, P., Chen, V., Fane, T.A.G., 2006. Fouling in membrane bioreactors used in wastewater treatment. J Memb Sci 284, 17–53.

Lee, H., Dellatore, S.M., Miller, W.M., Messersmith, P.B., 2007. Mussel-inspired surface chemistry for multifunctional coatings. Science (1979) 318, 426–430.

Lee, H., Rho, J., Messersmith, P.B., 2009. Facile conjugation of biomolecules onto surfaces via mussel adhesive protein inspired coatings. Advanced Materials 21, 431–434.

Lee, H., Scherer, N.F., Messersmith, P.B., 2006a. Single-molecule mechanics of mussel adhesion. Proceedings of the National Academy of Sciences 103, 12999–13003.

Lee, H., Scherer, N.F., Messersmith, P.B., 2006b. Single-molecule mechanics of mussel adhesion. Proceedings of the National Academy of Sciences 103, 12999–13003.

Lee, H., Scherer, N.F., Messersmith, P.B., 2006c. Single-molecule mechanics of mussel adhesion. Proceedings of the National Academy of Sciences 103, 12999 LP – 13003. https://doi.org/10.1073/pnas.0605552103

Lejars, M., Margaillan, A., Bressy, C., 2012. Fouling release coatings: a nontoxic alternative to biocidal antifouling coatings. Chem Rev 112, 4347–4390.

Leng, C., Hung, H.-C., Sun, S., Wang, D., Li, Y., Jiang, S., Chen, Z., 2015a. Probing the surface hydration of nonfouling zwitterionic and PEG materials in contact with proteins. ACS Appl Mater Interfaces 7, 16881–16888.

Leng, C., Hung, H.-C., Sun, S., Wang, D., Li, Y., Jiang, S., Chen, Z., 2015b. Probing the surface hydration of nonfouling zwitterionic and PEG materials in contact with proteins. ACS Appl Mater Interfaces 7, 16881–16888.

Li, D., Wei, Q., Wu, C., Zhang, X., Xue, Q., Zheng, T., Cao, M., 2020. Superhydrophilicity and strong salt-affinity: Zwitterionic polymer grafted surfaces with significant potentials particularly in biological systems. Adv Colloid Interface Sci 278, 102141.

Li, E., Du, Z., Yuan, S., 2013. Properties of a water layer on hydrophilic and hydrophobic self-assembled monolayer surfaces: A molecular dynamics study. Sci China Chem 56, 773–781.

Li, L., 2017. Mussel-inspired Multifunctional Polymeric Materials with Bioengineering Applications. University of Alberta.

Li, L., Yan, B., Zhang, L., Tian, Y., Zeng, H., 2015. Mussel-inspired antifouling coatings bearing polymer loops. Chemical Communications 51, 15780–15783.

Li, L., Zeng, H., 2016. Marine mussel adhesion and bio-inspired wet adhesives. Biotribology 5, 44–51.

Li, N., Li, T., Qiao, X.-Y., Li, R., Yao, Y., Gong, Y.-K., 2020. Universal strategy for efficient fabrication of blood compatible surfaces via polydopamine-assisted surface-initiated activators regenerated by electron transfer atom-transfer radical polymerization of zwitterions. ACS Appl Mater Interfaces 12, 12337–12344.

Li, P., Cai, X., Wang, D., Chen, S., Yuan, J., Li, L., Shen, J., 2013. Hemocompatibility and anti-biofouling property improvement of poly (ethylene terephthalate) via self-polymerization of dopamine and covalent graft of zwitterionic cysteine. Colloids Surf B Biointerfaces 110, 327–332.

Li, Q., Elimelech, M., 2004. Organic fouling and chemical cleaning of nanofiltration membranes: measurements and mechanisms. Environ Sci Technol 38, 4683–4693.

Li, S., Chen, J., Wang, J., Zeng, H., 2021. Anti-biofouling Materials and Surfaces based on Mussel-inspired Chemistry. Mater Adv.

Li, X., Chen, Y., Hu, X., Zhang, Y., Hu, L., 2014. Desalination of dye solution utilizing PVA/PVDF hollow fiber composite membrane modified with TiO2 nanoparticles. J Memb Sci 471, 118–129.

Li, Y., Qin, M., Li, Ying, Cao, Y., Wang, W., 2014. Single Molecule Evidence for the Adaptive Binding of DOPA to Different Wet Surfaces. Langmuir 30, 4358–4366. https://doi.org/10.1021/la501189n

Lim, C., Huang, J., Kim, S., Lee, H., Zeng, H., Hwang, D.S., 2016a. Nanomechanics of poly (catecholamine) coatings in aqueous solutions. Angewandte Chemie International Edition 55, 3342–3346.

Lim, C., Huang, J., Kim, S., Lee, H., Zeng, H., Hwang, D.S., 2016b. Nanomechanics of Poly(catecholamine) Coatings in Aqueous Solutions. Angewandte Chemie International Edition 55, 3342–3346. https://doi.org/https://doi.org/10.1002/anie.201510319

Lin, Q., Gourdon, D., Sun, C., Holten-Andersen, N., Anderson, T.H., Waite, J.H., Israelachvili, J.N., 2007a. Adhesion mechanisms of the mussel foot proteins mfp-1 and mfp-3. Proceedings of the National Academy of Sciences 104, 3782–3786.

Lin, Q., Gourdon, D., Sun, C., Holten-Andersen, N., Anderson, T.H., Waite, J.H., Israelachvili, J.N., 2007b. Adhesion mechanisms of the mussel foot proteins mfp-1 and mfp-3. Proceedings of the National Academy of Sciences 104, 3782 LP – 3786. https://doi.org/10.1073/pnas.0607852104

Liu, A., Zhao, L., Bai, H., Zhao, H., Xing, X., Shi, G., 2009. Polypyrrole actuator with a bioadhesive surface for accumulating bacteria from physiological media. ACS Appl Mater Interfaces 1, 951–955.

Liu, C., Song, D., Zhang, W., He, Q., Huangfu, X., Sun, S., Sun, Z., Cheng, W., Ma, J., 2020. Constructing zwitterionic polymer brush layer to enhance gravity-driven membrane performance by governing biofilm formation. Water Res 168, 115181.

Liu, H., Liu, G., Zhang, M., Zhao, H., Jiang, Y., Gao, J., 2020. Rapid preparation of Tannic acid (TA) based zwitterionic nanofiltration membrane via a multiple layer-by-layer (mLBL) assembly strategy for enhanced antifouling performance. Sep Purif Technol 253, 117519.

Liu, L., Liu, J., Gao, B., Yang, F., 2012. Minute electric field reduced membrane fouling and improved performance of membrane bioreactor. Sep Purif Technol 86, 106–112.

Liu, L., Shao, B., Yang, F., 2013. Polydopamine coating–surface modification of polyester filter and fouling reduction. Sep Purif Technol 118, 226–233.

Liu, M., Wang, S., Wei, Z., Song, Y., Jiang, L., 2009a. Bioinspired design of a superoleophobic and low adhesive water/solid interface. Advanced Materials 21, 665–669.

Liu, M., Wang, S., Wei, Z., Song, Y., Jiang, L., 2009b. Bioinspired Design of a Superoleophobic and Low Adhesive Water/Solid Interface. Advanced Materials 21, 665–669. https://doi.org/https://doi.org/10.1002/adma.200801782

Liu, M., Zhou, J., Yang, Y., Zheng, M., Yang, J., Tan, J., 2015. Surface modification of zirconia with polydopamine to enhance fibroblast response and decrease bacterial activity in vitro: A potential technique for soft tissue engineering applications. Colloids Surf B Biointerfaces 136, 74–83.

Liu, P., Liu, S., Yu, X., Zhang, Y., 2021. Silane-triggered fabrication of stable waterborne superamphiphobic coatings. Chemical Engineering Journal 406, 127153.

Liu, X., Cao, J., Li, H., Li, J., Jin, Q., Ren, K., Ji, J., 2013. Mussel-inspired polydopamine: a biocompatible and ultrastable coating for nanoparticles in vivo. ACS Nano 7, 9384–9395.

Liu, Y., Ai, K., Lu, L., 2014. Polydopamine and its derivative materials: synthesis and promising applications in energy, environmental, and biomedical fields. Chem Rev 114, 5057–5115.

Lou, S.-T., Ouyang, Z.-Q., Zhang, Y., Li, X.-J., Hu, J., Li, M.-Q., Yang, F.-J., 2000. Nanobubbles on solid surface imaged by atomic force microscopy. Journal of Vacuum Science & Technology B: Microelectronics and Nanometer Structures Processing, Measurement, and Phenomena 18, 2573–2575.

Lu, Q., Danner, E., Waite, J.H., Israelachvili, J.N., Zeng, H., Hwang, D.S., 2013a. Adhesion of mussel foot proteins to different substrate surfaces. J R Soc Interface 10, 20120759.

Lu, Q., Danner, E., Waite, J.H., Israelachvili, J.N., Zeng, H., Hwang, D.S., 2013b. Adhesion of mussel foot proteins to different substrate surfaces. J R Soc Interface 10, 20120759.

Lu, Q., Huang, J., Maan, O., Liu, Y., Zeng, H., 2018. Probing molecular interaction mechanisms of organic fouling on polyamide membrane using a surface forces apparatus: Implication for wastewater treatment. Science of The Total Environment 622, 644–654.

Lu, Q., Hwang, D.S., Liu, Y., Zeng, H., 2012a. Molecular interactions of mussel protective coating protein, mcfp-1, from Mytilus californianus. Biomaterials 33, 1903–1911.

Lu, Q., Hwang, D.S., Liu, Y., Zeng, H., 2012b. Molecular interactions of mussel protective coating protein, mcfp-1, from Mytilus californianus. Biomaterials 33, 1903–1911. https://doi.org/https://doi.org/10.1016/j.biomaterials.2011.11.021

Lu, Q., Oh, D.X., Lee, Y., Jho, Y., Hwang, D.S., Zeng, H., 2013c. Nanomechanics of cation–π interactions in aqueous solution. Angewandte Chemie 125, 4036–4040.

Lu, Q., Oh, D.X., Lee, Y., Jho, Y., Hwang, D.S., Zeng, H., 2013d. Nanomechanics of Cation–π Interactions in Aqueous Solution. Angewandte Chemie International Edition 52, 3944–3948. https://doi.org/https://doi.org/10.1002/anie.201210365

Lu, Q., Oh, D.X., Lee, Y., Jho, Y., Hwang, D.S., Zeng, H., 2013e. Nanomechanics of Cation–π Interactions in Aqueous Solution. Angewandte Chemie International Edition 52, 3944–3948. https://doi.org/https://doi.org/10.1002/anie.201210365

Lu, Y., He, G., Carmalt, C.J., Parkin, I.P., 2016. Synthesis and characterization of omniphobic surfaces with thermal, mechanical and chemical stability. RSC Adv 6, 106491–106499.

Lu, Z., Xiao, J., Wang, Y., Meng, M., 2015. In situ synthesis of silver nanoparticles uniformly distributed on polydopamine-coated silk fibers for antibacterial application. J Colloid Interface Sci 452, 8–14.

Lyu, N., Du, Z., Qiu, H., Gao, P., Yao, Q., Xiong, K., Tu, Q., Li, X., Chen, B., Wang, M., 2020. Mimicking the Nitric Oxide ‐ Releasing and Glycocalyx Functions of Endothelium on Vascular Stent Surfaces. Advanced Science 7, 2002330.

Ma, H., Gao, P., Zhang, Y., Fan, D., Li, G., Du, B., Wei, Q., 2013. Engineering microstructured porous films for multiple applications via mussel-inspired surface coating. RSC Adv 3, 25291–25295.

Ma, J.C., Dougherty, D.A., 1997. The cation− π interaction. Chem Rev 97, 1303–1324.

Magin, C.M., Alge, D.L., Anseth, K.S., 2016. Bio-inspired 3D microenvironments: a new dimension in tissue engineering. Biomedical Materials 11, 22001.

Matin, A., Khan, Z., Zaidi, S.M.J., Boyce, M.C., 2011. Biofouling in reverse osmosis membranes for seawater desalination: phenomena and prevention. Desalination 281, 1–16.

McCloskey, B.D., Park, H.B., Ju, H., Rowe, B.W., Miller, D.J., Chun, B.J., Kin, K., Freeman, B.D., 2010. Influence of polydopamine deposition conditions on pure water flux and foulant adhesion resistance of reverse osmosis, ultrafiltration, and microfiltration membranes. Polymer (Guildf) 51, 3472–3485.

Meng, F.-N., Zhang, M.-Q., Ding, K., Zhang, T., Gong, Y.-K., 2018. Cell membrane mimetic PVDF microfiltration membrane with enhanced antifouling and separation performance for oil/water mixtures. J Mater Chem A Mater 6, 3231–3241.

Miao, R., Wang, L., Zhu, M., Deng, D., Li, S., Wang, J., Liu, T., Lv, Y., 2017. Effect of hydration forces on protein fouling of ultrafiltration membranes: the role of protein charge, hydrated ion species, and membrane hydrophilicity. Environ Sci Technol 51, 167–174.

Monnier, C.A., DeMartini, D.G., Waite, J.H., 2018. Intertidal exposure favors the soft-studded armor of adaptive mussel coatings. Nat Commun 9, 1–9.

Moreira, F.C., Boaventura, R.A.R., Brillas, E., Vilar, V.J.P., 2017. Electrochemical advanced oxidation processes: A review on their application to synthetic and real wastewaters. Appl Catal B 202, 217–261. https://doi.org/https://doi.org/10.1016/j.apcatb.2016.08.037

Müller, W.E.G., Wang, X., Proksch, P., Perry, C.C., Osinga, R., Gardères, J., Schröder, H.C., 2013. Principles of biofouling protection in marine sponges: a model for the design of novel biomimetic and bio-inspired coatings in the marine environment? Marine biotechnology 15, 375–398.

Mutschler, A., Tallet, L., Rabineau, M., Dollinger, C., Metz-Boutigue, M.-H., Schneider, F., Senger, B., Vrana, N.E., Schaaf, P., Lavalle, P., 2016. Unexpected bactericidal activity of poly (arginine)/hyaluronan nanolayered coatings. Chemistry of Materials 28, 8700–8709.

Nguyen, A., Azari, S., Zou, L., 2013a. Coating zwitterionic amino acid l-DOPA to increase fouling resistance of forward osmosis membrane. Desalination 312, 82–87.

Nguyen, A., Azari, S., Zou, L., 2013b. Coating zwitterionic amino acid l-DOPA to increase fouling resistance of forward osmosis membrane. Desalination 312, 82–87.

Nicolas , B., J., H.D., Sung-Hei, H., A., R.S., Staffan, K., S., W.J., 2006. Involvement of Nitric Oxide in Biofilm Dispersal of Pseudomonas aeruginosa. J Bacteriol 188, 7344–7353. https://doi.org/10.1128/JB.00779-06

Nilsson, D., Chen, M., Kugler, T., Remonen, T., Armgarth, M., Berggren, M., 2002. Bi‐stable and dynamic current modulation in electrochemical organic transistors. Advanced Materials 14, 51–54.

Nilsson, D., Robinson, N., Berggren, M., Forchheimer, R., 2005. Electrochemical logic circuits. Advanced Materials 17, 353–358.

Palazon, F., Léonard, D., Le Mogne, T., Zuttion, F., Chevalier, C., Phaner-Goutorbe, M., Souteyrand, É., Chevolot, Y., Cloarec, J.-P., 2015. Orthogonal chemical functionalization of patterned gold on silica surfaces. Beilstein journal of nanotechnology 6, 2272–2277.

Park, H.-S., Ko, S.-J., Park, J.-S., Kim, J.Y., Song, H.-K., 2013. Redox-active charge carriers of conducting polymers as a tuner of conductivity and its potential window. Sci Rep 3, 2454.

Park, J.H., Bae, Y.H., 2002a. Hydrogels based on poly (ethylene oxide) and poly (tetramethylene oxide) or poly (dimethyl siloxane): synthesis, characterization, in vitro protein adsorption and platelet adhesion. Biomaterials 23, 1797–1808.

Park, J.H., Bae, Y.H., 2002b. Hydrogels based on poly(ethylene oxide) and poly(tetramethylene oxide) or poly(dimethyl siloxane): synthesis, characterization, in vitro protein adsorption and platelet adhesion. Biomaterials 23, 1797–1808. https://doi.org/https://doi.org/10.1016/S0142-9612(01)00306-4

Parsons, D.F., Eom, N., Walsh, R.B., Craig, V.S.J., 2019. A new DLVO-R theory: surface roughness and nanoparticle stability, in: Harnessing Nanoscale Surface Interactions. Elsevier, pp. 129–147.

Parsons, D.F., Walsh, R.B., Craig, V.S.J., 2014. Surface forces: Surface roughness in theory and experiment. J Chem Phys 140, 164701.

Peng, B., Wang, J., Peng, Z., Zhou, S., Wang, F., Ji, Y., Ye, Z., Zhou, X., Lin, T., Zhang, X., 2012. Studies on the synthesis, pungency and anti-biofouling performance of capsaicin analogues. Sci China Chem 55, 435–442.

Petsev, D.N., 2004. Emulsions: structure, stability and interactions. Elsevier.

Pezzotti, G., Boschetto, F., Ohgitani, E., Fujita, Y., Zhu, W., Marin, E., McEntire, B.J., Bal, B.S., Mazda, O., 2021. Silicon nitride: a potent solid-state bioceramic inactivator of ssRNA viruses. Sci Rep 11, 1–18.

Pietsch, W., Rumpf, H., 1967. Adhesion capillary pressure liquid volume and angle of contact of a liquid bridge between 2 spheres. Chemie Ingenieur Technik 39, 885.

Prikhno, I.A., Safronova, E.Y., Yaroslavtsev, A.B., 2016a. Hybrid materials based on perfluorosulfonic acid membrane and functionalized carbon nanotubes: Synthesis, investigation and transport properties. Int J Hydrogen Energy 41, 15585–15592. https://doi.org/https://doi.org/10.1016/j.ijhydene.2016.04.100

Prikhno, I.A., Safronova, E.Y., Yaroslavtsev, A.B., 2016b. Hybrid materials based on perfluorosulfonic acid membrane and functionalized carbon nanotubes: Synthesis, investigation and transport properties. Int J Hydrogen Energy 41, 15585–15592. https://doi.org/https://doi.org/10.1016/j.ijhydene.2016.04.100

Putatunda, S., Bhattacharya, S., Sen, D., Bhattacharjee, C., 2019. A review on the application of different treatment processes for emulsified oily wastewater. International journal of environmental science and technology 16, 2525–2536.

Raman, S., Utzig, T., Baimpos, T., Shrestha, B.R., Valtiner, M., 2014. Deciphering the scaling of single-molecule interactions using Jarzynski's equality. Nat Commun 5, 1–7.

Rana, D., Matsuura, T., 2010. Surface modifications for antifouling membranes. Chem Rev 110, 2448–2471.

Rebetez, G., Bardagot, O., Affolter, J., Réhault, J., Banerji, N., 2022. What drives the kinetics and doping level in the electrochemical reactions of PEDOT: PSS? Adv Funct Mater 32, 2105821.

Reyes-Bozo, L., Escudey, M., Vyhmeister, E., Higueras, P., Godoy-Faúndez, A., Salazar, J.L., Valdés-González, H., Wolf-Sepúlveda, G., Herrera-Urbina, R., 2015. Adsorption of biosolids and their main components on chalcopyrite, molybdenite and pyrite: Zeta potential and FTIR spectroscopy studies. Miner Eng 78, 128–135.

Reynolds, J.R., Thompson, B.C., Skotheim, T.A., 2019. Conjugated Polymers: Properties, Processing, and Applications. CRC press.

Ryu, J.H., Hong, S., Lee, H., 2015. Bio-inspired adhesive catechol-conjugated chitosan for biomedical applications: A mini review. Acta Biomater 27, 101–115.

Rzepecki, L.M., Hansen, K.M., Waite, J.H., 1992. Characterization of a cystine-rich polyphenolic protein family from the blue mussel Mytilus edulis L. Biol Bull 183, 123–137.

Sakarkar, S., Muthukumaran, S., Jegatheesan, V., 2021. Tailoring the effects of titanium dioxide (Tio2) and polyvinyl alcohol (pva) in the separation and antifouling performance of thin-film composite polyvinylidene fluoride (pvdf) membrane. Membranes (Basel) 11, 241.

Salgin, S., Salgin, U., Bahadir, S., 2012. Zeta potentials and isoelectric points of biomolecules: the effects of ion types and ionic strengths. Int. J. Electrochem. Sci 7, 12404–12414.

Salonen, L.M., Ellermann, M., Diederich, F., 2011. Aromatic rings in chemical and biological recognition: energetics and structures. Angewandte Chemie International Edition 50, 4808–4842.

Schlenoff, J.B., 2014. Zwitteration: coating surfaces with zwitterionic functionality to reduce nonspecific adsorption. Langmuir 30, 9625–9636.

Schultz, M.P., Bendick, J.A., Holm, E.R., Hertel, W.M., 2011. Economic impact of biofouling on a naval surface ship. Biofouling 27, 87–98.

Schultz, M.P., Kavanagh, C.J., Swain, G.W., 1999. Hydrodynamic forces on barnacles: Implications on detachment from fouling ‐ release surfaces. Biofouling 13, 323 ‐ 335.

Schulze, A., Went, M., Prager, A., 2016. Membrane functionalization with hyperbranched polymers. Materials 9, 706.

Seo, J., Kim, J.H., Lee, M., Moon, J., Yi, D.K., Paik, U., 2016. Size-dependent interactions of silica nanoparticles with a flat silica surface. J Colloid Interface Sci 483, 177–184.

Shannon, M.A., Bohn, P.W., Elimelech, M., Georgiadis, J.G., Marinas, B.J., Mayes, A.M., 2008. Science and technology for water purification in the coming decades. Nature 452, 301–310.

Shao, Q., Jiang, S., 2015. Molecular understanding and design of zwitterionic materials. Advanced Materials 27, 15–26.

Sheikholeslami, R., 1999. Composite fouling - inorganic and biological: A review. Environmental progress 18, 113 - 122.

Shi, C., Xie, L., Zhang, L., Lu, X., Zeng, H., 2020. Probing the interaction mechanism between oil droplets with asphaltenes and solid surfaces using AFM. J Colloid Interface Sci 558, 173–181.

Shirazi, S., Lin, C.-J., Chen, D., 2010. Inorganic fouling of pressure-driven membrane processes—A critical review. Desalination 250, 236–248.

Sileika, T.S., Kim, H.-D., Maniak, P., Messersmith, P.B., 2011. Antibacterial performance of polydopamine-modified polymer surfaces containing passive and active components. ACS Appl Mater Interfaces 3, 4602–4610.

Singh, V., Kumar, T., 2019. Study of modified PEDOT: PSS for tuning the optical properties of its conductive thin films. Journal of Science: Advanced Materials and Devices 4, 538–543.

Sirringhaus, H., Kawase, T., Friend, R.H., Shimoda, T., Inbasekaran, M., Wu, W., Woo, E.P., 2000. High-resolution inkjet printing of all-polymer transistor circuits. Science (1979) 290, 2123–2126.

Steinle-Darling, E., Zedda, M., Plumlee, M.H., Ridgway, H.F., Reinhard, M., 2007. Evaluating the impacts of membrane type, coating, fouling, chemical properties and water chemistry on reverse osmosis rejection of seven nitrosoalklyamines, including NDMA. Water Res 41, 3959–3967.

Stipp, S.L.S., Eggleston, C.M., Nielsen, B.S., 1994. Calcite surface structure observed at microtopographic and molecular scales with atomic force microscopy (AFM). Geochim Cosmochim Acta 58, 3023–3033.

Su, L., Yu, Y., Zhao, Y., Liang, F., Zhang, X., 2016. Strong antibacterial polydopamine coatings prepared by a shaking-assisted method. Sci Rep 6, 1–8.

Sui, Y., Gao, X., Wang, Z., Gao, C., 2012. Antifouling and antibacterial improvement of surface-functionalized poly (vinylidene fluoride) membrane prepared via dihydroxyphenylalanine-initiated atom transfer radical graft polymerizations. J Memb Sci 394, 107–119.

Takenaga, M., Jo, S., Graupe, M., Lee, T.R., 2008. Effective van der Waals surface energy of self-assembled monolayer films having systematically varying degrees of molecular fluorination. J Colloid Interface Sci 320, 264–267.

Tang, Y., Cai, X., Xiang, Y., Zhao, Y., Zhang, X., Wu, Z., 2017. Cross-linked antifouling polysaccharide hydrogel coating as extracellular matrix mimics for wound healing. J Mater Chem B 5, 2989–2999. https://doi.org/10.1039/C6TB03222B

Tanis-Kanbur, M.B., Velioğlu, S., Tanudjaja, H.J., Hu, X., Chew, J.W., 2018. Understanding membrane fouling by oil-in-water emulsion via experiments and molecular dynamics simulations. J Memb Sci 566, 140–150.

Taylor, S.W., Waite, J.H., Ross, M.M., Shabanowitz, J., Hunt, D.F., 1994. trans-2, 3-cis-3, 4-Dihydroxyproline, a new naturally occurring amino acid, is the sixth residue in the tandemly repeated consensus decapeptides of an adhesive protein from Mytilus edulis. J Am Chem Soc 116, 10803–10804.

Tehrani, P., Kanciurzewska, A., Crispin, X., Robinson, N.D., Fahlman, M., Berggren, M., 2007. The effect of pH on the electrochemical over-oxidation in PEDOT: PSS films. Solid State Ion 177, 3521–3527.

Tengvall, P., 2011. 4.406 - Protein Interactions with Biomaterials, in: Ducheyne, P.B.T.-C.B. (Ed.), . Elsevier, Oxford, pp. 63–73. https://doi.org/https://doi.org/10.1016/B978-0-08-055294-1.00006-4

Thakur, V.K., Lin, M.-F., Tan, E.J., Lee, P.S., 2012a. Green aqueous modification of fluoropolymers for energy storage applications. J Mater Chem 22, 5951–5959.

Thakur, V.K., Lin, M.-F., Tan, E.J., Lee, P.S., 2012b. Green aqueous modification of fluoropolymers for energy storage applications. J Mater Chem 22, 5951–5959.

Tong, M., Zhu, P., Jiang, X., Kim, H., 2011. Influence of natural organic matter on the deposition kinetics of extracellular polymeric substances (EPS) on silica. Colloids Surf B Biointerfaces 87, 151–158.

Tsai, W.-B., Chen, W.-T., Chien, H.-W., Kuo, W.-H., Wang, M.-J., 2011. Poly (dopamine) coating of scaffolds for articular cartilage tissue engineering. Acta Biomater 7, 4187–4194.

Utzig, T., Stock, P., Valtiner, M., 2016. Resolving Non ‐ Specific and Specific Adhesive Interactions of Catechols at Solid/Liquid Interfaces at the Molecular Scale. Angewandte Chemie 128, 9676 – 9680.

Vaisocherová, H., Brynda, E., Homola, J., 2015. Functionalizable low-fouling coatings for label-free biosensing in complex biological media: advances and applications. Anal Bioanal Chem 407, 3927–3953.

Valle-Delgado, J.J., Molina-Bolívar, J.A., Galisteo-González, F., Gálvez-Ruiz, M.J., Feiler, A., Rutland, M., 2004. Interactions between bovine serum albumin layers adsorbed on different substrates measured with an atomic force microscope. Physical Chemistry Chemical Physics 6, 1482–1486.

Vega, M., Martín del Valle, E.M., Pérez, M., Pecharromán, C., Marcelo, G., 2018. Color engineering of silicon nitride surfaces to characterize the polydopamine refractive index. ChemPhysChem 19, 3418–3424.

Velayi, E., Norouzbeigi, R., 2020. A mesh membrane coated with dual-scale superhydrophobic nano zinc oxide: Efficient oil-water separation. Surf Coat Technol 385, 125394.

Wai, K.P., Koo, C.H., Pang, Y.L., Chong, W.C., Lau, W.J., 2020. In situ immobilization of silver on polydopamine-coated composite membrane for enhanced antibacterial properties. Journal of Water Process Engineering 33, 100989.

Waite, J.H., 1983. Evidence for a repeating 3, 4-dihydroxyphenylalanine-and hydroxyproline-containing decapeptide in the adhesive protein of the mussel, Mytilus edulis L. Journal of Biological Chemistry 258, 2911–2915.

Waite, J.H., Qin, X., 2001. Polyphosphoprotein from the adhesive pads of Mytilus edulis. Biochemistry 40, 2887–2893.

Waite, J.H., Tanzer, M.L., 1981. Polyphenolic substance of Mytilus edulis: novel adhesive containing L-dopa and hydroxyproline. Science (1979) 212, 1038–1040.

WAITE, J.H., TANZER, M.L., 1981. Polyphenolic Substance of Mytilus edulis: Novel Adhesive Containing L-Dopa and Hydroxyproline. Science (1979) 212, 1038 LP – 1040. https://doi.org/10.1126/science.212.4498.1038

Wang, C., Hu, R., Morrissey, J.J., Kharasch, E.D., Singamaneni, S., 2017. Single molecule force spectroscopy to compare natural versus artificial antibody–antigen interaction. Small 13, 1604255.

Wang, C., Park, M.J., Seo, D.H., Shon, H.K., 2021. Inkjet printing of graphene oxide and dopamine on nanofiltration membranes for improved anti-fouling properties and chlorine resistance. Sep Purif Technol 254, 117604.

Wang, D., Zhang, W., Zhou, D., n.d. Supporting Information Antagonistic Effects of Humic Acid and Iron Oxyhydroxide Grain-Coating on Biochar Nanoparticle Transport in Saturated Sand.

Wang, J., Liu, Q., Zeng, H., 2013a. Understanding copper activation and xanthate adsorption on sphalerite by time-of-flight secondary ion mass spectrometry, X-ray photoelectron spectroscopy, and in situ scanning electrochemical microscopy. The Journal of Physical Chemistry C 117, 20089–20097.

Wang, J., Liu, Q., Zeng, H., 2013b. Understanding copper activation and xanthate adsorption on sphalerite by time-of-flight secondary ion mass spectrometry, X-ray photoelectron spectroscopy, and in situ scanning electrochemical microscopy. The Journal of Physical Chemistry C 117, 20089–20097.

Wang, J., Xie, L., Han, L., Wang, X., Wang, Jianmei, Zeng, H., 2021a. In-situ probing of electrochemical dissolution and surface properties of chalcopyrite with implications for the dissolution kinetics and passivation mechanism. J Colloid Interface Sci 584, 103–113.

Wang, J., Xie, L., Han, L., Wang, X., Wang, Jianmei, Zeng, H., 2021b. In-situ probing of electrochemical dissolution and surface properties of chalcopyrite with implications for the dissolution kinetics and passivation mechanism. J Colloid Interface Sci 584, 103–113.

Wang, J., Xie, L., Li, S., Wang, Jianmei, Zhang, J., Zeng, H., 2021c. Probing the In Situ Redox Behavior of Selenium on a Pyrite Surface by Scanning Electrochemical Microscopy. The Journal of Physical Chemistry C 125, 3018–3026.

Wang, Jingyi, Xie, L., Lu, Q., Wang, X., Wang, Jianmei, Zeng, H., 2020. Electrochemical investigation of the interactions of organic and inorganic depressants on basal and edge planes of molybdenite. J Colloid Interface Sci 570, 350–361.

Wang, S.-Y., Fang, L.-F., Cheng, L., Jeon, S., Kato, N., Matsuyama, H., 2018. Novel ultrafiltration membranes with excellent antifouling properties and chlorine resistance using a poly (vinyl chloride)-based copolymer. J Memb Sci 549, 101–110.

Wang, W., Zhu, L., Shan, B., Xie, C., Liu, C., Cui, F., Li, G., 2018. Preparation and characterization of SLS-CNT/PES ultrafiltration membrane with antifouling and antibacterial properties. J Memb Sci 548, 459–469. https://doi.org/https://doi.org/10.1016/j.memsci.2017.11.046

Wang, Z., Ou, J., Wang, Y., Xue, M., Wang, F., Pan, B., Li, C., Li, W., 2015. Anti-bacterial superhydrophobic silver on diverse substrates based on the mussel-inspired polydopamine. Surf Coat Technol 280, 378–383.

Wang, Z., Yang, H.-C., He, F., Peng, S., Li, Y., Shao, L., Darling, S.B., 2019. Mussel-inspired surface engineering for water-remediation materials. Matter 1, 115–155.

Warner, S.C., Waite, J.H., 1999. Expression of multiple forms of an adhesive plaque protein in an individual mussel, Mytilus edulis. Mar Biol 134, 729–734.

Wei, C., Bard, A.J., Mirkin, M. V, 1995. Scanning electrochemical microscopy. 31. Application of SECM to the study of charge transfer processes at the liquid/liquid interface. J Phys Chem 99, 16033–16042.

Wittstock, G., Kartio, I., Hirsch, D., Kunze, S., Szargan, R., 1996a. Oxidation of galena in acetate buffer investigated by atomic force microscopy and photoelectron spectroscopy. Langmuir 12, 5709–5721.

Wittstock, G., Kartio, I., Hirsch, D., Kunze, S., Szargan, R., 1996b. Oxidation of galena in acetate buffer investigated by atomic force microscopy and photoelectron spectroscopy. Langmuir 12, 5709–5721.

Wong, T.-S., Kang, S.H., Tang, S.K.Y., Smythe, E.J., Hatton, B.D., Grinthal, A., Aizenberg, J., 2011a. Bioinspired self-repairing slippery surfaces with pressure-stable omniphobicity. Nature 477, 443–447.

Wong, T.-S., Kang, S.H., Tang, S.K.Y., Smythe, E.J., Hatton, B.D., Grinthal, A., Aizenberg, J., 2011b. Bioinspired self-repairing slippery surfaces with pressure-stable omniphobicity. Nature 477, 443–447. https://doi.org/10.1038/nature10447

Wu, F., Pu, N., Ye, G., Sun, T., Wang, Z., Song, Y., Wang, W., Huo, X., Lu, Y., Chen, J., 2017. Performance and mechanism of uranium adsorption from seawater to poly (dopamine)-inspired sorbents. Environ Sci Technol 51, 4606–4614.

Xi, Z.-Y., Xu, Y.-Y., Zhu, L.-P., Wang, Y., Zhu, B.-K., 2009. A facile method of surface modification for hydrophobic polymer membranes based on the adhesive behavior of poly (DOPA) and poly (dopamine). J Memb Sci 327, 244–253.

Xie, L., Gong, L., Zhang, J., Han, L., Xiang, L., Chen, J., Liu, J., Yan, B., Zeng, H., 2019a. A wet adhesion strategy via synergistic cation–π and hydrogen bonding interactions of antifouling zwitterions and mussel-inspired binding moieties. J Mater Chem A Mater 7, 21944–21952.

Xie, L., Gong, L., Zhang, J., Han, L., Xiang, L., Chen, J., Liu, J., Yan, B., Zeng, H., 2019b. A wet adhesion strategy via synergistic cation–π and hydrogen bonding interactions of antifouling zwitterions and mussel-inspired binding moieties. J Mater Chem A Mater 7, 21944–21952.

Xie, L., Shi, C., Cui, X., Zeng, H., 2017. Surface forces and interaction mechanisms of emulsion drops and gas bubbles in complex fluids. Langmuir 33, 3911–3925.

Xie, L., Shi, C., Wang, J., Huang, J., Lu, Q., Liu, Q., Zeng, H., 2015. Probing the interaction between air bubble and sphalerite mineral surface using atomic force microscope. Langmuir 31, 2438–2446.

Xie, L., Wang, J., Shi, C., Huang, J., Zhang, H., Liu, Qi, Liu, Qingxia, Zeng, H., 2016a. Probing surface interactions of electrochemically active galena mineral surface using atomic force microscopy. The Journal of Physical Chemistry C 120, 22433–22442.

Xie, L., Wang, J., Shi, C., Huang, J., Zhang, H., Liu, Qi, Liu, Qingxia, Zeng, H., 2016b. Probing surface interactions of electrochemically active galena mineral surface using atomic force microscopy. The Journal of Physical Chemistry C 120, 22433–22442.

Xie, L., Wang, J., Shi, C., Huang, J., Zhang, H., Liu, Qi, Liu, Qingxia, Zeng, H., 2016c. Probing surface interactions of electrochemically active galena mineral surface using atomic force microscopy. The Journal of Physical Chemistry C 120, 22433–22442.

Xu, F., Wang, B., Yang, D., Ming, X., Jiang, Y., Hao, J., Qiao, Y., Tian, Y., 2018. TG-FTIR and Py-GC/MS study on pyrolysis mechanism and products distribution of waste bicycle tire. Energy Convers Manag 175, 288–297.

Xu, J., Ma, A., Liu, T., Lu, C., Wang, D., Xu, H., 2013a. Janus-like Pickering emulsions and their controllable coalescence. Chemical Communications 49, 10871–10873. https://doi.org/10.1039/C3CC46738D

Xu, J., Ma, A., Liu, T., Lu, C., Wang, D., Xu, H., 2013b. Janus-like Pickering emulsions and their controllable coalescence. Chemical Communications 49, 10871–10873. https://doi.org/10.1039/C3CC46738D

Xu, P., Wang, H., Tong, R., Du, Q., Zhong, W., 2006. Preparation and morphology of SiO2/PMMA nanohybrids by microemulsion polymerization. Colloid Polym Sci 284, 755–762.

Xu, Z., Zhang, J., Shan, M., Li, Y., Li, B., Niu, J., Zhou, B., Qian, X., 2014. Organosilane-functionalized graphene oxide for enhanced antifouling and mechanical properties of polyvinylidene fluoride ultrafiltration membranes. J Memb Sci 458, 1–13.

Yang, B., Lim, C., Hwang, D.S., Cha, H.J., 2016. Switch of surface adhesion to cohesion by Dopa-Fe3+ complexation, in response to microenvironment at the mussel plaque/substrate interface. Chemistry of Materials 28, 7982–7989.

Yang, C., Ding, X., Ono, R.J., Lee, H., Hsu, L.Y., Tong, Y.W., Hedrick, J., Yang, Y.Y., 2014a. Brush - like polycarbonates containing dopamine, cations, and PEG providing a broad ‑ spectrum, antibacterial, and antifouling surface via one ‑ step coating. Advanced Materials 26, 7346–7351.

Yang, C., Ding, X., Ono, R.J., Lee, H., Hsu, L.Y., Tong, Y.W., Hedrick, J., Yang, Y.Y., 2014b. Brush-Like Polycarbonates Containing Dopamine, Cations, and PEG Providing a Broad-Spectrum, Antibacterial, and Antifouling Surface via One-Step Coating. Advanced Materials 26, 7346–7351. https://doi.org/https://doi.org/10.1002/adma.201402059

Yang, H., Lan, Y., Zhu, W., Li, W., Xu, D., Cui, J., Shen, D., Li, G., 2012. Polydopamine-coated nanofibrous mats as a versatile platform for producing porous functional membranes. J Mater Chem 22, 16994–17001.

Yang, H., Waldman, R.Z., Wu, M., Hou, J., Chen, L., Darling, S.B., Xu, Z., 2018. Dopamine: just the right medicine for membranes. Adv Funct Mater 28, 1705327.

Yang, H.-C., Luo, J., Lv, Y., Shen, P., Xu, Z.-K., 2015a. Surface engineering of polymer membranes via mussel-inspired chemistry. J Memb Sci 483, 42–59.

Yang, H.-C., Luo, J., Lv, Y., Shen, P., Xu, Z.-K., 2015b. Surface engineering of polymer membranes via mussel-inspired chemistry. J Memb Sci 483, 42–59.

Yebra, D.M., Kiil, S., Dam-Johansen, K., 2004a. Antifouling technology—past, present and future steps towards efficient and environmentally friendly antifouling coatings. Prog Org Coat 50, 75–104.

Yebra, D.M., Kiil, S., Dam-Johansen, K., 2004b. Antifouling technology—past, present and future steps towards efficient and environmentally friendly antifouling coatings. Prog Org Coat 50, 75–104. https://doi.org/https://doi.org/10.1016/j.porgcoat.2003.06.001

Yi, G., Chen, S., Quan, X., Wei, G., Fan, X., Yu, H., 2018. Enhanced separation performance of carbon nanotube–polyvinyl alcohol composite membranes for emulsified oily wastewater treatment under electrical assistance. Sep Purif Technol 197, 107–115.

Yin, J., Mei, M.L., Li, Q., Xia, R., Zhang, Z., Chu, C.H., 2016. Self-cleaning and antibiofouling enamel surface by slippery liquid-infused technique. Sci Rep 6, 25924. https://doi.org/10.1038/srep25924

Yu, B., Liu, J., Liu, S., Zhou, F., 2010. Pdop layer exhibiting zwitterionicity: a simple electrochemical interface for governing ion permeability. Chemical communications 46, 5900–5902.

Yu, J., Wei, W., Danner, E., Ashley, R.K., Israelachvili, J.N., Waite, J.H., 2011. Mussel protein adhesion depends on interprotein thiol-mediated redox modulation. Nat Chem Biol 7, 588–590.

Yu, L., Han, M., He, F., 2017. A review of treating oily wastewater. Arabian journal of chemistry 10, S1913–S1922.

Yu, M., Hwang, J., Deming, T.J., 1999a. Role of L-3, 4-dihydroxyphenylalanine in mussel adhesive proteins. J Am Chem Soc 121, 5825–5826.

Yu, M., Hwang, J., Deming, T.J., 1999b. Role of l-3,4-Dihydroxyphenylalanine in Mussel Adhesive Proteins. J Am Chem Soc 121, 5825–5826. https://doi.org/10.1021/ja990469y

Yu, S., Li, G., Liu, R., Ma, D., Xue, W., 2018. Dendritic Fe3O4@ poly (dopamine)@ PAMAM nanocomposite as controllable NO ‐ releasing material: a synergistic photothermal and NO antibacterial study. Adv Funct Mater 28, 1707440.

Zeng, H., Hwang, D.S., Israelachvili, J.N., Waite, J.H., 2010. Strong reversible Fe3+-mediated bridging between dopa-containing protein films in water. Proceedings of the National Academy of Sciences 107, 12850–12853.

Zhang, C., Gong, L., Xiang, L., Du, Y., Hu, W., Zeng, H., Xu, Z.-K., 2017a. Deposition and adhesion of polydopamine on the surfaces of varying wettability. ACS Appl Mater Interfaces 9, 30943–30950.

Zhang, C., Li, H.-N., Du, Y., Ma, M.-Q., Xu, Z.-K., 2017b. CuSO4/H2O2-triggered polydopamine/poly (sulfobetaine methacrylate) coatings for antifouling membrane surfaces. Langmuir 33, 1210–1216.

Zhang, J., Cheah, Y.S., Santhanakrishnan, S., Neoh, K.G., Chai, C.L.L., 2017. Methoxy group substitution on catechol ring of dopamine facilitates its polymerization and formation of surface coatings. Polymer (Guildf) 116, 5–15.

Zhang, J., Sekyere, D.T., Niwamanya, N., Huang, Y., Barigye, A., Tian, Y., 2022. Study on the Staged and Direct Fast Pyrolysis Behavior of Waste Pine Sawdust Using High Heating Rate TG-FTIR and Py-GC/MS. ACS Omega.

Zhang, J., Xiang, L., Yan, B., Zeng, H., 2020a. Nanomechanics of Anion− Π Interaction in Aqueous Solution. J Am Chem Soc 142, 1710–1714.

Zhang, J., Xiang, L., Yan, B., Zeng, H., 2020b. Nanomechanics of Anion−π Interaction in Aqueous Solution. J Am Chem Soc 142, 1710–1714. https://doi.org/10.1021/jacs.9b11552

Zhang, P., Wang, Shasha, Wang, Shutao, Jiang, L., 2015a. Superwetting surfaces under different media: effects of surface topography on wettability. Small 11, 1939–1946.

Zhang, P., Wang, Shasha, Wang, Shutao, Jiang, L., 2015b. Superwetting Surfaces under Different Media: Effects of Surface Topography on Wettability. Small 11, 1939–1946. https://doi.org/https://doi.org/10.1002/smll.201401869

Zhang, W., Yang, F.K., Han, Y., Gaikwad, R., Leonenko, Z., Zhao, B., 2013. Surface and tribological behaviors of the bioinspired polydopamine thin films under dry and wet conditions. Biomacromolecules 14, 394–405.

Zhang, Y., Ma, J., Shao, L., 2020. Ultra-thin trinity coating enabled by competitive reactions for unparalleled molecular separation. J Mater Chem A Mater 8, 5078–5085.

Zhang, Z., Zhang, J., Zhang, B., Tang, J., 2013. Mussel-inspired functionalization of graphene for synthesizing Ag-polydopamine-graphene nanosheets as antibacterial materials. Nanoscale 5, 118–123.

Zhao, C., Zhang, G., Xu, X., Yang, F., Yang, Y., 2017. Rapidly self-assembled polydopamine coating membranes with polyhexamethylene guanidine: Formation, characterization and antifouling evaluation. Colloids Surf A Physicochem Eng Asp 512, 41–50.

Zhao, H., Waite, J.H., 2006a. Linking adhesive and structural proteins in the attachment plaque of Mytilus californianus. Journal of Biological Chemistry 281, 26150–26158.

Zhao, H., Waite, J.H., 2006b. Proteins in load-bearing junctions: the histidine-rich metal-binding protein of mussel byssus. Biochemistry 45, 14223–14231.

Zhao, J., Shi, Q., Luan, S., Song, L., Yang, H., Shi, H., Jin, J., Li, X., Yin, J., Stagnaro, P., 2011. Improved biocompatibility and antifouling property of polypropylene non-woven fabric membrane by surface grafting zwitterionic polymer. J Memb Sci 369, 5–12.

Zhao, W., Ye, Q., Hu, H., Wang, X., Zhou, F., 2014. Grafting zwitterionic polymer brushes via electrochemical surface-initiated atomic-transfer radical polymerization for anti-fouling applications. J Mater Chem B 2, 5352–5357.

Zheng, N., Huang, Y., Sun, W., Du, X., Liu, H.-Y., Moody, S., Gao, J., Mai, Y.-W., 2016. In-situ pull-off of ZnO nanowire from carbon fiber and improvement of interlaminar toughness of hierarchical ZnO nanowire/carbon fiber hydrid composite laminates. Carbon N Y 110, 69–78.

Zhou, Q.L.B.Y.W.Y.F., 2011. Highly Selective Uptake and Release of Charged Molecules by pH‐Responsive Polydopamine Microcapsules. Macromol Biosci 11, 1227‐1234.

Zhu, B., Edmondson, S., 2011. Polydopamine-melanin initiators for surface-initiated ATRP. Polymer (Guildf) 52, 2141–2149.

Zhu, J., 2010. Bioactive modification of poly(ethylene glycol) hydrogels for tissue engineering. Biomaterials 31, 4639–4656.